Exploring the coordination chemistry of thallium-201 and its therapeutic potential for use in molecular radionuclide therapy

Rigby, Alex

Awarding institution:
King's College London

Exploring the coordination chemistry of thallium-201 and its therapeutic potential for use in molecular radionuclide therapy

Alex Charles Rigby

Department of Imaging Chemistry & Biology
School of Biomedical Engineering and Imaging Sciences
King's College London
Rayne Institute, 4th Floor Lambeth Wing
St Thomas' Hospital
London, SE1 7EH

ABSTRACT

^{201}Tl ($t_{1/2}$ = 73 hours) can be tracked *in vivo* by SPECT via its gamma emissions, whilst simultaneously delivering a potentially therapeutic dose to tumours via its low-energy Auger electron emissions (~37 Auger electrons/decay). Their high linear energy transfer (LET) and short range (typically <1 micrometre) make Auger electron-emitters attractive for molecular radionuclide therapy (MRT). Targeted delivery of ^{201}Tl has been hindered due to lack of suitable bifunctional chelator chemistry. We aimed to find a chelator that forms a kinetically stable complex with Tl^{3+} and move on to developing a bioconjugate to selectively deliver radiotherapy to cancer cells.

A wide range of oxidation methods and chelators for Tl^{3+} have been evaluated, including DOTA, DTPA and H_4pypa. The DNA damaging potential of [^{201}Tl]Tl^{+} and [^{201}Tl]Tl^{3+} was demonstrated using a cell free isolated plasmid DNA damage assay. Serum stability of radiolabelled [^{201}Tl]Tl^{3+} complexes, incubated 37 °C, were monitored by RP-TLC at various time points (up to 144 h). These complexes were also investigated using MS, NMR and X-ray crystallography. Furthermore, a PSMA-targeting bioconjugate of H_4pypa coupled to a PSMA peptide via a lipophilic linker, based on the structure of PSMA-617, was developed. This was subsequently radiolabelled with [^{201}Tl]Tl^{3+}. SPECT imaging was used to probe the *in vivo* biodistribution and stability of the [^{201}Tl]Tl-pypa-PSMA bioconjugate in healthy SCID/beige mice, and compared to [^{201}Tl]TlCl and [^{201}Tl]$TlCl_3$. Additionally, DU145 PSMA-positive and PSMA-negative prostate cancer tumour xenograft models were used to investigate the bioconjugate's biodistribution.

Using iodobeads and HCl (0.5 M), [^{201}T]Tl^{3+} was generated from commercially available [^{201}Tl]Tl^{+} in a quick, simple and biologically friendly way. Gel electrophoresis results showed that [^{201}Tl]Tl^{+} and [^{201}Tl]Tl^{3+} both cause single and double strand breaks in DNA after incubation up to 144

hours. [$^{nat/201}$Tl]Tl^{3+} was then shown to be chelated by various commercially available chelators such as DTPA and DOTA, as well as novel chelators such as H_4pypa and H_4noneunpa. H_4pypa was radiolabelled in high radiochemical yields (98 $\pm$ 2 %) at RT within 15 minutes. The complex remained intact in serum for an hour, but integrity dropped to 61 % after 24 h and 44 % after 48 h. *In vivo* experiments using [^{201}Tl]Tl-pypa-PSMA showed excretion through the kidneys and bladder with little heart uptake observed at early time points, suggesting adequate in vivo stability for delivery to tumours. In contrast, [^{201}Tl]TlCl and [^{201}Tl]$TlCl_3$ both showed high heart uptake at 15 minutes, and renal excretion over the following hour. The DU145 PSMA positive and negative tumour models showed higher uptake in the positive tumour compared to the negative. However, due to the reduction potential of Tl^{3+}, the radiometal is likely to be reduced, dissociate from the chelator and then be effluxed from the tumour cells.

[^{201}Tl]$TlCl_3$ can be readily produced from [$^{nat/201}$Tl]TlCl and both oxidation states can cause SSBs and DSBs to DNA. [^{201}Tl]Tl^{3+} can be chelated at RT within 15 minutes using a number of chelators. The [^{201}Tl]Tl-pypa complex showed good serum stability in human serum. A PSMA bioconjugate was synthesised and radiolabelled, followed by *in vivo* biodistribution studies that revealed fast renal clearance with no evidence of [^{201}Tl]Tl^{3+} release. Promising radiobiological evaluation of the ^{201}Tl in a plasmid assay highlights the potential use of ^{201}Tl for use as a theragnostic agent to deliver a therapeutic dose, while being tracked within the body using SPECT imaging.

ACKNOWLEDGEMENTS

Firstly, I would like to thank my supervisors Dr Sam Terry and Prof Phil Blower for their support and guidance over the last 4 years. I appreciate your advice, patience and for pushing me to be a better scientist. I am well aware I have not been the easiest PhD student to manage, but you have both always been very supportive and encouraging which I greatly appreciate. In addition, I want to thank Dr Michelle Ma, who I see as my unofficial third supervisor, for all the chemistry help throughout my PhD.

I would like to give a big shoutout to Dr Charlotte Rivas, who did not need to spend so much time helping me, but without it I would have been lost! The synthetic chemistry lab has been such an enjoyable place to work, and that has largely been down to the fantastic environment you have helped to cultivate. Another big thanks to Dr Julia Blower for helping me get to grips with radiochemistry right at the start of my PhD and proofreading my terrible writing throughout. I am hoping it has improved over the years…

I want to also thank members of both the Blower group and Terry group, past and present, for their help. So, thank you Jen Young, Cinzia Imberti, Joanna Bartnicka, Afnan Darwesh, Sophie Langdon, Jordan Cheng, Connor Townsend and Elise Verger.

The beauty of being a member of the CDT is the chance to be part of a cohort of students, all going through their PhD's together. We have had a lot of highs and some lows, but they have always been there for a beer when needed, so I want to say thanks to Matt Farleigh, Federico Luzi, Aish Mishra, Vittorio De Santis and Ines Costa. But especially George Firth and Vassilis Baltatzis who I wouldn't have got through this PhD without! I would also like to thank the CDT management, Dr Valeria De Marco, Prof Julia Schnabel and Prof Nick Long for all their help over the years!

I would like to thank David Thakor, Jana Kim, Kavitha Sunassee, Lisa Sanderson, Jayanta Bordoloi and Steve Catchpole for efficient running of all the labs and their technical support. I would especially like to thank Matt Hutchings for being so dependable and always being there for help, be that changing gas cylinders or chemistry pointers. For other support around the office and labs, thanks to George Keeling, Jess Jackson, Aidan Michaels, Renee Flaherty, Truc Pham, Peter Gawne, Fred Baark, Rich Edwards, IB Hungnes, Hannah Greenwood, Will Tyrell, Lydia Smith, Natasha Patel, Azalea Khan, and many others, too many to name everyone individually, but cheers and I appreciate everything! Laura Stennett also deserves a special mention for being an excellent friend throughout my time at King's.

I need to thank my collaborators Prof Chris Orvig, Luke Wharton and Aidan Ingham at the University of British Columbia for the chelators and enjoyable Zoom chats, hopefully the paper will be published soon! I appreciate all the help you have given me over the last few years.

During my undergraduate I was certain that I would never do a PhD, but during my year abroad at the University of Toronto, the lab that welcomed me caused me to rethink that. I know if I had not met such incredible people, things would have ended up very differently for me, so thank you Dr Stacey-Lynn Paiva, Dr David Rosa, Dr Daniel Ball, Dr Jay Bassan and Jose Mendez Campos!

Finally, thank you to my parents Linda and David, my brother Charles, but especially my grandparents Charlie and Audrey, who without their encouragement, drive and enthusiasm, I know I would not be where I am today.

FUNDING STATEMENT

This work was funded by the EPSRC Centre for Doctoral Training in Medical Imaging [EP/L015226/1], the Wellcome/EPSRC Centre for Medical Engineering [WT/203148/Z/16/Z], and the EPSRC programme for next generation molecular imaging and therapy with radionuclides [EP/S032789/1 “MITHRAS”].]. Further support comes from a Wellcome Trust Multiuser Equipment Grant: A multiuser radioanalytical facility for molecular imaging and radionuclide therapy research and the National Institute for Health Research (NIHR) Biomedical Research Centre based at Guy's and St Thomas' NHS Foundation Trust and KCL [grant number IS-BRC-1215-20006]. PET and SPECT scanning equipment at KCL was funded by an equipment grant from the Wellcome Trust under grant number WT 084052/Z/07/Z. This work was also supported by the Rosetrees Trust (M786).

DECLARATION

I, Alex Charles Rigby, confirm that no part of this thesis has been submitted in support of any other application for a degree or qualification of King's College London, or any other university or institute of learning. I confirm that this work is my own. Where information has been derived from other sources it has been indicated in this thesis.

PUBLICATIONS

The following publications arising from this PhD include:

A. Rigby, J. E. Blower, P. J. Blower, S. Y. A. Terry and V. Abbate, Targeted auger electron-emitter therapy: Radiochemical approaches for thallium-201 radiopharmaceuticals, *Nucl. Med. Biol.*, 2021, 98–99, 1–7.

A. Rigby, G. Firth, C. Rivas, T. Pham, J. Kim, A. Phanopoulos, L. Wharton, A. Ingham, L. Li, M. Ma. C. Orvig, P. J. Blower, S. Y. A. Terry and V. Abbate, Towards bifunctional chelators for thallium-201 for use in nuclear medicine, *Bioconjugate Chemistry*, submitted.

A. Frei, **A. Rigby**, T.T.,C, Yue, G. Firth, M.T. Ma, N.J. Long, To Chelate Thallium(I) – Synthesis and Evaluation of Kryptofix-based Chelators for ^{201}Tl, *Dalton Transactions,* submitted.

TABLE OF CONTENTS

LIST OF FIGURES

LIST OF TABLES

TABLE OF ABBREVIATIONS

% ID	Percentage injected dose
% IA	Percentage injected activity
AE	Auger electron
APCI	Atmospheric pressure chemical ionisation
ASPA	Animal (Scientific Procedures) Act
ATP	Adenosine triphosphate
BFC	Bifunctional chelator
Boc	*Tert*-butyloxycarbonyl
COSY	Homonuclear correlation spectroscopy
CPM	Counts per minute
CPS	Counts per second
CT	Computed tomography
DCIBzL	((S)-2-(3-((S)-1-carboxy-(4-iodobenzamido)pentyl)ureido)pentanedioic acid)
DCM	Dichloromethane
DFO	Deferoxamine B
DIPEA	N,N-diisopropylethylamine
DMF	Dimethylformaminde
DMSO	Dimethyl sulfoxide
DNA	Deoxyribonucleic acid

DOTA	1,4,7,10-tetraazacyclododecane-1,4,7,10-tetraacetic acid
DTPA	Diethylenetriaminepentaacetic acid
DU145	Cell line – human prostate carcinoma derived from a brain metastatic site
EDTA	Ethylenediaminetetraacetic acid
ESI	Electrospray ionisation
FACS	Fluorescence activated cell sorting
FDA	Food and Drug Administration
FDG	Fluoro-2-deoxy-D-glucose
GMP	Good manufacturing practice
HATU	1-[Bis(dimethylamino)methylene]-1H-1,2,3-triazolo[4,5-b]pyridinium 3-oxide hexafluorophosphate
HEPES	4-(2-hydroxyethyl)-1-piperazineethanesulfonic acid
HPLC	High performance liquid chromatography
HSAB	Hard soft acid base
IPE	Inert pair effect
ITLC	Instant thin layer chromatography
LET	Linear energy transfer
LNCaP	Cell line – human prostate carcinoma derived from a left supraclavicular lymph node metastatic site
m/z	Mass/charge
MeCN	Acetonitrile

MBq	Mega Becquerel
MRI	Magnetic resonance imaging
MS	Mass spectroscopy
NHS	National Health Service
NMR	Nuclear Magnetic Resonance
NOTA	1,4,7-triazacyclononane-1,4,7-triacetic acid
PBS	Phosphate buffered saline
PC3	Cell line – human prostate carcinoma derived from bone metastatic site
PET	Positron Emission Tomography
PMPA	2-(phosphonomethyl)pentane-1,5-dioic acid
PMT	Photomultiplier tube
PSMA	Prostate specific membrane antigen
QC	Quality control
RCP	Radiochemical purity
R_f	Retention factor
ROS	Reactive oxygen species
ROI	Region of interest
RP	Reverse phase
SD	Standard deviation
SPECT	Single Photon Emission Computed Tomography

SSTR	Somatostatin receptor
SUV	Standard uptake value
TFA	Trifluoroacetic acid
THP	*Tris*(hydroxypyridinone)
TOF	Time of flight
t_R	Retention time
UV	Ultraviolet

1 INTRODUCTION

1.1 Medical imaging

Medical imaging encompasses a variety of complementary approaches that are used to visualise the structure and function of tissues within the body in a non-invasive manner. These include ultrasound, X-ray, or computed tomography (CT) imaging, magnetic resonance imaging (MRI), single photon emission computed tomography (SPECT) and positron emission tomography (PET) with each technique varying in usefulness, cost and sensitivity.

1.1.1 Molecular imaging

Molecular imaging techniques are used to measure and visualise biological activities at a cellular and subcellular level. They provide a tool to characterise diseases, based on the biological information obtained. Nuclear imaging, PET and SPECT, both rely on emissions from the decay of a radioactive molecule that can be incorporated or attached to a molecule with a biological purpose, providing functional imaging information. However, both PET and SPECT techniques struggle to provide high-resolution anatomical information, which is why they are often coupled with CT and more recently MRI to provide the anatomical background.

1.1.2 Single positron emission computed tomography (SPECT)

SPECT imaging uses radionuclides which decay via the emission of gamma rays, with different radionuclides emitting at different energies, that can be detected using gamma cameras. A selection of commonly used SPECT radionuclides and their properties can be found in Table 1. Scanners are made up of a collection of gamma cameras fronted by an array of collimators (Figure 1.1). The collimators ensure only gamma rays of the correct path reach the sodium iodide

crystal, preventing scattered images. This leads to much of the gamma emissions not being detected by the photomultiplier tubes (PMT), with only around 0.1% actually reaching the detector.[1] Preclinical SPECT scanners have a spatial resolution of less than 1 mm which increases in clinical whole body SPECT scanners to a spatial resolution of about 10 mm.[2] Around 80% of the diagnostic nuclear imaging scans across the globe today use SPECT (or scintigraphy-planar imaging), due to the availability of the isotopes, availability of SPECT/gamma cameras in hospitals and because they are relatively "cheap" compared to a PET scan (£253 vs £1484, using the NIHR costing tool, based on an [^{99m}Tc]Tc-MDP SPECT scan and [^{18}F]FDG PET scan, respectively).[3] The accessibility and ease of use of ^{99m}Tc ($t_{1/2}$ = 6.02 h) generators has led to it becoming the most popular isotope used in SPECT scans.[4] The radiometal has ideal characteristics for imaging, with gamma ray emissions at 140 keV and a short half-life to minimise the ionising radiation dose to hospital staff and patients.[4,5] ^{99m}Tc is formed by decay of ^{99}Mo ($t_{1/2}$ = 66 h), which once loaded onto an alumina support can be eluted from a benchtop generator with saline to deliver ^{99m}Tc in the form of [^{99m}Tc]TcO_4^-.[6–9] These generators can be eluted multiple times a day if required and usually last about a week before a new one is needed.[10] Generator based radionuclides offer a reliable source of radioactivity for radiopharmacies that are situated far from a cyclotron or nuclear reactors, making nuclear imaging more accessible.

Another reason ^{99m}Tc has thrived is because of the large number of kit-based radiopharmaceuticals on offer. The generator is eluted into a vial, then transferred into the kit via a syringe, containing the tracer formulation. The reaction is a simple and a single step process, without the need for further purification and a simple quality control (QC) method to calculate radiochemical purity.

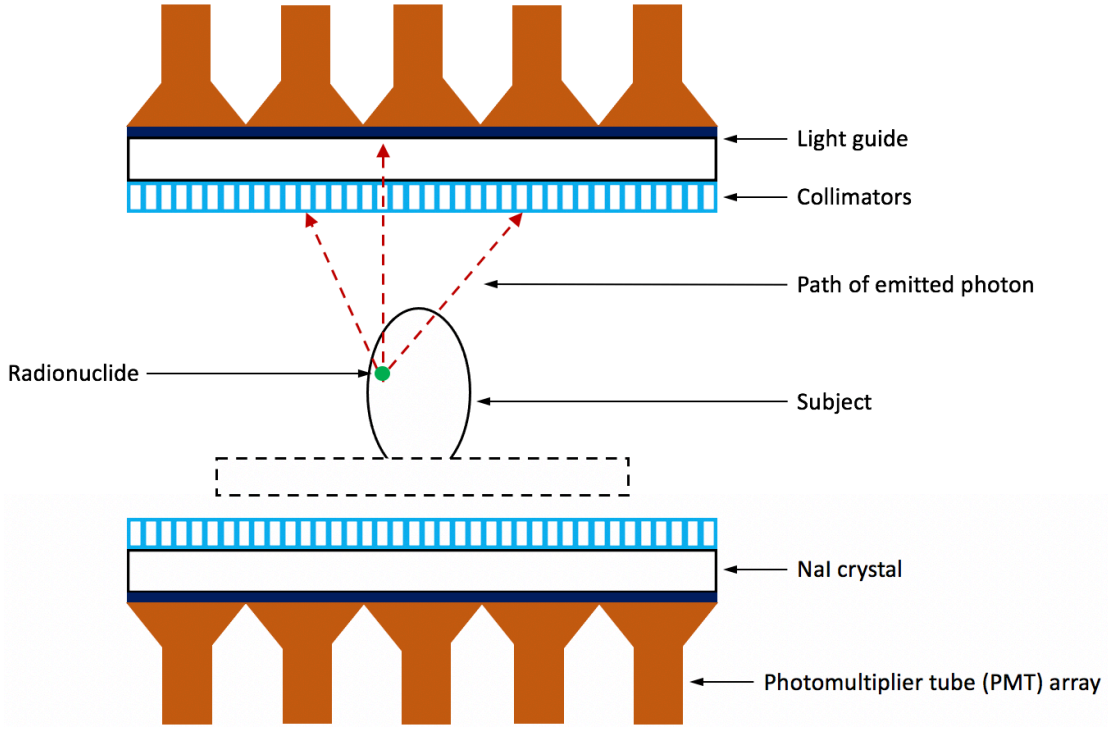

Figure 1.1 – The basic structure of a SPECT scanner.

Table 1 – Radiometals used in SPECT imaging, their half-lives and gamma energies

Radionuclide	Half-life (h)	Energy (keV)
^{99m}Tc	6.02	140
^{111}In	67.2	171, 245
^{201}Tl	73	69-83, 135, 167
^{67}Ga	78.2	93, 185, 288, 394
^{131}I	192.5	192, 364
^{123}I	13.2	159

1.2 Radiopharmaceuticals for cancer imaging and treatment

A fundamental requirement of radiometal based radiopharmaceuticals is that in order to deliver them selectively, a bifunctional chelator (BFC) is needed. There are examples where a BFC is not required to target the radiometal to a specific biological target. These include, pertechnetate ($[^{99m}Tc]TcO_4^{2-}$) as an iodide mimic, having uptake in tissues expressing the sodium iodide symporter (NIS) or [^{99m}Tc]Tc-sestamibi, which accumulates in tissues with large numbers of mitochondria and a negative membrane potential.[10]

BFCs are designed to include three essential parts. Firstly, a chelator that can bind a radiometal and form a complex which is stable *in vivo,* ensuring the metal is not released before delivery to the intended target. Secondly, a targeting vector which has biological activity, for example a small peptide which binds to a receptor overexpressed in cancer cells. Thirdly, a linker molecule to connect the chelator to the targeting vector, which in some cases can be designed to improve binding of the targeting moiety or the biodistribution or metabolism of the conjugate. A basic BFC system in shown in Figure 1.2.

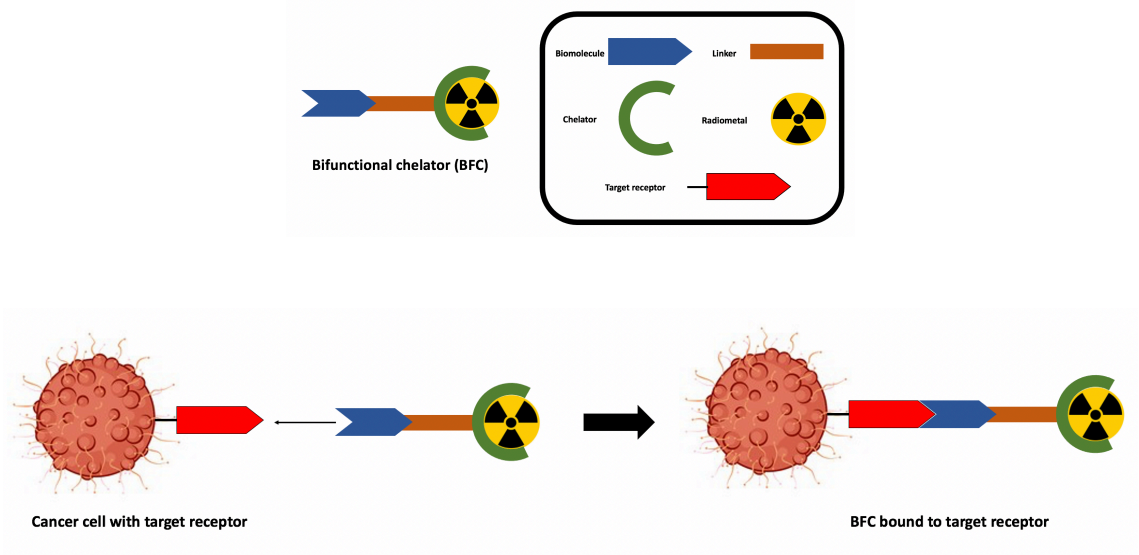

Figure 1.2 – An illustration of the structure of a bifunctional chelator (BFC) and how the BFC binds to the target receptor on the surface of a cancer cell.

Chelators used in BFCs vary depending on which radiometal is being used i.e., DFO for ^{89}Zr or DOTA for ^{177}Lu. As well as the chelator, there are a large variety of biomolecules, from several classes, that can be used, as summarised in Table 2, along with their biological half-life. One of the most common methods of conjugation involves the use of an isothiocyanate (NCS) moiety to attach a chelator via a primary amine forming a thiourea bond to a biological targeting vector. The chelator and biological targeting vector can be tuned to serve the desired purpose, be that to image or treat a disease. Recent discoveries have shown that there are an array of overexpressed receptors on cancer cells, which would allow bioconjugates to targeted these receptors.[11] Different biomolecules have different biological behaviours within the body, for example antibodies are large in molecular weight and often have long circulation times in the blood stream before localising in the biological target. Smaller antibody fragments have much shorter circulation time, and faster accumulation, with small peptides having still faster blood clearance and accumulation.

Table 2 – Biomolecules used in bifunctional chelators and their biological half lives in humans[12]

Biomolecule	**Biological half life**
Antibodies (Ab)	10-15 days
Antibody fragment	2 - 10 hours
Peptides	10-60 minutes

As well as being used for PET or SPECT imaging, certain radionuclides can also be applied for molecular radionuclide therapy (MRT). In general, this form of radiotherapy, which is an alternative to external beam radiotherapy (EBRT). Radiotherapy works by damaging cancer cells beyond repair causing them to die and thus triggering their breakdown and removal by the body. EBRT works by targeting a high energy particle (electrons or protons) or an X-ray beam at the tumour from outside the body. EBRT has been proven to be effective at killing cancer cells, but it can also cause undesired damage to healthy tissue. However, unlike EBRT, MRT works by targeting a high energy particle (electrons or protons) at the tumour from inside the body. Whereas EBRT has been proven to be effective at killing cancer cells, which is why it is used in treatment regimens of 50% of all cancer cases, it can also cause undesired damage to healthy tissue. MRT, on the other hand can deliver radioactivity selectively to the target tissue and is still very effective when tumours have metastasised.

α in the form of targeted alpha therapies (TAT) have been FDA approved for cancer treatments since 2013, primarily focusing on ^{223}Ra ($t_{1/2}$ = 11.4 days) with future therapeutics possibly using other isotopes such as ^{227}Th ($t_{1/2}$ = 18.7 days) and ^{225}Ac ($t_{1/2}$ = 10 days). β^- particle emitter iodine-131 ($t_{1/2}$ = 8 days), has been used to treat thyroid conditions since the 1940s, mainly focusing on hyperthyroidism by destroying sufficient thyroid tissue to reduce function.[13] An example of a

recently FDA approved β^- particle emitting radiometal based therapeutic includes [^{177}Lu]Lu-DOTATATE. ^{177}Lu is a β^- particle emitter which can irradiate a tumour from within the body.[14] β^- particles emitted by ^{177}Lu can travel around 670 µm in soft tissue.[15] However, high energy β^- particles emitted by ^{90}Y or ^{188}Re for example, can travel up to 1 cm within the body, so also pose the risk of damaging healthy tissue.[16] Auger electron-emitters could be excellent for minimising the damage to healthy tissue, due to the short range of Auger electrons (typical range 1 nm to 1 µm).[16] Research has shown the radiotoxic potential of Auger electron-emitting radioisotopes like ^{111}In, ^{67}Ga, ^{99m}Tc, ^{123}I and ^{125}I.[17–20] However, an Auger electron-emitting radionuclide that has been neglected in current literature is thallium-201. The schematic in Figure 1.3 highlights the particle range of different particulate ionising radiation. The following sections will go into more detail about radiopharmaceuticals that emit beta or alpha particles and Auger electrons.

Table 3 – The types of radioactive emissions used in radiotherapy and corresponding linear energy transfer (LET), range in tissue and examples of radiometals used for therapy.[16,21]

Particle	Energy (MeV)	LET (keV/µm)	Particle range	Suitable for tumour size	Example isotopes
α	5-8 (High)	80-100	40-80 µm 1-3 cell diameter	Small (< 10 mm)	^{225}Ac, $^{212/213}$Bi
β	0.1-2.2 (High-medium)	0.2	0.1-10 mm 50-1000 cell diameter	Large (> 50 mm)	^{177}Lu, ^{90}Y

Auger electron	1-10 (Low)	4-26	1-20 µm subcellular	Small (< 10 mm)	^{201}Tl, ^{111}In

Frequently, uptake of radiotherapeutics is not homogeneous, leading to cell death via the crossfire effect. This effect uses the longer range of mainly β^- particle emitters, to not only target the cell that the radiotherapeutic is bound to but the surrounding cells. This can be a major advantage in larger solid tumours, allowing the ionising radiation to penetrate further, leading to the possibility of more cell death.[22–25] The therapeutic used will have to be tuned to the tumour size, as β^- particles would not effectively treat small tumours or clusters, and instead predominantly damage normal tissue.[26] α or AE emitters would suit smaller or micrometastases due to their shorter path length. The development of α therapeutics have been on the rise over the last decade, and beta particle emitters being used routinely since the 1940s. Auger electron emitters however remain unproven in the clinic.

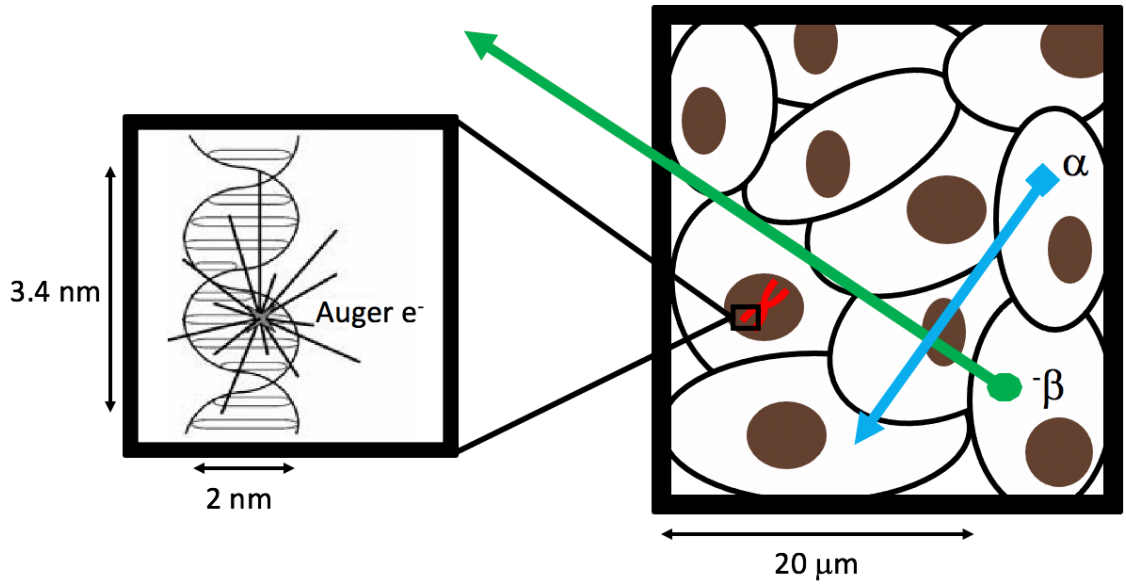

Figure 1.3 – A diagram to present the radiation path lengths of α, β^- and Auger electrons in a cellular (α and β^-) and subcellular (Auger) environment (scale not accurate). Based on a figure from Buchegger.[16]

1.2.1.1 *α* particles

α particles consist of two protons and two neutrons bound together - a helium nucleus. They have a high linear energy transfer (LET) (the amount of energy deposited by an ionising particle transfers per unit path length) of 100 keV/μM and medium particle range of 40-80 μm making them ideal for small tumour clusters, as the particles can travel around five cell diameters. The lethality of α particles is independent of what stage of the cell cycle the cancers are in, nor is it dependant on the oxygenation state.[27] The DNA damage is often in the form of complex double strand breaks (DSBs) which are more challenging for the cancer cells to repair than simple single strand breaks (SSBs).[27] Humm *et al.* have estimated that in order to kill a single cell with 99.99% probability, tens of thousands of β^- particle transits will be needed, whereas only a few α particles will achieve the same kill probability.[28] Nikula *et al.* have gone on to predict that a single α particle traversal is enough to kill a cell.[29] [^{223}Ra]$RaCl_2$ is a Food and Drug Administration (FDA) approved (May 2013) palliative α particle therapeutic, sold by Bayer under the name Xofigo. It

is used to treat castration-resistant prostate cancer and has been used in 108 clinical trials within the US alone. From one of these trials patients with skeletal metastases described substantial pain relief 8 weeks post treatment and the median survival exceeded 20 months.[30] Additionally, preclinical and clinical studies using α emitters has been investigated for treatment of various cancers including brain tumours, ovarian cancer and non-Hodgkin lymphoma, with most research focused on prostate and neuroendocrine cancers.[27]

Table 4 – α particle emitting radiometal isotopes, their decay path and particulate energy (keV).

Isotope	Half-life (h)	Decay path	Particulate energy (keV)
^{225}**Ac**	240	α (100%)	6000-8400
^{212}**Bi**	1	α (35.94%), β^- (64.06%)	6100
^{213}**Bi**	0.77	α (2.2%), β^- (97.8%)	8400
^{223}**Ra**	274	α (100%)	5980
^{212}**Pb**	11	α (33%), β^- (67%)	2600

1.2.1.2 *β*$^-$ particles

β^- particles are high energy negatively charged electrons that are ejected from the nucleus of unstable atoms.[31] The long path length of the particle and small energy deposition leads to a relatively small LET of 0.2 keV/μm.[16] The majority of radionuclide-based studies have used highly energetic β^- particles, with low *in vitro* toxicity observed.[32] β^- particle emitters have continued to be pursued for use in therapy, as they are readily available and have favourable characteristics (i.e., imageable gamma emission energy, physical half-lives compatible with biological targeting vectors, range of emitted particle leading to useful cross-fire effect).[33] Radionuclides used for therapy can damage cells via self-dose, when irradiation takes place from radionuclides located on or within the targeted cells (Auger) or via the cross-fire effect, where irradiation comes from radionuclide located outside the cell or on a neighbouring or distant cell.[34] A benefit of the cross-fire effect is that it negates the necessity to deliver the radiotherapeutic to every single target cell. This has potential to counteract differing degrees of tumour heterogeneity. The main disadvantage of it is the possible damage to off-target healthy tissue.

Lutathera, [^{177}Lu]Lu-DOTA-TATE, is a β^- particle emitter approved by the FDA (2018), EMA (2017) and Canada Health (2019) for the treatment of somatostatin receptor (SSTR) positive gastroenteropancreatic neuroendocrine tumours.[35] It was also approved for use in a theranostic pair with ^{68}Ga ([^{68}Ga]Ga-DOTA-TOC) to monitor treatment response using PET. The phase III clinical trials showed longer progression free survival and a significantly higher response rate than high-dose octreotide among patients with advanced midgut neuroendocrine tumours.[36]

Table 5 – A selection of β^- particle emitting radiometal isotopes in clinical use, their decay path and particulate energy (keV)

Isotope	Half-life (h)	Decay path	Particulate energy (keV)
^{90}Y	64.1	β^- (100%)	934
^{177}Lu	159.4	β^- (82.4%), gamma (17.7%)	134
^{188}Re	17	β^- (85%), gamma (15%)	2100
^{131}I	192.5	β^- (92.8%), gamma (7.2%)	182
^{161}Tb	165	β^- (100%)	154

1.2.1.3 Auger electrons

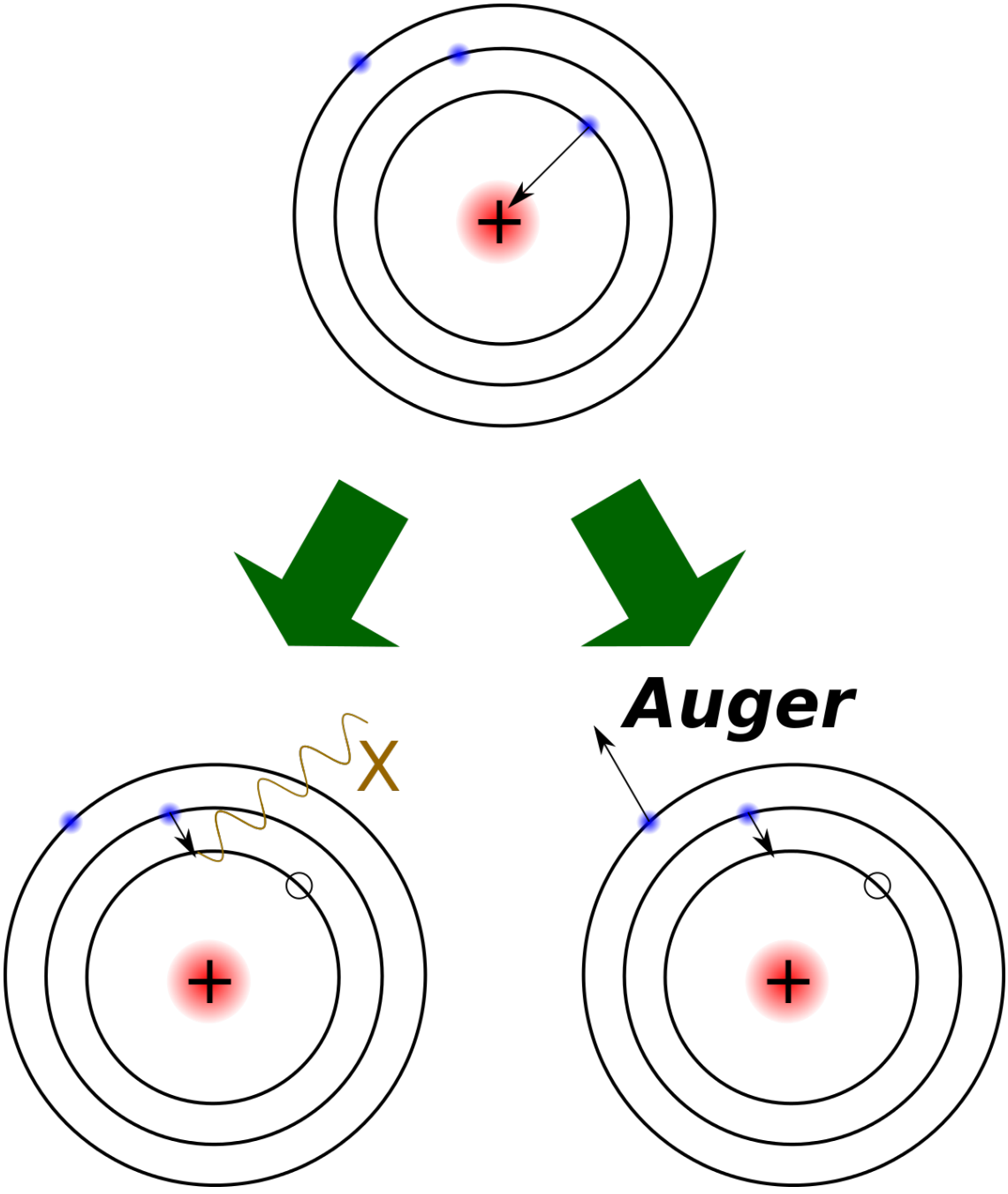

Figure 1.4 – A diagrammatic representation of how Auger electrons are generated.

Auger electrons arise due to radionuclides decaying via electron capture or internal conversion. Electron capture is where an inner shell electron is drawn into the nucleus of an atom. This process creates an electron vacancy, which can be filled by a higher energy electron dropping down, releasing energy as an X-ray or by ejection of an outer electron, or both, and the process

occurs in cascade (Figure 1.4).[16] These Auger electrons, coupled with gamma emissions, have therapeutic potential and hence Auger electron emitting radionuclides may have use as theranostics, where the same radionuclide can be used for diagnosis and treatment of the disease. Additionally, periodically timed imaging can be used to investigate treatment response or provide accurate dosimetry.

Since first being described by Lise Meitner and Pierre Auger in the 1920s, Auger electrons (AEs) have been investigated for use in molecular radionuclide therapy (MRT). As previously described, AEs are a product of radionuclide decay, typically via electron capture, occurring in large numbers (4.7 – 36.9 per disintegration) and at low energies (<25 keV).[16] However, this energy is deposited across a small distance (<0.5 μm), leading to higher linear energy transfer than radiotherapies involving, for example, β^- particles with energies up to 2 MeV, where energy is deposited over 0.1 – 10 mm.[37] AE-emitters could therefore permit highly targeted therapies, capable of extreme radiotoxicity, even in micrometastases and single circulating tumour cells, but only if they can be delivered to one or multiple valid cellular targets such as the cell nucleus, membrane or mitochondria, leading to cell death.[38,39]

Table 6 – Examples of Auger electron emitting radiometal isotopes, their decay path and production method

Isotope	Half-life (h)	Decay path	AE energy/ decay (keV)	Production method
^{67}Ga	78.2	EC (100%)	6.3	Cyclotron, ^{68}Zr(*p,2n*)^{67}Ga
^{111}In	67.2	EC (100%)	6.8	Cyclotron, ^{111}Cd(*p,n*)^{111m,g}In
^{201}Tl	73	EC (100%)	15.3	Cyclotron, ^{203}Tl(*p,2n*)^{201}Tl
^{123}I	13.2	EC (100%)	7.4	Cyclotron, ^{124}Te(*p,2n*)^{123}I
^{125}I	1428	EC (100%)	12.2	Cyclotron, ^{124}Xe(*n,*)^{125m}Xe -> ^{125}I

1.2.2 Clinical and preclinical applications of Auger electrons

The use of AEs in clinical studies has been very limited, with only a handful of trials conducted. In 1996, Macapinlac and co-workers used [^{125}I]I-IUdR (185 MBq) and [^{131}I]I-IUdR (370 MBq) to calculate dosimetry in 4 patients with colorectal cancer metastatic to the liver using hepatic artery infusion (Figure 1.5).[40] Due to the low amounts of radioactivity injected, no tumour response was observed (or expected), however the images revealed no retention in the bone marrow or in normal tissue, with no side effect observed. Further studies using [^{125}I]I-IUdR by Rebischung and co-workers used intrathecal injection (administration of drugs via injection into the spinal canal) in a patient with advanced pancreatic cancer with resistant neoplastic meningitis.[41] 1850 MBq of [^{125}I]I-IUdR was administered following 4 doses of methotrexate (a chemotherapy agent and immunosuppressant). A dramatical decrease in cerebrospinal carbohydrate antigen 19.9 (CA 19.9), an important biomarker in pancreatic cancer was observed and no central nervous system (CNS) toxicity was found. The authors concluded that [^{125}I]I-IUdR could be an effective treatment for neoplastic meningitis in the future.

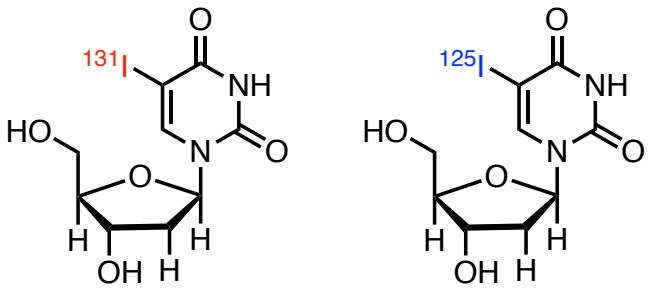

Figure 1.5 – Structures of [^{131}I]I-IUdR (left) and [^{125}I]I-IUdR (right)

As well as small molecules, peptides and proteins have also been used to deliver AE emitters to malignancies in clinical studies. Recently, promising studies using the human epidermal growth factor (hEGF) conjugated with DTPA, and subsequently radiolabelled with ^{111}In have highlighted

the potential of ^{111}In as a therapeutic. Vallis *et al.* have performed Phase 1 clinical trials using [^{111}In]-DTPA-hEGF in 16 patients with metastatic EGFR-positive breast cancer. 370-2220 MBq was administered, utilising SPECT imaging to assess the tumour uptake and biodistribution in normal tissue to estimate radiation dose to the organs. At these amounts, no renal or hepatic toxicity was observed. Even at the highest dose (2.2 GBq), the radiation dose to the kidneys and liver was still within radiation toxicity limits (1.64 and 1.9 Gy respectively), based on external beam radiotherapy (EBRT). Interestingly, the only side effects discovered were related to the hEGF moiety, including vomiting and chills. The authors go on to state that further dose escalation will be needed to achieve a therapeutic effect, but due to the adverse effect of hEGF, it will require even higher specific activity of ^{111}In to minimise the amount of hEGF injected. In the future, Reilly *et al.* have suggested that anti-EGFR monoclonal antibodies (mAbs) labelled with ^{111}In may be a promising alternative for AE therapy for EGFR-overexpressing breast cancer, avoiding the adverse effect described above.[42]

Clinical trials using murine anti-EGFR mAb (mAb 425) radiolabelled with ^{125}I by Li and co-workers, resulted in improved overall survival for the 192 patients with glioblastoma multiforme (GBM).[43] Patients were given up to 3 weekly i.v. injections of 1.8 GBq [^{125}I]-mAb 425 with a maximum cumulative amount of 5.4 GBq. Patients were split into two groups; one received [^{125}I]-mAb 425 alone (132 patients) and the other received [^{125}I]-mAb 425 in combination with temozolomide (TMZ, a commonly used chemotherapy for GBM) (60 patients). Both treatments increased overall survival with median survival for the mAb alone group being 14.5 months and the combination group being 20.4 months, compared to a control group, who did not receive the mAb, median survival of 10.2 months. Only 7 out of 192 patients suffered acute side effects like nausea, skin irritation and hypertension.

Octreotide is a synthetic version of the peptide hormone somatostatin and binds to the somatostatin receptors SSTR2 and SSTR5.[44] One of the most studied radiolabelled derivatives is

[^{111}In]In-DTPA-octreotide. Phase 1 clinical trials by Krenning and co-workers treated 30 patients with advanced SST-2 positive neuroendocrine tumours.[45] Patients were given up to 14 doses of 6-7 GBq of [^{111}In]In-DTPA-octreotide, administered at least two weeks apart with a cumulative dose of 74 GBq. Six patients demonstrated a reduction in tumour size and 8 patients showed stable disease. Two years post treatment, no major side effects were noted, with only a transient decrease in platelets and lymphocytes observed in some patients.

Furthermore, Valkema and co-workers have reported Phase 1 clinical studies using [^{111}In]In-DTPA-octreotide.[46] The therapeutic agent was administered from two-week- to several month intervals, with 12 or more doses (2-11 GBq) delivered, cumulating in a total of 20-160 GBq in 50 patients with SST-2 positive tumours. In the 40 evaluable patients, a therapeutic benefit was observed in 52.5% of the patient. Within the group that had a therapeutic benefit, 35% of patients saw no disease progression, 15% had minor remission and one patient had partial remission.[46] However, mild hematopoietic toxicity was observed, and of the 6 patients who received a total dose of >100 GBq, 3 developed myelodysplasia or leukaemia. Despite a high kidney dose (45 Gy) from an administered dose of 100 GBq, which is twice the accepted limit for EBRT, none of the patients developed conditions expected with renal toxicity such as hypertension or serum creatinine.

Further work by Limouris has shown the therapeutic potential of [^{111}In]In-DTPA-octreotide administered via the hepatic artery, for the treatment of inoperable SST-2 positive liver metastases.[47] Of the 17 patients to take part, one experienced a complete response, eight exhibited a partial remission and 3 had stable disease, leading to a median survival of 32 months in the 12 patients that responded to treatment.

The majority of preclinical and clinical AE-emitting MRT studies have utilised ^{111}In and ^{125}I.[48–57] However, others have focused on the use of radionuclides like ^{195m}Pt, ^{67}Ga and ^{99m}Tc. Despite being one of the main types of chemotherapeutic, platinum-based agents, such as cisplatin, have as yet poorly understood biological profiles. These compounds are heavy metal antineoplastic agents which are usually used in combination with other chemotherapy drugs as treatment for human solid malignancies.[58] The side effects of platinum-based agents can be wide-ranging, with high toxicity to the kidneys, leading to reduced renal function as well as vomiting, nausea and ototoxicity.[59,60] Incorporating ^{195m}Pt ($t_{1/2}$ = 4.02 days) into cisplatin allows the drug's biology to be explored further using SPECT imaging and as it is an AE emitter, it warrants evaluation as a therapeutic.[61] Zeevaart and co-workers have recently explored the biodistribution of [^{195m}Pt]Cisplatin (Figure 1.6) in heathy volunteers, showing that the majority of the injected activity is excreted in the urine within 5 hours.[62] The kidneys received a high dose of 2.68 ± 1.5 mGy/MBq (mean), followed by the spleen (1.6 ± 0.8 mGy/MBq, mean) and liver (1.45 ± 0.38 mGy/MBq, mean). The authors concluded that [^{195m}Pt]Cisplatin would be a safe radiopharmaceutical for early imaging studies.

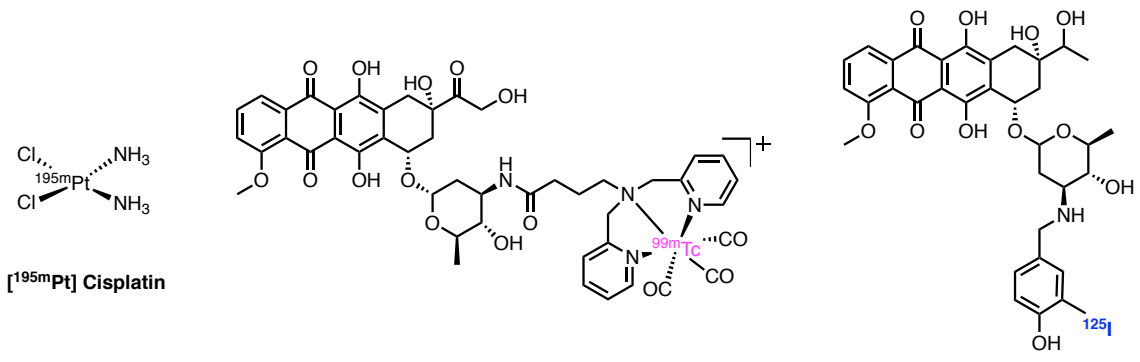

Figure 1.6 – Structure of [^{195m}Pt]Cisplatin (left), [^{99m}Tc]Tc-DOX (middle) and [^{125}I]IComp1 (right)

As well as Cisplatin, other commonly used chemotherapy drugs have been radiolabelled with AE emitters including doxorubicin (DOX) and daunorubicin (DAU). DOX and DAU contain planar

aromatic moieties which intercalate between the base pairs of DNA, leading to DNA damage response being deregulated in DOX/DAU exposed cells.[63] Similar to Cisplatin, by adding an AE emitter, more DNA damage will be caused due to the combination of AEs and the drugs inherent chemical toxicity. Alberto *et al.* have developed a BFC with DOX, taking advantage of the [^{99m}Tc]Tc-tricarbonyl complex and a dipicolylamine moiety (Figure 1.6).[64] The authors used a non-radioactive Re analogue to show the BFC version mimics DOX *in vitro* behaviour, highlighting the similar cellular distribution and high nucleus accumulation using fluorescence microscopy. In B16F1 (murine melanoma) cells, [^{99m}Tc]Tc-DOX exhibited a dose dependant reduction in cell viability of up to 80% due to the Auger electron emissions. [^{99m}Tc]TcO_4^- was used as a negative control which was not efficiently internalised into cells and did not have a radiotoxic effect. The AE emitting compound inhibited cell survival at concentrations far lower than the native compound. The authors state that combining a DNA binding agent with an AE emitter could lead to the mitigation of dose dependant adverse effects as subnanomolar concentrations are unlikely to elicit a pharmacological response. For ^{99m}Tc to have such a profound cytotoxic effect on these cells is interesting as it is far from the perfect AE emitter as it only emits 4.4 AEs per decay which is far lower than ^{111}In, ^{67}Ga or ^{201}Tl (Table 6). This approach has the potential to be a game changer in AE molecular radiotherapy. By exchanging the ^{99m}Tc for a more potent AE emitter, the DNA damage caused to the cancer cells could be far higher.

Another example of combining AE emitters with chemotherapeutics is work published by Ickenstein and co-workers.[65] The authors developed [^{125}I]-Comp1 (Figure 1.6), an ^{125}I-labelled version of DAU, and like the [^{99m}Tc]Tc-DOX tracer, exhibited high accumulation in the nucleus of cancer cells (SK-BR-3, human breast adenocarcinoma) like the native compound. When the SK-BR-3 cells were incubated with [^{125}I]-Comp1 (0.5 ng mL^{-1}) the mean number of living cells dropped from 10^5 to just 1200 after 3 weeks, making the fraction of surviving cells 0.05%. When cells were incubated with non-radioactive ([^{127}I]-Comp1) or DAU at a concentration of 0.5 ng,

the number of living cells were not significantly different to untreated cells. As with the DOX labelled drug, the authors hope to avoid the adverse dose limiting effects of DAU (leukopenia, alopecia, cardio toxicity to name a few) by using very low concentrations using AEs to cause the DNA damage to cancer cells.

Jannetti and co-workers published in 2018 the synthesis of a ^{131}I-labelled poly(ADP-ribose) polymerase 1 (PARP1) inhibitor, [^{131}I]I-MAPi (Figure 1.7) based on the structure of the well-investigated PARP1 inhibitor Olaparib.[66] PARP1 is responsible for mediating multiple DNA damage repair pathways,[67] and hence is a biomarker for multiple cancers including GBM, as it is recruited to the cancer cell nucleus and binds to the DNA as a single strand break repair enzyme.[68] The radiotherapeutic was shown to be very cytotoxic in GBM mouse models, with median survival being increased by 45%. Building upon the encouraging results of this β^- particle emitter, the authors have translated it to AE therapy using ^{123}I in place of ^{131}I. [^{123}I]I-MAPi (Figure 1.7) in GBM models was presented.[69,70] Using a convection enhanced delivery (CED), the authors implanted osmotic pumps subcutaneously to slowly deliver an infusion of [^{123}I]I-MAPi (481 ± 111 kBq in 100 uL) or the control vehicle ([^{127}I]I-MAPi) into the brain and removed after 5 days. When compared, the [^{123}I]I-MAPi (68.9 ± 1.1 nmol/L) was shown to have an EC_{50} 16-fold greater than the [^{131}I]I-MAPi (1148 ± 1 nmol/L) version in U251 GBM cells. This work really highlights the cytotoxic potential of AE emitters if delivered effectively to the nucleus of cancer cells.

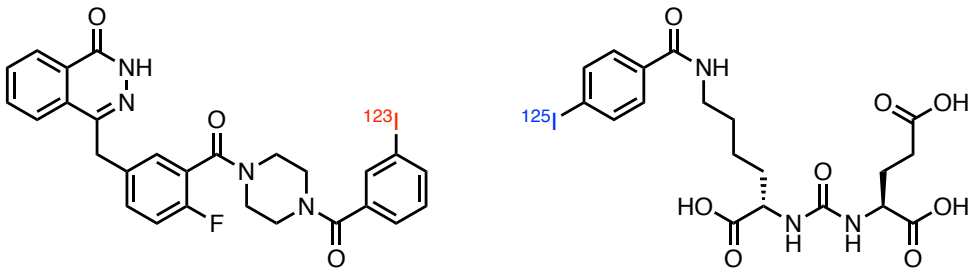

[123I]I-MAPi **[125I]I-DCIBzL**

Figure 1.7 – Structures of [123I]I-MAPi (left) and [125I]I-DCIBzL (right)

In 2020, Shen and co-workers used [125I]I-DCIBzL, a PSMA targeting peptide (Figure 1.7), to target micrometastases in a PC3-ML PSMA positive prostate cancer model.[71] [125I]I-DCIBzL has previously been shown to have a therapeutic effect in other preclinical *in vivo* models.[72,73] The authors used a murine model of human metastatic prostate cancer, PSMA positive PC3-ML cells, which express firefly luciferase in NSG mice, which were monitored using bioluminescence imaging (BLI). Their results showed that doses of 18.5 MBq or higher were able to prolong survival of the mice and significantly delay the development of detectable metastatic disease using BLI. The authors concluded that [125I]I-DCIBzL should be considered for further development as a treatment for metastatic prostate cancer.

Work by Othman and co-workers has recently shown results for the potential use of ^{67}Ga in MRT.[19,20] They have shown that ^{67}Ga can cause a comparable amount of DNA damage to ^{111}In using an isolated cell-free plasmid DNA model. Additionally, it was demonstrated for ^{67}Ga that the A_{50} (internalised activity of the oxine complexes per cell required to kill 50% of cells) was 0.3 Bq/cell, which is lower than that of ^{111}In (0.7 Bq/cell) using clonogenic assays, highlighting the cytotoxic potential of ^{67}Ga. This work was followed up by the conjugation of ^{67}Ga to trastuzumab via the chelator, THP-NCS, and compared to an ^{111}In control using DOTA-NCS, both conjugated through lysine residues on the antibody. In HER2 expressing HCC1954 cells, both the [^{67}Ga]Ga-

THP-trastuzumab and [^{111}In]In-DOTA-trastuzumab significantly decreased clonogenic survival compared to the untreated controls. Additionally, [^{67}Ga]Ga-THP-trastuzumab was shown to be 1.4 fold more toxic than [^{111}In]In-DOTA-trastuzumab, based on clonogenic assays.

Others have successfully used antibodies incorporating a nuclear localisation sequence (NLS) to amplify the effectiveness of AEs.[50] Fasih *et al.* used an anti-epidermal growth factor receptor (EGFR) mAb (nimotuzumab) modified with the 13-mer peptide NLS (*CGYGPKKKRKVGG*) radiolabelled using ^{111}In via DTPA.[74] The authors demonstrated that adding the NLS can increase the nucleus uptake 2 fold in EGFR-positive MDA-MB-468 human breast cancer cells compared to non-modified nimotuzumab. Their results showed a 7-fold reduction in the cell survival of the MDA-MB-468 cells and 2-fold more DNA double strand breaks (DSBs) detected using immunofluorescence for gammaH2AX foci in the nucleus.[74] Costantini and co-workers have used the same NLS sequence to modify trastuzumab along with DTPA to test its efficacy for MRT in SK-BR-3 (HER2 positive breast cancer cells).[75] Their results showed that [^{111}In]In-DTPA-NLS-trastuzumab bound to receptor, was internalised and then transported to the cell nucleus where it caused extensive DNA DSBs and reduced the clonogenic survival by >90%. At the same concentration, non-labelled trastuzumab decreased the clonogenic survival by 35%. The authors went on to publish further results in human breast cancer xenograft models.[50] Firstly they established a dose of [^{111}In]In-DTPA-NLS-trastuzumab that did not cause any observable adverse effects on the mouse's body weight as well as hematopoietic, liver or kidney function. One injection of [^{111}In]In-DTPA-NLS-trastuzumab (9.25 MBq, 4 mg/kg) was administered to mice bearing subcutaneous MDA-MB-361 xenografts. A 4-fold reduction in tumour growth was observed, which was 3-fold more effective compared to the non-labelled trastuzumab (4 mg/kg).

The previously mentioned AE therapeutics have focused on multiple cellular targets, for example the cell membrane, mitochondria or nucleus. Pouget and co-workers in 2008 described how the

cell membrane may be a more sensitive target than the cytoplasm to AEs.[38] They used clonogenic assays to measure cell survival using different ^{125}I-labelled vectors (at varying activities, 0-4 MBq/mL) targeting different regions of A-431 and SK-OV-3 carcinoma cells. The vectors include internalising anti-HER1 (m225), anti-HER2 (trastuzumab), non-internalising anti-CEA (35A7) mAbs and finally a TAT peptide. Their results indicate that the cell membrane is as sensitive a target as the nucleus, so therefore, a valid target for AE emitters. Pouget *et al* have followed up this work with a few more recent papers further developing targeted radioimmunotherapy (RIT) for the cell membrane.[39,76]

Future AE-emitting MRTs may be more successful if a more potent AE-emitting radionuclide was used that emitted many AEs per decay, such as ^{201}Tl.

1.2.3 Limitation of AE clinical translation

Generally, despite excellent preclinical results, translation of AE to the clinic has been met with limited therapeutic impact due to their inability to deliver a lethal dose to the tumour.[51] One reason for this is the difficulty in predicting the therapeutic response from the AE radiopharmaceuticals in patients. This is due to inaccuracies in dose estimates based on imaging data, lack of knowledge of the distribution at sub-cellular level, heterogeneous tumour uptake and radiobiological factors like sensitivity of tumours to radiation be that AE, EBRT or other ionising particles.

Another big limitation of AE is the need for very high specific activity (SA) of the radiopharmaceuticals. Results from Ngo Ndjock Mbong and co-workers have shown the dramatic effect SA can have using ^{111}In labelled mAbs (< 1 MBq/ug), where there may be as few as 1 in 50 antibody molecules radiolabelled. This will severely limit the effectiveness for killing cancer if non-radiolabelled antibody is blocking uptake and or does not have a cytotoxic effect.[77] In comparison, [^{177}Lu]Lu-DOTA-TATE is regularly produced at a specific activity of 850 GBq/mg for clinical use, which is substantially higher.[78] Terry *et al* have used oxine with to form a neutral lipophilic complex to deliver the radiometals *in vitro*, yielding 9.09 ± 1.33 Bq/cell for [^{111}In]In-oxine and 1.12 ± 0.20 Bq/cell for [^{67}Ga]Ga-oxine which showed a decrease in cellular viability. However, moving into an *in vivo* setting it is unclear how this amount of activity would be delivered to cancer cells as oxine is not specific.

1.3 Prostate Cancer

According to figures from the World Health Organisation (WHO) Cancer Mortality Database, prostate cancer is the most commonly diagnosed malignancy in men and the second leading cause of cancer-related deaths in the western world.[79] Initial treatment options include prostatectomy (the surgical removal of the prostate) and a combination of external beam radiotherapy (EBRT) with surgery. Localised treatment for prostate cancer is often highly effective, but many patients progress to metastatic castration resistant prostate cancer (mCRPC).[80] This often requires more forceful treatments including chemotherapies, immunotherapies and radiotherapies. mCRPC also has a shorter median survival of 13-32 months and a 5-year survival rate of only 15%.

Despite these statistics, prostate cancer is a promising target for radiotherapies for a number of reasons. The prostate is a non-essential organ, allowing for tissue-specific targeting. Metastases most commonly involve the lymph nodes or bones which are areas of the body that can receive high concentration of circulating antibodies.[81] Prostate cancer metastases are usually small in volume which allows antibodies to penetrate the tumours efficiently.[81] The prostate-specific antigen (PSA) serum biomarker can be used to monitor the therapy administered and can detect metastases from the blood test.[81]

1.3.1 Prostate Specific Membrane Antigen (PSMA)

There are a number of molecular therapy targets for prostate cancer including the prostate stem cell antigen (PSCA), the six-transmembrane epithelial antigen of the prostate (STEAP) and G-protein coupled receptor (5-oxoER), but herein the focus will be on the prostate specific membrane antigen (PSMA).[81] PSMA, also known as *N*-acetyl-alpha-linked acidic dipeptidase I (NAALA-Dase), glutamate carboxy-pepidase II or folate hydrolase, is a type II membrane glycoprotein. It is about 100 kDa in size, with a short intracellular domain of 19 amino acids, a transmembrane domain of 24 amino acids and glycosylated extracellular domain of 707 amino acids.[82–84] PSMA is highly expressed in prostate cancer cells, but is also expressed in other normal healthy tissue such as the small intestine, renal tubular cells and the salivary glands.[85,86] Expression in these normal tissues is 100-1000 fold less than in prostate cancer.[85,86]

1.3.2 Radionuclide therapies for the treatment of prostate cancer

Substantial work has been poured into the use of radiolabelled antibodies, as well as small PSMA targeted antibody fragments such as minibodies and diabodies as radiotherapeutics for imaging and treatment of prostate cancer.[87–91] In addition, small molecule inhibitors of PSMA, mainly containing a glutamate-urea-lysine motif, as with the structure of PSMA-617 (Figure 1.8), have been used as radiotherapeutics for prostate cancer.[92–94] The commercialisation of PSMA-617 has allowed the prostate cancer therapy field to be explored further.[95]

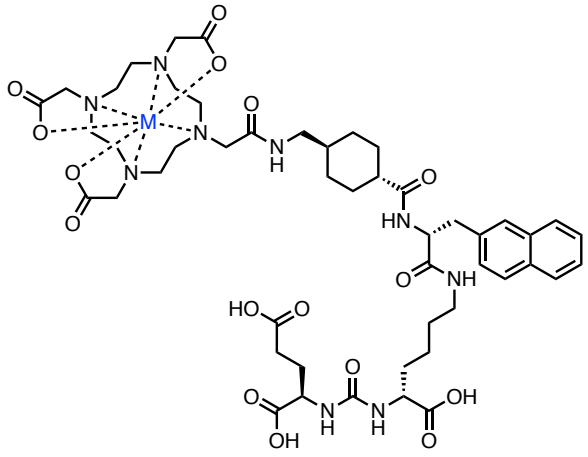

PSMA-617
M = ^{177}Lu, ^{225}Ac, ^{213}Bi, ^{161}Tb

Figure 1.8 – The structure of PSMA-617

Kopka and co-workers developed [^{177}Lu]Lu-PSMA-617 in 2015, which demonstrated excellent prostate cancer cell targeting and pharmacokinetic properties.[94,96] A patient treated with two cycles of the β^- particle emitter [^{177}Lu]Lu-PSMA-617, with a combined dose of 7.4 GBq, showed a PSA decrease from 38.0 to 4.6 ng/mL suggesting therapeutic response.[97] The images in Figure 1.9 show a significant decrease in the number of malignant areas from images a to d, following the two treatments of [^{177}Lu]Lu-PSMA-617.[97] [^{177}Lu]Lu-PSMA-617 has gone onto clinical studies, and as with the patient previously mentioned, the majority of patients treated see a PSA decline,

indicating a reduction in the disease progression.[98–100] Following encouraging results from a very recently published report in *The New England Journal of Medicine* the FDA have granted a priority review for the use of [^{177}Lu]Lu-PSMA-617 in patients with mCRPC, with a decision expected in the first half of 2022.[101,102] The Novartis-funded Phase III trial showed that, compared to standard of care practices, progression-free and overall survival was prolonged. The authors did report incidences of minor adverse events following [^{177}Lu]Lu-PSMA-617 treatment, but the patients' quality of life was not adversely affected.[103]

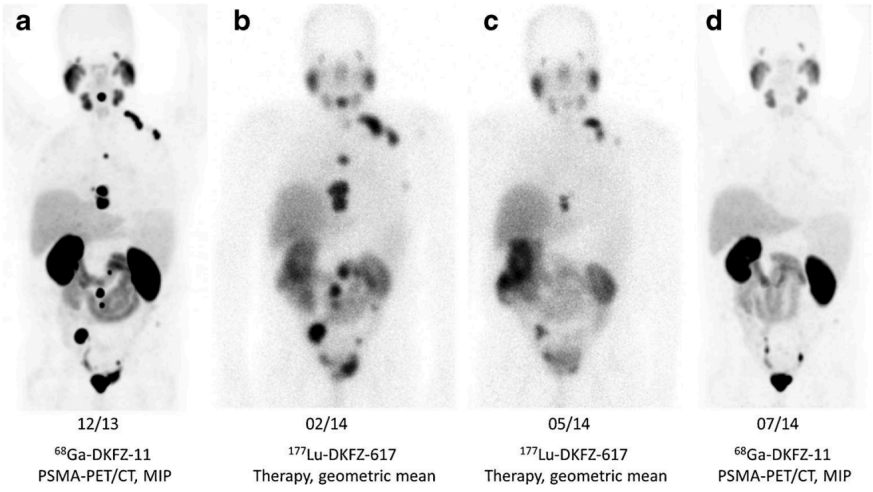

Figure 1.9 – PET image of a patient pre-treatment (a), SPECT images of the same patient following two rounds of ^{177}Lu treatment (b and c) and PET image of the same patient showing the response to the ^{177}Lu treatment (d).

PSMA-617 has also been used with α particle emitters ^{225}Ac and ^{213}Bi. The effectiveness of [^{225}Ac]Ac-PSMA-617 was highlighted in humans; in two patients, their prostate cancer was progressing following [^{177}Lu]Lu-PSMA-617 therapy.[104] PET/CT images in Figure 1.10 show one of the patients pre [^{225}Ac]Ac-PSMA-617 treatment (A), then two months after receiving three cycles of [^{225}Ac]Ac-PSMA-617 (9 – 10 MBq) (B) and then finally two months later after receiving a final dose of [^{225}Ac]Ac-PSMA-617 (6 MBq). Images B and C show the huge decline in the number of PSMA-positive lesions, with them virtually disappearing. These are supported by the PSA levels

in the patients' blood reducing from 2923 ng/mL pre-treatment to <0.1 ng/mL after the final round of [^{225}Ac]Ac-PSMA-617.[104] As of 2020, [^{225}Ac]Ac-PSMA-617 has been in 4 clinical trials, involving 150 patients with mCRPC, showing that it could be another treatment option for patients, especially if other established treatments have failed.[105–107]

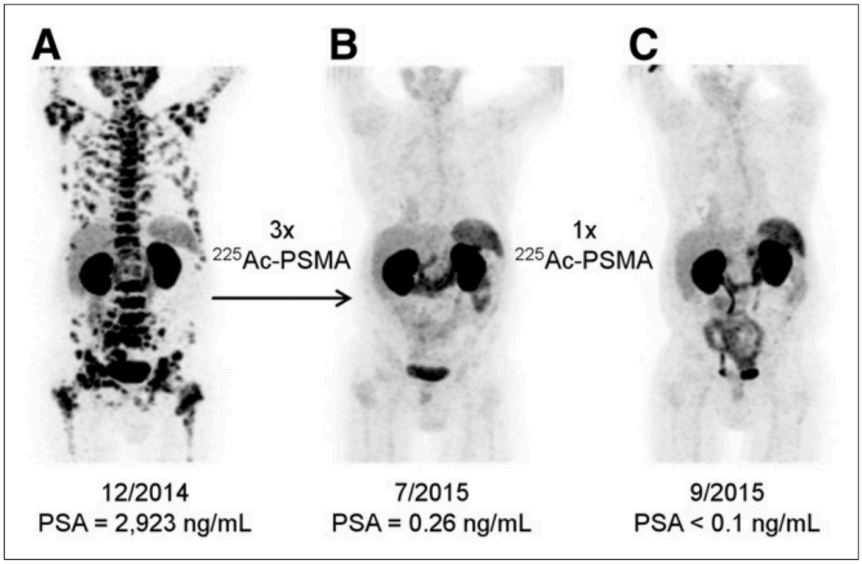

Figure 1.10 – [^{68}Ga]Ga-PSMA-HBED PET/CT images of a patient. The pre-treatment image showing extensive disease progression (A). Restaging 2 months post three cycles of [^{225}Ac]Ac-PSMA-617 (B). Restaging 2 months following one further treatment of [^{225}Ac]Ac-PSMA-617 (C).[104]

Another promising α emitter used with PSMA-617 is ^{213}Bi. Sathekge *et al.* published the first in-human treatment using [^{213}Bi]Bi-PSMA-617 in one patient with mCRPC that had progressed under normal treatment.[108] Following two cycles of [^{213}Bi]Bi-PSMA-617 (cumulative dose of 592 MBq) the patient showed a significant decrease in PSA levels.

Muller and co-workers have also used PSMA-617 with ^{161}Tb ($t_{1/2}$ = 6.86 days), which decays via a combination of β^- particles and Auger electrons.[109] Their results demonstrated that [^{161}Tb]Tb-PSMA-617 was a more effective therapy than [^{177}Lu]Lu-PSMA-617, with dosimetric calculations

suggesting the terbium compound is 3 fold more effective than the lutetium compound *in vitro*.[109] The authors attribute the additional potency of the ^{161}Tb tracer to the AEs. Both therapeutics had similar pharmacokinetics and the same biodistribution. This work highlights the potential of AE emitters for the treatment of prostate cancer and could be an alternative treatment option in the future.

1.4 Thallium

Thallium was first discovered by William Crookes in 1861 while searching for tellurium in residues from sulfuric acid production plants, hence given the Latin name thallus, often used to describe the green tint of young vegetation. The chemistry of thallium has been little explored, but its toxicity was made famous by Agatha Christie's novel 'The Pale Horse' written in 1961. The main use of thallium has been in the electronics industry, where it is commonly used to increase the density and refractive index of glass for semiconductors. By coincidence to this thesis is the use of thallium in photomultiplier tubes to activate NaI and NaCl crystals used in scintillation counters. Within organic chemistry, thallium compounds are more commonly used as catalysts or intermediates and 'regarded as essential reagents for modern organic synthesis'.[110]

1.4.1 Chemical toxicity

As is common with heavy metals, thallium is very toxic. Ingestion of thallium mainly effects the nervous system and gastrointestinal tract.[111–113] For humans, the minimum lethal dose of thallium is 8-12 mg per kilogram of weight.[114,115]

Schelbert and co-workers have calculated the dose administered for a diagnostic imaging study using 74 MBq (2 mCi) delivered around 0.07-0.15 ng per kilogram of body weight and blood concentrations averaged 0.0017 mg per 100 mL.[115] Based on these numbers, a dose around 10,000 times higher would be needed in order for thallium-201 to exhibit chemical lethality.[116]

1.4.2 Thallium as a potassium analogue and its biodistribution

Although not indigenous to the human body, Tl^+ is an analogue of the potassium ion due to the similarity in ionic radii and hydration tendency between Tl^+ and K^+ taking advantage of potassium channels, such as the sodium potassium ATPase pump, in the cell membranes to gain entry into cells.[10]

Mullins and Moore in the 1960s used an isolated frog sartorius muscle to demonstrate how the muscle fibre membrane could not distinguish between the "toxic heavy metal Tl^+ and K^+ provided concentration of the former are kept low".[117] Their experiments also showed that the efflux of Tl^+ increased during stimulation to the same extent as that of K^+. Further biological similarities between Tl^+ and K^+ were found by Gehring and Hammond, who found thallium could activate the Na^+ and K^+ adenosine triphosphatase when substituted for potassium in rabbit erythrocytes, rats and dogs.[118,119]

Work by Sessler and co-workers investigated this mechanism using ouabain and furosemide, which are known inhibitors of the sodium-potassium ATPase pump.[120] The cells were first incubated with the inhibitors and then $[^{201}Tl]Tl^+$ was introduced. The results showed that cellular uptake of $[^{201}Tl]Tl^+$ was reduced in the presence of the inhibitors.

1.4.3 ^{201}Tl as a myocardial perfusion imaging agent

Historically, thallium-201 has been used clinically for myocardial imaging studies. It is delivered to the patient intravenously as thallous chloride, [^{201}Tl]TlCl.[12] The tracer is cleared from circulating blood in less than a minute and is rapidly taken up by different tissues, especially heart and skeletal muscle.[121] The mechanism of thallium-201 uptake in cells has been investigated over the last 60 years and has been found to be influenced by a number of factors.

Researchers have correlated thallium-201 concentrations in myocardial biopsies with regional sodium potassium ATPase activity as well as perfusion.[122,123] These results led to the conclusion that the reduction of thallium-201 uptake in ischaemic myocardium is due to the decrease in sodium potassium ATPase activity as well as poor perfusion.

Other than the heart, Bradley-Moore and co-workers found the greatest areas of thallium-201 accumulation were in the kidneys and liver, with maximum myocardial uptake being achieved 10 minutes post injection.[116] Atkins and co-workers have reported rapid blood clearance of [^{201}Tl]TlCl, with only 5-8% of injected activity remaining in the blood after five minutes.[124] They fitted a biexponential disappearance curve to the data which showed 91.5% of the blood activity cleared within five minutes, but the remainder had a half-life of 40 hours. The slower clearing fraction was found to be in equilibrium between red blood cells and plasma. The biodistribution of [^{201}Tl]TlCl has been reported in the literature to be very similar in mice, goats, rats, dogs and humans.[116]

^{201}Tl has been preplaced in myocardial perfusion imaging by ^{99m}Tc agents such as tetrofosmin and sestamibi due to the shorter half-life, better imaging energies and reduced radiation dose to the patient.

1.4.4 Use in cancer imaging

Charkes and Lebowitz have demonstrated that taking advantage of [^{201}Tl]Tl^{+} acting as a K^{+} mimic, can lead to uptake in tumours.[125,126] The first reported use of thallium-201 investigating tumour uptake was by Cox and co-workers in 1976.[127] They state uptake was observed in a primary bronchial carcinoma tumour of a human male. Furthermore, Tonami *et al.* also identified a primary lung cancer tumour during a patients myocardial evaluation.[128] They investigated this further, comparing the detection rate of malignant tumours with [^{67}Ga]Ga-citrate. From the patients with thyroid cancer, 95% (14 out of 15) showed thallium-201 uptake and 72% (10 out of 14) of the lung cancer patients also had thallium-201 uptake.

One of the contributing factors is the perfusion of malignant tissue, which is essential for effective delivery of imaging and therapeutic agents.[129] It has been found that, as expected, increased vascularisation around a tumour will lead to a greater amount of tracer uptake and hence a more intense signal. However, others have suggested that there are more important factors. Ramanna and co-workers suggest that the intensity of [^{201}Tl]Tl^{+} uptake is related to the cell type.[130] The group performed work using a lymphoma model in which they observed large-cell lymphomas, which are highly vascularised aggressive tumours, to have less ^{201}Tl^{+} uptake than low grade lymphomas (slower growing tumours). The authors do not speculate as to the reason for higher uptake, which may be due to increased sodium potassium ATPase activity in the low-grade tumours.

There have been several papers published involving ^{201}Tl where toxicity has been investigated as an effect of imaging. Early studies in the 1980s highlighted toxicity of ^{201}Tl in V79 Chinese hamster lung fibroblasts.[131] Others have relied on *in silico* simulations. For example, Monte Carlo computational methods were used to accurately model the radiation dose from ^{201}Tl at target volumes of <1 mm in diameter by taking into account the contribution from AEs.[132–135] More

recently a radiobiology study using Geant4-DNA, another Monte Carlo simulation toolkit, demonstrated the theoretical number of single and double strand breaks that could be produced by AE-emitters on the DNA scale; ^{201}Tl was amongst the most effective in causing DNA damage.[136]

A recent report has shown that non-targeted delivery of ^{201}Tl shows short and long-term toxicity in prostate cancer cells.[137] A decrease in clonogenic survival was achieved at only 0.29 Bq/cell, significantly lower than for other AE-emitting radionuclides such as ^{67}Ga and ^{111}In.[19,138] However, as $^{201}Tl^{+}$ accumulates in the heart, and so a targeted approach is required *in vivo* if this radiometal is to be useful in MRT.[139] To date, targeted delivery of ^{201}Tl to cancer cells has been hindered due to the lack of suitable bifunctional chelator chemistry. Despite the high importance of ^{201}Tl during the early years of nuclear medicine, thallium chelation has been poorly investigated. This lack of inquiry has left a big opportunity for the chelation and therapeutic potential of ^{201}Tl to be explored.

1.5 Chemistry of thallium

The chemistry of thallium has not been effectively investigated over the past 30 years, which is likely due to the high toxicity of the metal. However, other than its use in medical imaging, thallium has been used extensively in the semiconductor field, and as an additive in glass manufacture to increase the density and refractive index of the material. Thallium has also been frequently used in rat poisons, insecticides and is referred to in a number of works of literature as a murder weapon.

Thallium is a post-transition metal in group 13 of the periodic table. It is most commonly found in either +3 or +1 oxidation states. The inert pair effect (IPE) plays a dominating role in the chemistry of thallium-201.[140] The IPE is a feature of the heavier elements in groups 13-17 - they often have oxidation states two lower than their maximum predicted value for their respective group. This means the valence electrons (for thallium, $6s^2$) are less reactive than expected.[140] Tl^+ chemistry is most commonly related to that of the alkali metals in group 1 with an oxidation of +1, whereas Tl^{3+} chemistry resembles group 13 elements such as gallium and indium. Tl^+ complexes tend to be unstable due to the s^2 electrons being σ-antibonding in all stereochemistries.

Both the Tl^+ and Tl^{3+} chloride salts have been well characterised in previous literature. $[^{nat}Tl]TlCl_3$, like the other metal chlorides of group 13, behaves as a Lewis acid.[141] $[^{nat}Tl]TlCl_3$ has relatively weak Tl-Cl bonds, and the trivalent chloride salt is the least stable complex compared to the lighter group 13 metals. $TlCl_3$ is very hygroscopic and water soluble, with aqueous solutions being acidic due to the comprehensive hydrolysis of the compound.

Nuclear magnetic resonance (NMR) spectroscopy of the thallium nucleus can be used as an interesting tool to investigate thallium chemistry. Both of the stable isotopes of thallium, ^{203}Tl (29.5%) and ^{205}Tl (70.5%), are NMR active with spin ½ nuclei.

1.5.1 Radioactive isotopes of thallium

Thallium-201 can be produced by irradiation *via* a cyclotron using thallium-203 and has a half-life of 73 hours.[124] It involves thallium-203 being bombarded with protons, releasing three neutrons, forming lead-201, with a half-life of 9.3 hours, which then decays via electron capture and positron emission to the desired thallium-201. This then goes on to decay into mercury-201, which is stable.

A β^+ emitting isotope of Tl, ^{199}Tl ($t_{1/2}$ = 7.4 h) , can be produced via alpha bombardment of gold foil (^{197}Au).[142] Chernov and co-workers have gone on to use ^{199}Tl in a comparative imaging study with ^{201}Tl, highlighting that when injected with the same amount of activity, the total radiation dose was 3.6-15.5 times lower, due to the shorter half-life.[143]

Table 7 – A table of the radioactive isotopes of thallium, their half lives, emission energies and decay products

Isotope	Half-life (hours)	Decay mode	Emissions (keV)	Decay product
^{199}Tl	7.4	β^+	81, 118, 199	^{199}Hg
^{201}Tl	72.9	EC	67-82 (Auger e^-, 88 %) 135, 167 (γ, 12 %)	^{201}Hg

1.5.2 Coordination chemistry

The chelate effect outlines the lower entropic cost of coordinating a single multidentate ligand, relative to multiple, monodentate ligands, hence high denticity chelators are desirable to enhance stability.[144] The macrocyclic effect is similar to the chelate effect but reinforced by the use of a cyclic ligand.[145] Macrocyclic ligands are multidentate ligands, but also constrain the metal ion into a set conformation allowing less conformational freedom. Generally, macrocyclic complexes tend to be more kinetically inert than complexes of acyclic chelators, even in the small number of cases when they have comparable thermodynamic stabilities.[145] Macrocyclic chelators also require minimal conformational change when binding to metal ions, as they are often partially preorganised binding sites for metal ions that reduce the entropy penalty for wrapping around the metal centre.[146] In comparison, acyclic chelators usually must undergo a large conformational change in solution to coordinate a metal ion or have to go through highly strained conformations in transition states during complexation and decomplexation, hence a high kinetic stability.[145] Ultimately, kinetic inertness *in vivo* is the overall objective for a therapeutic agent to ensure maximum damage to the target tissue for a sustained period, while minimizing off target damage.

According to hard soft acid base theory (HSAB), a hard metal ion, like Ga^{3+} for example, is small in size, having a high charge density and predominantly forming ionic bonds. A soft metal, such as Tl^{+}, is described as being large in size and having a relatively low charge density. Due to this softness, Tl^{3+} is understood to interact strongly with soft donor ligands such as thiols.[147,148]

Thermodynamic stability (formation) constants are a way of measuring the strength of interaction between a ligand and a metal to react and form a complex (K_{ML} = [ML]/[M][L]).[145] However, performing these experiments under conditions relevant to *in vivo* stability can be

challenging. Stability constants calculated this way are an efficient way to compare different chelators with a metal ion but cannot be used for predicting *in vivo* kinetic stability.

DOTA (Figure 1.11) is one of the most commonly used chelators in medical imaging with various radiometals across the periodic table. Despite its versatility, there are many metal-DOTA complexes that are unstable, due to poor chelator-metal interactions. These interactions, based on metal ion characteristics such as charge, softness/hardness and atomic radii, vary from metal to metal and have a huge influence on the stability of the complex. The stability of complexes is determined by the coordination number of the ligand and the complex adopting the favoured geometry of the metal ion. The favoured conformation of the complex and ensuring the metal ion is coordinately saturated should prevent competition for the metal ion from external reducing agents.

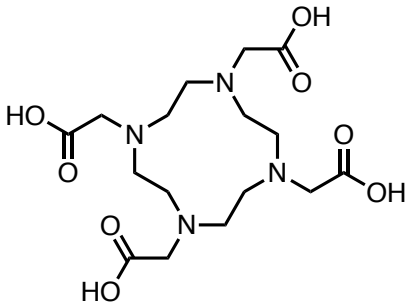

DOTA

Figure 1.11 - Structure of 1,4,7,10-tetraazacylcododecane-1,4,7,10-tetraacetic acid (DOTA)

1.5.2.1 Coordination chemistry of Tl^+

Crown ethers

As previously mentioned, Tl^+ acts as a weak Lewis acid and has similar aqueous solution chemistry to the alkali metals and as such can generally only form weak complexes.[141] However, there is literature to suggest that crown ethers, especially 18-membered rings, can from complexes with Tl^+ in organic solvents, but they have not been explored under biological conditions.[149] Ouchu and Hakushi have stated that the size of the macrocyclic cavity is crucial for the formation of a stable Tl^+ complex, with more stable complexes observed when the metal is bound within the macrocyclic ring and not above the ring.[150] Work by Tamura and co-workers has shown that unsymmetrical benzo-type crown ethers possess high selectivity for Tl^+ selectively over K^+ and Rb^+ but the stability of the complex was not assessed.[151] The structures of such ligands can be seen in Figure 1.12. There have been comparisons between the chemistry of Tl^+ and that of other soft metals Ag^+, Rb^+ and Hg^{2+}, due to similarities in ionic radii (127, 158 and 116 pm respectively). This makes crown ethers an interesting group of chelators to explore in the future with $[^{201}Tl]Tl^+$.

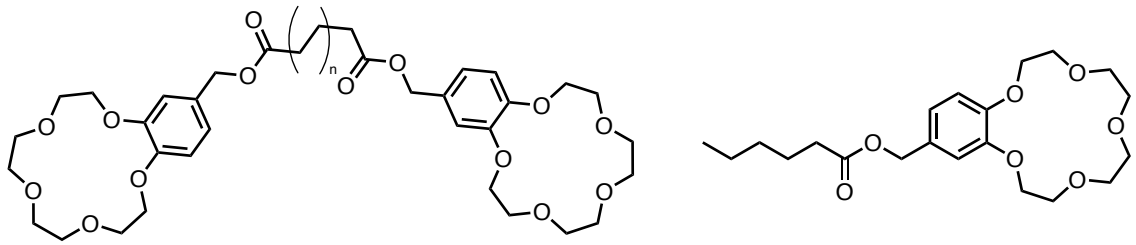

Figure 1.12 – The structure of bis(crown ethers) and a monocyclic crown ether that have been investigated for use with Tl^+

Schröder and co-workers have explored the coordination chemistry of thioether ligands with Tl^+.[152,153] The structures can be seen in Figure 1.13. The group determined crystal structures for

the thallium complexes using the chelators in Figure 1.14. $[Tl([18]aneN_2S_2)]PF_6$ and $[Tl([18]aneS_6)]PF_6$ have similar overall geometries, with very long metal-donor bond lengths illustrating the discrepancy between metal ion radius and macrocyclic cavity size; the crystal structures can be seen in Figure 1.14. The single crystal structures of $[Tl([24]aneS_8)]PF_6$ and $[Tl([28]aneS_8)]PF_6$ showed the metal centres are coordinated by two half ligands in a 'sandwich' structure.[146] $[Tl([9]aneS_3)]PF_6$ shows a 1:1 ratio of Tl to $[9]aneS_3$ with very long Tl-S bonds.[152,154]

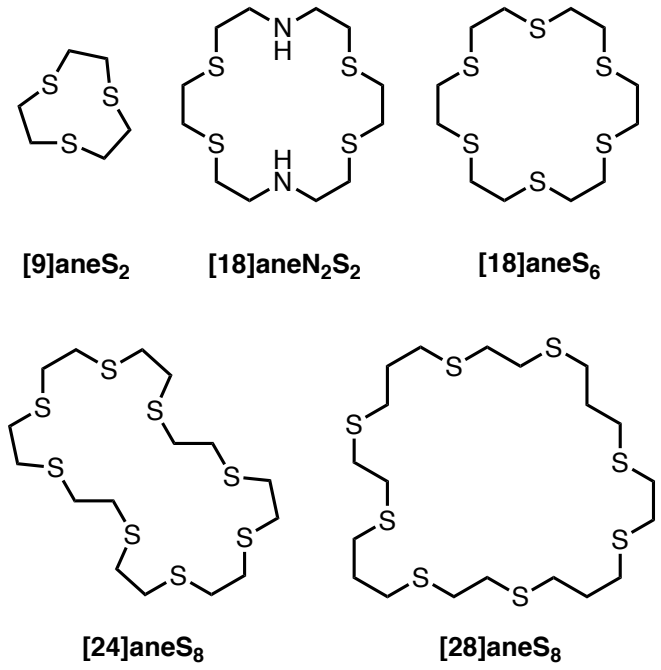

Figure 1.13 - The structures of 5 thio crown ethers shown by Schroder and co-workers to have chelated Tl^+

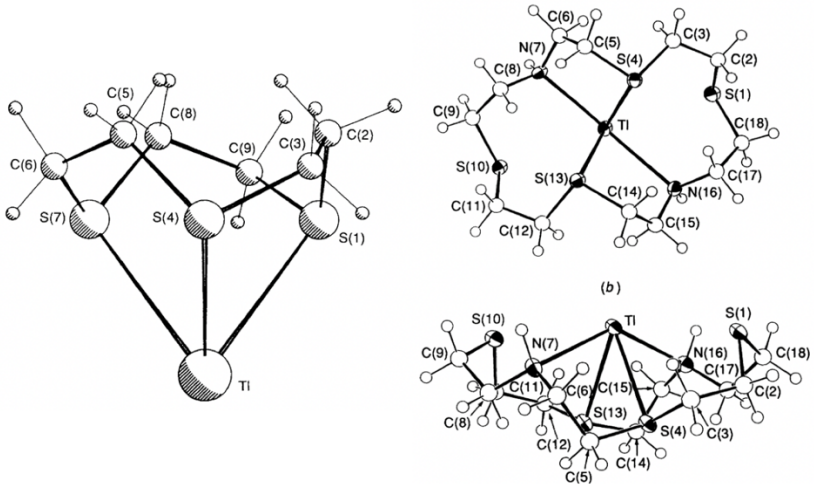

Figure 1.14 – Crystal structure of $[Tl([9]aneS_3)]^+$ (left) and $[Tl([18]aneN_2S_3)]^+$ (right, two different angles)

Diethyldithiocarbamate (DDC)

Van Der Schoot and co-workers have described the preparation and quality control (QC) methods of a neutral lipophilic Tl^+ complex, using sodium diethyldithiocarbamate (NaDDC), the structure of which can be seen in Figure 1.15.[155] NaDDC has been previously used as a treatment for Tl intoxication to increase urinary excretion of the metal. During NaDDC treatment for Tl intoxication, neurological symptoms worsened which was due to Tl being redeposited across the blood brain barrier (BBB).[155] The authors went on to investigate the biodistribution of [^{201}Tl]Tl-DDC *in vivo* to probe if significant amounts of [^{201}Tl]Tl-DDC crossed the BBB.[155] Their results show a substantial amount of radioactivity accumulates in the brain during the first 60 minutes, but after 24 hours almost all activity has been cleared from the brain, leading to accumulation in liver and kidneys.[155] The structure of the complex was not confirmed, but the proposed structure can be seen in (Figure 1.15). The main observation here is that [^{201}Tl]Tl-DDC does not show the same biodistribution as [^{201}Tl]TlCl *in vivo*, demonstrating some complex stability, long enough to get into brain. [^{201}Tl]Tl-DDC has not been used for delivery to tumours,

which could be explored at some point in the future. Additionally, applications of the [^{201}Tl]Tl-DDC complex could include incorporation into liposomes, similar to that of [^{89}Zr]Zr-oxine, for delivery of the radiometal to malignant tissue via the EPR effect or targeted delivery using functionalised nanoparticles.[156–158]

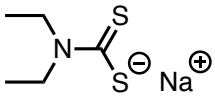

Sodium diethyldithiocarbamate (DDC)

[^{201}Tl]Tl-DDC

Figure 1.15 - Structure of sodium diethyldithiocarbamate (top) and the radiolabelling reaction to form [^{201}Tl]Tl-DDC (bottom).

Using the encouraging results from their previous reports, Van Der Schoot and co-workers have investigated the biodistribution of [^{201}Tl]Tl-DDC further. When compared to *N*-isopropyl-(^{123}I)-*p*-iodoamphetamine (IMP), a commercially available tracer used for cerebral blood perfusion imaging also with SPECT, [^{201}Tl]Tl-DDC had a comparable biodistribution in rabbits.[159] The percentage brain uptake was similar, with comparable grey/white matter ratios, as well as similar uptake in the kidneys. The biggest difference in biodistribution was found in the lungs with IMP having significantly higher uptake (8.32 %ID/g) compared to [^{201}Tl]Tl-DDC, which had low retention in the lungs (0.53 %ID/g). However higher uptake of [^{201}Tl]Tl-DDC was observed in the liver (14.36 %ID/g), when compared to IMP (8.68 %ID/g).[159] If ^{201}Tl was to be used as a therapeutic in the future, dose from the Auger electrons to organs in the excretion pathway would have to be assessed.

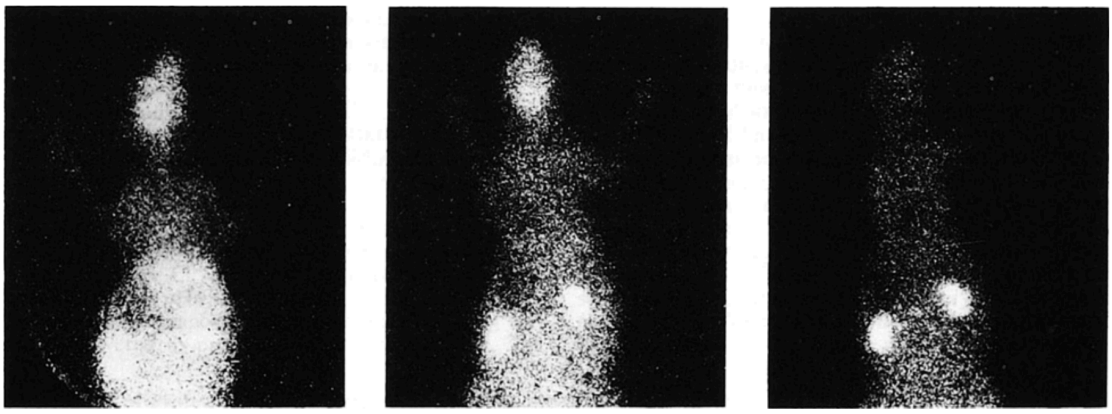

Figure 1.16 – 40 minutes after [^{201}Tl]Tl-DDC administration (left), 4 hours after [^{201}Tl]Tl-DDC administration (middle) and 4 hours after [^{201}Tl]TlCl administration (right).

In addition to rabbits, the authors performed biodistribution studies of [^{201}Tl]Tl-DDC in two human volunteers.[160] The high brain uptake after 2 minutes was comparable to what was found in rabbits (Figure 1.16) and the activity was constant in the brain for at least 2 hours. A comparison of the whole body distribution in humans comparing [^{201}Tl]TlCl and [^{201}Tl]Tl-DDC can be seen in Figure 1.17, however the authors did not state at what time point these images were taken or if both these images are of the same volunteer. Further human studies led to the authors proposing the mechanism for [^{201}Tl]Tl-DDC uptake in the brain. They hypothesised that after the first passage through the brain, little to no further uptake of [^{201}Tl]Tl-DDC in the brain was observed, likely due to the complex falling apart and then redistribution as the [^{201}Tl]Tl^+ cation, hence the similar distribution to [^{201}Tl]TlCl.[160] The authors suggested that the DDC served as a carrier to enable [^{201}Tl]Tl^+ to cross the BBB, due to the complex's lipophilicity and neutral charge. Once in the brain, it was not known whether the distribution occurred as [^{201}Tl]Tl^+ or [^{201}Tl]Tl-DDC. DDC has the possibility to be used in the future for therapeutic delivery of ^{201}Tl, as an alternative mechanism of getting a cytotoxic dose of ^{201}Tl into cells, instead of via potassium channels. If the structure could be adapted to effectively target cancer cells, it may be a useful ligand in subsequent investigations.

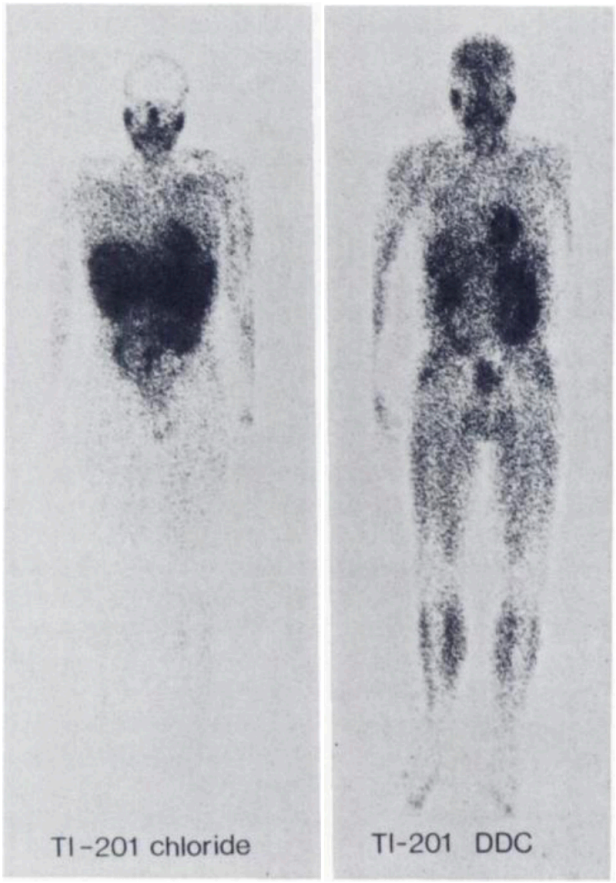

Figure 1.17 – Whole body SPECT images of [^{201}Tl]TlCl (left) and [^{201}Tl]Tl-DDC (right) at 3.5 hours post injection

1.5.2.2 Coordination chemistry of Tl^{3+}

DOTA

DOTA is the only reported macrocyclic chelator published in the literature that has been used with ^{201}Tl. Hijnen and co-workers have shown that [^{201}Tl]Tl-DOTA remains stable in both human and mouse serum for greater than 48 hours.[161] [^{201}Tl]$TlCl_3$ was generated from [^{201}Tl]TlCl using an ozone mediated oxidation reaction and chelated by DOTA at room temperature within 90 minutes, achieving a radiochemical yield of 80%. The complex was then purified using Sep-Pak cartridges. The characterisation of [^{201}Tl]Tl-DOTA is incomplete, as HPLC analysis has not been performed to validate their TLC method (reverse phase TLC). There was also a lack of validation for their oxidation method to confirm the production of Tl^{3+} using non-radioactive Tl.[29] However, the authors suggest from their [^{201}Tl]Tl-DOTA *in vivo* results that the metal is being reduced and released from the chelator, hence the similar biodistribution to [^{201}Tl]TlCl from SPECT images. However, the authors have not published *ex vivo* biodistribution results in this paper or any subsequent paper. Their conclusions imply an alternative chelator is needed to prevent the *in vivo* reduction and dissociation of [^{201}Tl]Tl^{3+}. The authors also suggest from their results that less than 20% of the complex remained stable long enough for urinary excretion. However, they do not explain what form the remaining 80% of activity is and do not show any HPLC traces or TLC data showing how they came to this number. Further *in vivo* results using [^{201}Tl]TlCl show initial heart uptake and then clearance through the kidneys after 1 hour. Missing from this report is an additional control experiment showing the biodistribution of [^{201}Tl]$TlCl_3$. It is likely that Tl^{3+} will be reduced to Tl^{+} without the protection of a chelator; this needs to be confirmed experimentally. The [^{201}Tl]TlCl *in vivo* images presented in the paper are also at different time points (5 mins and 1 hour) to the [^{201}Tl]Tl-DOTA *in vivo* images which are at a much later time point (4 hours) so cannot be directly compared.[161] The missing data from this report means the *in vivo* stability of [^{201}Tl]Tl-DOTA is not clear and requires further investigation.

Recently there have been results published on the stability of [^{nat}Tl]Tl-DOTA.[162] Fodor *et al* formed the complex by firstly preparing $Tl(ClO_4)_3$ from $TlClO_4$ using electrolysis in perchloric acid (6 M). $Tl(ClO_4)_3$ was then added dropwise to a stirring solution of DOTA in a mildly basic solution pH ~ 8 at room temperature. The solution was then neutralised using 20% NaOH. The authors had also prepared [^{nat}Tl]Tl-DOTA using $Tl(CH_3COOH)_3$, generated by adding a 10-fold excess of acetic acid/sodium acetate buffer to $Tl(ClO_4)_3$. Perchlorate salts tend to have greater solubility in water compared to chloride salts which will have an effect on chelation. They found that the DOTA complex is stable after incubation with NaBr (0.5 M) and $HClO_4$ (0.1 - 1.0 M).

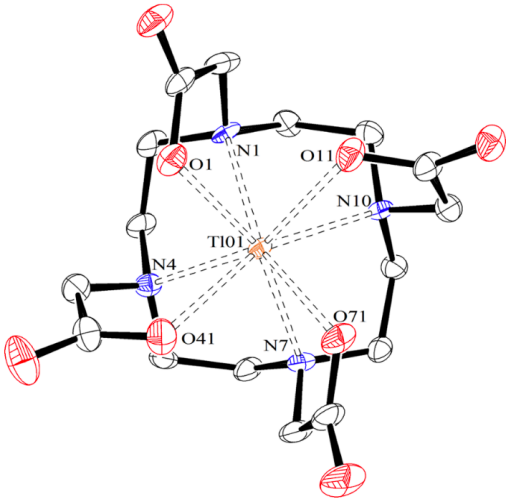

Figure 1.18 – The crystal structure of [^{nat}Tl]Tl-DOTA from Fodor and co-workers [162]

The authors described [^{nat}Tl]Tl-DOTA as a very inert complex and resistant to coordination by external anions. They obtained a crystal structure (Figure 1.18) of the complex which showed the thallium ion directly coordinated to the eight donor atoms in a twisted square antiprismatic (TSAP) coordination, and performed an extensive spectroscopic study to further supplement the structure of [^{nat}Tl]Tl-DOTA, which can be seen in (Figure 1.18).[162] The group also found that the complex did not react with hydroxide anions, and formed only a weak complex with cyanide anion using UV-vis and NMR studies. It must be taken into account that they did not test the stability of the complex under biological or aqueous conditions, but further research must be

done to confirm the results obtained by Hijnen.[161] It is possible to conclude from the previous literature that it is likely [^{nat}Tl]Tl-DOTA is stable in the absence of reducing agents. However, under biological conditions (where reducing agents may be present) it may be vulnerable to reductive dissociation, despite the high affinity of DOTA for Tl^{3+}. This aspect will need further investigation to confirm the instability.

EDTA

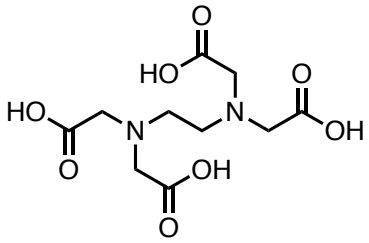

EDTA

Figure 1.19 - Structure of ethylenediaminetetraacetic acid (EDTA)

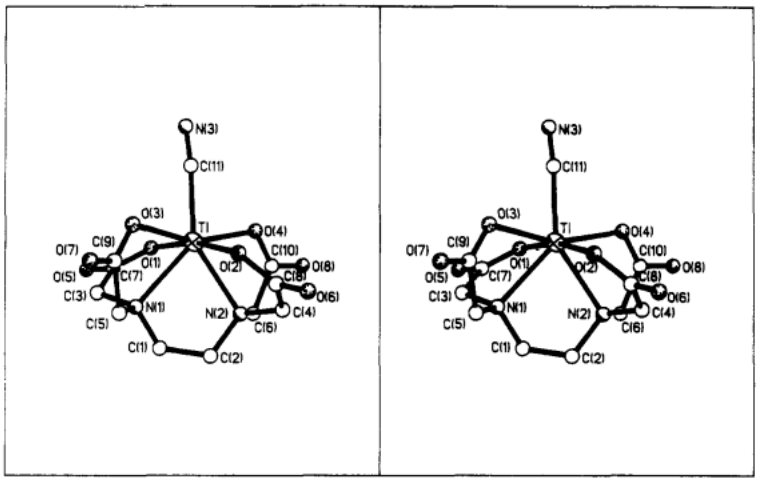

Figure 1.20 - Crystal structure of the complex Tl(EDTA)CN^{2-}grown from a solution of $Na_2Tl(EDTA)CN.3H_2O$

Blixt *et al.* have shown the [^{nat}Tl][Tl(EDTA)$^-$] complex to be "one of the most stable metal-EDTA complexes" known, with a K_d = 37.8 M.[163] The only EDTA complex more stable than the Tl^{3+}

complex was [^{nat}Co][Co(EDTA)$^{-}$]. The authors stated that Tl(EDTA)$_{aq}^{-}$ ion does not dissociate in aqueous solution, so can be treated as a metal ion with one free coordination site.

The crystal structure of [Tl-EDTA(CN)]$^{2-}$ shows the usual bowl structure for a 3+ metal-EDTA complex (Figure 1.20). Coordination from all four oxygen atoms and both nitrogen atoms to the metal is observed, with oxygen atoms "lying in a tetrahedrally distorted plane". This crystal structure highlights the large size of the Tl^{3+} ion, with EDTA unable to encapsulate the metal within the chelator. As the metal is coordinatively unsaturated, this allows the CN^{-} anion to also coordinate to the metal centre, giving it an overall coordination number of 7. As described by Blixt, smaller metal ions, for example Co^{3+} (radii = 0.63 A), can be complexly encapsulated by EDTA. On moving to slightly larger metal ions like Ti^{4+} (radii = 68 pm) and Mn^{2+} (radii = 80 pm), the metal ions sit above the "bowl", so extra coordination sites are exposed, hence coordination numbers above 6 are observed with Tl^{3+} being larger again with an ionic radii of 102 pm.[154]

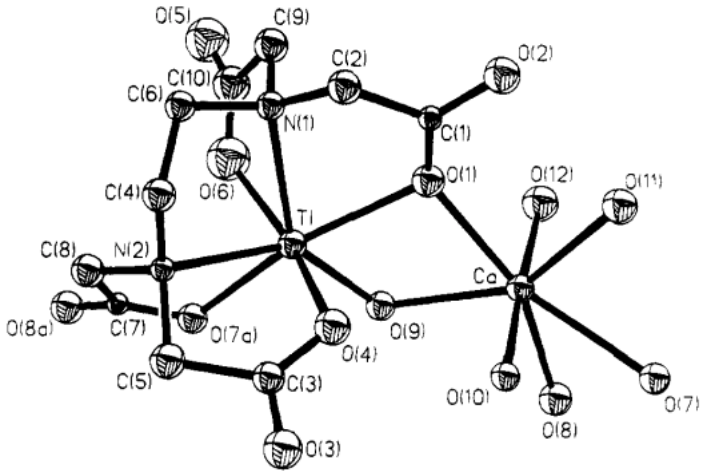

Figure 1.21 - Crystal structure of Ca[Tl(EDTA)(OH)].3H$_2$O from Musso and co-workers [164]

The crystal structure shown in (Figure 1.21) is another [^{nat}Tl]Tl-EDTA complex grown by Musso and co-workers.[164] Like the crystal structure obtained by Blixt *et al.*, this structure also shows a 7 coordinate Tl metal centre, made up of the six donor atoms of EDTA and the coordination of a hydroxyl anion.[163] The Musso structure was found to be in the form of long chains, where 7

coordinate Ca atoms link two Tl-EDTA units. The Ca coordination sphere is comprised of three water molecules, three carboxylate oxygens of adjacent [^{nat}Tl]Tl-EDTA moieties and a bridging hydroxyl anion. The authors conclude that EDTA occupies slightly more than half of the coordination sphere of Tl^{3+}. The [^{nat}Tl]Tl-EDTA complex has very high thermodynamic resistance to dissociation, however this does not imply kinetic stability and also it does not imply that the complex will be stable in the presence of potential reducing agents – as would occur under biological conditions *in vivo*.

DTPA

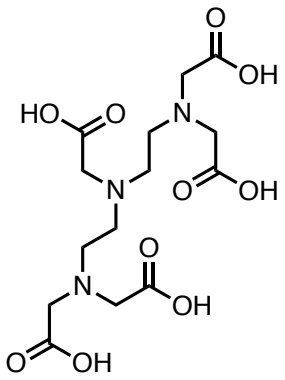

DTPA

Figure 1.22 – Structure of diethylenetriaminepentaacetic acid (DTPA).

Hijnen and co-workers radiolabelled DTPA at pH 8, by stirring for 60 minutes at 18 °C giving a radiochemical yield of >95%.[161] Their results showed that [^{201}Tl]Tl-DTPA completely decomposed after incubation in both human and mouse serum after 4 hours. They hypothesised that the radiometal is reduced to Tl^{+} under these *in vitro* conditions and the metal dissociates from the chelator. In contrast, Jalilian and co-workers have extensively evaluated [^{201}Tl]Tl-DTPA *in vivo* with numerous bioconjugations to proteins and antibodies.[30–32] The authors claimed [^{201}Tl]Tl-DTPA is stable in aqueous solution and human serum for >3 days. The stability in aqueous solution is in agreement with reports from Hijnen and co-workers, but serum stability results are

inconsistent. Hijnen *et al.* used reverse phase TLC plate with MeCN (30%) in water as the mobile phase to evaluate serum stability, whereas Jalilian *et al.* use Sepharose columns (1 x 30 cm), with 0.5 mL fractions collected, eluting with PBS. However, it is unclear how the authors evaluated these fractions to determine complex stability and draw the conclusions they do as their experimental does not explain this.[165] From these reports, it is possible to conclude that there remains no credible evidence that DTPA is an effective chelator of Tl^{3+} for use *in vivo*.

TPEN and CDTA

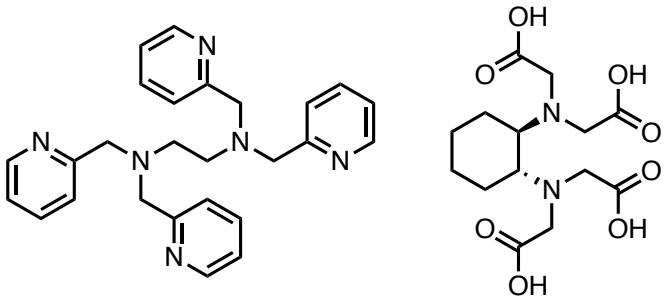

Figure 1.23 - Structure of TPEN (left) and CDTA (right)

In the early 1990s, Musso *et al* investigated the formation of a series of mixed-ligand chelate complexes of Tl^{3+}, including EDTA, CDTA and TPEN with different co-ligands, namely OH^-, Cl^- and SCN^-.[164] The authors used X-ray crystallography to probe the binding of Tl^{3+} by TPEN, which can be seen in Figure 1.24.

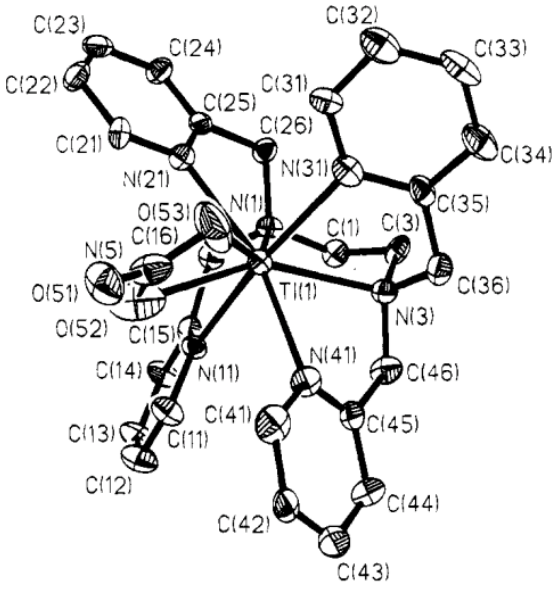

Figure 1.24 - ORTEP view of the complex cation $[Tl(TPEN)(NO_3)][ClO_4]_2$ [164]

The crystal structure in Figure 1.24 shows an octa-coordinated Tl^{3+} isolated from a solution of $TPEN.4HClO_4$ and $Tl(NO_3)_3$ in nitric acid. The crystal structure also shows the coordination of a perchlorate anion, despite the large concentration of nitrate anions in solution. The authors also hypothesise that the coordination of the nitrate ligand questions the thermodynamic stability of Tl^{3+} nitrate complexes and the appropriateness of using it as an "inert" electrolyte in determining stability constants.

Tl^{3+} complexes formed with three different dithiocarbamates have been investigated and the structures determined from crystals grown by Sivagurunathan and co-workers.[166] The structures of cyclohexylmethyl dithiocarbamate (CHMDTC), cyclohexylethyl dithiocarbamate (CHEDTC) and dicyclohexyl dithiocarbamate (DCHDTC) can be seen in Figure 1.25. The stabilities of the complexes were not evaluated. The crystals from which the structures in Figure 1.26 were derived were grown from a reaction between $[^{nat}Tl]TlCl_3$ and the ligands in a 1 to 3 molar ratio. Given the coordination number of Tl^{3+} is >8, it is curious that the authors did not investigate larger molar ratios. Nonetheless, these crystal structures provide some information on the

coordination chemistry of Tl^{3+}. All three complexes have a distorted octahedral geometry, due to them only being 6-coordinate in contrast to the previously mentioned chelators, with increasing Tl-S bond lengths and increasing steric hinderance on the ligand (DCHDTC > CHEDTC > CHMDTC). Tl^{+} complexes with CHMDTC, CHEDTC and DCHDTC have also previously been reported and shown to be polymeric in nature.[167]

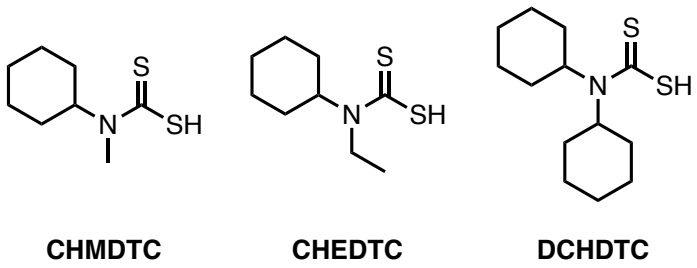

Figure 1.25 - Structure of cyclohexylmethyl dithiocarbamate (CHMDTC), cyclohexylethyl dithiocarbamate (CHEDTC) and dicyclohexyl dithiocarbamate (DCHDTC)

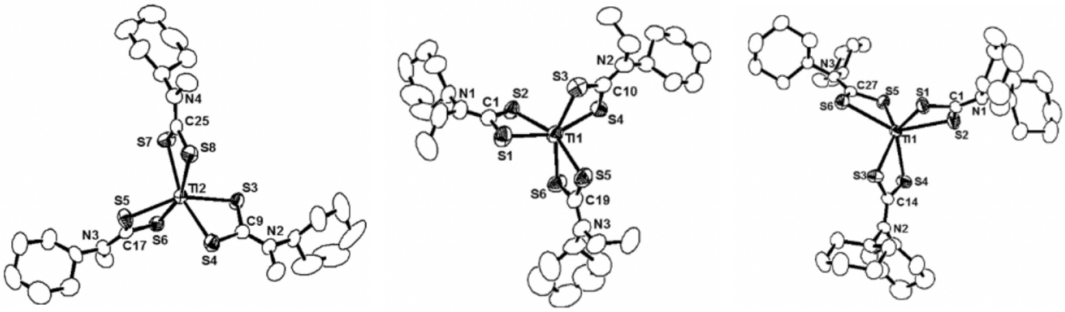

Figure 1.26 - The crystal structures of $[Tl(CHMDTC)_3]$ (left), $[Tl(CHEDTC)_3]$ (middle), $[Tl(DCHDTC)_3]$ (right)

1.6 Designing a better chelator for Tl^+

Recent work published by Brotin *et al.* have used a water soluble cryptophane system bearing three phenol and three carboxylic acid moieties to bind Tl^+.[168–171] Figure 1.27 shows the structure of three cryptophane compounds with varying amounts of carboxylic acid and phenol groups. Cryptophane 1, which contains only phenol donors, has high affinity for Tl^+ whereas cryptophane 2, containing carboxylate donors, has no affinity for Tl^+. Cryptophane 3 has a combination of three phenol and three carboxylate donors and has lower affinity for Tl^+ than Cryptophane 1. This highlights the importance of the phenol moiety for binding Tl^+ in these cryptophane systems. The group intended to use these compounds for environmental chemistry related to the removal of trace Tl^+ from polluted water, and so the ligands have not been tested under biological conditions appropriate to imaging. However, if these compounds could be radiolabelled and their stabilities evaluated, the structures could allow a bioconjugate to be synthesised in the future.

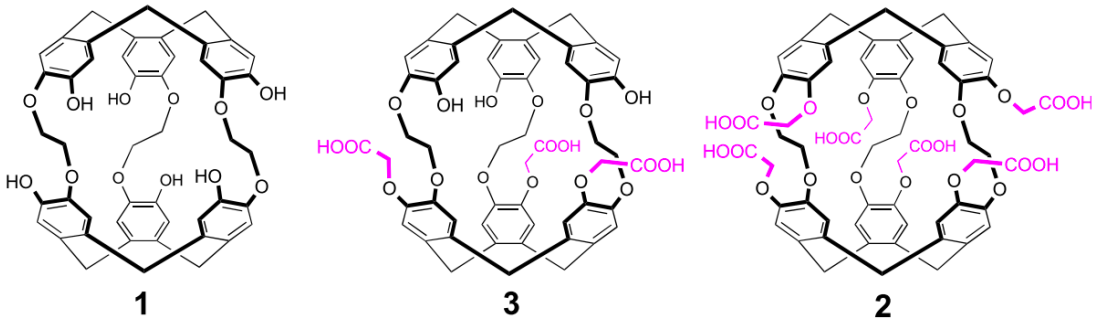

Figure 1.27 – The structure of three cryptophanes investigated for use with Tl^+

Alternatively, recent work on the chelation of $[^{203}Pb]Pb^{2+}$ by McDonagh and co-workers highlights the possibility of using a [2,2,2]-cryptand with heavy metals.[172] They developed antibody bioconjugates using a *trans*-cyclooctene and tetrazine residue through an inverse

electron demand Diels-Alder reaction and via an isothiocyanate group generating a thiourea, as shown in Figure 1.28. As shown in Table 8, Pb^{2+} has an ionic radius comparable to that of Tl^{+}, so the metal should fit into the cavity. Additionally, the authors calculated the cavity size to be 280 pm, so Tl^{+} would fit into the cavity of the [2,2,2]-cryptand. The X-ray crystal structure shows Pb^{2+} sitting in the centre of the cavity bound by the 8 N_2O_6 donor atoms as well as both oxygen atoms from the perchlorate counterion, forming a 10-coordinate complex, as shown in Figure 1.29. As well as evaluation with Tl^{+}, the 3+ oxidation state could be investigated for use with the cryptand. Using a cage like cryptand could help to prevent reducing agents reaching a metal hence delaying dissociation from the chelator. Despite the high affinity for alkali metal ions, due to only a hexadentate complex being formed with [^{nat}Tl]Tl^{+}, it is likely that the [^{nat}Tl]Tl-[2,2,2]-cryptand will be unstable under biological conditions.

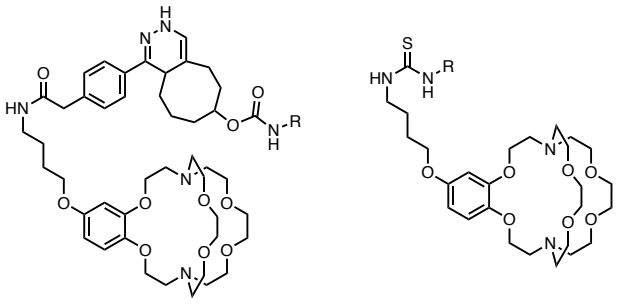

Figure 1.28 – The structure of the cryptand ligand conjugated to the antibody Trastuzumab (R group) in two different ways, using a *trans*-cyclooctene and tetrazine residue through an inverse electron demand Diels-Alder reaction or via an isothiocyanate group (right).

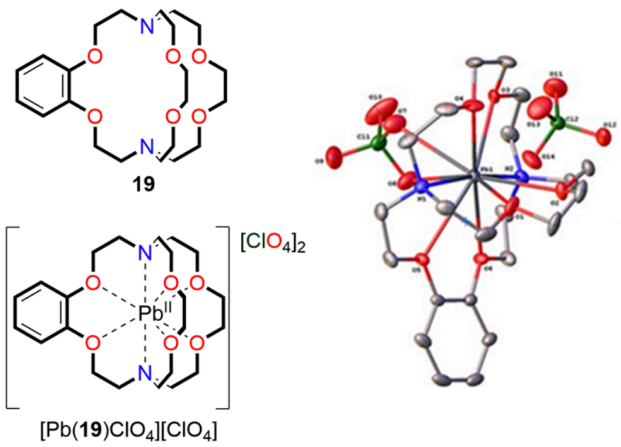

Figure 1.29 – Solid state X-ray crystal structure of [Pb(cryptand)ClO_4][ClO_4] using a non-bifunctional version of the cryptand.

Table 8 – A summary of the ionic radii of various metals that have comparable ionic radii to Tl^{3+}

Metal	Ionic radii (pm)
In^{3+}	92
Tl^{+}	150
Tl^{3+}	102
Y^{3+}	102
La^{3+}	103
Bi^{3+}	117
Pb^{2+}	130

1.7 Designing a better chelator for Tl^{3+}

The background described above suggests that alternative chelators for complexation of Tl^{3+}, forming complexes with greater resistance to dissociation/transmetalation, are required if molecular targeting of ^{201}Tl to cancer cells is to be achieved. Due to the minimal research done into the chelation of Tl^{3+}, there is very little information to work with. With this lack of knowledge, a reasonable strategy might be to apply periodic analogy and use knowledge of In^{3+} chelators as an initial starting point for finding a good chelator for Tl^{3+}. In^{3+} has a similar ionic radius to Tl^{3+}, and both metals are in group 13 of the periodic table having a 3+ charge (Table 8). Evaluating good In^{3+} chelators for the chelation of Tl^{3+} would allow more information to be learnt about the coordination chemistry of Tl^{3+} and could influence which chelators are explored next if these are not suitable. Indium has been thoroughly investigated in nuclear medicine for many years and a huge number of chelators have been designed and developed, leading to successful clinical translation of several targeted radiopharmaceuticals for imaging and therapy as previously described. This means there is a large library of In^{3+} chelators that can be assessed for

the chelation of Tl^{3+}. This extensive and thorough process is yet to be done with thallium. Additionally, the unavailability of [^{111}In]InCl does not allow for direct contrast to [^{201}Tl]TlCl.

In addition to indium, inspiration for novel chelators can also be sought from other metals which have similar ionic radii to Tl^{3+} , such as bismuth, yttrium and lead (ionic radii can be seen in Table 8).[154] Both lead and bismuth are in period 6 of the periodic table in group 14 and 15 respectively, sitting next to thallium while yttrium has a very similar ionic radius and has a 3+ charge. Of the chelators chosen in Chapter 3, the number of donor atoms varies as well as characteristics such as their relative basicity and chemical hardness of donors. Additionally, they have varying structures, cyclic and acyclic, as well as differing cavity sizes; comparison may help understand how the structural differences affect the stability of the complex. The major difference between Tl^{3+} and the other metals in Table 8 is that in addition to binding Tl^{3+}, the chelator will need to protect the metal from reduction.

1.8 Aims

The overarching aim of this project was to validate the concept of molecular radionuclide therapy (MRT) with ^{201}Tl, taking advantage of the large number of Auger electrons that are emitted per decay from the radiometal.

To achieve this aim, firstly, the development of a mild oxidation reaction is needed to convert commercially available [^{201}Tl]Tl^{+} to [^{201}Tl]Tl^{3+}, as the current literature methods use concentrated acid, high temperatures and/or strong oxidising agents. A mild oxidation reaction, that does not require purification, is essential to prevent the degradation of biomolecules, such as large peptide and antibodies during radiolabelling. This work is described in **Chapter 2**.

Secondly, the radiotoxicity of ^{201}Tl needed to be assessed. Isolated plasmid DNA damage assessment was used to demonstrate that [^{201}Tl]Tl^{+} and [^{201}Tl]Tl^{3+} can cause SSBs and DSBs to DNA in a cell free environment. This work is described in **Chapter 3**. Further investigations were performed within our group, in parallel to this, by Katarzyna Osytek, who used γH2AX fluorescence imaging and clonogenic assays to quantify the damage [^{201}Tl]TlCl could do to DU145 prostate cancer cells and MDA-MB-231 breast cancer cells.[137]

Thirdly, the chelation chemistry of [$^{nat/201}$Tl]Tl^{3+} was explored in **Chapter 4**. As the reports in the literature described conflicting and inconsistent conclusions about the stability of [^{201}Tl]Tl-DTPA and [^{201}Tl]Tl-DOTA, these were initially investigated. Due to complex instability, alternative chelators were pursued, using chelators for radiometals with similar ionic radii as a guide.

Finally, a PSMA targeting bioconjugate using H_4pypa as the [^{201}Tl]Tl^{3+} chelator was synthesised and radiolabelled. It was then evaluated *in vivo* using healthy male SCID/beige mice, followed by mice bearing DU145 PSMA positive and PSMA negative prostate cancer xenografts. This work is described in **Chapter 5**.

2 OXIDATION OF $[^{201}Tl]Tl^{+}$ TO $[^{201}Tl]Tl^{3+}$

2.1 Introduction

It is expected that ^{201}Tl needs to be converted from the commercially available 1+ oxidation state to a 3+ oxidation state, which is more amenable to complexation by multi-dentate ligands, as described in Chapter 1.

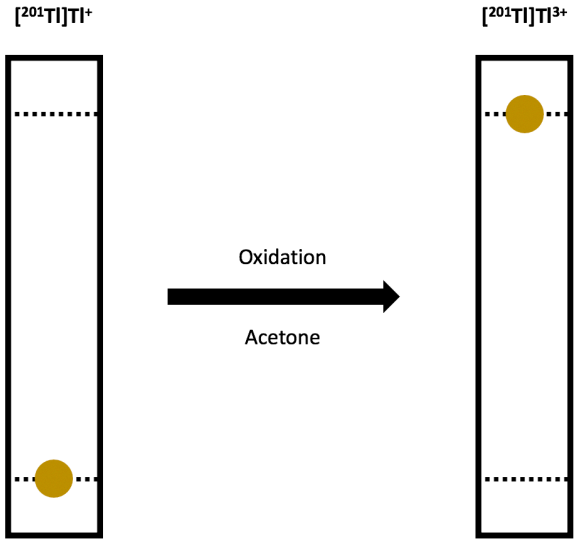

Figure 2.1 – An example of the ITLC of the oxidation reaction to generate $[^{201}Tl]Tl^{3+}$ from $[^{201}Tl]Tl^{+}$ using acetone as the mobile phase and ITLC-SG as the solid phase. $[^{201}Tl]Tl^{3+}$ moves with the solvent front (R_f = 1) whereas $[^{201}Tl]Tl^{+}$ remains at the origin (R_f = 0).

There are a number of published methods that describe the oxidation of Tl^{+} to Tl^{3+}. They include the use of ozone, hydrogen peroxide and HCl (6 M) or a combination of multiple oxidising agents and heating till evaporation (Figure 2.4).[161,173–177] However, the use of strong acid, as well as toxic oxidising agents like hydrogen peroxide (H_2O_2), complicate the subsequent radiolabelling steps. The boiling of aqueous solutions containing radioactivity, also containing strong oxidising agents, is not practical for the chelation and biomolecule work moving forward, hence alternative

methods need to be explored. For example, high temperature conditions accelerates various degradation pathways of antibodies leading to formation of aggregates.[178,179] Very acidic pHs can also have a detrimental effect on antibodies, leading to fragmentation at hinge joints and the formation of aggregates.[180] Increased temperature and acidic pH is less likely to adversely affect the stability of small peptides, as in the literature they often require heating, but will also lead to the degradation of larger proteins.[49]

These methods also have limited scope for possible translation to clinical setting due to the use of toxic reagents or a cumbersome reaction set up. The removal of excess oxidising agent will be essential for accurate assessment of the therapeutic response to ^{201}Tl containing agents, both for *in vitro* and *in vivo* studies. In particular, hydrogen peroxide plays a significant role in biological formation of reactive oxygen species (ROS). Despite these drawbacks, Jalilian and co-workers have published accurate chromatographic methods for the oxidation reaction which have been used in this work.[174] An example of the ITLCs can be seen in Figure 2.1.

The ideal radiolabelling 'product' to use in MRT with ^{201}Tl would use a kit-based system, like many of the radiotracers used within the field such as [^{99m}Tc]Tc-DMSA and [^{68}Ga]Ga-THP-PSMA.[181,182] Figure 2.2 demonstrates diagrammatically how tested published literature methods did not provide a basis to develop kits using the stated reaction conditions.

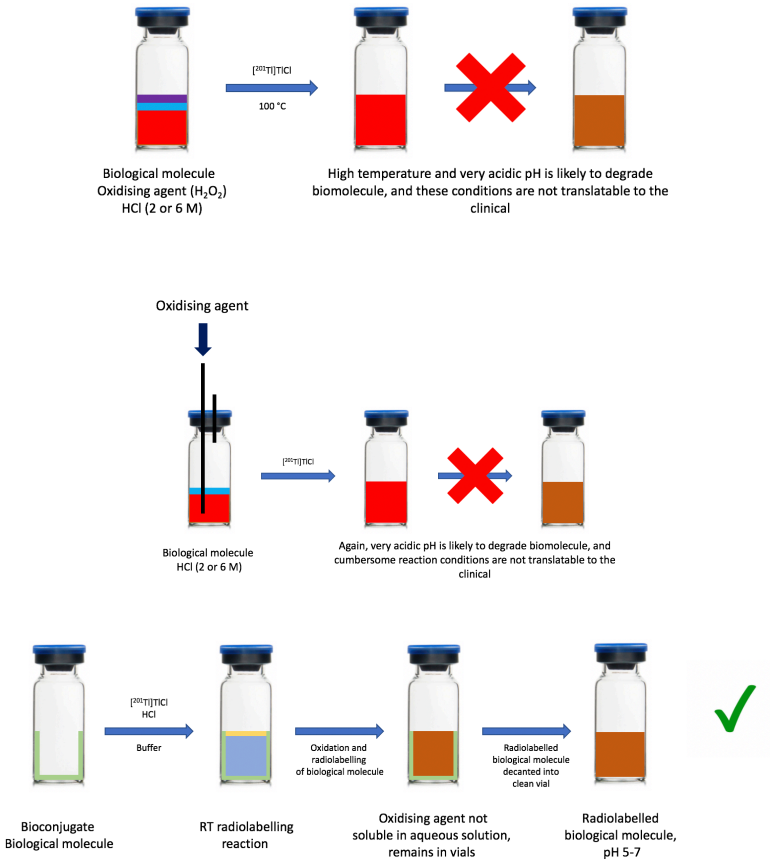

Figure 2.2 – Three diagrams highlighting that the current literature methods for the oxidation of $[^{201}Tl]TlCl$ to $[^{201}Tl]TlCl_3$ are not usable for a kit-based system and the 'ideal' kit reaction conditions for possible clinical translation

2.2 Material and methods

Unless stated otherwise, chemicals and solvents were purchased from commercial suppliers (Merck, Fisher Scientific, CheMatech). [^{201}Tl]TlCl in saline was purchased from Curium Pharma, UK. Nine methods, described below and summarised in Figure 2.3, were evaluated for the conversion of Tl(I) to [^{201}Tl]$TlCl_3$.

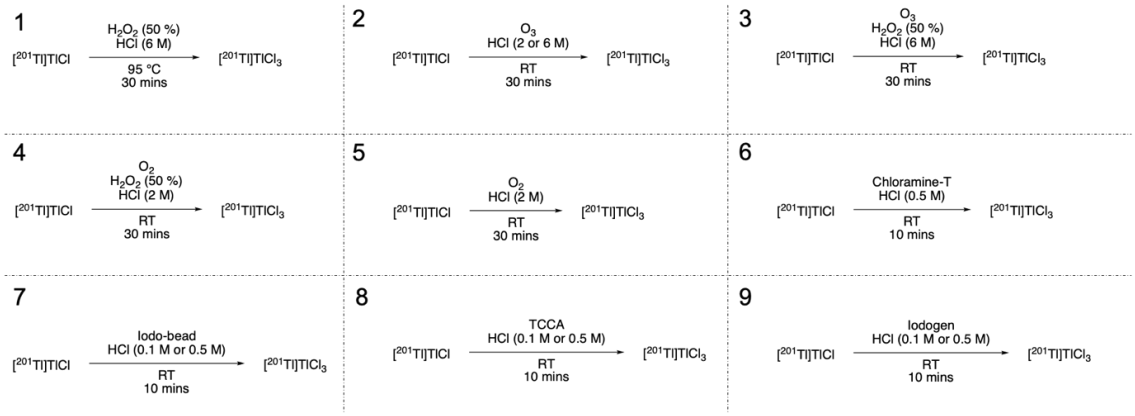

Figure 2.3 – Oxidation methods evaluated to convert [^{201}Tl]TlCl to [^{201}Tl]$TlCl_3$

Oxidation method 1 - HCl (6 M), H_2O_2, and 95 °C

HCl (6 M, 300 μL) was added to [^{201}Tl]TlCl (11.2 MBq, 200 μL). Hydrogen peroxide (50% in water, 100 μL) was then added and the solution vortexed for 10 seconds and placed in a pre-heated heat block at 95 °C for 30 minutes.[174]

Oxidation method 2 – HCl (2 (a) or 6 M (b)) and ozone

HCl (2 or 6 M, 200 μL) was added to [^{201}Tl]TlCl (11.2 MBq, 200 μL). Ozone produced from medical grade oxygen via an ozone generator (1KNT-24 from Enaly, China) was bubbled through the radioactive solution via a glass pipette for 30 minutes.[161,173]

Oxidation method 3 – HCl (6 M), H_2O_2 and ozone

HCl (6 M, 200 μL) and hydrogen peroxide (50% in water, 50 μL) were added to [^{201}Tl]TlCl (16.8 MBq, 300 μL). Ozone was used as in method 2.[183]

Oxidation method 4 – HCl (2 M), H_2O_2 and oxygen

HCl (2 M, 200 μL) and hydrogen peroxide (50% in water, 50 μL) were added to [^{201}Tl]TlCl (11.2 MBq, 200 μL). Oxygen, directly from a medical grade oxygen cylinder, was bubbled through the radioactive solution via a glass pipette for 30 minutes.

Oxidation method 5 – HCl (2 M) and oxygen

HCl (2 M, 200 μL) was added to [^{201}Tl]TlCl (11.2 MBq, 200 μL). Oxygen was used as in method 4.

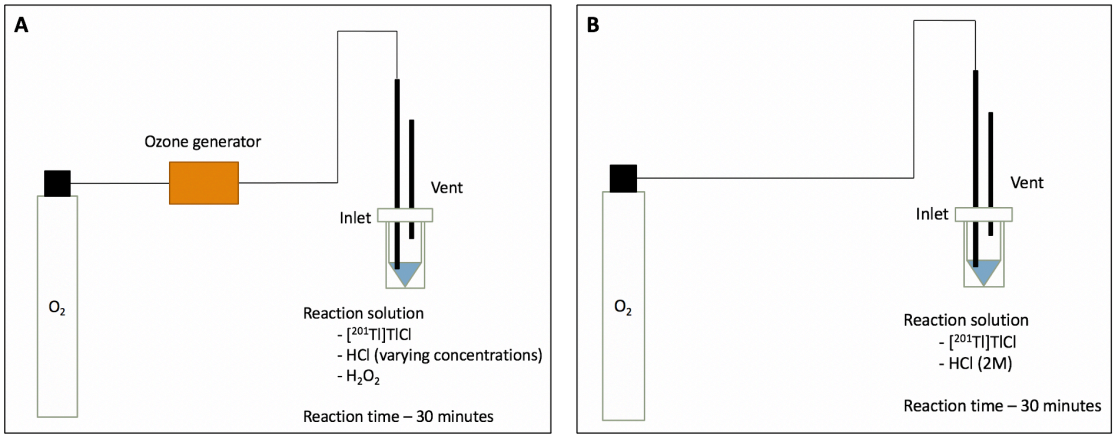

Figure 2.4 – A diagram describing the reaction set up of oxidation methods 2 – 5.

Oxidation method 6 – Chloramine-T

Chloramine-T (*N*-chlorotoluenesulfonamide; 1 mg) in water was added to a minicentrifuge tube. [^{201}Tl]TlCl (5.2 MBq, 100 μL) was then added and the mixture was agitated for 10 minutes. Once dissolved, HCl (0.5 M, 100 μL) was added. A white solid precipitated from the solution. The

solution was then agitated for 2 minutes, centrifuged for 30 seconds using a mini benchtop centrifuge to pellet the solid. The supernatant, containing [^{201}Tl]Tl^{3+}, was then added to a clean flask and used for the chelator studies.

A variable amount (10 ng - 0.1 mg) of chloramine-T, dissolved in water, was added to clean reaction flasks. [^{201}Tl]TlCl (1 MBq, 25 μL) was then added to the tubes containing the chloramine-T solution, followed by HCl (0.1 M, 0.5 M or no acid added, 2.5 μL), vortexed and pipetted into a flask.

Non-radioactive chloramine-T oxidation

A non-radioactive version of the reaction in method 6 was performed and the white solid precipitate was analysed using proton NMR. NMR spectra were recorded on a Bruker Ultrashield 400WB PLUS 9.4 T spectrometer (1H NMR at 400 MHz). All chemical shifts were referenced to residual solvent peaks and are quoted in ppm. ^{1}H NMR (400 MHz, Chloroform-*d*) δ 7.79 (d, *J* = 8.4 Hz, 2H, Ar-H$_a$), 7.29 (d, *J* = 8.0 Hz, 2H, Ar-H$_b$), 2.41 (s, 3H, Me).

Oxidation method 7 - Iodo-bead

[^{201}Tl]TlCl (0.5 MBq, 100 μL) was added to one iodo-bead (Thermo Fisher). HCl (0.1 M or 0.5 M, 10 μL) was then added to the reaction and vortexed for 10 seconds.

Oxidation methods 8 and 9 - Trichloroisocyanuric acid (TCCA) and iodogen

In direct comparative studies, varying amounts of iodogen and TCCA (10 ng - 0.1 mg), both dissolved in chloroform and left in a fume hood overnight for the chloroform to evaporate, were added to clean reaction flasks. [^{201}Tl]TlCl (1 MBq, 25 μL) was then added to the pre-coated tubes, followed by HCl (0.1 M, 0.5 M or no acid added, 2.5 μL), vortexed and pipetted into a clean flask.

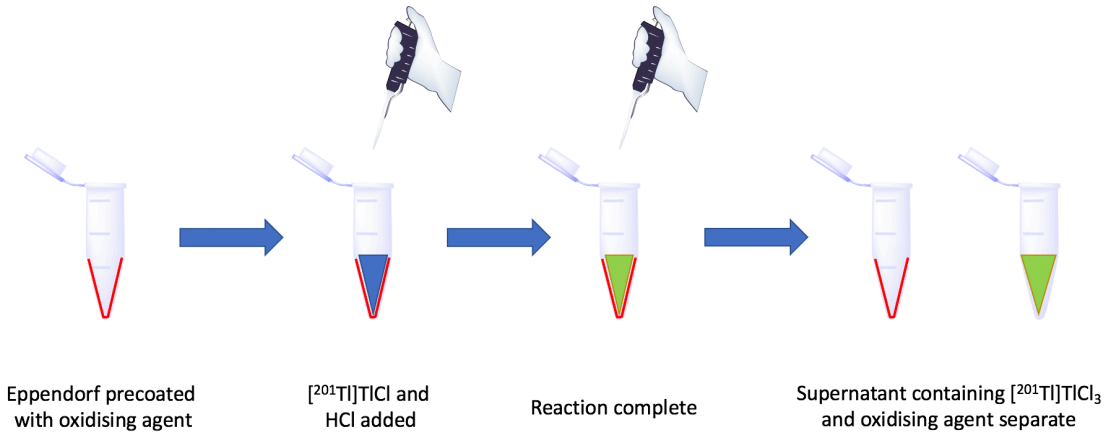

Figure 2.5 – A systematic diagram of the 'ideal' oxidation method. The oxidising agent is insoluble in aqueous solution so can be separated post reaction, so $[^{201}Tl]TlCl_3$ can be used without further purification.

Thin layer chromatography

Oxidation from $[^{201}Tl]Tl^{+}$ to $[^{201}Tl]Tl^{3+}$ was analysed by instant thin layer chromatography (ITLC) with acetone as the mobile phase and silica gel ITLC strips (ITLC-SG) as the stationary phase, giving good separation between $[^{201}Tl]Tl^{+}$ ($R_f = 0$) and $[^{201}Tl]Tl^{3+}$ ($R_f = 1$).

2.3 Results

2.3.1 Oxidation of $[^{201}Tl]Tl^{+}$ to $[^{201}Tl]Tl^{3+}$

Ozone and oxygen oxidation

The $[^{201}Tl]TlCl$ control ITLC is shown in Figure 2.6A. Radiochemical yields of method 1 were 98 $\pm$ 2% (Figure 2.6B) whereas oxidation method 2 using a low concentration of HCl (2 M) with ozone yielded little to no $[^{201}Tl]Tl^{3+}$ (3 $\pm$ 2%) (Figure 2.6C). Increasing the concentration to 6 M HCl slightly improved radiochemical yields to 12 $\pm$ 3% (Figure 2.6D). In a further attempt to oxidise ^{201}Tl at room temperature, oxidation method 3, which used a mixture of ozone, hydrogen peroxide and 6 M HCl was evaluated. This produced $[^{201}Tl]Tl^{3+}$ after 30 minutes (95 $\pm$ 5%, Figure 2.6E). Using oxygen instead of ozone and decreasing the pH to 2M still yielded quantitative conversion from $[^{201}Tl]Tl^{+}$ to $[^{201}Tl]Tl^{3+}$ (99 $\pm$ 1%; method 4). The further removal of hydrogen peroxide from the reaction still led to $[^{201}Tl]Tl^{3+}$ yield of 94 $\pm$ 6% (method 5). Table 9 summarises radiochemical yields obtained.

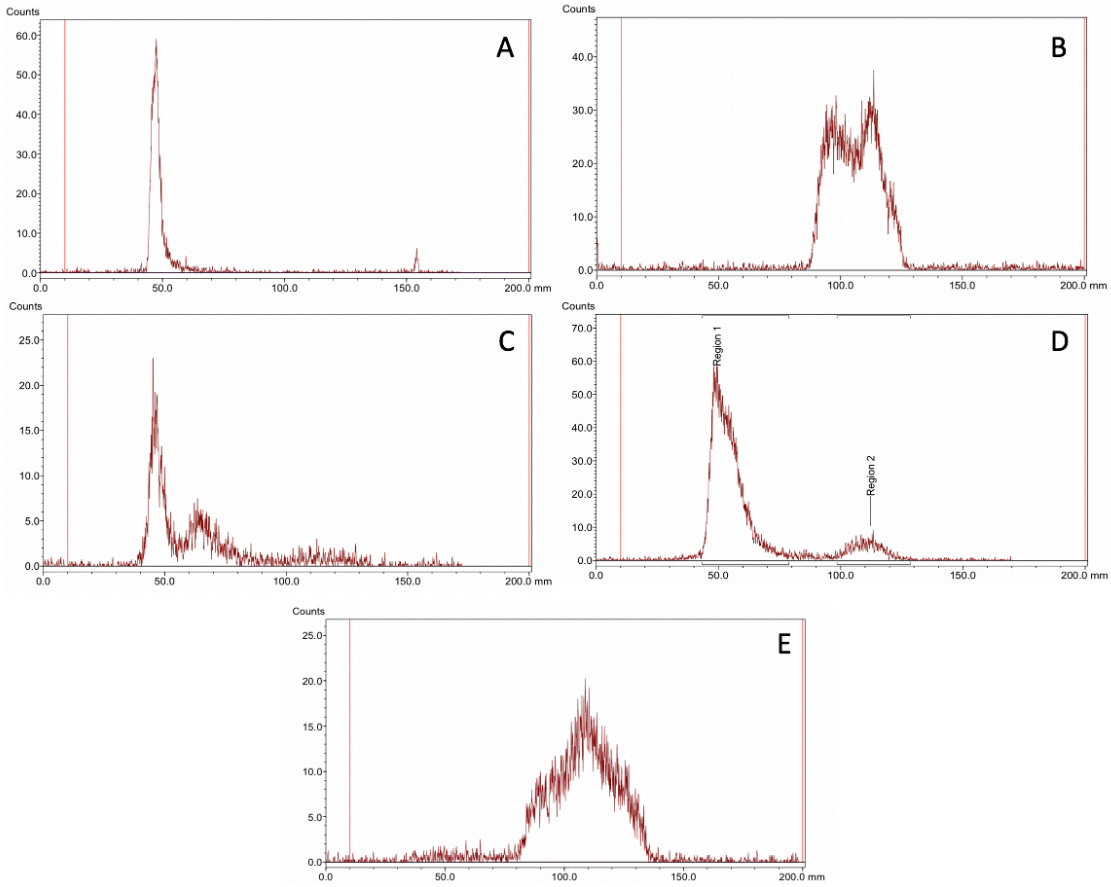

Figure 2.6 - Radiochromatogram of ITLC [^{201}TlTlCl control (A), oxidation method 1 - HCl (6 M), H_2O_2, and 95 °C (B), oxidation method 2A - HCl (2 M) and ozone (C), oxidation method 2B – HCl (6 M) and ozone (D) and oxidation method 3 – HCl (6 M), H_2O_2 and ozone. Solid phase = ITLC-SG, and mobile phase = acetone. R_f 0 (50 mm) = [^{201}Tl^{+}, R_f 1 (150 mm) = [^{201}Tl^{3+}.

Chloramine-T oxidation and NMR

ITLC analysis of the supernatant containing $[^{201}Tl]Tl^{3+}$ showed that quantitative yields were obtained using 10 mg Chloramine-T (99 $\pm$ 1%; method 6), and that the presence of acid was required (Figure 2.7). When 0.1 M HCl was used, a mixture of $[^{201}Tl]Tl^{+}$ and $[^{201}Tl]Tl^{3+}$ was observed with 100 ng – 0.1 mg; no oxidation occurred at 10 ng. However, with the use of 0.5 M HCl, a yield of >99% for $[^{201}Tl]Tl^{3+}$ was observed at all concentrations at or above 0.01 mg (Figure 2.7) NMR spectroscopy showed the white precipitate to be *p*-toluenesulfonamide, an expected by-product of the chloramine-T oxidation (Figure 2.8).[184]

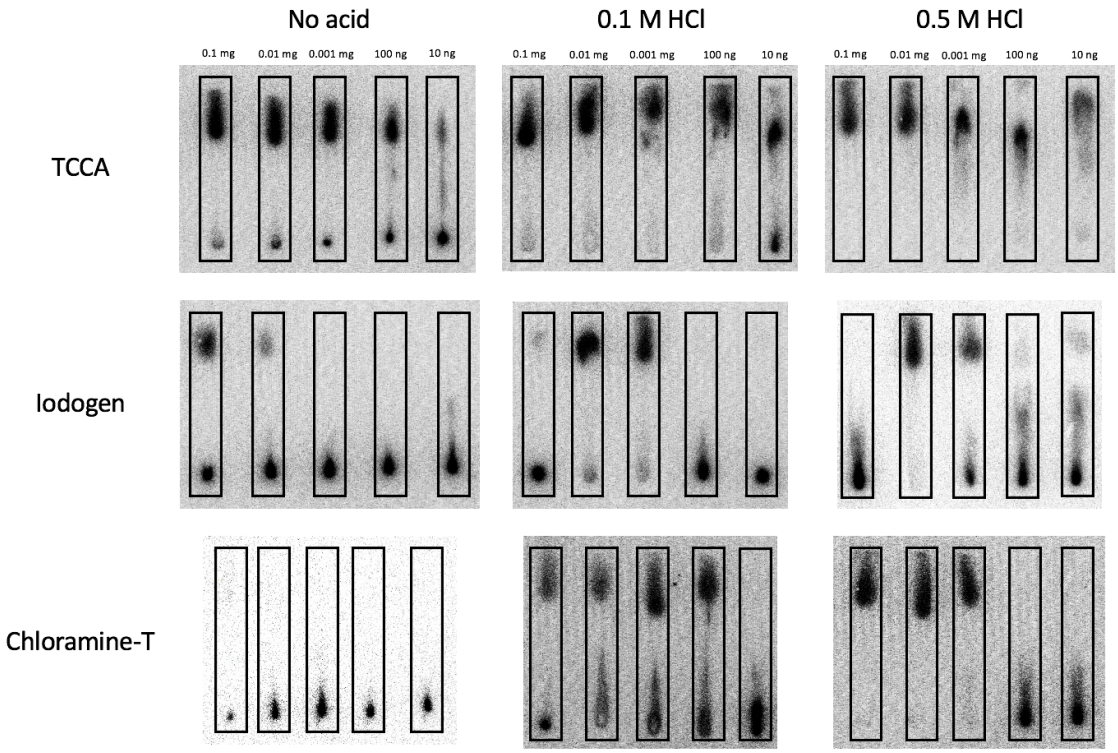

Figure 2.7 - ITLC images of oxidation of $[^{201}Tl]TlCl$ to $[^{201}Tl]TlCl_3$ using trichloroisocyanuric acid (TCCA; top row), iodogen (middle row) and chloramine-T (bottom row) in the presence and absence of 0.1 or 0.5 M HCl (methods 6, 8, and 9). Solid phase = ITLC-SG, and mobile phase = acetone. R_f 0 = $[^{201}Tl]Tl^{+}$, R_f 1 = $[^{201}Tl]Tl^{3+}$.

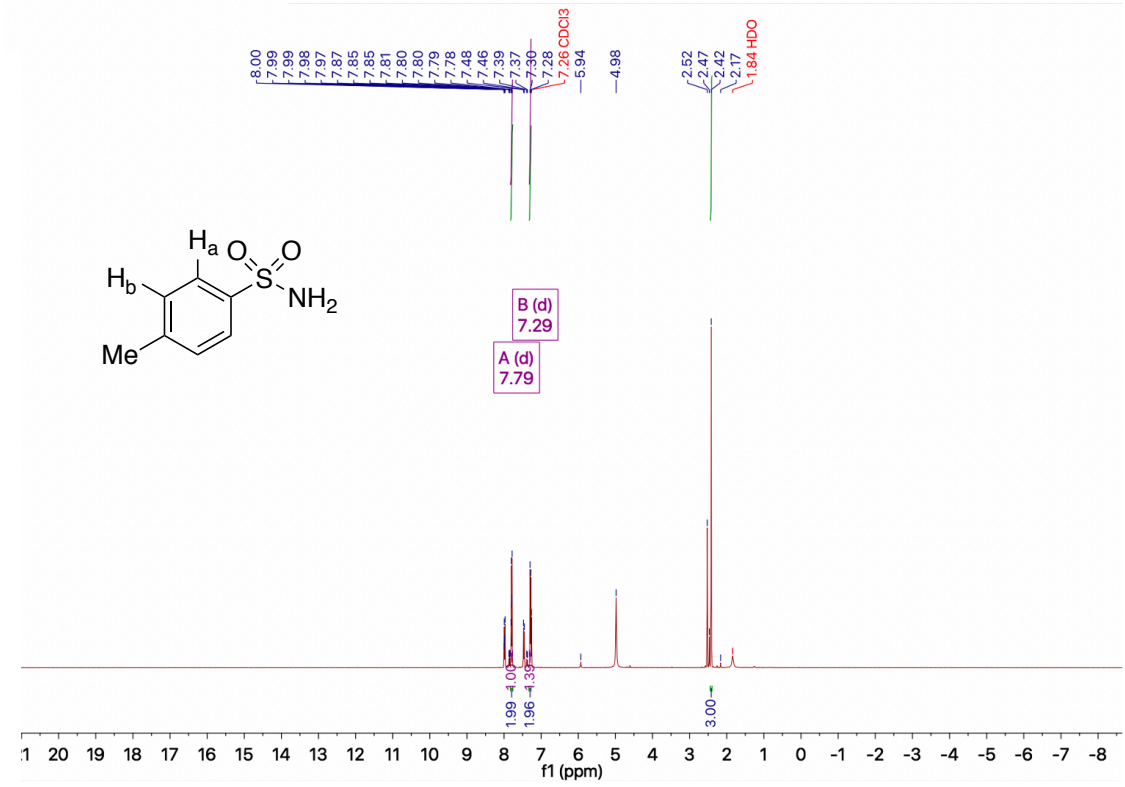

Figure 2.8 - ^{1}H NMR spectrum of the white solid produced from the chloramine-T oxidation reaction. ^{1}H NMR (400 MHz, Chloroform-*d*) δ 7.79 (d, *J* = 8.4 Hz, 2H, Ar-H$_a$), 7.29 (d, *J* = 8.0 Hz, 2H, Ar-H$_b$), 2.41 (s, 3H, Me). Amine protons not observed due to exchange with the solvent.

Solid phase oxidants

Iodo-beads, incubated with [^{201}Tl]TlCl in the presence of 0.5 M HCl, led to the formation of [^{201}Tl]Tl^{3+} in 99 ± 1% yield (method 7A, Figure 2.9). Using 0.1 M HCl instead decreased the radiochemical yield of [^{201}Tl]Tl^{3+} to 62 ± 8% (method 7B, Figure 2.7). TCCA alone (10 ng – 0.1 mg), without HCl, produced 88-90% conversion to [^{201}Tl]Tl^{3+} within 10 minutes at room temperature (Figure 2.7). Upon addition of 0.5 M HCl, full conversion (99 ± 1%) was observed between 10 ng – 0.1 mg TCCA (method 8A, Figure 2.7). When using 0.1 mg iodogen without HCl, a radiochemical yield of [^{201}Tl]Tl^{3+} at 74 ± 3% was observed (Figure 2.7). Upon the addition of 0.1 M HCl using 0.001-0.01 mg iodogen led to a 95 ± 3% radiochemical yield, which further increased to 99% ± 1% when using 0.5 M HCl (Figure 2.7).

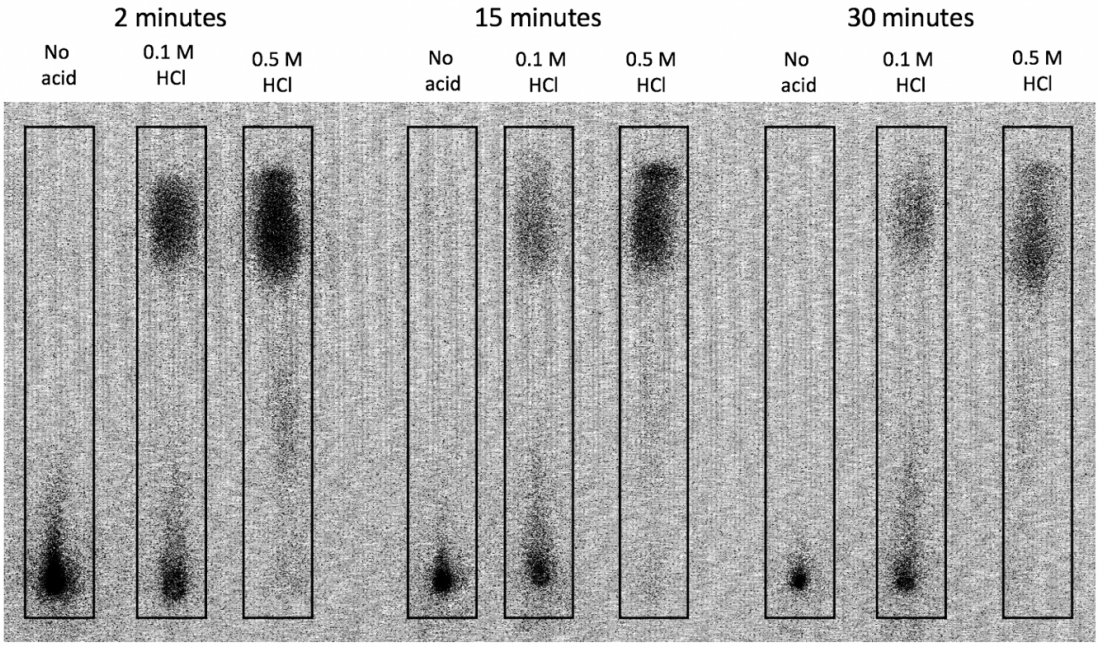

Figure 2.9 - ITLC images of the [^{201}TlTlCl oxidation to [^{201}TlTlCl$_3$ using an iodo-bead with no acid, and HCl (0.1 M or 0.5 M). Aliquots (2 µL) were removed at 2, 15 and 30 minutes for analysis (method 7). Solid phase = ITLC-SG, and mobile phase = acetone. R_f 0 = [^{201}Tl]Tl$^+$, R_f 1 = [^{201}Tl]Tl^{3+}.

Table 9 – Conversion yields of $[^{201}Tl]Tl^{+}$ to $[^{201}Tl]Tl^{3+}$ using oxidation methods 1-9. Values are an average +- standard deviation (n=3). Also shown are the characteristics of the nine oxidation methods in terms of simple set up, ability to remove the oxidising reagent after the reaction and whether the oxidation process is compatible with radiolabelling biomolecules such as antibodies.

Oxidation method	Conversion yield	Simple set-up	Oxidant removed	Biomolecule compatible
1: HCl (6 M), H_2O_2, and 95 °C	98 ± 2 %	Yes	No	No
2A: HCl (2 M) and ozone	3 ± 2 %	No	Yes	No
2B: HCl (6 M) and ozone	12 ± 3 %	No	Yes	No
3: HCl (6 M), H_2O_2 and ozone	95 ± 5 %	No	No	No
4: HCl (2 M), H_2O_2 and oxygen	99 ± 1 %	No	No	No
5: HCl (2 M) and oxygen	94 ± 6 %	No	Yes	No
6A: Chloramine-T (0.5 M HCl)	99 ± 1 %	Yes	No	Yes
6B: Chloramine-T (0.1 M HCl)	69 ± 3 %	Yes	No	Yes
7A: Iodo-bead (0.5 M HCl)	99 ± 1 %	Yes	Yes	Yes
7B: Iodo-bead (0.1 M HCl)	62 ± 8 %	Yes	Yes	Yes
8A: Trichloroisocyanuric acid (0.5 M HCl)	99 ± 1 %	Yes	Yes	Yes
8B: Trichloroisocyanuric acid (0.1 M HCl)	96 ± 2 %	Yes	Yes	Yes
9A: Iodogen (0.5 M HCl)	99 ± 1 %	Yes	Yes	Yes
9B: Iodogen (0.1 M HCl)	95 ± 3 %	Yes	Yes	Yes

2.4 Discussion

Thallium is stable under ambient conditions in oxidation states 1+ and 3+. In oxidation state 1+, thallium is known to be strongly hydrated and behaves biologically much like the alkali metals; for example, like potassium; it is a substrate for the sodium-potassium ATPase pump.[10] Its electronic structure features a sterically active lone pair of electrons. With these properties, it is hard to conceive a likely kinetically stable Tl^{+} chelate complex. On the other hand, Tl^{3+} is electronically analogous to In^{3+} for which a range of highly stable chelates is known with well-established uses in nuclear medicine. Based on these considerations, Tl^{3+} would appear to be the more attractive option for developing future suitable chelation systems. A prerequisite for developing such a platform is to find an efficient and convenient method to oxidise [^{201}Tl]TlCl, the form in which ^{201}Tl is manufactured and supplied, to Tl^{3+}. Such a method would need to be sufficiently mild to be used in the context of labelling sensitive biomolecules. The Tl^{+}/Tl^{3+} redox couple has a standard redox potential of +0.77 V, suggesting that unless the metal ion can be stabilised by a chelator, it may be reduced back to Tl^{+}.

Published methods to oxidise [^{201}Tl]Tl^{+} to [^{201}Tl]Tl^{3+} included ozone, hydrogen peroxide, HCl or a combination of oxidising agents and high temperatures (95°C).[161,176,185] In our hands, using ITLC-SG plates and acetone as an effective and reliable method to distinguish Tl^{+} from Tl^{3+}, the published oxidation methods (methods 1-4) did not always prove successful.[176] For example, in method 2, the conversion yield was between 3 and 12**%.** Although oxidation method 1 was reproducible, heating at 95°C is not compatible with biological molecules (Table 2). As explained in the introduction, high temperatures and very acidic pH can lead to degradation of biological molecules such as antibodies, so would not be appropriate for use in nuclear medicine.

Oxidation methods 3-5 used ozone or oxygen as oxidants and avoided the need for high temperatures. Comparing conversion yields obtained from either method 2 or 3 showed the importance of hydrogen peroxide for the oxidation using ozone, although this appeared less important for oxygen (method 5), despite the decrease in oxidation potential from +2.07 V to +1.78 V.[186] Although the solution could be neutralised, this would dilute the radionuclide and increase the complexity of the labelling procedure. Equally, the practical set-up of bubbling oxygen through a reaction vessel using a large cylinder of compressed oxygen adds undesirable complexity and hazard (Table 2). Therefore, alternative, safer methods of oxidation were investigated.

A range of biocompatible oxidising agents has been available for many years, developed for the purpose of radiolabelling biomolecules with radioiodine. Chloramine-T, first used by Greenwood *et al.* in the 1960s, is still popular in this field.[187] During the oxidation of ^{201}Tl, it was found that conversion yields for chloramine-T were 99%, even at the low amounts previously used to synthesise [^{123}I]diiodotyrosyl-salmon calcitonin (0.1 mg).[188] Although chloramine-T is relatively biocompatible, it is known to cause some protein damage in some cases, and its presence could also lead to misleading stability results or damage cells during *in vitro* and stability studies described below.[184] It should, therefore, ideally be quenched or removed from the reaction solution prior to introducing the biomolecules. This step is not always simple due to its water solubility. Chloramine-T also has an oxidation potential of +1.14 V under acidic conditions, so marginally lower than that of oxygen.[189]

We therefore also evaluated a range of solid-phase oxidants that could easily be removed after oxidation is complete. Iodo-beads (method 7), for example, consist of a chloramine-T analogue covalently bound to a solid polystyrene bead, allowing the supernatant containing [^{201}Tl]Tl^{3+} to be easily removed from the vessel; this is also an advantage when using iodogen or TCCA (methods 8-9; Table 2). All three oxidants gave a good conversion yield (99%) from [^{201}Tl]Tl^{+} to

$[^{201}Tl]Tl^{3+}$. An extra advantage of iodogen and TCCA over chloramine T is their solubility in organic solvents and low solubility in water; this enables pre-coated tubes to be created with the volatile solvent evaporating during the process. Additionally, TCCA has an oxidation potential of +4.84 V which is far higher than ozone and oxygen.[190] Methods 7-9, using iodo-beads, TCCA or iodogen, are thus excellent oxidation methods to convert $[^{201}Tl]Tl^{+}$ to $[^{201}Tl]Tl^{3+}$ for future MRT using ^{201}Tl. However, in the absence of acid, no conversion to $[^{201}Tl]Tl^{3+}$ was observed. For all the oxidising agents, using 0.1 M HCl, leads to a mixture of the starting material and product whereas using 0.5 M HCl leads to the majority of product formation.

Moving forward, the iodobead oxidising agent in combination with 0.5 M HCl as the oxidation method was chosen to continue with further studies. This was due to the reliable results it provided and the very simple set up. As the iodobeads are purchased and used without need for pretreatment, there is no additional work required to precoat the reaction tubes. The cost of each iodobead (£3.52 a bead, as of November 2021) is relatively low considering one is used per reaction.

2.5 Conclusions

The chapter has described the evaluation of numerous methods for the oxidation of $[^{201}Tl]Tl^{+}$ to $[^{201}Tl]Tl^{3+}$ using a range of oxidation agents. Literature methods using concentrated HCl (6 M), ozone and hydrogen peroxide in combination with high temperatures yielded varying amounts of $[^{201}Tl]Tl^{3+}$ (3 - 99% yield). For future use with biomolecule, these methods would not be appropriate as they would lead to degradation of the biomolecule. The use of chloramine-T in combination with HCl (0.5 M) was then investigated and shown to be very effective for the generation of $[^{201}Tl]Tl^{3+}$ (99 % yield). However, as chloramine-T is soluble in aqueous solution, further purification would be needed to remove excess oxidising agent. To avoid this, oxidising agents that are insoluble in aqueous solutions were pursued. Iodo-beads (chloramine-T embedded on a polystyrene bead), TCCA and iodogen again in combination with HCl (0.5 M) all were effective at oxidising $[^{201}Tl]Tl^{+}$ to $[^{201}Tl]Tl^{3+}$ in good yields (99 %). Due to the convivence of using a single iodo-bead per oxidation reaction, this method was used in future studies. This reaction has a simple set up, is very convenient and uses very mild reactions to generate $[^{201}Tl]Tl^{3+}$.

3 DNA DAMAGE ASSESSMENT

3.1 Introduction

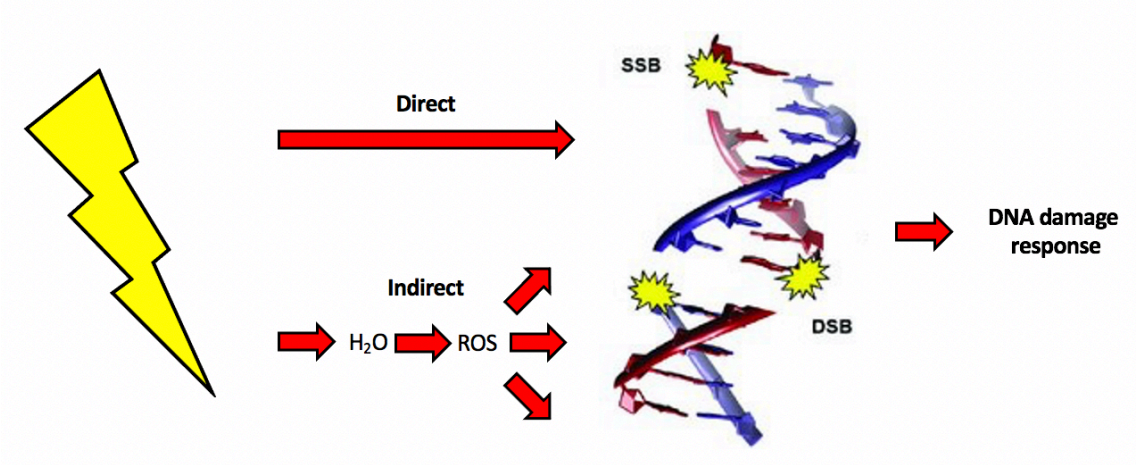

Figure 3.1 – A simplified representation of DNA damage caused by ionising radiation. ROS = reactive oxygen species, SSB = single strand break, DSB = double strand break. (adapted from Vallis *et al*).[191]

A simple cell free system like plasmids in solution has commonly been used in previous work with AE emitters to show the DNA damaging and therapeutic potential of AE-emitters.[20,192–196] The plasmid method removes factors that may have an influence on DNA damage that usually are present in cells, for example repair mechanisms. Although not a true reflection of what processes take place in a biological system, the results allow radionuclides to be directly compared in an identical, simple system, which restricts the number of variables and can be easily quantified.

Damage to the plasmid DNA can occur following incubation with radionuclides via two mechanisms, direct or indirect.[194,197,198] A simplified diagram representing the DNA damage mechanisms induced by ionising radiation can be seen in Figure 3.1.[191] The direct mechanism arises from ionisation of the DNA backbone from the ionised particle which causes the SSB and

DSBs. As the name implies, for the indirect mechanism, damage is not done by the ionising particle itself, but water molecules that have been ionised generating free radicals in solution. ROS are highly reactive and include superoxide anion (O_2^-), peroxide (O_2^{2-}) and hydroxyl ion (HO^-). The previous articles in the literature have shown both direct and indirect mechanisms can cause significant DNA damage to plasmid DNA using AE emitters.[20] The distance between the plasmid DNA and radionuclide was also investigated, showing that as the distance increases, the damage mechanism is driven toward indirect over direct.[192,194,197,199] This highlights the need for the close proximity to DNA to generate direct DNA damage.

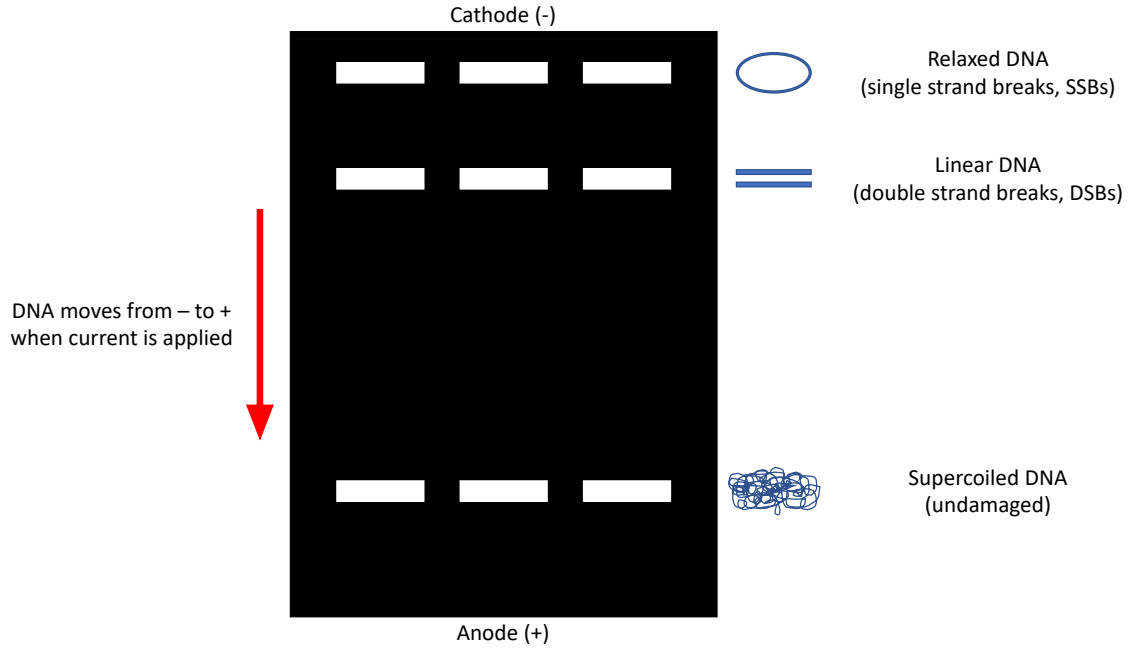

Figure 3.2 – An example diagram of the agarose DNA damage gels used to assess the damage done by radionuclides. The top band corresponds to DNA in the relaxed form following a single strand break (SSB), the middle band corresponds to DNA in the linear form following a double strand break (DSB) and finally the bottom band is undamaged DNA in the supercoiled form. The DNA moves through the electrophoresis gel from the negatively charged cathode to the positively charged anode.

For this work, gel electrophoresis has been used to quantify the plasmid DNA damage caused by ^{201}Tl. The agarose gel uses an electric current to separate the plasmid based on its conformation

which changes due to DNA damage. Supercoiled, undamaged plasmid DNA moves easily through the gel so corresponds to the bottom band. Following a SSB, the conformation changes to a relaxed form which is round, and uncoiled. This moves more slowly through the gel, so corresponds to the top band. When the plasmid DNA undergoes a DSB, it adopts a linear conformation which corresponds to the middle band on the gel. An exemplar agarose gel can be seen in Figure 3.2.

This work aims to determine the DNA damaging potential of ^{201}Tl.

3.2 Material and methods

Plasmid DNA damage

pBR322 DNA plasmid (New England Biolabs, UK) in PBS (100 ng, 20 µL) was incubated with 0.5 MBq (8 µL) [^{201}Tl]$TlCl_3$ for up to 144 hours. [^{201}Tl]$TlCl_3$, originally formed using chloramine-T (method 6), was neutralised with Na_2CO_3 (0.1 M). Controls included untreated plasmid in PBS and equivalent amounts of non-radioactive [^{nat}Tl]$TlCl_3$ (Sigma). After treatment, plasmid (50 ng in PBS) was mixed with 6X loading dye (16 µL total volume), loaded onto a 0.8% agarose gel containing 10 µL GelRed Nucleic Acid stain (Biotium, USA) and run at 100 V (400 mA, 50 W) for 40 minutes. Gels, imaged using a GelDoc-ItTS2 310 Imager system (BioRad, UK) coupled with a Benchtop UV transilluminator (UVP) and GelCam 310, were analysed by ImageJ, measuring supercoiled (intact DNA), relaxed circular (single strand breaks) and linear band (double strand breaks) percentages within a lane (n=3-12).[200]

Statistical analysis

Plasmid electrophoresis results are shown as mean percentage of total DNA, i.e. supercoiled + relaxed + linear topologies, $\pm$ standard deviation. Two-way ANOVA statistical analyses were carried out using Tukey's multiple comparisons test in GraphPad Prism 7.0c. $P<0.05$ was deemed significant.

3.3 Results

3.3.1 Assessment of ^{201}Tl damage to plasmid DNA

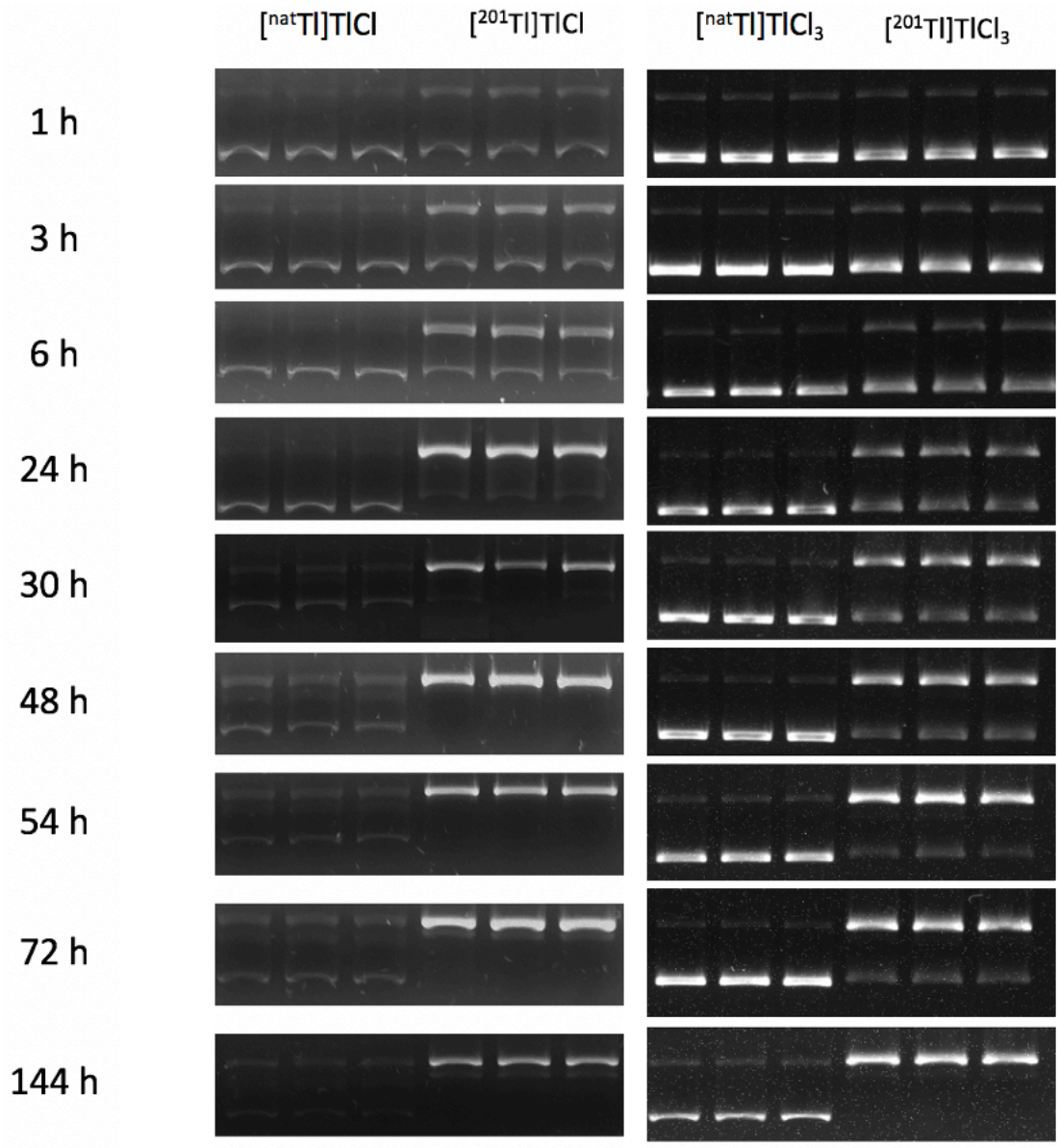

Figure 3.3 - Representative agarose gels of plasmid DNA incubated with non-radioactive [^{nat}Tl]TlCl, [^{nat}Tl]TlCl$_3$, [^{201}Tl]TlCl or [^{201}Tl]TlCl$_3$ (in triplicate lanes). Bottom band = undamaged, supercoiled DNA, middle band = linear DNA caused by double strand breaks in the DNA and top band = relaxed DNA caused by a single strand break in the DNA

Agarose gels were used to demonstrate and quantify the damage done to DNA following incubation with either the non-radioactive or radioactive thallium chloride salts (Figure 3.3). For plasmid DNA incubated with $[^{201}Tl]Tl^{3+}$ (0.5 MBq), increasing the incubation time decreased the percentage of supercoiled DNA from 88 ± 1 % to 51 ± 2 % at 1 and 24 hours, respectively (Figure 3.4). When plasmid DNA was incubated with $[^{201}Tl]Tl^{+}$ (0.5 MBq), the same effect was observed with 87 ± 1 % at 1 hour to 49 ± 1 % after 24 hours. Using $[^{201}Tl]Tl^{3+}$, relaxed DNA increased from 12 ± 1% at 1 h to 49 ± 2% at 24 hours, whereas linear DNA was first detectable (6.27 ± 0.15 %) at 144 hours. In comparison, for $[^{201}Tl]Tl^{+}$, relaxed DNA increased from 36 ± 1% at 1 h to 97 ± 2% at 24 hours, whereas linear DNA was first detectable (10.5 ± 0.5 %) at 72 hours. In all studies, negative controls consisting of the addition of PBS, non-radioactive $[^{nat}Tl]Tl^{+}$ or $[^{nat}Tl]Tl^{3+}$ to the plasmid did not show evidence of damage over the corresponding timeframe within the errors associated with the measurement (Figure 3.4; $p=0.22$).

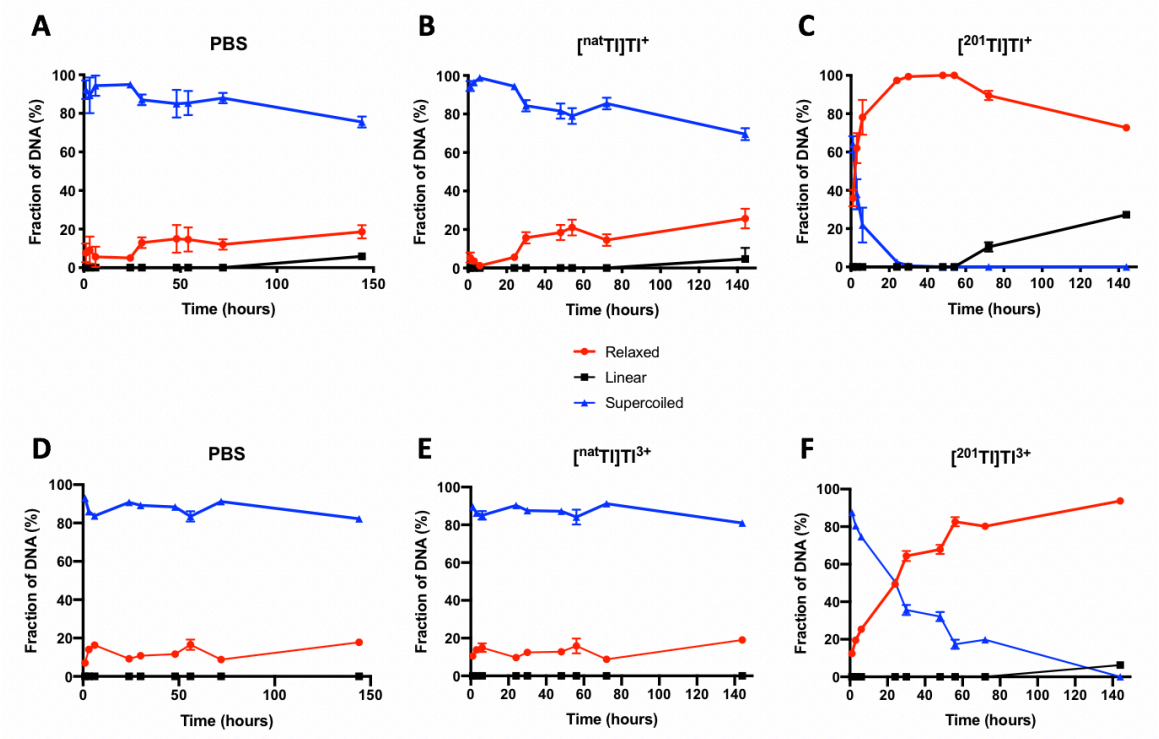

Figure 3.4 – The percentage of DNA damage when plasmid DNA was incubated with PBS (A and D), [^{nat}Tl]TlCl (B), [^{201}Tl]TlCl (C), [^{nat}Tl]$TlCl_3$ (E) or [^{201}Tl]$TlCl_3$ (F). Blue line = supercoiled, undamaged DNA. Red line = DNA in relaxed form after a single strand break. Black line = DNA in the linear form after a double strand break.

3.4 Discussion

Having successfully converted [^{201}Tl]Tl^{+} to [^{201}Tl]Tl^{3+}, the next step was to determine whether either thallium-201 oxidation states could damage DNA, often considered to be a critical first step in killing cancer cells. It was confirmed for the first time using the isolated DNA plasmid method that [^{201}Tl]Tl^{+} and [^{201}Tl]Tl^{3+} cause DNA damage; this method has previously been used by ourselves and others to investigate other AE-emitting radionuclides.[138,197,208,199,201–207] The data shown in Figure 3.3 and Figure 3.4 shows that using this isolated DNA damage method, [^{201}Tl]Tl^{+} causes more damage to DNA than [^{201}Tl]Tl^{3+}. This is likely due to [^{201}Tl]Tl^{+} being a K^{+} mimic, allowing it to bind to the electronegative sites of DNA bases in both the major and minor grooves where K^{+} would normally bind.[209] This close proximity to DNA will allow the Auger electrons to cause significant damage. Due to its reduced ionic radii, [^{201}Tl]Tl^{3+} (unless reduced to [^{201}Tl]Tl^{+}) is unlikely to bind to these same sites, hence the reduction in DNA damage. Despite the increase in DNA damage using [^{201}Tl]Tl^{+}, due to the difficulties in chelating the 1+ metal, it was not feasible to use this oxidation state in further chelation studies.

When compared to the ^{111}In and ^{67}Ga results from Othman and co-workers, both oxidation states of ^{201}Tl are showing a similar trend of increasing DNA damage over time.[138] Further experiments using DMSO as a ROS scavenger from ^{201}Tl would help to differentiate between damage done by direct or indirect mechanisms as done by Othman *et al*.[196]

Recent *in vitro* work has shown that non-targeted delivery of ^{201}Tl shows short and long-term toxicity in prostate cancer cells.[137] Following treatment of DU145 cells with ^{201}Tl, a 90 % decrease in clonogenic survival was achieved at only 0.29 Bq/cell, significantly lower than for other AE-emitting radionuclides such as ^{67}Ga and ^{111}In.[19,138] It does have to be noted that the cell studies are not directly comparable, due to Othman and co-workers using oxine complexes of ^{111}In and ^{67}Ga to allow the radiometal to enter the cells, whereas ^{201}Tl enters via potassium channels.

Oxine complexes enter cells due to their neutral charge and being highly lipophilic, allowing them to diffuse into cells through the membrane. Once in cells, the complexes can break down and the radiometal can bind to cellular proteins.

3.5 Conclusion

The results is this chapter have demonstrated that [^{201}Tl]Tl^{+} and [^{201}Tl]Tl^{3+} can cause a large amount of SSBs, with [^{201}Tl]Tl^{+} also causing significant DSBs to DNA. By using a cell free isolated DNA plasmid method to evaluate DNA damage, is it possible to compare the DNA damage from the literature. The damage caused by ^{201}Tl was comparable to that caused by other Auger electron emitters ^{111}In and ^{67}Ga. The [^{nat}Tl]Tl^{+} and [^{nat}Tl]Tl^{3+} controls showed a similar trend in DNA damage to the PBS control, demonstrating that at concentrations used in these experiments, no inherent chemical toxicity was observed from the metal. Despite causing more DNA damage to the plasmid, the chelation of [^{201}Tl]Tl^{+} will be very challenging (as described in Chapter 1), hence the use of [^{201}Tl]Tl^{3+} was explored further.

The data obtained is this chapter shows that ^{201}Tl is worth pursuing in the context of MRT.

4 CHELATION OF [^{201}Tl]Tl^{3+}

4.1 Introduction

In the pursuit of new chelators for Tl^{3+}, both established and novel chelators in the nuclear medicine field need to be evaluated. As described in Chapter 1, there are multiple inconclusive and incomplete reports on the stability of the Tl complexes of EDTA, DTPA and DOTA, so a thorough investigation into these complexes is a good starting point to build upon, and this chapter begins by describing experimental evaluation of these ligands for binding Tl^{3+}. Furthermore, over the last 12 years, the Orvig group have developed a large number of acyclic chelators, combining picolinic acid and carboxylate moieties to bind an array of large radiometals, such as [^{177}Lu]Lu^{3+}, [^{111}In]In^{3+} and [^{225}Ac]Ac^{3+}; a selection of these ligands too are investigated in this chapter as thallium chelators.

Only some of these Orvig ligands have been published to date. One such example is H_4octapa (N_4O_4) is an octadentate chelator (Figure 4.1) for which has been used with ^{111}In and ^{177}Lu.[210] Radiolabelling with both metals takes place at RT in less than 10 minutes, leading to the development of a Trastuzumab bioconjugate which showed high tumour uptake in an ovarian cancer model *in vivo*.[211] Using the same diaminedipicolinic acid backbone, a number of other derivatives have been developed and used for complexation with ^{64}Cu, ^{67}Ga and ^{89}Zr.[212,213] This highlights the versatility of these ligands to coordinate different metals with varying soft and hard character, justifying investigation with Tl^{3+}.

Figure 4.1 – Structure of H_4pypa, H_4octapa and H_5decapa.

Chelators with larger number of donor atoms, for example H_5decapa (N_5O_5) (Figure 4.1) have also been developed.[210] Again, it was radiolabelled within 10 minutes at RT and showed good stability in human serum (> 89% after 24 hours) when radiolabelled using ^{111}In. However, the *in vivo* stability in mice was suboptimal when compared to the biodistribution of [^{111}In]In-octapa, with slow blood clearance, high persistent kidney uptake and bone uptake observed. Off target uptake and retention in excretion organs using ^{201}Tl would likely lead to unwanted cell damage in healthy tissues. The 10 possible binding sites of H_5decapa present an opportunity for radiometals with a large ionic radius, such as Tl^{3+}, that can fit well into the large cavity of the chelator.

In 2019, Li and co-workers published the synthesis of a pyridinecarboxylate-based ligand H_4pypa (Figure 4.1).[214] Using non-radioactive In^{3+}, as well as the largest lanthanide, La^{3+} and the smallest lanthanide, Lu^{3+}, NMR studies showed that both form rigid coordination complexes with H_4pypa, with sharp ^{1}H peaks observed. The authors grew X-ray quality crystals of the [^{nat}Lu][Lu(pypa)]H complex, crystallography of which shows that when grown from a solution at pH 2 two of the coordinated carboxylic acid groups on the ligand are protonated (Figure 4.2). It clearly shows the Lu sitting within the cavity of the ligand with distorted square antiprismatic geometry. As described in Chapter 1 (Table 8), the ionic radii of La^{3+} and Tl^{3+} are similar, hence the investigation with Tl^{3+}.

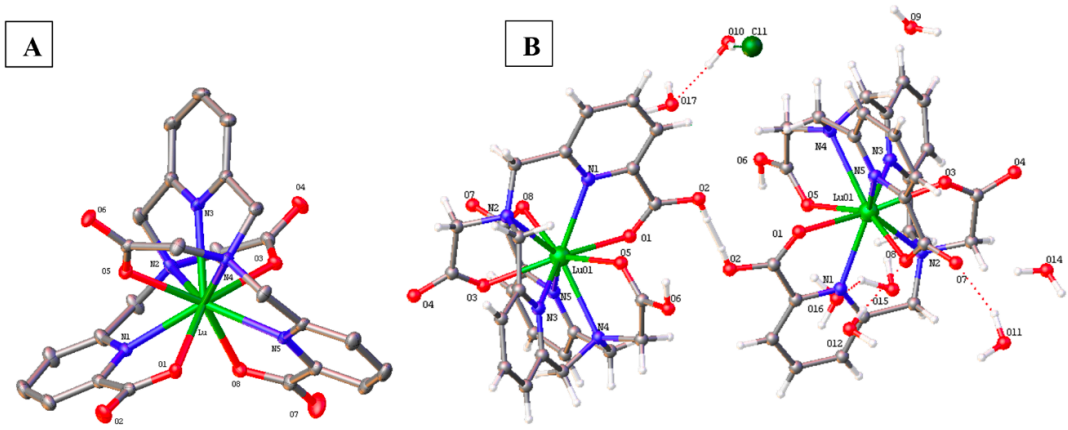

Figure 4.2 – X-ray crystal structures of the anion of H[Lu(pypa)] (A) and $C_{50}H_{79}ClLu_2N_{10}O_{33}$ (B).[214]

The Orvig group went on to radiolabelling studies using ^{177}Lu and ^{111}In and achieved > 98% RCY within 10 minutes with low concentrations of ligand (10^{-6} M) at pH 7. Both pypa complexes were shown to be kinetically inert with <1 % transmetalation to serum proteins over 7 days for [^{177}Lu]Lu-pypa and 5 days for [^{111}In]In-pypa. Li and co-workers have gone on to use H_4pypa to chelate ^{nat}Sc and ^{44}Sc.[215] The ^{1}H NMR spectrum of [Sc(pypa)]$^-$ in aqueous solution at pH 7 shows the existence of two isomers, a major and a minor in equilibrium. Subsequent radiolabelling at low concentrations and at RT resulted in a highly stable complex, which showed minimal degradation after six days in mouse serum. They also synthesised a PSMA targeting bioconjugate which will be discussed in Chapter 5.

Moving toward potential use in therapy, Li and co-workers have investigated the use of ^{86}Y as an analogue for the beta emitter ^{90}Y and conjugated it to TRC105, an anti-CD105 monoclonal antibody known to inhibit angiogenesis and tumour growth.[216–218] The versatility of H_4pypa has been demonstrated with radiolabelling using [^{86}Y]YCl_3 in HEPES buffer (0.5 M, pH 7) at RT. The stability of [^{86}Y]Y-pypa was evaluated in mouse serum which showed only a 3% degradation after 48 hours at 37°C. The authors synthesised an isothiocyanate (NCS) bifunctional version of

H_4pypa to conjugate the chelator to TRC105. This was then radiolabelled with ^{86}Y and ^{44}Sc and the biodistribution of [^{86}Y]Y-pypa-TRC105/[^{44}Sc]Sc-pypa-TRC105 investigated in female Balb/c mice bearing 4T1 murine breast cancer tumours. As is typical for antibodies, [^{86}Y]Y-pypa-TRC105 and [^{44}Sc]Sc-pypa-TRC105 have a long circulation time in the blood, with accumulation in the tumour, liver, kidney and the spleen. Additionally there was high lung uptake, which has previously been described for TRC105 constructs.[219–221] Over the time course of the experiment, bone uptake increased over 48 hours from 2.1 ± 0.3% ID/g at 30 minutes p.i. to 5.7 ± 0.5% ID/g, suggesting compound instability, as unchelated ^{86}Y is rapidly taken up by bone.[222,223] This instability was not observed for the ^{44}Sc counterpart.

A final use of H_4pypa has also been investigated for use in targeted alpha therapy using ^{226}Th ($t_{1/2}$ = 30.57 minutes) and ^{227}Th ($t_{1/2}$ = 18.7 days).[224] However, Ferrier and co-workers found that the radiolabelling of H_4pypa gave inconsistent radiochemical yields, multiple and broad peaks using radio-HPLC. This further supports the investigation with $Tl^{3+,}$ as Th^{4+} is a comparable size.

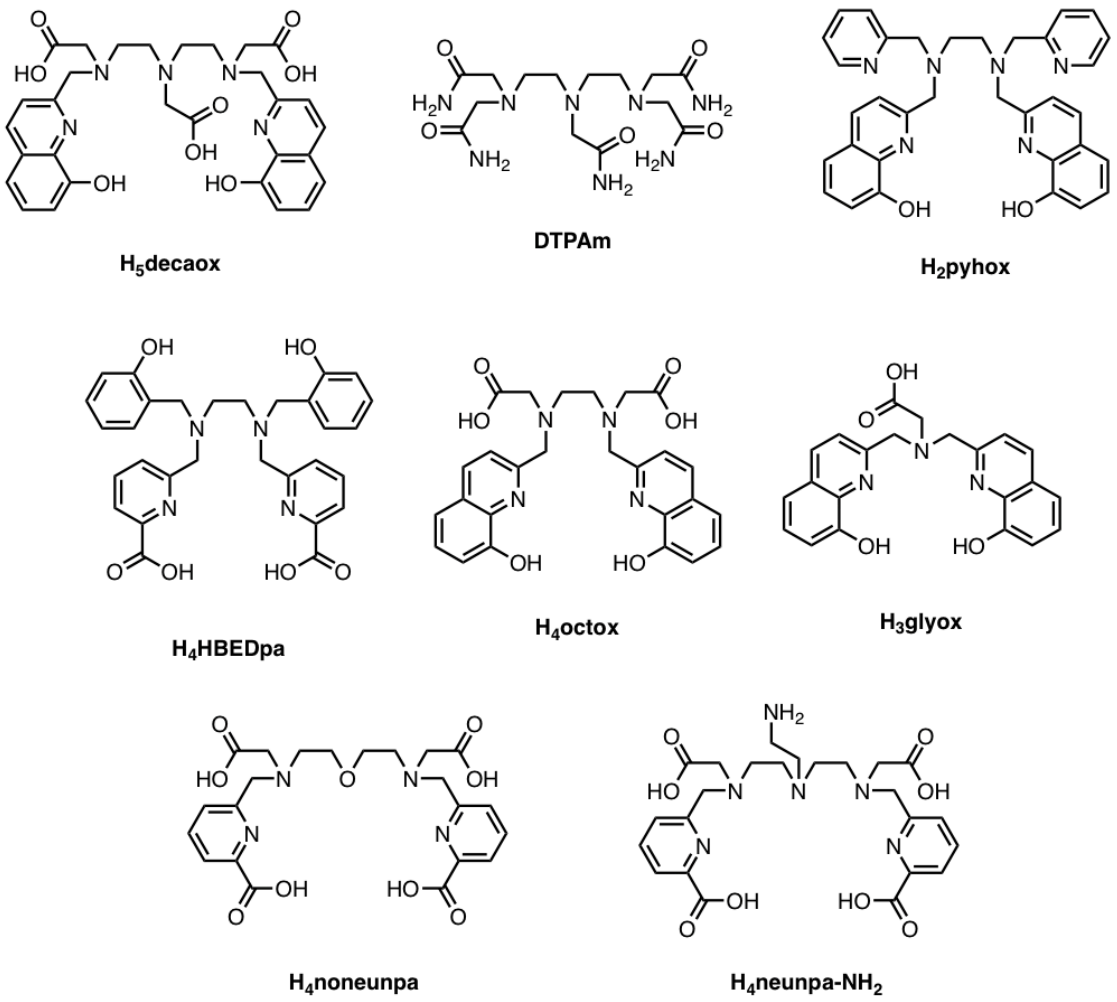

Figure 4.3 – Structures of various chelators published by the Orvig group

H_5decaox is a decadentate ligand, comprised of a diethylenetriamine backbone with oxine moieties and carboxylate arms (Figure 4.3).[225] It has been evaluated with radiometals ^{111}In and ^{89}Zr, achieving high radiochemical yields at micromolar concentrations. Stability of [^{89}Zr]Zr-decaox in human serum showed comparable stability to [^{89}Zr]Zr-DFO and [^{89}Zr]Zr-decapa, with 74.6 ± 0.1 % remaining after 7 days incubation.[226] Another chelator, developed by Ingham *et al* and Burdinski *et al*, DTPAm is an amide version of DTPA. Burdinski and coworkers were developing Yb based agents to use the chemical exchange-dependent saturation transfer (CEST) effect for MRI.[227] Ingham and co-workers were using the octadentate DTPAm to chelate

$^{203/212}Pb^{2+}$ for use in SPECT imaging and MRT.[228] The X-ray crystal structure of [Pb(DTPAm)] cation in Figure 4.4 shows an octadentate DTPAm coordinated by [^{nat}Pb]Pb^{2+} with distorted square antiprism geometry. Radiolabelling with [^{203}Pb]Pb^{2+} takes place with low concentrations of ligand (10^{-5} M), at RT and within 15 minutes. Their studies showed DTPAm to be an excellent candidate for biofunctionalisation in the future, as highlighted by the numerous applications of DTPA.[229,230]

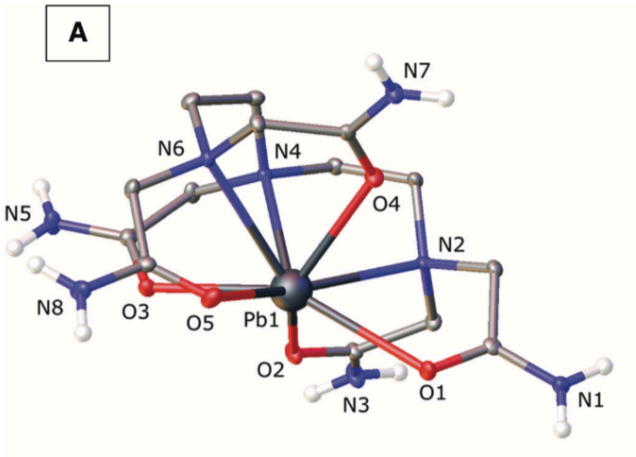

Figure 4.4 – ORTEP diagram of the cation of [Pb(DTPAm)]$(NO_3)_2$

H_2pyhox (Figure 4.3) has been used for the chelation of ^{64}Cu and ^{111}In. Like various other Orvig chelators, it contains oxine moieties as well as pyridine donor groups on an ethylenediamine backbone.[231] The X-ray crystal structure of [Cu(pyhox)] can be seen in Figure 4.5A, showing the two pyridine pendant arms unbound, due to the small size of Cu^{2+} (0.73), in a distorted octahedral geometry. Figure 4.5B shows the X-ray crystal structure of the [In(pyhox)][ClO_4] cation, and despite the chelator being octadentate, In^{3+} prefers hexacoordination over octacoordination with H_2pyhox. In^{3+} has a preference for the pyridine ligands over the ethylenediamine backbone. The [^{111}In][In(pyhox)]$^+$ complex was shown to be kinetically inert *in*

vitro, and the [^{64}Cu][Cu(pyhox)] highlighted to withstand competition from superoxide dismutase (SOD) and EDTA.

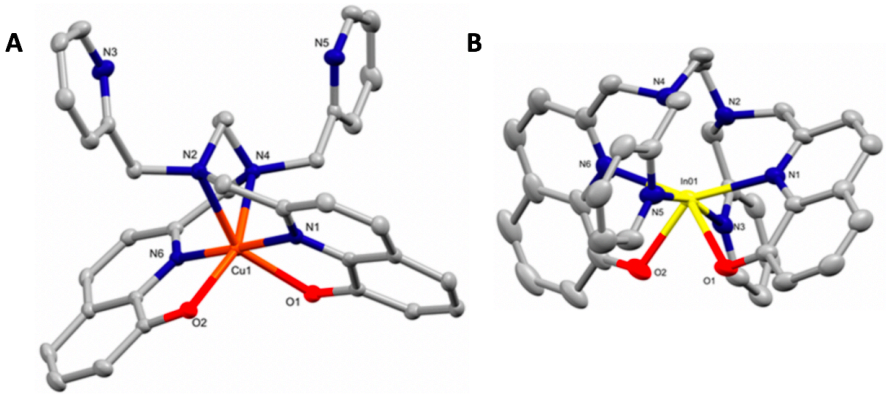

Figure 4.5 – ORTEP diagrams of [Cu(pyhox)] (A) and the cation of [In(pyhox)][ClO_4] (B)

Building upon the chelator HBED, developed by Arthur E. Martell in the 1960s, Choudhary *et al* have designed H_4HBEDpa, as a combination of HBED and H_2dedpa (Figure 4.3).[232] The authors demonstrate that the chelator binds both Fe^{3+} and Ga^{3+}. They go on to use density functional theory (DFT) to infer that Lu and Sc complexes of HBEDpa will have lower complexation energies than that of Ga, suggesting thermodynamically more stable complexes.[232]

The bisoxine hexadentate chelator H_3glyox (Figure 4.3) has been investigated for use with Mn^{2+}, Cu^{2+} and Lu^{3+}, with all three metals being highly relevant to the nuclear medicine community.[233] The authors showed the chelator bound [^{52}Mn]Mn^{2+} and [^{64}Cu]Cu^{2+} efficiently, and [^{177}Lu]Lu^{3+} to a lesser extent. All radiolabellings took place at RT, low concentration (10^{-5} M) and within 15 minutes. Future use of H_3glyox could possibly include use of the chelator with Mn^{2+} as an MRI contrast agent.

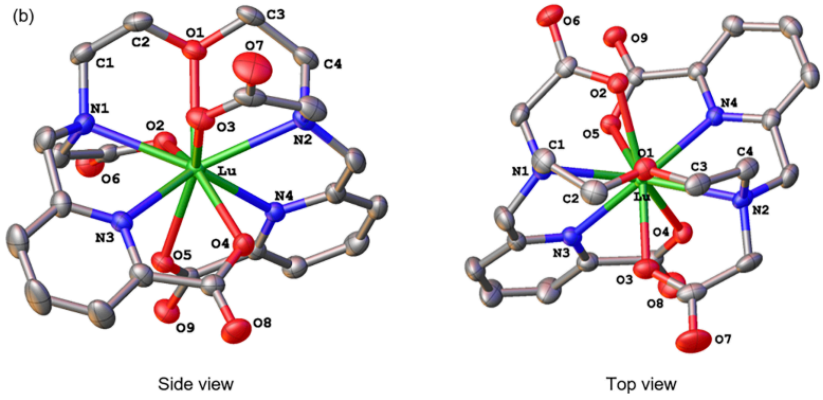

Figure 4.6 – X-ray crystal structure of [^{nat}Lu]Lu-noneunpa from Hu and co-workers

Justin Wilson's group have recently published the synthesis of oxyaapa (H_4noneunpa, Figure 4.3) and the X-ray crystal structure can be seen in Figure 4.6. It shows all nine donor atoms are coordinating to the Lu, with a distorted C_2 symmetry and spherical capped square antiprism geometry.[234] Wharton and co-workers have gone on to evaluate H_4noneunpa as well as H_4neunpa-NH_2 with [^{177}Lu]Lu^{3+}, [^{111}In]In^{3+}, [^{44}Sc]Sc^{3+} and [^{225}Ac]Ac^{3+}.[235] Their results showed dramatic differences in preferences for radiometals between H_4noneunpa and H_4neunpa-NH_2. H_4noneunpa was shown to be very versatile, demonstrating effective coordination of all the radiometals tested, with excellent kinetic inertness after incubation in human serum. In contrast, H_4neunpa-NH_2 exhibited high affinity for [^{111}In]In^{3+}, radiolabelling the metal at very low concentrations (10^{-7}) at RT in 10 minutes, with excellent serum stability (98 % intact after 5 days).[235] However, the chelator showed low affinity for the other radiometals evaluated in the paper.

Using Bi^{3+} as inspiration, due to its comparable ionic radius to Tl^{3+}, L_{py} (structure shown in Figure 4.7) was chosen for this project with Tl^{3+} due to the fast-radiolabelling kinetics and high stability when radiolabelled with $^{207}Bi^{3+}$.[42] The radiolabelling can be performed at room temperature and under acidic pH (3.5). The radiolabelling yield was measured at ligand concentrations of 10, 100

and 1000 μM, with 100 μM having the optimal radiolabelling conditions. The [Bi(L_{py})] complex also showed good stability in competition with EDTA. When incubated in solution with a large excess of EDTA in PBS at pH 7.4, after 7 days over 90 % of the complex remained intact, which was found to be similar to DOTA but better than DTPA. However, the group have only analysed this using ITLC not HPLC. [Bi(L_{py})] also showed excellent resistance to endogenous metal ions, such as Cu^{2+}, Zn^{2+} and Fe^{3+}, following incubation for up to 7 days.

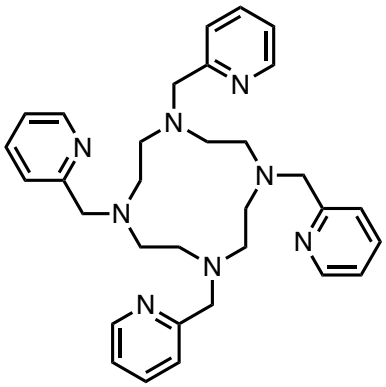

Figure 4.7 - The structure of L_{py}

This chapter will describe the investigation of EDTA, DTPA and DOTA with [$^{nat/201}$Tl]Tl^{3+} and the assessment of the complexes stabilities in human serum. Additionally, a large number of chelators have been screened for use with [$^{nat/201}$Tl]Tl^{3+}, bearing a range of different donor moieties, differences in total number of donors and varying cavity sizes. This was to find common characteristics between the chelators that bind Tl^{3+} and to develop more of an understanding about the chelation chemistry of Tl^{3+}.

4.2 Material and methods

Unless stated otherwise, chemicals and solvents were purchased from commercial suppliers (Merck, Fisher Scientific, Fluorochem). EDTA (Fisher Scientific), DTPA (Sigma) and DOTA (Chematech) were purchased from commercial suppliers. H_4pypa was kindly provided by members of the Orvig group; in addition, larger batches of H_4pypa were synthesised in house following previously described procedures.[214] H_4noneunpa, H_4octapa, H_5decaox, DTPAm, H_2pyhox, H_4octox, H_3glyox, H_5decapa, H_4neunpa-NH_2 and H_4HBEDpa were kindly provided by members of the Orvig group having been synthesised as previously published.[225,228,231,235,236] H_4picoopa, H_2amidohox, noctapa, H_2amidoC3hox, H_2noonpa, H_2ampa, H_4neunox, H_4tetrapa-NH_2, H_4noneunpaX and H_4picOpa were kindly provided by members of the Orvig group, but the synthesis is as yet unpublished. L_{py} and DFO-HOPO were synthesised as previously described.[237,238]

[^{201}Tl]TlCl in saline was purchased from Curium Pharma, UK. Oxidation was performed using Pierce Iodination beads (Thermo Scientific). ^{1}H, ^{13}C NMR, HSQC and COSY data were acquired on a Bruker 400 MHz and analysed using MestReNova software. Flash chromatography purification was performed on Biotage Isolera 4 flash chromatography system, using Sfar chromatography columns (silica and C18). HPLC was performed on an Agilent 1260 Infinity instrument with UV spectroscopic detection at 254 nm and Lablogic Flow-Count detector with Bioscan Inc. B-FC-3200 photomultiplier tube detector and analysed using Lablogic Laura software. The mobile phase used for analytical and semipreparative reverse-phase HPLC was composed of A: water with 0.1% TFA and B: MeCN with 0.1% TFA. LC/MS data were acquired on an Agilent 1200 Series Liquid Chromatograph with UV spectroscopic detection at 254 nm and same column details as in reverse-phase HPLC, interfaced with an Advion Expression LC/MS mass spectrometer with electrospray ionisation source. The mobile phase used for LC/MS was composed of A: water with

0.1% formic acid; and B: MeCN with 0.1% formic acid. Lyophilisation was performed using an Edwards Freeze-Dryer Modulyo.

Synthesis

[^{nat}Tl]Tl-EDTA

$TlCl_3$ hydrate (0.12 g, 410 µmol) was dissolved in MeCN (5 mL) and added to a solution of EDTA (Thermofisher) (0.1 g, 342 µmol) dissolved in water (15 mL). The solution was left stirring at RT for 6 hours, after which the solvent was removed to yield the product as a white solid. (0.158 g, 94%) ESI-MS: calc for $[C_{10}H_{12}N_2O_8{}^{205}Tl + H]^+$ 492.58; found 494.1. ^1H and ^{13}C NMR spectra are shown in Figure 4.8.

[^{nat}Tl]Tl-DTPA

$TlCl_3$ hydrate (0.095 g, 305 µmol) was dissolved in MeCN (5 mL) and added to a solution of DTPA (Sigma) (0.1 g, 254 µmol) dissolved in water (15 mL). The solution was left stirring at RT for 6 hours, after which the solvent was removed to yield the product as a white solid. (0.13 g, 89%) ESI-MS: calc for $[C_{14}H_{18}N_3O_{10}{}^{205}Tl + H]^+$ 592.69; found 594.0. ^1H and ^{13}C NMR spectra are shown in Figure 4.8.

[^{nat}Tl]Tl-DOTA

$TlCl_3$ hydrate (0.076 g, 247 µmol) was dissolved in MeCN (5 mL) and added to a solution of DOTA.HCl (Chematech Ltd) (0.1 g, 247 µmol) dissolved in water (15 mL). The solution was left stirring at RT for 60 minutes, after which a precipitate formed. This was separated via filtration and dried *in vacuo* without further purification, to yield the product as a white solid. (0.103 g, 73%) ESI-MS: calc for $[C_{16}H_{24}N_4O_8{}^{205}Tl + H]^+$ 605.13; found 605.43. ^1H and ^{13}C NMR spectra are shown in Figure 4.9.

[^{nat}Tl]Tl-pypa

$TlCl_3$ hydrate (0.05 g, 96 µmol) was dissolved in ammonium acetate solution (1M, pH 5, 0.5 mL) and added to a solution of H_4pypa (0.037 g, 96 µmol) also dissolved in ammonium acetate solution (1 M, pH 5, 0.5 mL). The reaction was agitated for 5 minutes at RT. The complex was purified using reverse phase prep HPLC (A: MeCN/0.1% TFA, B: H_2O/0.1% TFA, 5-60% A over 40 minutes, 10 mL/min). UV active fractions were analysed using LC-MS (HPLC method B), pure fractions were combined and freeze dried to yield the product as a white solid. (0.055 g, 80%) HR-ESI-MS: calc for $[C_{25}H_{23}N_5O_8{}^{205}Tl + H]^+$ 726.1291; found 726.1306. ^{1}H NMR spectra can be seen in Figure 4.14 and the COSY NMR can be seen in Figure 4.15.

1,4,7,10-Tetrakis(2-pyridylmethyl)-1,4,7,10-tetraazacyclododecane (L_{py})

Cyclen (Chematech Ltd) (0.33 g, 1.9 mmol) was dissolved in MeCN (8 mL) to which Cs_2CO_3 (12.5 g, 38.3 mmol) was added, forming a suspension. 2-Picolylchloride hydrochloride (1.3 g, 7.7 mmol) was dissolved separately in MeCN (8 mL) and added dropwise to the stirring cyclen solution. The reaction was heated to reflux for 24 hours, after which the reaction was filtered to remove the inorganic salts and solvent removed *in vacuo*. The crude solid was then recrystallised from hot MeCN (50 mL) to yield the desired product as a crystalline solid (0.8 g, 80%). Characterisation matched the previous published literature synthesis.[237]

DFO-HOPO

This procedure was adapted from Allott *et al*.[238] Thionyl chloride (1 mL) was added to a suspension of 1,6-dihydroxy-1,6-dihydropyridine-2-carboxylic acid (**1**) (synthesised by Dr Charlotte Rivas) (50 mg, 0.32 mmol) in dry THF (1 mL) and the reaction heated to 75 °C overnight. After cooling, the solvent was removed *in vacuo* to yield **2** as a yellow oil which was used without further purification. This was redissolved in dry DMF (2 mL), and added to deferoxamine

mesylate (200 mg, 0.32 mmol), followed by NEt_3 (45 μL, 0.32 mmol) and stirred at RT overnight. The solvent was removed *in vacuo*, and the residue washed with acetone (1 mL), resulting in the formation of a white precipitate. This solid was separated via centrifugation, washed with more acetone (3-4 mL). It was then purified using semi-preparative reverse phase HPLC. Solvent A = H_2O (0.1% TFA), solvent B = MeCN (0.1% TFA) 0-30 minutes, 3-90% B, 30.1-31 minutes 90-3% B, 40 minutes 3% B at 3 mL/min. Characterisation matched the previous published literature synthesis.[238]

Radiolabelling of EDTA, DTPA and DOTA with $[^{201}Tl]Tl^{3+}$

These procedures were adapted from Hijnen *et al*.[161] $[^{201}Tl]TlCl_3$ (40 μL, 3 MBq), produced using iodobeads (Chapter 2), was added to Eppendorf tubes containing 1 mg/mL EDTA (0.34 μmol), DTPA (0.25 μmol), DOTA (0.25 μmol) or TETA (0.23 μmol) in ammonium acetate buffer (0.25 M, pH 5, 100 μL). The mixture was vortexed and agitated for 10 (EDTA or DTPA) or 60 minutes (DOTA or TETA) at room temperature. Reverse phase TLC plates (TLC Silica Gel 60 RP-18 F254s MS-grade) were used as the stationary phase and acetonitrile (30%) with water as the mobile phase $[^{201}Tl]Tl^+$ (R_f = 0) or $[^{201}Tl]Tl^{3+}$ (R_f = 0) and [^{201}Tl]Tl-EDTA/DTPA/DOTA (R_f = 1). All TLC plates were imaged using a Cyclone Plus Phosphor Imager (PerkinElmer, Inc. USA).

General experimental for radiolabelling of the chelators 1-17 with $[^{201}Tl]Tl^{3+}$

Chelator (1 mg/mL in water, 20 μL) was added to $[^{201}Tl]TlCl_3$, produced using iodobeads (39.5 MBq, 108 μL) and 1M ammonium acetate (pH 5, 20 μL) giving the combined solution a pH of 5. This was vortexed and agitated in a Thermomixer (500 rpm) at RT for 10 minutes. Radiochemical yield and purity was evaluated using RP-ITLC, as described above (unbound $[^{201}Tl]Tl^+$, $[^{201}Tl]Tl^{3+}$ R_f = 0, $[^{201}Tl]Tl^{3+}$ complex R_f = 1) and HPLC (method A).

General experimental for evaluating the stability of [^{201}Tl]Tl-complexes

Human serum (300 µL, Merck) was added to an Eppendorf tube, followed by the addition of [^{201}Tl]Tl-complexes (200 kBq, 12-15 µL). These were then incubated at 37 °C for up to 48 hours. An aliquot (2 µL) was removed and analysed using RP-TLC (TLC Silica Gel 60 RP-18 F254s MS-grade) to assess the stability. In addition to human serum, this process was repeated using ammonium acetate solution (1 M, pH 5). Similar stability studies were also carried out for [^{201}Tl]Tl-DOTA incubated in cell culture medium (RPMI-1640) supplemented with 10% foetal bovine serum, 2 mM L-glutamine, and penicillin/streptomycin or in 0.25 M ammonium acetate buffer (pH 5) at 37 °C for up to 144 h. These were analysed using RP-TLC plates as described previously.

4.3 Results

4.3.1 EDTA, DTPA and DOTA evaluation with Tl^{3+}

For the complexation with EDTA and DTPA, the ligands were dissolved in water, added to [^{nat}Tl]$TlCl_3$ (in excess, dissolved in MeCN) and left stirring for the six hours at RT. The solvent was then removed, and the resulting white solids evaluated using NMR (Figure 4.8). The [^{nat}Tl]Tl-EDTA ^{1}H NMR (Figure 4.8), run in D_2O, suggests the presence of a single species in solution, and the complex has a very different spectrum to the ligand alone. Each of the carboxylate arms are now inequivalent to each other, and the ethylene backbone protons are also inequivalent.

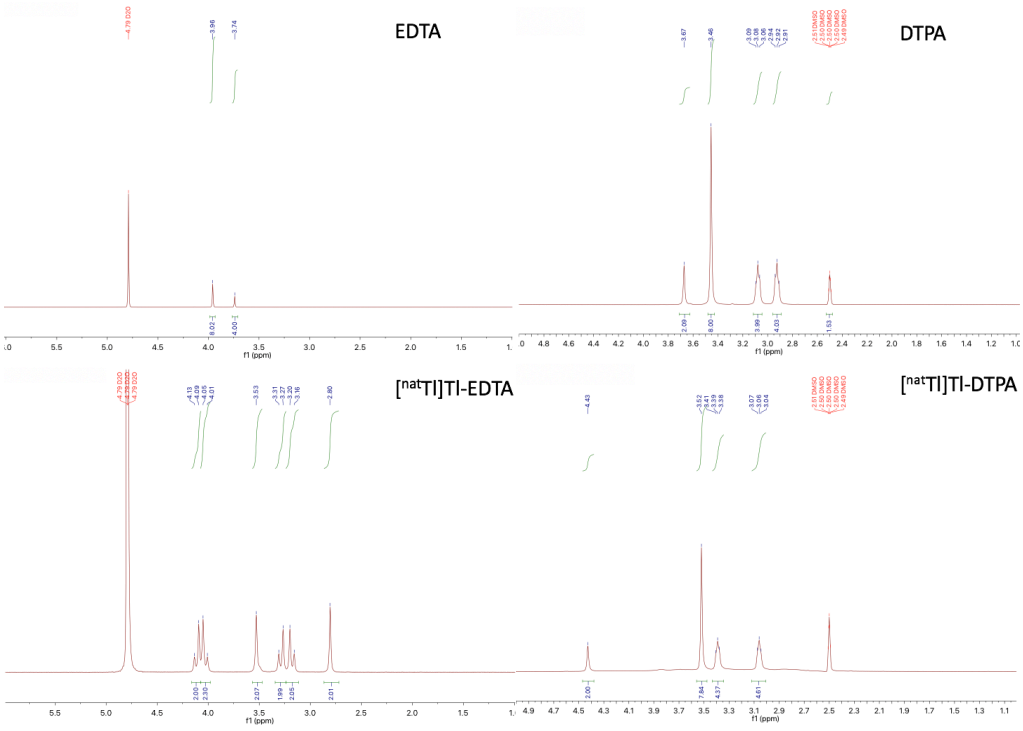

Figure 4.8 – ^{1}H NMR spectra of EDTA and [^{nat}Tl]Tl-EDTA in D_2O, DTPA and [^{nat}Tl]Tl-DTPA in DMSO-*d6*.

The [^{nat}Tl]Tl-DTPA ^{1}H NMR (Figure 4.8), run in DMSO-*d*$_6$, also suggests the presence of a single species in solution. All peaks have been shifted downfield when compared to the chelator alone, with the middle carboxylate arm protons shifting the most (3.67 ppm to 4.43 ppm).

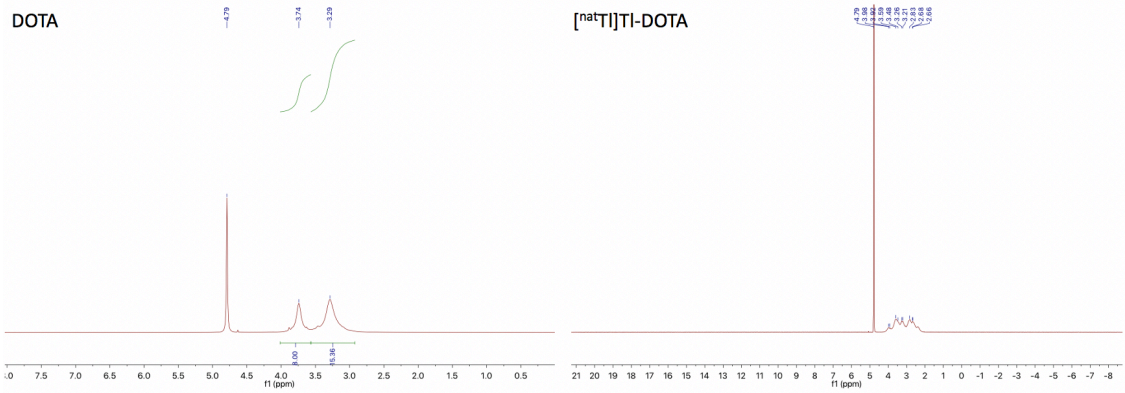

Figure 4.9 - ^{1}H NMR spectra of DOTA and [^{nat}Tl]Tl-DOTA in D_2O

To complex [^{nat}Tl]Tl^{3+} with DOTA, the ligand was dissolved in water, added to [^{nat}Tl]TlCl$_3$ (dissolved in MeCN) and left stirring for an hour at RT. After this time, a white solid precipitated from solution, which was filtered, washed with water and dried under reduced pressure. The resulting white solid was evaluated using NMR (Figure 4.9). The solid was suspended in D_2O, and the pH adjusted to pH to 8 using Na_2CO_3 (1 M, in D_2O) where the complex completely dissolved. The ^{1}H NMR of DOTA alone shows two broad peaks, which may be due to the motion of the molecule rotating in solution on an NMR timescale, or proton exchange between bulk water protons and labile protons of DOTA (Figure 4.9). The ^{1}H NMR of the complex has very broad set of multiplets between 2 and 4 ppm, which is similar to what has been reported by Fodor and co-workers.[162] They found similar results with the finely resolved multiplets only being seen using variable temperature NMR.[162]

Radiochemistry with EDTA, DTPA and DOTA

In order to confirm thallium has been chelated, a simple TLC method has to be developed as a quick alternative to the use of HPLC. Jalilian *et al.* have published results using a 1:1 mixture of ammonium acetate (1 M) and methanol to differentiate between free metal and complexes.[174,176,177,185,239,240] The authors claim that the complexes move up the TLC plate, leaving free metal at the baseline. However, under these conditions both oxidation states of the metal moved up the plate so are indistinguishable from complexed thallium (Figure 4.10); hence an alternative method was needed.

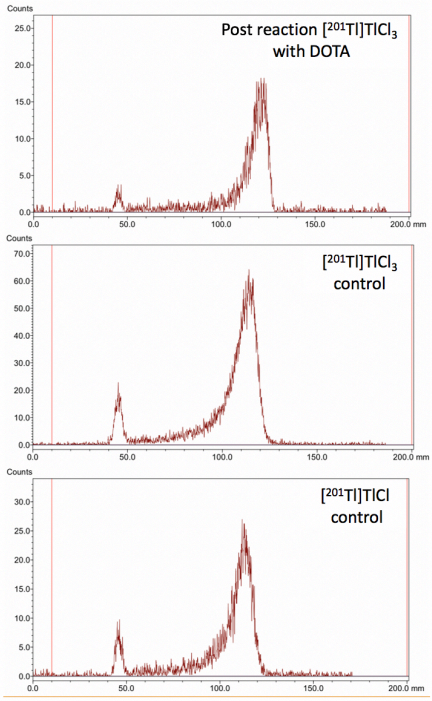

Figure 4.10 – ITLC results using a 1:1 mixture of ammonium acetate (1 M) and methanol. The product of the reaction between $[^{201}Tl]TlCl_3$ and DOTA (top) has the same R_f as the $[^{201}Tl]TlCl_3$ (middle) and $[^{201}Tl]TlCl$ (bottom), demonstrating this is not a viable ITLC method for use with ^{201}Tl.

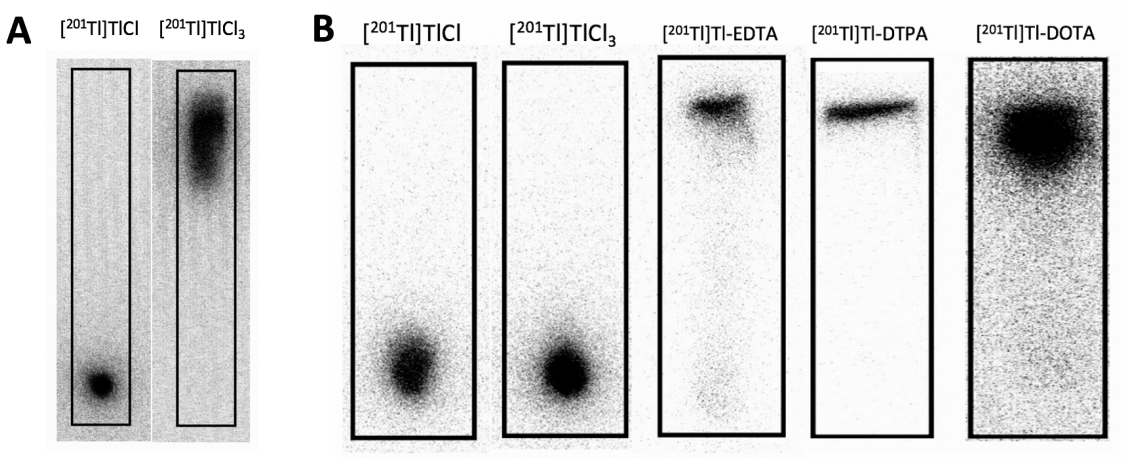

Figure 4.11 – Representative phosphor images of ITLCs for the $[^{201}Tl]Tl^{+}$ to $[^{201}Tl]Tl^{3+}$ oxidation (A). Solid phase = ITLC-SG, mobile phase = acetone. $[^{201}Tl]Tl^{+}$ $R_f = 0$, $[^{201}Tl]Tl^{3+}$ $R_f = 1$. Representative phosphor images of reverse phase TLCs of $[^{201}Tl]TlCl$, $[^{201}Tl]TlCl_3$, $[^{201}Tl]Tl$-EDTA, $[^{201}Tl]Tl$-DTPA and $[^{201}Tl]Tl$-DOTA (B). $[^{201}Tl]Tl^{+}$ $R_f = 0$, $[^{201}Tl]Tl^{3+}$ $R_f = 0$, $[^{201}Tl]Tl$ chelates, $R_f = 1$.

$[^{201}Tl]Tl^{3+}$ formed using chloramine-T (oxidation method 6, Chapter 2) was reacted with chelators EDTA, DTPA and DOTA. Reverse phase TLC plates, using MeCN (30%):water as the mobile phase, gave excellent separation of $[^{201}Tl]Tl$-EDTA, $[^{201}Tl]Tl$-DTPA and $[^{201}Tl]Tl$-DOTA from uncomplexed ^{201}Tl and showed >95% radiolabelling yield in all cases (n = 3; Figure 4.11).

4.3.2 Serum stability of [^{201}Tl]Tl-EDTA, [^{201}Tl]Tl-DTPA and [^{201}Tl]Tl-DOTA

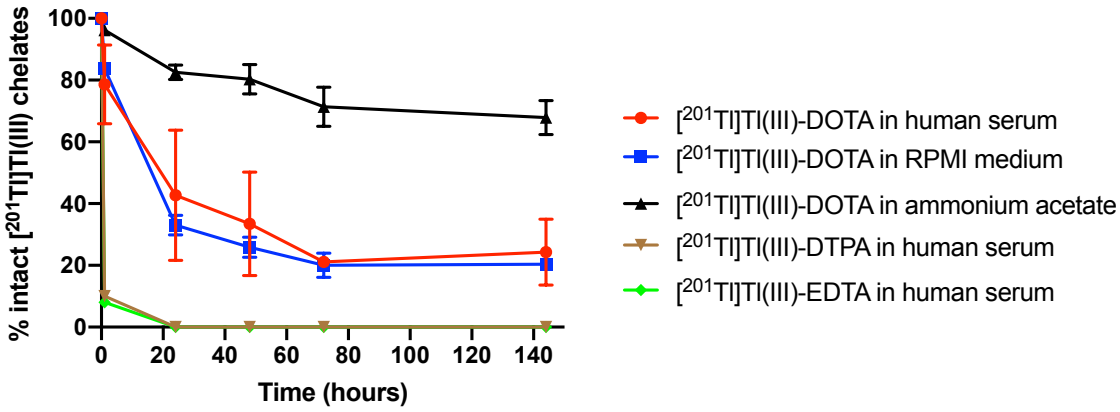

Figure 4.12 – Stability of [^{201}Tl]Tl-EDTA, [^{201}Tl]Tl-DTPA and [^{201}Tl]Tl-DOTA in human serum and of [^{201}Tl]Tl-DOTA in RPMI-1640 cell culture medium and ammonium acetate buffer (0.25 M, pH 5) at 37 °C over 144 hours. Values are average +- standard deviation (n = 3).

After 1 hour in serum, of the [^{201}Tl]Tl-DTPA and [^{201}Tl]Tl-EDTA formed after the initial complexation, only 9 ± 2 % remained; the complexes had completely dissociated by 24 hours (Figure 4). Serum stability was evaluated using reverse phase TLCs, with protein bound or unbound metal remaining at the baseline and intact complex migrating with the solvent front. [^{201}Tl]Tl-DOTA dissociated at a slower rate than [^{201}Tl]Tl-DTPA and [^{201}Tl]Tl-EDTA, with 78 ± 12 % of the complex remaining at 1 hour, and 24 ± 13 % of [^{201}Tl]Tl-DOTA still intact at 144 hours. Similarly, [^{201}Tl]Tl-DOTA appeared relatively stable in RPMI-1640 medium, with 84 ± 2 % remaining after 1 hour incubation, decreasing to 20 ± 2 % at 144 hours. The complex was more stable in ammonium acetate buffer with 68 ± 6 % of the complex remaining after 144 hours incubation (Figure 4.12).

4.3.3 H_4pypa evaluation

Initial studies using H_4pypa were performed using a small amount kindly supplied by members of Prof Chris Orvig's group at the University of British Columbia, Canada. With further experiments needed I synthesised a larger batch of H_4pypa, according to the published literature synthesis.[214] Characterisation data matched the previous reports.[214] H_4pypa was reacted with thallium trichloride hydrate ($[^{nat}Tl]TlCl_3(H_2O)_4$) in ammonium acetate solution (pH = 5) at RT for 15 minutes, to yield [Tl(Hpypa)] as a white solid.[214] Following purification, the complex was characterised using high-resolution electrospray ionisation mass spectrometry (HR-ESI-MS, Figure 4.13), nuclear magnetic resonance (NMR) (Figure 4.14). HRMS data shows the formation of a 1:1 complex of pypa with Tl^{3+}. Due to the insolubility of [Tl(Hpypa)] in D_2O, a small amount of Na_2CO_3 (in D_2O) was added adjusting the pH to 8-9 to greatly increase solubility. This could be due to deprotonation or to counter ion exchange, enabling NMR (^1H, ^{13}C and 2D NMR) spectroscopic studies. Previous reports in the literature show that H_4pypa forms rigid complexes with In^{3+}, Lu^{3+} and La^{3+} ions with sharp ^1H NMR peaks suggesting little fluxionality. However, the ^1H and COSY NMR data of $[Tl(pypa)]^-$ suggest there are two species in solution (Figure 4.15). In complexes of pypa, ethylene protons are diastereotopic, with coupling between geminal, diastereotopic ethylene protons. In the ^1H COSY spectrum of the pypa complex of Tl^{3+}, more than six crosspeaks (at least 10 crosspeaks) between ethylene protons are observed, indicating that at least two chemically distinct Tl-pypa complexes are present in solution that do not interconvert rapidly on the NMR timescale. In the [Tl(Hpypa)] crystal structure, low symmetry is observed due to the uncoordinated carboxyl group, whereas the NMR suggests the symmetry is higher with the carboxyl group coordinated to the metal. Numerous attempts were made to grow at X-ray quality crystal at neutral pH or with an alternative counter ion, for example TBAF, but these were not fruitful. Under these conditions it is likely that the carboxylate arm would be

bound to the metal ion, allowing for a higher degree of symmetry in accordance with the NMR results.

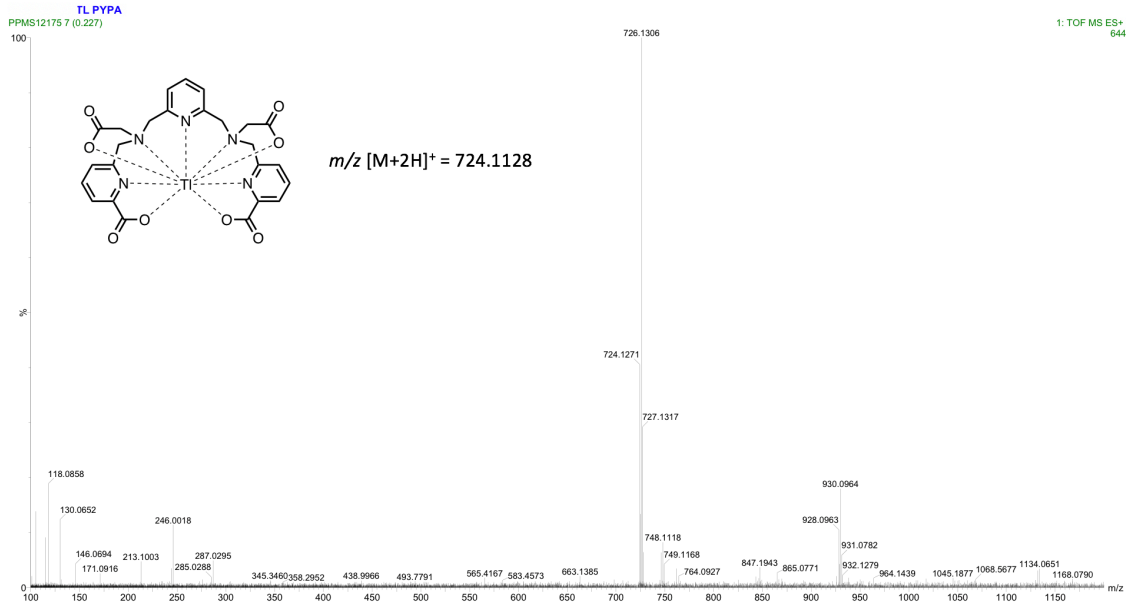

Figure 4.13 - High resolution mass spectrometry chromatogram for [^{nat}Tl]Tl-pypa

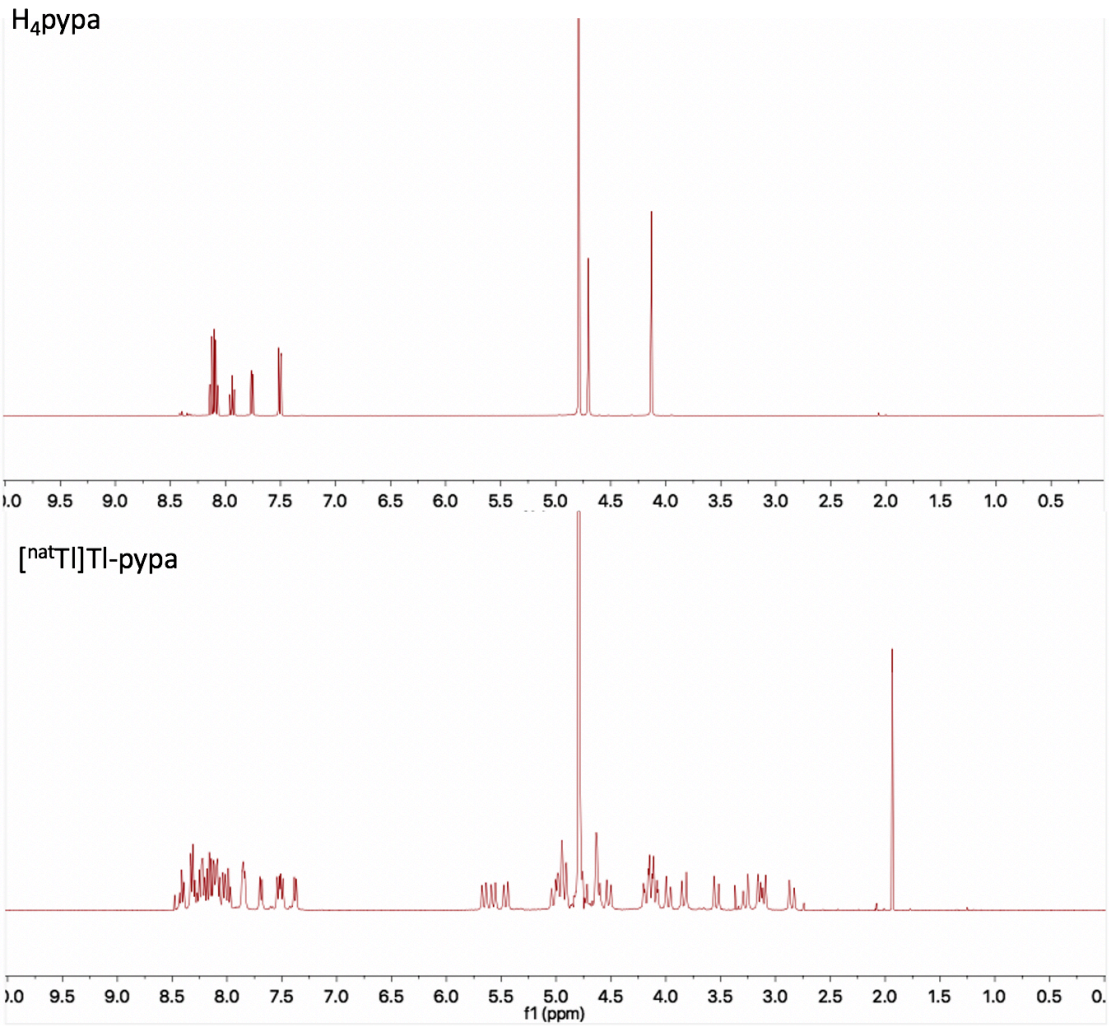

Figure 4.14 - ^{1}H NMR spectra of H_4pypa (top) and [^{nat}Tl]Tl-pypa (bottom)

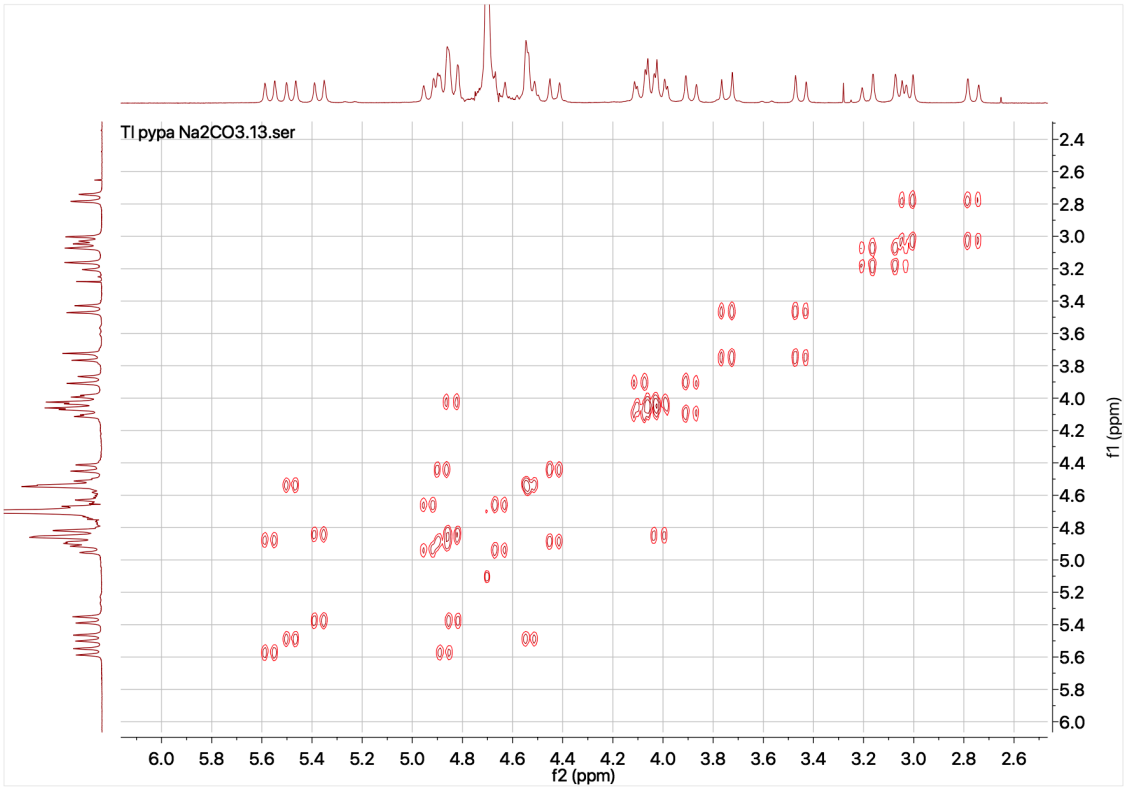

Figure 4.15 – ^{1}H COSY NMR spectrum of [^{nat}Tl]Tl-pypa

X-ray quality single crystals of [Tl(Hpypa)] were obtained by the slow evaporation of 1:1 $TlCl_3$ and H_4pypa solutions in water with the pH adjusted to 2 via the addition of HCl (0.1 M). The crystal structure of [Tl(Hpypa)] is shown in Figure 4.16, with the bottom structure having a second $TlCl_3$ coordinating to one of the carboxylate group (O008). This group also has a water molecule bound to the metal centre, completing the coordination sphere in a trigonal bipyramidal conformation. Selected bond lengths can be found in Table 10. The full crystallographic information can be found in the methods. The crystal structure shows the complex has a distorted square antiprismatic geometry and that when grown from a solution at pH 2, one of the carboxylic acid groups is protonated and not coordinating to Tl. The crystal structure for H[Lu(pypa)] shows that two of the carboxylic acid groups are protonated when crystallised from a solution at pH 2.[214] The Tl^{3+} ion is coordinated by eight (N_5O_3) donor atoms of the ligand. The Tl – O bond lengths are between 2.258(6) – 2.496(5) Å and Tl – N bond lengths

are between 2.311(7) – 2.525(7) Å. These are comparable to bond lengths previously reported for Tl^{3+} complexes in the literature.[162,164,241]

The X-ray crystal structure of [Tl(Hpypa)][$TlCl_3(H_2O)$]. The unit cell was found to contain two Tl^{3+} centres. One sitting at the centre of the pypa ligand while the other is a $TlCl_3$ unit (presumably from the starting material) located at the extremity and coordinated by one carboxylate group from the pypa ligand and another H_2O molecule. Crystals were grown directly from a reaction mixture of $TlCl_3$ and pypa ligand at pH 2. One chloride ligand was found to be disordered and was modelled over two positions (Cl3A and Cl3B) with relative occupancy of 86% and 14%. These were modelled anisotropically and isotropically, respectively.

$C_{25}H_{24}Cl_3N_5O_9Tl_2$, M = 1053.58, triclinic, P-1 (no. 2), a = 9.0552(4), b = 11.4821(7), c = 15.7252(10) Å, α = 71.114(6), β = 75.497(5), γ = 83.697(4)°, V = 1496.94(16) $Å^3$, Z = 2, D_c = 2.337 g cm^{-3}, μ(Cu-Kα) = 23.432 mm^{-1}, T = 173 K, colourless plates, 5668 independent measured reflections (R_{int} = 0.0365), F^2 refinement, R_1(obs) = 0.0372, wR_2(all) = 0.0985, 4629 independent observed absorption-corrected reflections [$|F_0|$] > 4σ($|F_0|$), $2\theta_{max}$ = 147°], 404 parameters. CCDC 2115641.

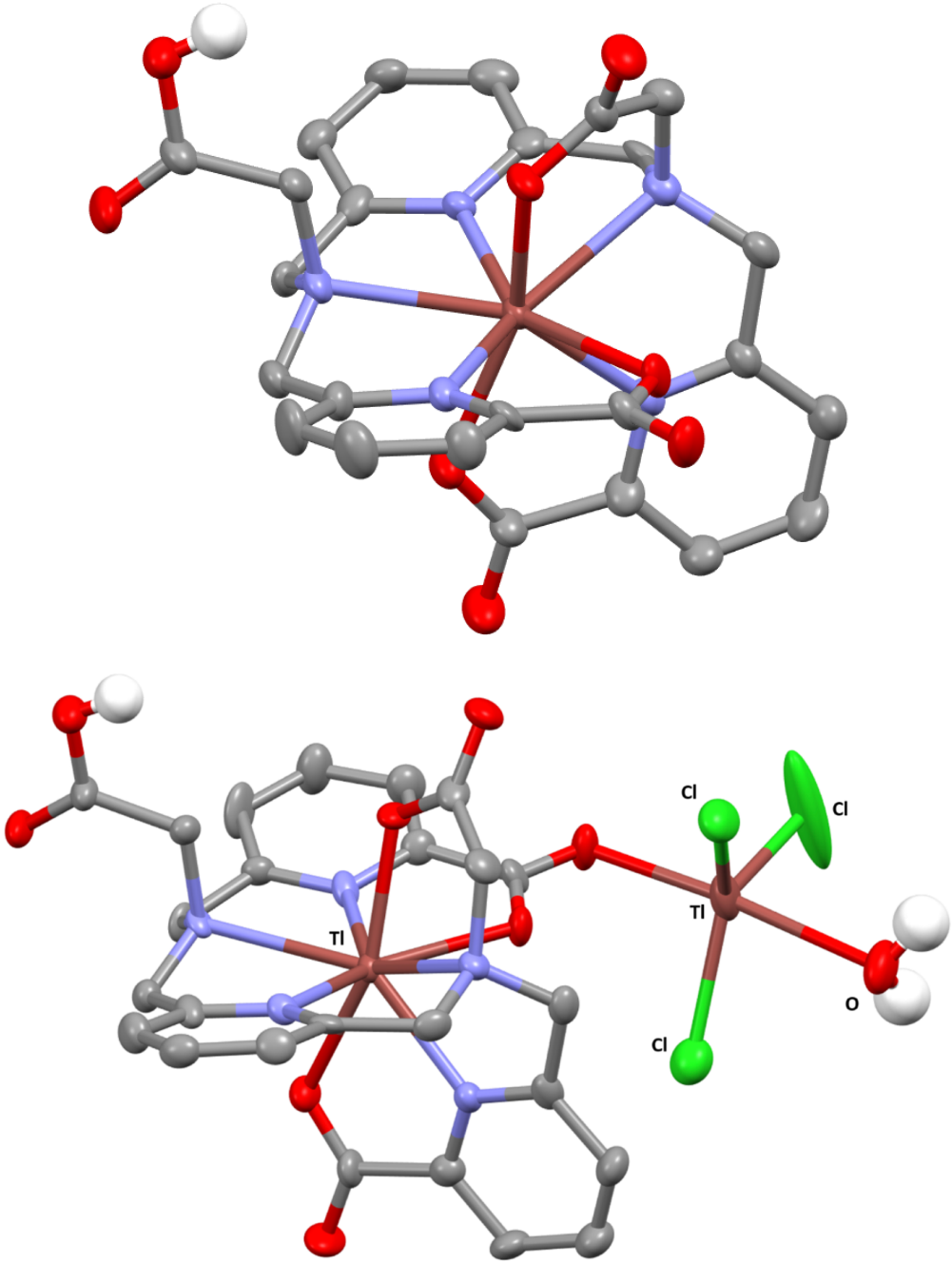

Figure 4.16 - Crystal structure of Tl(Hpypa) (50% probability ellipsoids). The top image has had the second [^{nat}Tl]$TlCl_3$ omitted for clarity.

Table 10 – Selected bond lengths in [Tl(Hpypa)]

Bond lengths (Å)		
Atom	**Atom**	**Length (Å)**
Tl(1)	O006	2.496(5)
Tl(1)	O007	2.258(6)
Tl(1)	O00A	2.370(6)
Tl(1)	N00E	2.358(6)
Tl(1)	N00F	2.348(7)
Tl(1)	N00G	2.311(7)
Tl(1)	N00H	2.530(6)
Tl(1)	N00J	2.525(7)

In the preliminary screening radiochemical studies, we oxidised $[^{201}Tl]Tl^{+}$ to $[^{201}Tl]Tl^{3+}$ (using iodobeads, Chapter 2) and assessed radiolabelling reactions of $^{201}Tl^{3+}$ with each of the chelators, H_4pypa, H_5decapa, H_4noneunpa, and H_4neunpa-NH_2.[242] Each chelator (20 µL, 0.02 mg) was incubated with $[^{201}Tl]Tl^{3+}$ (5-10 MBq) in aqueous solution at pH 5 at ambient temperature for 10 minutes, followed by HPLC and or RP-TLC analysis.[242] Using HPLC method A, [^{201}Tl]Tl-pypa eluted at t_R = 10.09 minutes (Figure 4.17), in excellent radiochemical yields. Stability experiments in human serum (incubated at 37 °C) showed no significant degradation after 1 hour. At 24 hours in human serum, 68.7 ± 6.5% of the intact complex was still detected, and this decreased to 57.7 ± 15.1% after 48 hours (Figure 4.19C).

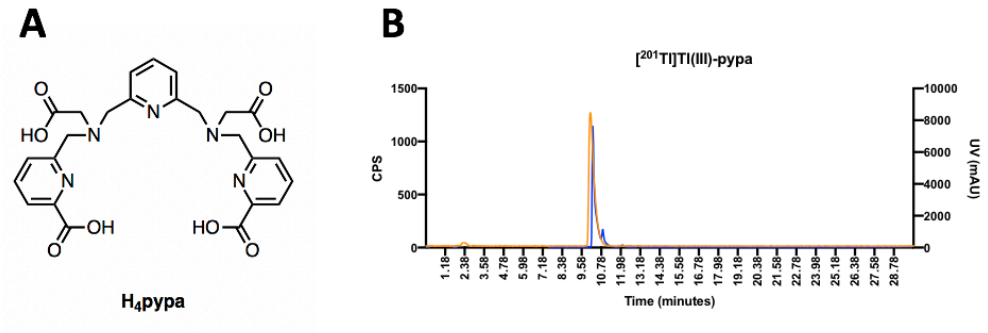

Figure 4.17 - A. Structures of H_4pypa B. Analytical HPLC trace of [^{201}Tl]Tl-pypa (orange = counts per second, blue = UV (ligand).

4.3.4 *In vitro* evaluation of [^{201}Tl]Tl-pypa

Previous *in vitro* data using the DOTA bioconjugates **9** and **11**, which were evaluated using ^{201}Tl and ^{111}In. The results demonstrated an inherent instability of the ^{201}Tl complexes under these *in vitro* conditions. Hence, moving forward with the aim to develop a quick screening method to evaluate the stability of ^{201}Tl complexes under *in vitro* conditions. [^{201}Tl]Tl-pypa was tested with DU145 PSMA positive and negative prostate cancer cells, which can be seen in Figure 4.18. Without an appropriate moiety to target a receptor such as PSMA, [^{201}Tl]Tl-pypa is unlikely to enter cells transiently, so should remain in the cell culture media. However, if the complex degrades, ^{201}Tl is likely to be reduced and dissociate from the chelator, then it is likely that $^{201}Tl^{+}$ will enter the cells via the potassium channels. This uptake can then be compared to the [^{201}Tl]TlCl control, and compared at each time point. These were theorised as quick experiments that could mitigate the need to pursue long and complicated bioconjugate synthesis, just for the compound to not behave as expected *in vitro*, potentially saving time and lab resources.

Cell stability studies with DU145-PSMA or DU145 cells (Figure 4.18) show a significant ($p = 0.0110$) difference in uptake between [^{201}Tl]TlCl (3.77 ± 0.43% and 3.50 ± 1.45%, respectively) and [^{201}Tl]Tl-pypa (1.70 ± 0.30% and 1.82 ± 0.15%) after 15 minutes in both cell lines. Cellular uptake is enhanced at 60 minutes incubation. A KCl block reduces the uptake to 0.79 ± 0.31% in DU145-PSMA cells and 0.62 ± 0.12% in DU145 cells. As previously reported, the addition of KCl blocks cellular uptake of free thallium.[137] The data suggests that although Tl^{3+} is reduced to Tl^{+}, thereby entering the cells non-specifically via potassium channels, there is a portion of [^{201}Tl]Tl-pypa that is not reduced.

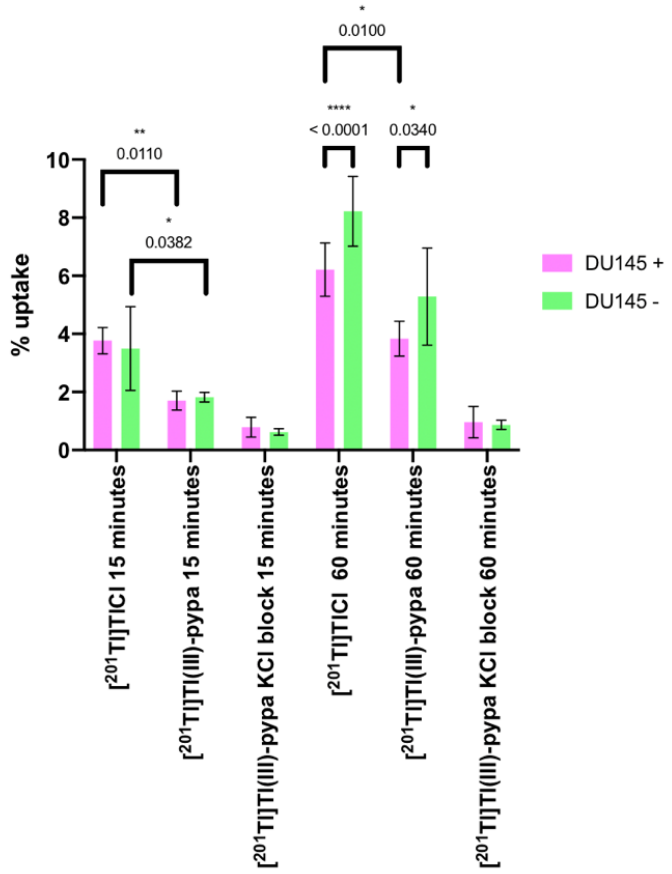

Figure 4.18 - Cell uptake studies using DU145 PSMA positive (purple) and DU145 PSMA negative (cyan) after incubation with [^{201}Tl]TlCl or [^{201}Tl]Tl(III)l-pypa (with and without a KCl block).

4.3.5 H_5decapa, H_4neunpa-NH_2 and H_4noneunpa evaluation

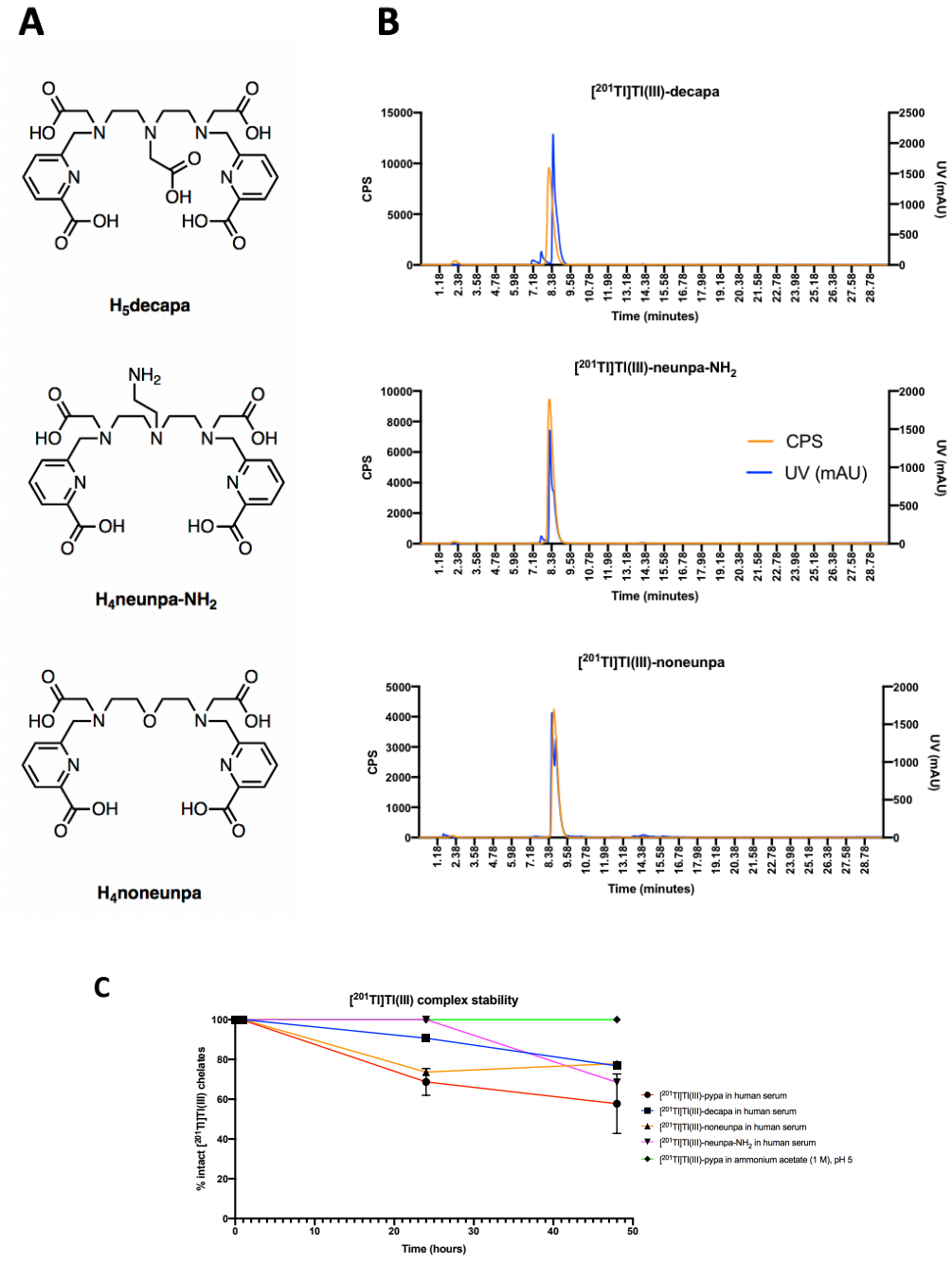

Figure 4.19 - A. Structures of H_5decapa, H_4neunpa-NH_2 and H_4noneunpa. B. Analytical HPLC trace of [^{201}Tl]Tl-decapa, [^{201}Tl]Tl-neunpa-NH_2 and [^{201}Tl]Tl-noneunpa (orange = counts per second, blue = UV (ligand). C. Stability studies of [^{201}Tl]Tl-pypa (ammonium acetate solution (1 M), pH 5 and human serum), [^{201}Tl]Tl-decapa, [^{201}Tl]Tl-neunpa-NH_2 and [^{201}Tl]Tl-noneunpa in human serum (n=2-3).

Under the HPLC conditions employed here (HPLC method A), [^{201}Tl]Tl-decapa eluted at 8.15 minutes, [^{201}Tl]Tl-noneunpa, eluted at 8.44 minutes and [^{201}Tl]Tl-neunpa-NH_2 eluted at 8.17 minutes, whereas unchelated [^{201}Tl]$TlCl_3$ eluted earlier at 2.03 min. Radiolabelling was rapid in all cases: radiochromatograms (Figure 4.19) show radiochemical yields of >97% after only 10 minutes incubation at RT. Each chelator was also evaluated with [^{201}Tl]Tl^+ (i.e. without prior treatment with Iodobeads) and no reaction was observed by HPLC. Additionally, LC-MS analysis of the reaction between H_5decapa and [^{nat}Tl]$TlCl_3$ in Figure 4.20, shows the mass corresponding to the $[M+H]^+$.

In human serum at 37 °C, [^{201}Tl]Tl-neunpa-NH_2 suffered no detectable degradation after 24 hours incubation, which decreased to 68.5 % after 48 hours. [^{201}Tl]Tl-decapa degraded to 90.7 % after 24 hours and 76.8% remained after 48 hours. [^{201}Tl]Tl-noneunpa decreased to 73.7 % at 24 hours, and remained at 76.8 % after 48 hours.

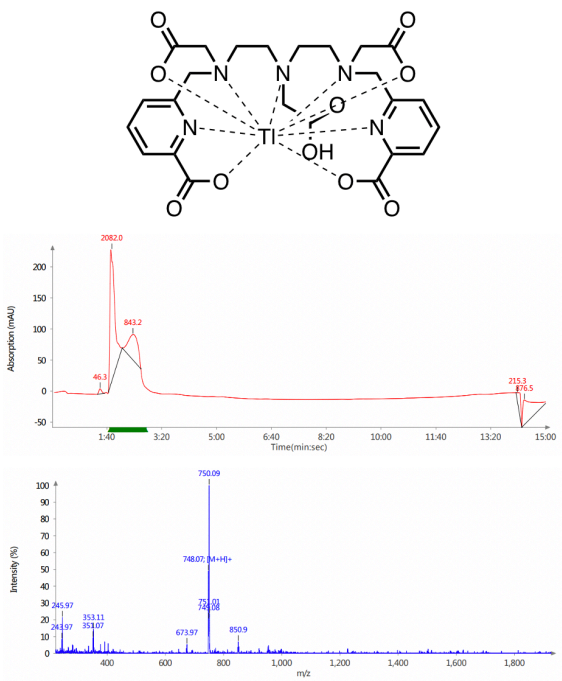

Figure 4.20 - The proposed structure of [^{nat}Tl]Tl-decapa complex and the LC-MS of the reaction (UV and mass signal)

4.3.6 Evaluation of chelators 1-17

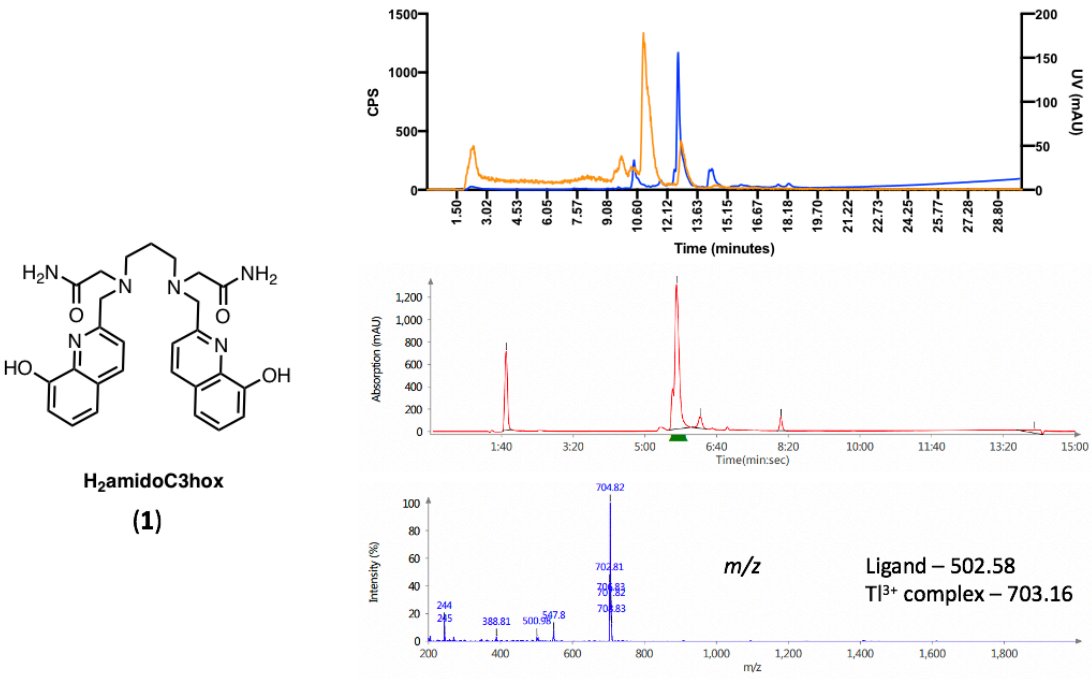

Figure 4.21 - Analytical HPLC trace of [^{201}Tl]Tl-amidoC3hox (orange = counts per second, blue = UV (ligand) (top), [^{nat}Tl]Tl-amidoC3hox UV trace from LC-MS (middle) and mass detected from LC-MS (bottom).

As with the previously described chelators, [^{201}Tl]$TlCl_3$ was prepared using iodobeads, and reactions were evaluated using HPLC method A. The analytical HPLC traces of the reaction between [^{201}Tl]Tl^{3+} with H_2amidoC3hox in Figure 4.21, along with the UV trace and mass detected from an LC-MS sample of [^{nat}Tl]Tl-amidoC3hox. The chelators were mixed with [^{201}Tl]Tl^{3+} (both dissolved in 1M ammonium acetate buffer), agitated for 10 minutes and then analysed using the LC-MS. The radioactive trace (orange) in Figure 4.21 shows multiple species in solution with H_2amidoC3hox, as well as unbound [^{201}Tl]Tl^{3+} which eluted at t_R = 2.03 minutes. The LC-MS data supports the radiolabelling with several peaks in the UV signal observed, but the main peak does correspond to [^{nat}Tl]Tl-amidoC3hox *m/z* $[M+H]^+$ = 704.82.

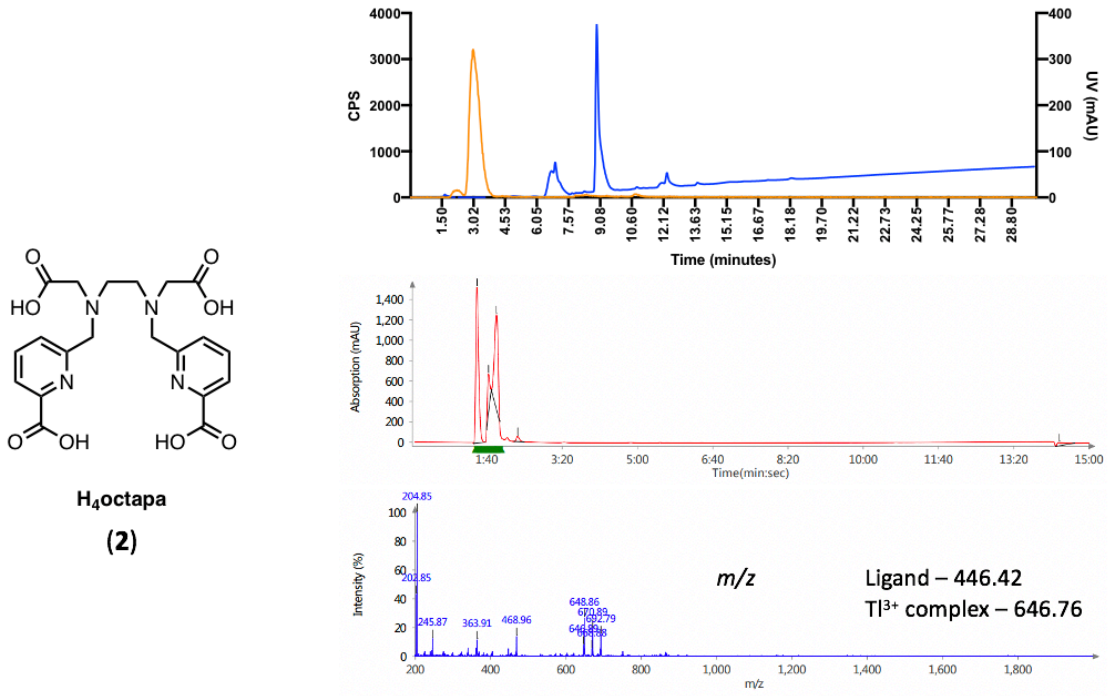

Figure 4.22 – Analytical HPLC trace of [^{201}Tl]Tl-octapa (orange = counts per second, blue = UV (ligand) (top), [^{nat}Tl]Tl-octapa UV trace from LC-MS (middle) and mass detected from LC-MS (bottom).

The analytical HPLC trace in Figure 4.22 shows a small peak at t_R = 2.03 minutes for unbound $^{201}Tl^{3+}$ and another peak around 3 minutes for the [^{201}Tl]Tl-octapa. This matches up with one of the peaks from the LC-MS, which also elutes early in the method, corresponding to the mass of the [^{nat}Tl]Tl-octapa complex.

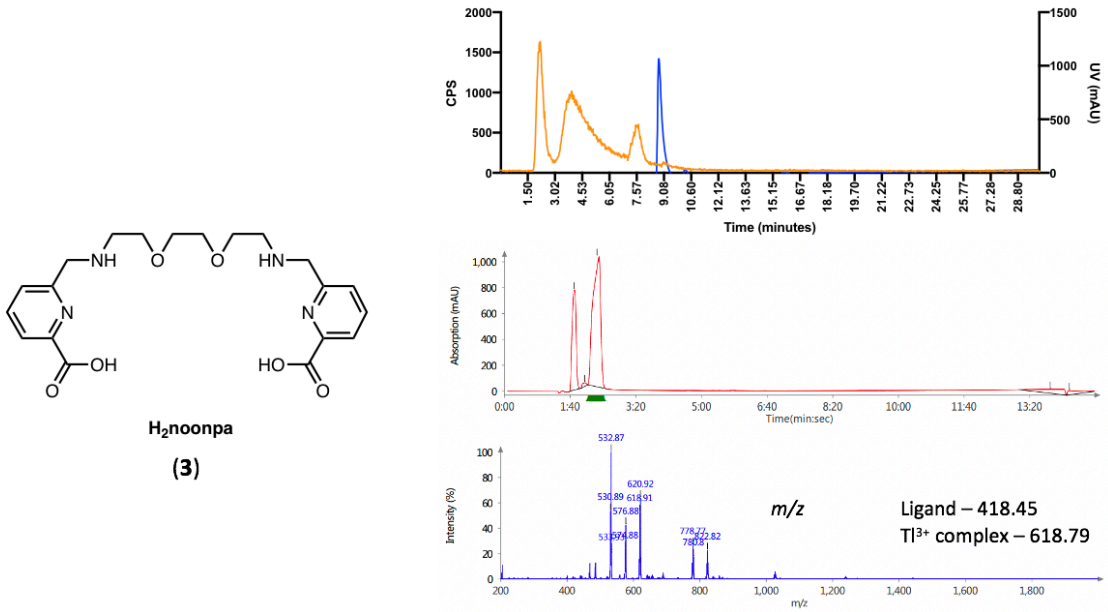

Figure 4.23 - Analytical HPLC trace of [^{201}Tl]Tl-noonpa (orange = counts per second, blue = UV (ligand) (top), [^{nat}Tl]Tl-noonpa UV trace from LC-MS (middle) and mass detected from LC-MS (bottom).

Evaluation of H_2noonpa can be seen in Figure 4.23, with the analytical HPLC showing unbound $^{201}Tl^{3+}$, as well as multiple other peaks; a broad peak between 4-5 minutes and a smaller peak at 8 minutes. There is also a peak in the LC-MS that corresponds to the mass of the [^{nat}Tl]Tl-noonpa complex.

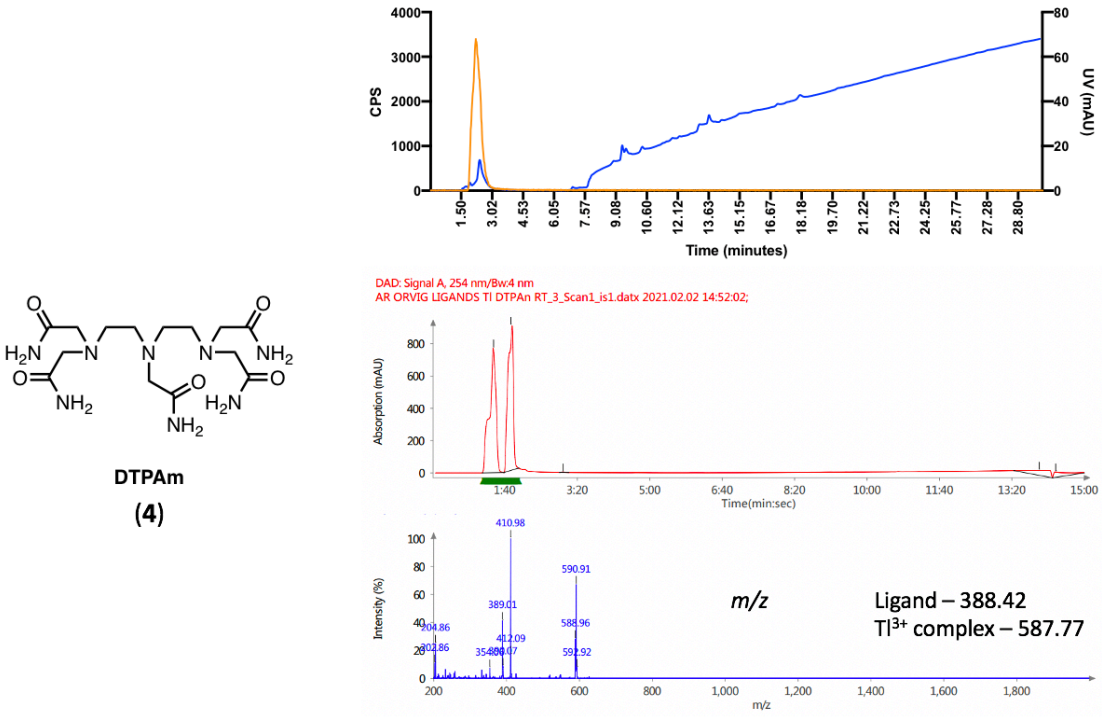

Figure 4.24 - Analytical HPLC trace of [^{201}Tl]Tl-DTPAm (orange = counts per second, blue = UV (ligand) (top), [^{nat}Tl]Tl-DTPAm UV trace from LC-MS (middle) and mass detected from LC-MS (bottom).

The analytical HPLC traces of the reaction between [^{201}Tl]Tl^{3+} with DTPAm can be seen in Figure 4.24. The radioactive trace (orange) in shows a single, broad peak eluting at a similar retention time to unbound [^{201}Tl]Tl^{3+} (t_R = 2.03 minutes). The LC-MS trace shows unbound [^{nat}Tl]Tl^{3+} (*m/z* = 204.38) in addition to the [^{nat}Tl]-DTPAm complex and ligand.

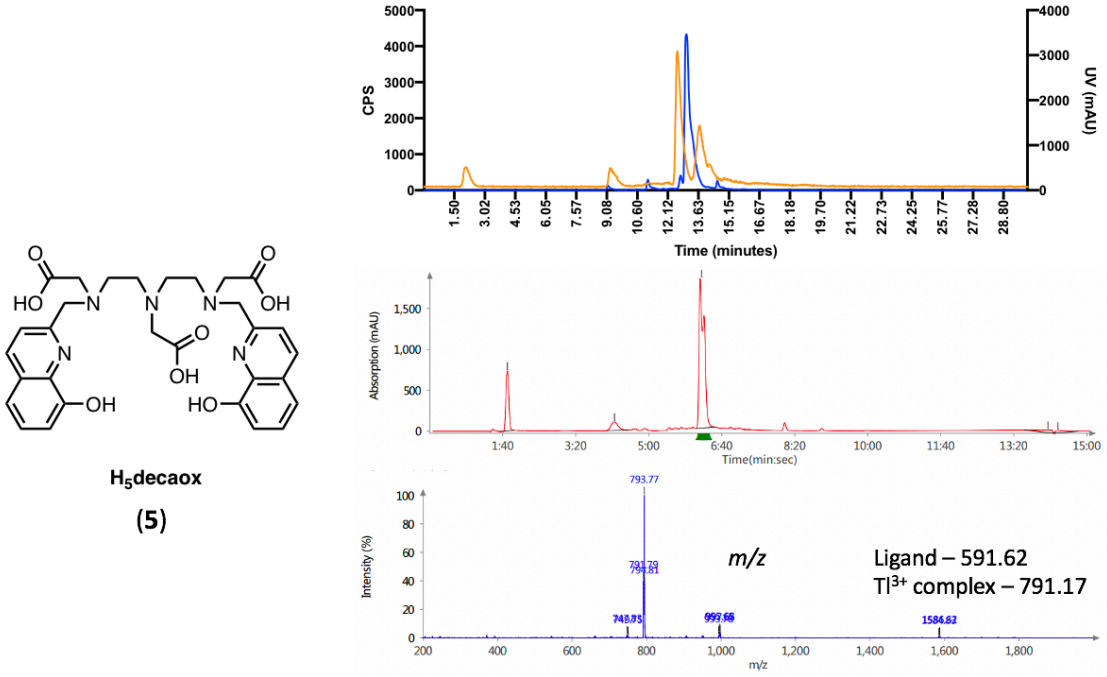

Figure 4.25 - Analytical HPLC trace of [^{201}Tl]Tl-decaox (orange = counts per second, blue = UV (ligand) (top), [^{nat}Tl]Tl-decaox UV trace from LC-MS (middle) and mass detected from LC-MS (bottom).

As with H_2noonpa, H_5decaox and [^{201}Tl]Tl^{3+} form multiple species in solution, as well as unbound [^{201}Tl]Tl^{3+}, as shown by the analytical HPLC in Figure 4.25. The LC-MS trace also shows several peaks in the UV signal, with the major peak corresponding to the mass of [^{nat}Tl]Tl-decaox.

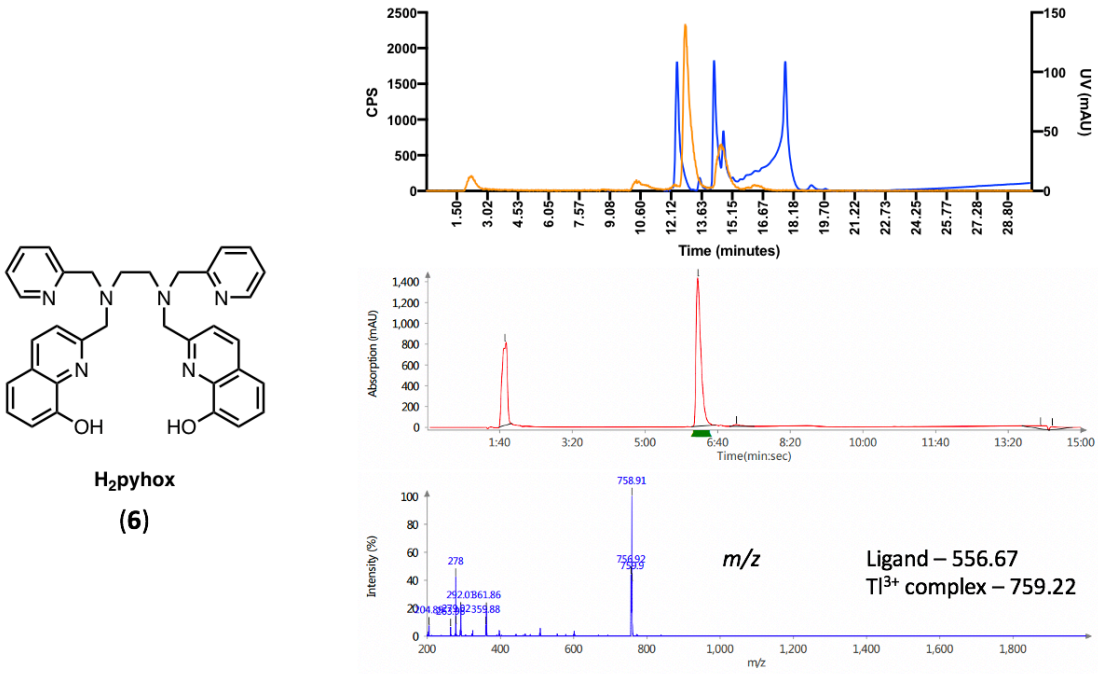

Figure 4.26 - Analytical HPLC trace of [^{201}Tl]Tl-pyhox (orange = counts per second, blue = UV (ligand) (top), [^{nat}Tl]Tl-pyhox UV trace from LC-MS (middle) and mass detected from LC-MS (bottom).

LC-MS of [^{nat}Tl]Tl-pyhox in Figure 4.26 show a UV peak at t_R = 6.22 minutes (RCY = 84%), which corresponds to the mass of the thallium complex, as well as unbound [^{nat}Tl]Tl^{3+} eluting at the solvent front at t_R = 1.46 minutes. In the radiochromatogram, several peaks are observed with the major peak at t_R = 12.9 minutes, in addition to the unbound [^{201}Tl]Tl^{3+} peak at the solvent front.

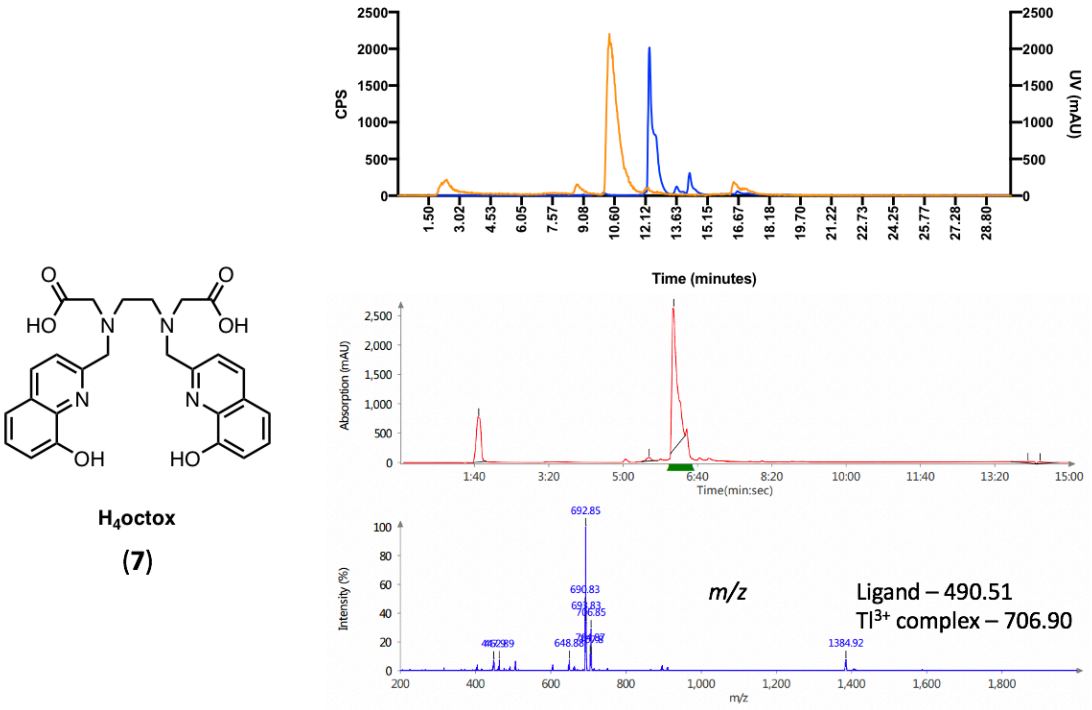

Figure 4.27 - Analytical HPLC trace of [^{201}Tl]Tl-octox (orange = counts per second, blue = UV (ligand) (top), [^{nat}Tl]Tl-octox UV trace from LC-MS (middle) and mass detected from LC-MS (bottom).

The analytical HPLC in Figure 4.27 shows a major radiopeak at t_R = 10.6 minutes (RCY = 89%), with three other small peaks in addition to unbound [^{201}Tl]Tl^{3+} at t_R = 2.03 minutes. Complexation of Tl^{3+} is supported by the LC-MS data also in Figure 4.27, showing unbound [^{nat}Tl]Tl^{3+} at the solvent front and a major peak at t_R = 6.13 minutes which mass corresponds to the mass of [^{nat}Tl]Tl-octox.

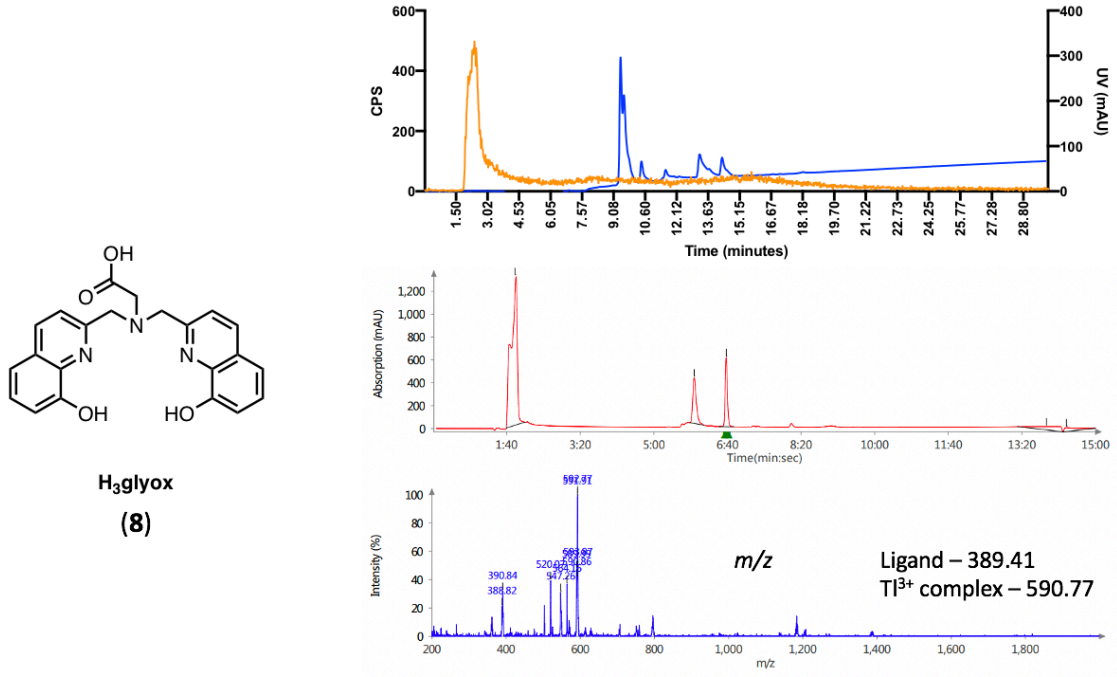

Figure 4.28 – Analytical HPLC trace of [^{201}Tl]Tl-glyox (orange = counts per second, blue = UV (ligand) (top), [^{nat}Tl]Tl-glyox UV trace from LC-MS (middle) and mass detected from LC-MS (bottom).

Radiolabelling H_3glyox with [^{201}Tl]Tl^{3+} was less successful as the radiochromatogram in Figure 4.28 shows a large unbound [^{201}Tl]Tl^{3+} peak followed by a very broad trace. The LC-MS trace also supports this with a very small peak corresponding to the [^{nat}Tl]Tl-glyox mass, but the mass of the ligand alone is also observed, highlighting minimal complexation. There is also a large peak at the solvent front corresponding the unbound [^{nat}Tl]Tl^{3+}.

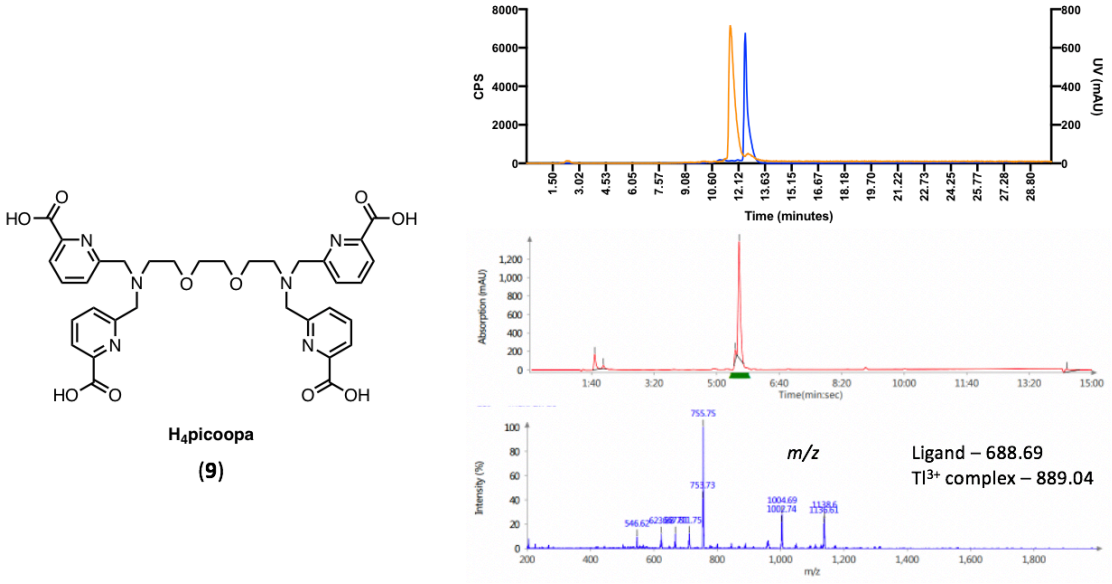

Figure 4.29 - Analytical HPLC trace of [^{201}Tl]Tl-picoopa (orange = counts per second, blue = UV (ligand) (top), [^{nat}Tl]Tl-picoopa UV trace from LC-MS (middle) and mass detected from LC-MS (bottom).

In contrast, the analytical HPLC radiochromatogram in Figure 4.29 shows no significant unbound [^{201}Tl]Tl^{3+} with a large peak observed at t_R =11.34 minutes (RCY = 98%), matching up closely with the UV trace of the ligand. However, the LC-MS data which shows one major peak, with a small amount of unbound [^{nat}Tl]Tl^{3+}, but the masses shown do not correspond to the [^{nat}Tl]Tl-picoopa complex. Further experiments using NMR and X-ray crystallography can be used to determine how [^{nat}Tl]Tl^{3+} is binding H_4picoopa.

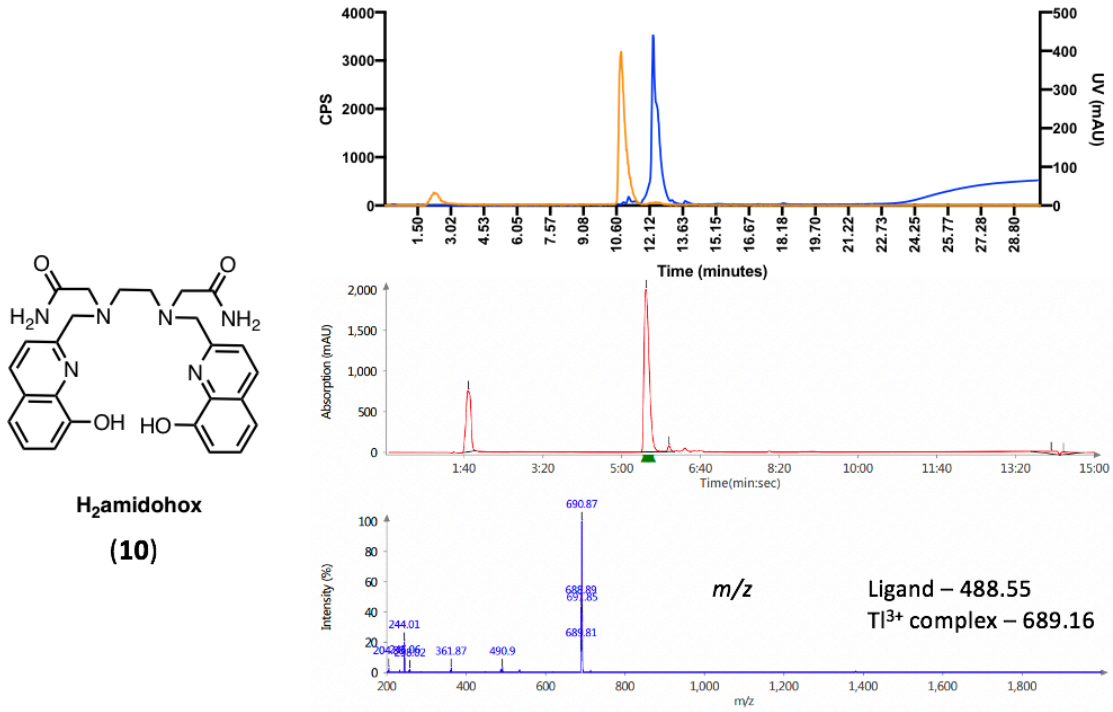

Figure 4.30 - Analytical HPLC trace of [^{201}Tl]Tl-amidohox (orange = counts per second, blue = UV (ligand) (top), [^{nat}Tl]Tl-amidohox UV trace from LC-MS (middle) and mass detected from LC-MS (bottom).

The reaction between H_2amidohox and [^{201}Tl]Tl^{3+} can be seen in Figure 4.30, showing a small unbound [^{201}Tl]Tl^{3+} peak and the large peak at t_R = 10.7 minutes, likely to correspond to [^{201}Tl]Tl-amidohox (RCY = 97%). This conclusion is supported by the LC-MS data, showing a large UV peak, as well as unbound [^{nat}Tl]Tl^{3+}, with the mass corresponding to that of [^{nat}Tl]Tl-amidohox.

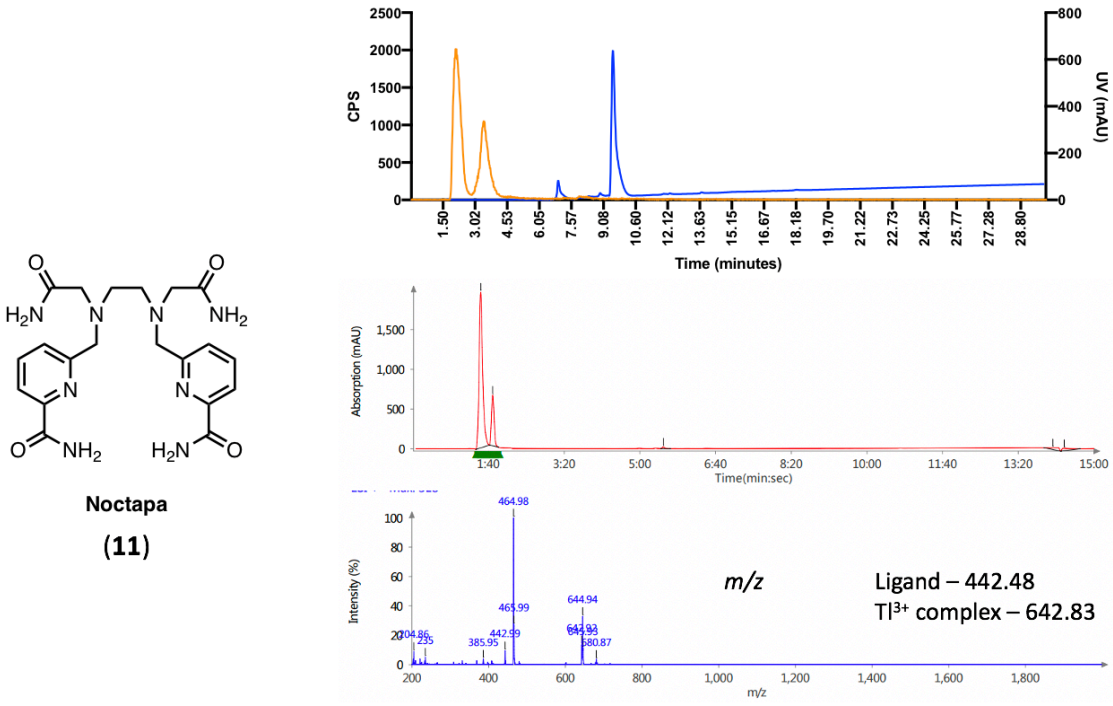

Figure 4.31 - Analytical HPLC trace of [^{201}Tl]Tl-noctapa (orange = counts per second, blue = UV (ligand) (top), [^{nat}Tl]Tl-noctapa UV trace from LC-MS (middle) and mass detected from LC-MS (bottom).

The analytical HPLC trace in Figure 4.31 shows two peaks in the radiochromatogram. The t_R = 2.03 minutes corresponds to unbound [^{201}Tl]Tl^{3+} with another peak eluting 90 seconds later, at a low radiochemical yield. This HPLC trace looks very similar to the LC-MS trace which also has two peaks. The masses of unbound [^{nat}Tl]Tl^{3+}, ligand and well as [^{201}Tl]Tl-noctapa, demonstrating complexation.

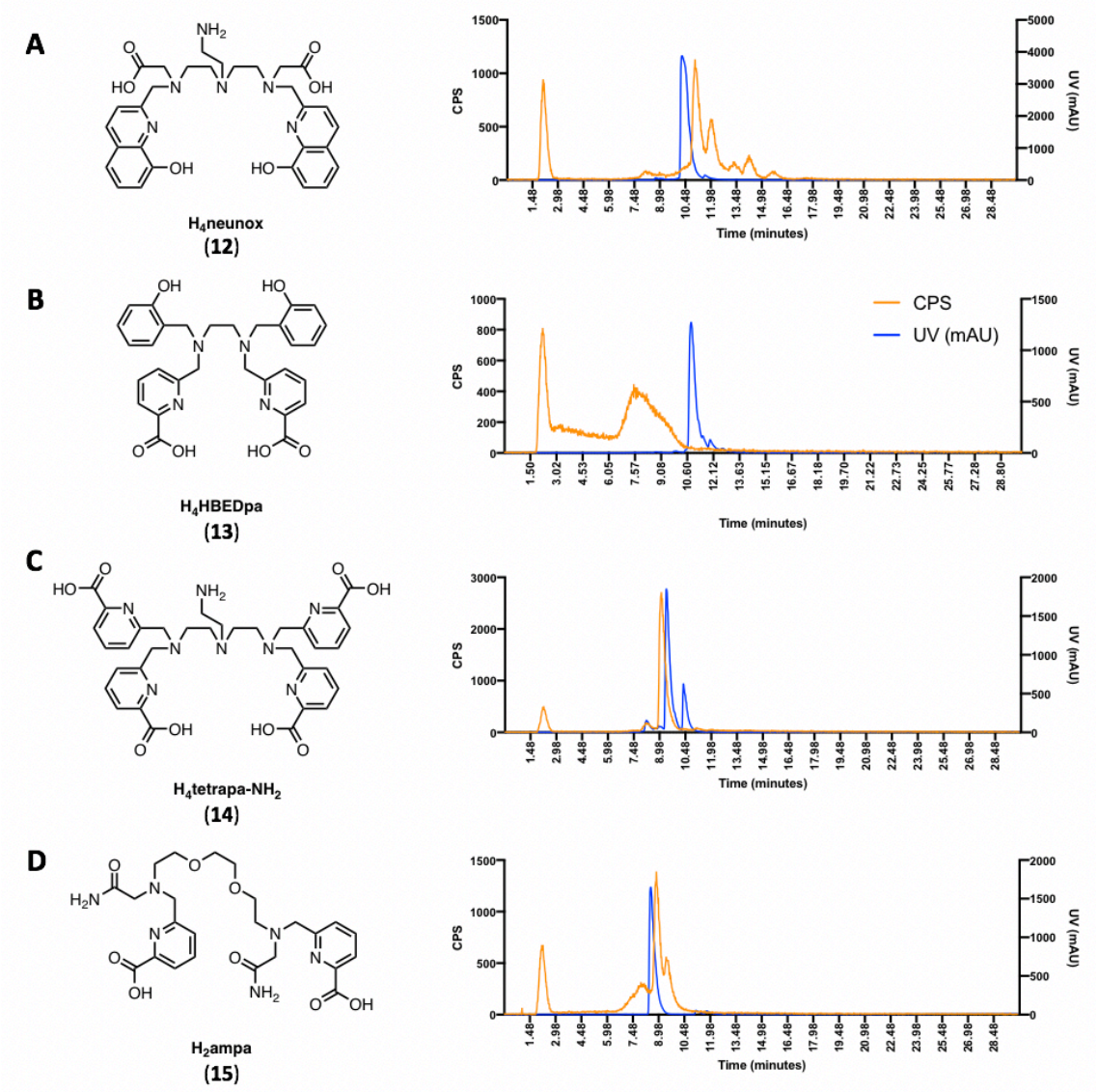

Figure 4.32 - Analytical HPLC trace of [^{201}Tl]Tl-neunox (A), [^{201}Tl]Tl-HBEDpa (B), [^{201}Tl]Tl-tetrapa-NH_2 (C) and [^{201}Tl]Tl-ampa (D) (orange = counts per second, blue = UV (ligand).

The analytical HPLC traces of the reaction between [^{201}Tl]Tl^{3+} with H_4HBEDpa, H_4tetrapa-NH_2 and H_2ampa can be seen in Figure 4.32. All four complexes show a mixture of unbound [^{201}Tl]Tl^{3+} and a mixture of species in solution. H_4tetrapa-NH_2 shows the most promise from this batch of chelators with a single major peak eluting at t_R = 9 minutes in addition to the unbound radiometal.

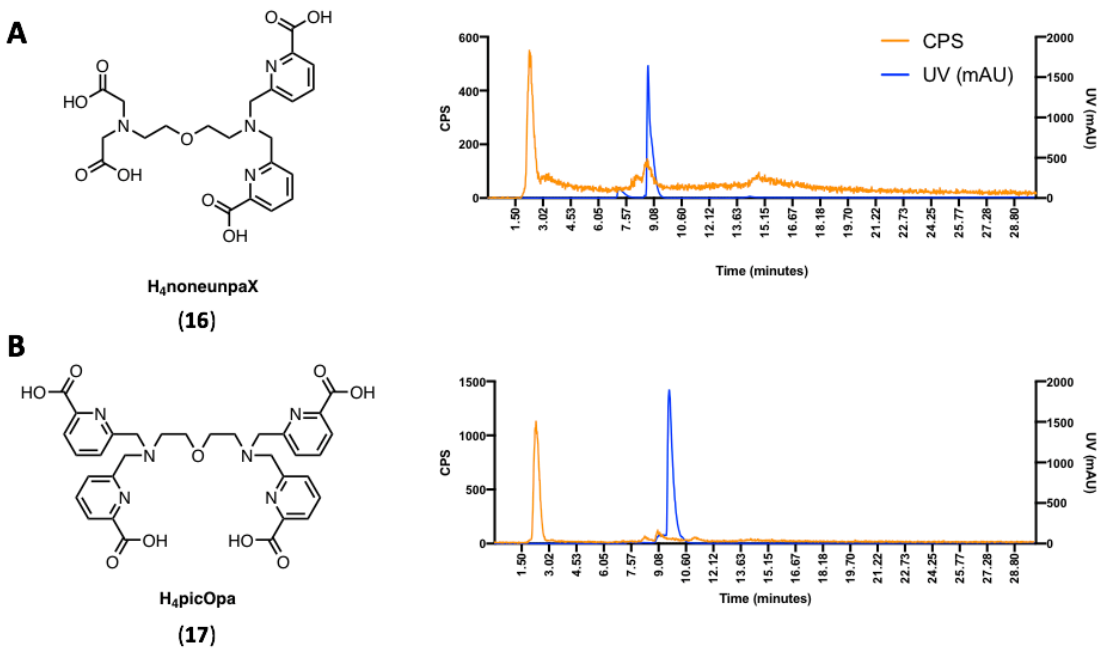

Figure 4.33 - Analytical HPLC trace of [^{201}Tl]Tl-noneunpaX (A) and [^{201}Tl]Tl-picOpa (B) (orange = counts per second, blue = UV (ligand).

The reaction between [^{201}Tl]Tl^{3+} with H_4noneunpaX and H_4picOpa was evaluated using HPLC which can be seen in Figure 4.33. The reaction with H_4noneunpaX shows the majority of the activity is unbound [^{201}Tl]Tl^{3+} followed by a broad trace with a small peak at t_R = 9.08 minutes, overlapping with the UV trace. The H_4picOpa reaction shows nearly all the activity in solution is unbound [^{201}Tl]Tl^{3+}.

Table 11 – Summary of the chelators 1-17, their coordination number and the reaction with [$^{nat/201}$Tl]Tl^{3+} (red = no Tl^{3+} complexation, orange = mixture of unbound Tl^{3+} and complexed Tl^{3+}, requires more experiments, green = complexation of Tl^{3+} at RT

Chelator	Coordination number	Chelate Tl^{3+}?
H_2amidohox (**10**) (N_6O_2)	8	✓
H_4octox (**7**) (N_4O_2)	8	✓
H_4pypa (N_5O_4)	9	✓
H_5decaox (**5**) (N_5O_5)	10	✓
H_5decapa (N_5O_5)	10	✓
H_4nenpa-NH_2 (N_5O_4)	9	✓
H_4noneunpa (N_4O_5)	11	✓
H_2amidoC3hox (**1**) (N_6O_2)	8	~
DTPAm (**4**) (N_8)	8	~
H_2pyhox (**6**) (N_6O_2)	8	~
H_5HBEDpa (**13**) (N_4O_5)	9	~
H_4neunox (**12**) (N_5O_4)	9	~
H_2ampa (**15**) (N_6O_4)	10	~
H_4tetrapa-NH_2 (**14**) (N_7O_4)	11	~
H_4picoopa (**9**) (N_6O_6)	12	~
H_3glyox (**8**) (N_3O_3)	6	✗
H_2noonpa (**3**) (N_4O_4)	8	✗
Noctapa (**11**) (N_8)	8	✗
H_4octapa (**2**) (N_4O_2)	8	✗
H_4noneunpaX (**16**) (N_4O_5)	9	✗
H_4picOpa (**17**) (N_6O_5)	11	✗

4.3.7 Additional chelators

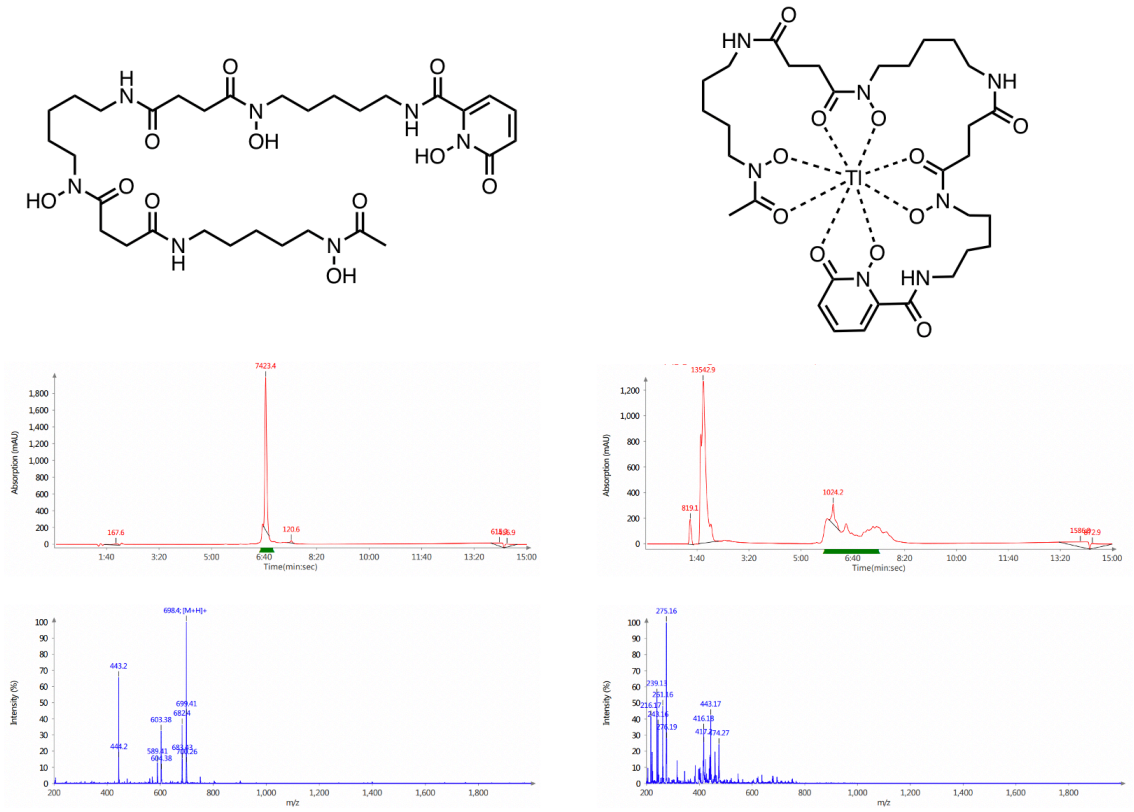

Figure 4.34 - The structure of DFO-HOPO with an LC-MS of the chelator (UV and mass signal) (left) and the proposed structure of [^{nat}Tl]Tl-DFO-HOPO with the LC-MS of the reaction (UV and mass signal) (right).

The structure of DFO-HOPO can be seen in Figure 4.34, as well as the LC-MS of the ligand alone, showing the $[M+H]^+$ mass. An LC-MS of the reaction between DFO-HOPO and [^{nat}Tl]$TlCl_3$ can be seen in Figure 4.34. However, the mass of the [^{nat}Tl]Tl-DFO-HOPO was not observed in the LC-MS.

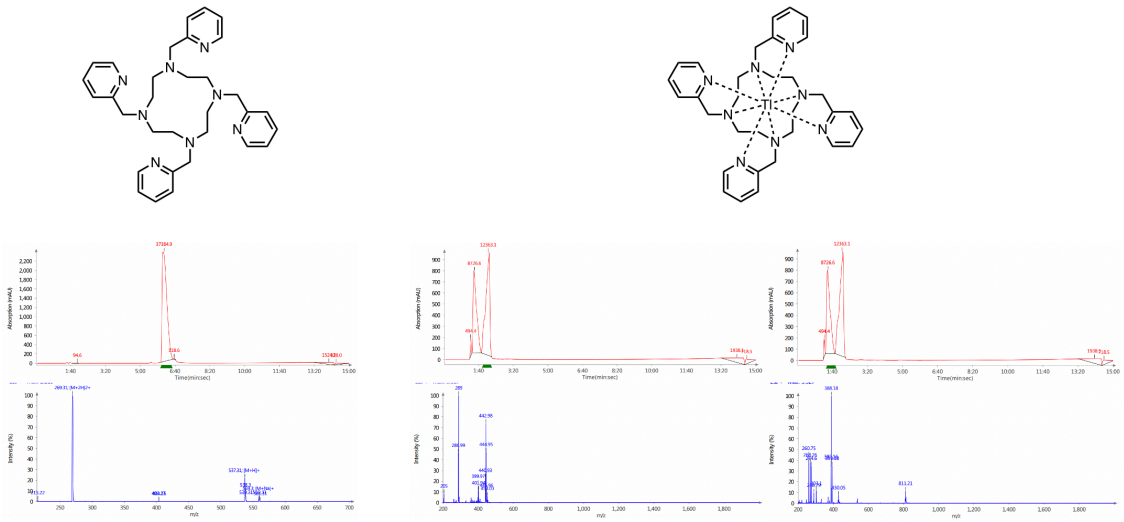

Figure 4.35 - The structure of L_{py} with an LC-MS of the chelator (UV and mass signal) (left) and the proposed structure of [^{nat}Tl]Tl-L_{py} with the LC-MS of the reaction (UV and mass signal) (right).

LC-MS results for L_{py} and its structure can be seen in Figure 4.35. An LC-MS of the ligand alone, showing the $[M+H]^+$, $[M+2H]^{2+}$ and $[M+Na]^+$ masses. An LC-MS of the reaction between L_{py} and [^{nat}Tl]$TlCl_3$ can be seen in Figure 4.35, with two major peaks observed. However, the mass of the [^{nat}Tl]Tl-L_{py} was not observed in either of peaks in the LC-MS.

4.4 Discussion

Chelation studies showed that both EDTA and DTPA form single species when chelating Tl^{3+}, while DOTA showing peak broadening in the ^{1}H NMR, similar to what has previously been published by Fodor *et al*.[162] [^{201}Tl]Tl-EDTA and [^{201}Tl]Tl-DTPA were however unstable in serum, whereas the macrocyclic chelator DOTA performed better (Figure 4.12) in this respect. As DTPA and EDTA are both acyclic chelators, with 6 and 8 donor atoms, respectively, this instability is likely due to low free energy barriers to conformational changes required to dissociate but cannot exclude reduction to Tl^{+}. The complexes are thermodynamically favourable and quick to form but not kinetically stable. These results conflict with claims in previous studies that [^{201}Tl]Tl-DTPA-HIgG, is stable in human serum for more than 24 hour.[165] Jalilian *et al* who report this stable [^{201}Tl]Tl-DTPA complex use the TLC method shown in Figure 4.10, where unchelated metal has the same retention factor as complexed metal. This may have led the authors to think the complex is more stable than it actually is if the correct controls were not used. Additionally, the chelator for Tl^{3+} needs to protect the metal from external reducing agents to prevent reduction back to Tl^{+}, where this will not be required for In^{3+} or Bi^{3+} as they are not affected by the IPE.

[^{201}Tl]Tl-DOTA on the other hand required longer for the complex to initially form than [^{201}Tl]Tl-EDTA and [^{201}Tl]Tl-DTPA . A crystal structure of [^{nat}Tl]Tl-DOTA obtained by Fodor *et al* shows the metal sitting above the cyclen ring. The crystal structure they obtained of the complex showed the thallium ion directly coordinated to the eight donor atoms in a twisted square antiprismatic (TSAP) coordination and previous work has indicated that DOTA does indeed enable more stable chelation of [^{201}Tl]Tl^{3+} than DTPA, at least *in vitro.*[161,162] As such, DOTA looks a more promising chelator of [^{201}Tl]Tl^{3+} for MRT than DTPA or EDTA, but it still is far from ideal as it lacks adequate kinetic stability in biological media.

None of the chelators evaluated are ideal in all respects, and therefore this work represents only a step on the path towards the goal of a stable Tl^{3+} chelator for radiopharmaceutical application. It is essential for these chelators for Tl^{3+} to protect the metal from reducing agents, preventing reduction back to Tl^{+}. However, it is clear from these results that none of the chelators evaluated are up to a high enough standard to prevent the reduction of Tl^{3+} to Tl^{+}, but they are a significant step forward.

From the results of the Orvig chelators (**1**-**17**), Tl^{3+} appears to have a preference for higher dentate chelators (> 9), as highlighted in the summary of the results Table 11. The majority of the more successful chelators have a di-nitrogen or tri-nitrogen backbone, with a either oxine or picolinic acid donor groups in combination with carboxylate arms. The exceptions are H_2amidohox (which has primary amine donor in place of carboxylate arms) and H_4noneunpa (which has a nitrogen-oxygen-nitrogen backbone). The results using DFO-HOPO and L_{py} suggest that using pyridine donors and hydroxamic acid residues are not advantageous for use with Tl^{3+}.

The stability of [^{201}Tl]Tl-EDTA, [^{201}Tl]Tl-DTPA and [^{201}Tl]Tl-DOTA have been assessed and shown to be inadequate for use as a targeted radiopharmaceutical. As previously stated, the chelators evaluated have been shown to be far from ideal as a chelator for Tl^{3+}, and hence this work represents a step forwards towards finding a stable Tl^{3+} chelator for radiopharmaceutical application. From the chelators tested, H_4pypa can quantitatively radiolabel ^{201}Tl very quickly (less than 15 minutes) at RT and under mild conditions. The non-radioactive [^{nat}Tl]Tl-pypa has been thoroughly evaluated using HR-ESI-MS, NMR and X-ray crystallography, helping to shed more light on the coordination chemistry of thallium. A number of other chelators developed by the Orvig group have shown good radiolabelling kinetics with [$^{nat/201}$Tl]Tl^{3+}, for example H_4noneunpa, H_5decapa and H_4neunpa-NH_2, which will require further investigation. From these

studies, it can be hypothesised that the ideal chelator for Tl^{3+} will have a tri-nitrogen backbone, contain oxygen donor groups and have a large number of donors (> 9).

4.5 Conclusions

One conclusion is that as well as stabilising the Tl complex against simple dissociation, the chelator must also protect against reduction. It is clear from this data that the chelators evaluated do not substantially protect against reduction. Moving forwards, when designing a new chelator for Tl^{3+}, encapsulating the metal within the chelator and saturating the coordination sphere to prevent the donation of electrons from reducing agents. In the future, combining the biological stability assays described in this chapter with cyclic voltammetry would be useful to evaluate if there is a trend between *in vitro* stability and reduction potential of the Tl^{3+} complexes.

5 DEVELOPMENT OF A PROSTATE SPECIFIC MEMBRANE ANTIGEN TARGETTING RADIOPHARMACEUTICAL

5.1 Introduction

Building upon some of the data described in Chapter 4, where the stability of [^{201}Tl]Tl-DOTA and [^{201}Tl]Tl-pypa were evaluated, this chapter will describe work to create PSMA targeting radiopharmaceuticals using chelators DOTA and H_4pypa.

Previous research using [^{nat}Tl]Tl^{3+} and DOTA has shown that all four carboxylate arms are needed to fully coordinate thallium.[162] The PSMA targeted bioconjugates were pursued, with their structure being based on that of PSMA-617. However, DOTA in PSMA-617 only has three carboxylate arms available for coordination, as the fourth arm has been used for conjugation to the linker and PSMA targeting moiety (Figure 1.8). Hence there is a need to develop a modified version where all four arms are available for coordination. An alternative version of DOTA, bearing an isothiocyanate group off a prosthetic group from one of the ethylene backbones of the cyclen ring is commercially available from Macrocyclics Ltd for bioconjugation reactions.

In order to deliver ^{201}Tl to PSMA expressing cells, an isothiocyanate version of DOTA allowing all four carboxylate arms to bind Tl^{3+} was needed to allow it to be coupled to a PSMA targeting vector, via a linker molecule. The C7 linker used here has been chosen due to the desirable characteristics of PSMA-617 *in vivo*.[243] Structure-activity relationships (SARs) of several PSMA targeting variants have demonstrated the significant role that linker design can have on the pharmacokinetic profile of a tracer; the combination of 2-naphthyl-D-alanine and trans-(aminomethyl)-cyclohexanecarboxylic acid led to faster renal clearance (Scheme 1).[243] Additionally, the lipophilic linker helps with binding to

the hydrophobic PSMA pocket, leading to a high tumour to background ratio, due to having high affinity.[243] Both of these attributes are essential for a radiotherapeutic drug to minimise damage to the excretion pathway, and enable high uptake to ensure maximum damage to tumour cells.

As described in Chapter 4, H_4pypa has been utilised for targeting the PSMA and conjugated to an antibody in the literature. The authors have synthesised an isothiocyanate (NCS) version of H_4pypa in order to conjugate the chelator to a targeting moiety. The encouraging stability data in Chapter 4 for [^{201}Tl]Tl-pypa, lays the foundation to build upon using a bioconjugate of H_4pypa targeted to PSMA. A description of biological targets can be found in Chapter 1, and stability followed by the slow degradation of both the [^{201}Tl]Tl-DOTA and [^{201}Tl]Tl-pypa complexes (more so for [^{201}Tl]Tl-DOTA) fits the biological half-life of small peptides.

Li *et al* synthesised a PSMA targeting H_4pypa bioconjugate (Figure 5.1) and performed SPECT imaging studies in NODSCID ILRgammaKO male mice bearing LNCaP tumours using both ^{111}In and ^{177}Lu.[214] The *ex vivo* biodistribution showed that the tracers were renally excreted, with fast blood clearances. There was low non-specific organ and tissue uptake, with high accumulation in PSMA expressing tissues like the kidneys, spleen and tumour. At 4 hours post injection there was 60 % higher tumour uptake of [^{177}Lu]Lu-pypa-C7-PSMA617 when compared to [^{177}Lu]Lu-PSMA-617.[244]

Further *in vivo* studies using [^{44}Sc]Sc-pypa-C7-PSMA617 (Figure 5.1) in nude male mice bearing a PC3-PIP (PSMA positive) tumour on the left shoulder and a PC3-FLU (PSMA negative) tumour on the right shoulder were performed. As with the ^{111}In and ^{177}Lu tracers, the ^{44}Sc labelled H_4pypa-C7-PSMA617 was renally excreted and there was PSMA specific accumulation in tissue. The authors investigated the effect of molar activity on the pharmacokinetics of the tracer and report that the lower molar activity (7.4 GBq/µmol) had a substantially increased tumour to background ratio compared to the higher molar activity (74 GBq/µmol).

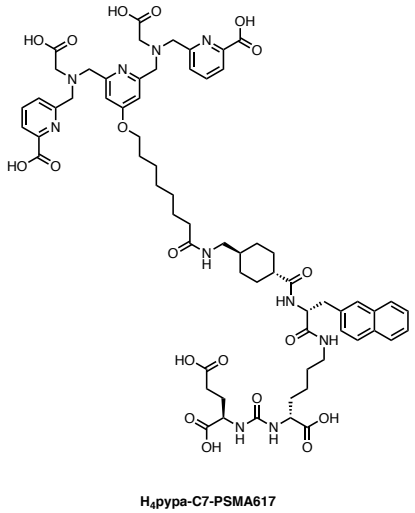

Figure 5.1 – Structure of the PSMA targeting bioconjugate H_4pypa-C7-PSMA617[214,215]

The use of small peptides to target PSMA on prostate cancer cells was chosen as an initial proof of concept to validate the use of ^{201}Tl for MRT. PSMA peptides have been thoroughly investigated in the literature, and mouse models are well-established using a number of PSMA expressing cell lines, including DU145 PSMA positive and PSMA negative. This method has previously used to successfully demonstrate specificity of compounds for PSMA.[182] The aim of using an entrenched model like this limits the number of variables, allowing the basics of probing a new probe to be investigated. The purpose of these experiments is to firstly find a chelator that can form a kinetically stable complex with Tl^{3+}. Secondly, it is to see if it is possible to deliver the radiometal to the PSMA biological target, using a BFC, and assess accumulation in target tissue. Finally, if the first two points are successful, to assess the effectiveness of the radiopharmaceutical against prostate cancer cells.

In this chapter, we describe investigation of use of DOTA with ^{111}In and ^{201}Tl. Additionally, for the first time, H_4pypa, and the potential utility of PSMA bioconjugates of these chelates for targeting prostate cancer was tested in DU145 PSMA positive and negative cells in *in vivo* xenograft models.

5.2 Material and methods

Chemicals, radioactivity and equipment used are identical to what has previously been described in Chapter 4. Unless stated otherwise, chemicals and solvents were purchased from commercial suppliers (Merck, Fisher Scientific, Fluorochem). High Resolution Electrospray Mass Spectrometry was carried out by Dr Lisa Haigh of the mass spectrometry service at Imperial College. Crystallographic data were collected using an Agilent Xcalibur PX Ultra A diffractometer, and the structures were refined using the SHELXTL[245] and SHELX-2013[246] program systems. Radioactive samples were measured using a Capintec CRC25R or an LKB Wallac 1282 Compugamma CS for which data were collected using EdenTerm software. SPECT/CT images were acquired using a NanoSPECT/CT scanner (Mediso Ltd., Budapest, Hungary), with 1.3 mm pinhole collimators, and with two energy windows at 72.3keV ± 10% and 140.51keV ± 10%. Images were reconstructed using the software package HiSPECT (ScivisGmbH) and images were analysed using VivoQuant software (version 3.5, InviCRO Inc.).

Synthesis

Di-tert-butyl (1H-imidazole-1-carbonyl)glutamate (**1**)

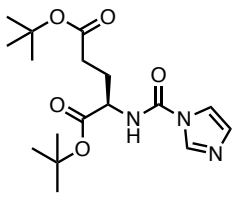

1

1 was synthesised using a method previously reported by Duspara et al.[247] L-glutamic acid di-tert-butyl hydrochloride (3.56 g, 12.04 mmol) and carbonyldiimidazole (2.15 g, 13.24 mmol) were dissolved in a 1:5 mixture of DMF/MeCN (50 mL) and stirred at RT overnight. MeCN was then removed in vacuo and the remaining DMF diluted with EtOAc (100 mL) was washed with water (3 x 50 mL) and brine (3 x 50 mL). The organic layer was then dried over magnesium sulfate and the solvent removed in vacuo. Crude product was then purified using a Biotage Isolera flash chromatography system (20-80% EtOAc:pet ether) to yield the desired product as a colourless oil which solidified upon standing. (2.1 g, 51%). ^{1}H NMR (400 MHz, Chloroform-d) δ 8.16 (t, J = 1.1 Hz, 1H), 7.57 (d, J = 6.8 Hz, 1H), 7.41 (t, J = 1.5 Hz, 1H), 7.07 (dd, J = 1.6, 0.9 Hz, 1H), 2.48 – 2.38 (m, 2H), 2.27 – 2.05 (m, 2H), 1.47 (s, 9H, 1 x ^{t}Butyl), 1.43 (s, 9H, 1 x ^{t}Butyl). ^{13}C NMR (101 MHz, Chloroform-d) δ 174.0, 173.5, 173.3, 171.7, 162.8, 157.4, 149.1, 136.2, 135.2, 123.0, 121.7, 116.4, 77.4, 77.1, 76.8, 53.5, 52.7, 52.5, 52.4, 52.4, 52.1, 51.8, 51.8, 36.6, 31.5, 30.3, 30.1, 28.0, 27.9, 27.8, 26.2. ESI-MS: calc for $[C_{17}H_{27}N_3O_5 + H]^+$ 354.42 found 354.35.

Tri-tert-butyl 3,11-dioxo-1-phenyl-2-oxa-4,10,12-triazapentadecane-9,13,15-tricarboxylate (**2**)

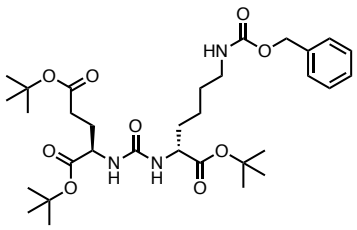

2

2 was synthesised by adapting a previously reported method by Duspara et al.[247] H-Lys(Z)-OtBu.HCl (3.47 g, 9.34 mmol) was dissolved in DMF (20 mL). DIPEA (1.63 mL, 9.34 mmol) was added to the reaction, followed by **1** (3 g, 8.49 mmol) (dissolved in 10 mL DMF) dropwise and allowed to stir overnight at RT. The reaction was diluted with EtOAc (100 mL) washed with water (3 x 100 mL) and brine (3 x 100 mL). The organic layer was then dried over magnesium sulfate and the solvent removed in vacuo. Crude product was then purified using a Biotage Isolera flash chromatography system (20-80% EtOAc:petroleum ether) to yield the desired product as a colourless oil. (4.5 g, 83%) ^{1}H NMR (400 MHz, Chloroform-d) δ 7.38 – 7.30 (m, 5H, Ar-H), 5.22 – 5.02 (m, 4H), 4.33 (dd, J = 8.1, 4.9 Hz, 2H), 3.17 (dd, J = 6.4, 3.7 Hz, 2H), 2.28 (td, J = 9.6, 6.4 Hz, 2H), 1.44 (d, J = 1.1 Hz, 18H, 2 x ^{t}Butyl), 1.43 (s, 9H, 1 x ^{t}Butyl). ^{13}C NMR (101 MHz, Chloroform-d) δ 172.4, 156.9, 156.6, 136.7, 128.5, 128.1, 128.0, 82.1, 81.8, 80.5, 77.3, 77.0, 76.7, 66.6, 53.3, 53.0, 40.7, 32.7, 31.6, 29.4, 28.4, 28.1, 28.0, 28.0, 22.2. ESI-MS: calc for $[C_{32}H_{51}N_3O_9 + H]^+$ 622.36 found 622.3.

Di-tert-butyl ((6-amino-1-(tert-butoxy)-1-oxohexan-2-yl)carbamoyl)glutamate (**3**)

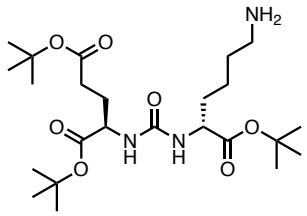

3

The cbz protected urea **2** (3.6 g, 5.79 mmol) was dissolved in methanol (20 mL) and added to Pd/C (10%) (0.125 g, 1.16 mmol). The reaction flask was evacuated before being flushed with two balloons of hydrogen gas and a third balloon left in the vessel for the duration of the experiment. TLC analysis of the reaction showed completion after 90 minutes. The Pd/C was removed via filtration through Celite and the solvent removed in vacuo, to yield colourless oil. This was then purified using a Biotage Isolera flash chromatography system (reverse phase SFar C18 column, 0-60% MeCN/0.1% FA:H_2O/0.1% FA) to yield the desired product as a colourless oil which solidified under vacuum. (2.62 g, 92%). ^{1}H NMR (400 MHz, Chloroform-d) δ 6.37 (d, J = 8.1 Hz, 1H), 6.23 (d, J = 8.0 Hz, 1H), 4.31 (s, 2H), 2.98 (s, 2H), 2.32 (dd, J = 6.5, 3.2 Hz, 2H), 1.71 (s, 4H), 1.44 (d, J = 1.8 Hz, 18H, 2 x ^{t}Butyl), 1.43 (s, 9H, 1 x ^{t}Butyl). ^{13}C NMR (101 MHz, Chloroform-d) δ 173.6, 172.8, 172.4, 157.7, 82.1, 81.5, 80.5, 77.3, 77.0, 76.7, 53.1, 52.9, 39.2, 31.8, 31.3, 28.1, 28.0, 27.2, 21.7. ESI-MS: calc for $[C_{24}H_{45}N_3O_7 + H]^+$ 488.64 found 488.45.

Di-tert-butyl ((6-(2-(((benzyloxy)carbonyl)amino)-3-(naphthalen-2-yl)propanamido)-1-(tert-butoxy)-1-oxohexan-2-yl)carbamoyl)glutamate (**4**)

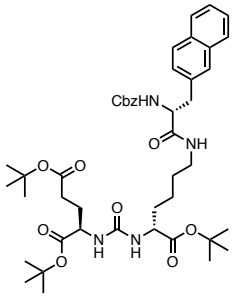

4

Z-3-(2-naphthyl)-D-alanine (0.395 g, 1.13 mmol) and HATU (0.858 g, 2.26 mmol) were dissolved in dry DMF (10 mL), followed by the addition of DIPEA (0.54 mL, 3.08 mmol) with the solution turning from colourless to yellow. This was left to stir for 15 minutes at RT, after which **3** (0.5 g, 1.03 mmol), dissolved in dry DMF (5 mL), was added to the stirring solution and left at RT to stir overnight. During this time the reaction had turned dark brown in colour. The reaction was diluted with EtOAc (100 mL) washed with water (3 x 50 mL) and brine (3 x 50 mL). The organic layer was then dried over magnesium sulfate and the solvent removed in vacuo. Crude product was then purified using a Biotage Isolera flash chromatography system (20-70% EtOAc:pet ether) to yield the desired product as a yellow oil (0.46 g, 55%). ^{1}H NMR (400 MHz, Chloroform-d) δ 7.83 (s, 3H), 7.77 (s, 1H), 7.71 (d, J = 8.2 Hz, 3H), 7.66 (s, 2H), 7.59 (d, J = 10.9 Hz, 3H), 7.51 – 7.33 (m, 4H), 7.27 (d, J = 11.8 Hz, 4H), 7.22 – 7.11 (m, 1H), 5.09 (s, 5H), 4.96 (d, J = 13.0 Hz, 1H), 4.35 (s, 1H), 4.12 (q, J = 7.1 Hz, 1H), 3.43 (s, 1H), 3.23 (s, 1H), 3.19 – 3.03 (m, 1H), 3.03 – 2.73 (m, 1H), 1.93 – 1.64 (m, 2H), 1.44 (d, J = 2.5 Hz, 18H, 2 x ^{t}Butyl), 1.41 (s, 9H, 1 x ^{t}Butyl). ^{13}C NMR (101 MHz, Chloroform-d) δ 133.5, 132.4, 128.5, 128.3, 128.1, 127.7, 126.2, 80.6, 77.3, 77.0, 76.7, 60.4, 53.4, 53.1, 31.8, 28.1, 28.0, 21.0, 14.2. HR-ESI-MS: calc for $[C_{45}H_{62}N_4O_{10} + H]^+$ 819.4544 found 819.4550.

Di-tert-butyl ((6-(2-amino-3-(naphthalen-2-yl)propanamido)-1-(tert-butoxy)-1-oxohexan-2-yl)carbamoyl)glutamate (**5**)

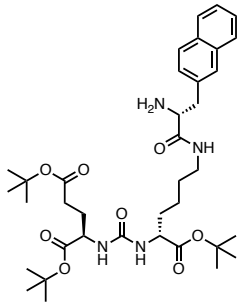

5

4 (0.185 g, 0.24 mmol) was dissolved in methanol (10 mL) and added to Pd/C (10%) (0.007 g, 0.05 mmol). The reaction flask was evacuated before being flushed with two balloons of hydrogen gas and a third balloon left in the vessel for the duration of the experiment. TLC analysis of the reaction showed completion after stirring overnight. The Pd/C was removed via filtration through Celite and the solvent removed in vacuo, to yield a pale-yellow oil (0.149 g, 89%). ^{1}H NMR (400 MHz, Chloroform-d) δ 7.84 – 7.73 (m, 3H), 7.67 (s, 1H), 7.57 (s, 1H), 7.47 – 7.41 (m, 2H), 7.35 (d, J = 8.2 Hz, 1H), 4.29 (s, 1H), 4.19 (s, 2H), 3.32 (s, 1H), 3.20 (s, 1H), 3.08 (s, 2H), 2.38 – 2.19 (m, 2H), 2.13 – 1.95 (m, 1H), 1.91 – 1.78 (m, 1H), 1.74 (t, J = 3.3 Hz, 2H), 1.41 (s, 9H, 1 x ^{t}Butyl), 1.40 (d, J = 1.6 Hz, 18H, 2 x ^{t}Butyl). ^{13}C NMR (101 MHz, Chloroform-d) δ 172.9, 172.8, 172.5, 170.7, 157.4, 133.4, 133.2, 132.5, 128.5, 128.4, 127.7, 127.6, 127.3, 126.3, 125.9, 82.1, 81.6, 80.6, 77.4, 77.0, 76.7, 55.4, 53.4, 53.0, 39.0, 38.7, 31.7, 28.6, 28.3, 28.1, 28.0, 22.0. HR-ESI-MS: calc for $[C_{37}H_{56}N_4O_8 + H]^+$ 685.4176 found 685.4188.

Di-tert-butyl ((6-(2-(4-((((benzyloxy)carbonyl)amino)methyl)cyclohexane-1-carboxamido)-3-(naphthalen-2-yl)propanamido)-1-(tert-butoxy)-1-oxohexan-2-yl)carbamoyl)glutamate (**6**)

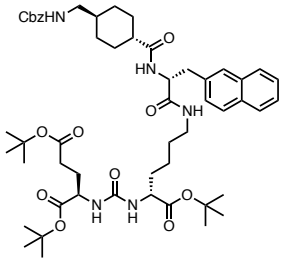

6

Trans-4-(cbz-amino)cyclohexanecarboxylic acid (0.153 g, 0.53 mmol) and HATU (0.852 g, 1.1 mmol) were dissolved in dry DMF, followed by the addition of DIPEA (0.16 mL, 1.56 mmol) with the solution turning from colourless to yellow. This was left to stir for 15 minutes at RT, after which **5** (0.3 g, 0.44 mmol), dissolved in dry DMF (5 mL), was added dropwise to a stirring reaction and left to stir overnight. During this time the reaction had turned dark brown in colour. The reaction was diluted with EtOAc (100 mL) washed with water (3 x 50 mL) and brine (3 x 50 mL). The organic layer was then dried over magnesium sulfate and the solvent removed in vacuo. Crude product was then purified using a Biotage Isolera flash chromatography system (20-70% EtOAc:pet ether) to yield the desired product as a yellow oil (0.24 g, 63%). ^{1}H NMR (400 MHz, Chloroform-d) δ 7.89 – 7.78 (m, 1H), 7.73 (t, J = 6.9 Hz, 2H), 7.63 (d, J = 1.6 Hz, 1H), 7.52 – 7.42 (m, 2H), 7.34 (d, J = 4.6 Hz, 6H), 5.26 (d, J = 7.7 Hz, 1H), 5.20 (d, J = 8.3 Hz, 1H), 4.90 (s, 1H), 4.71 (d, J = 7.4 Hz, 1H), 4.37 – 4.26 (m, 1H), 4.14 (q, J = 4.1 Hz, 1H), 3.39 – 3.26 (m, 1H), 3.20 (d, J = 6.4 Hz, 1H), 3.17 – 3.07 (m, 4H), 3.02 (t, J = 6.4 Hz, 2H), 2.32 (td, J = 9.5, 6.4 Hz, 2H), 2.06 (tdd, J = 11.3, 5.2, 3.1 Hz, 2H), 1.89 – 1.72 (m, 8H), 1.70 – 1.61 (m, 2H), 1.44 (d, J = 1.5 Hz, 18H, 2 x ^{t}Butyl), 1.42 (s, 9H, 1 x ^{t}Butyl). ^{13}C NMR (101 MHz, Chloroform-d) δ 175.8, 172.8, 172.5, 172.5, 171.5, 157.0, 136.6, 134.5, 133.4, 132.3, 128.5, 128.1, 127.6, 126.2, 125.8, 82.1, 81.5, 80.6, 77.3,

77.0, 76.7, 66.7, 54.8, 53.2, 52.9, 45.0, 39.2, 38.4, 37.6, 31.8, 31.7, 29.7, 28.9, 28.7, 28.6, 28.5, 28.1, 28.0, 21.9. HR-ESI-MS: calc for $[C_{53}H_{75}N_5O_{11} + H]^+$ 958.5541 found 958.5559.

Di-tert-butyl ((6-(2-(4-(aminomethyl)cyclohexane-1-carboxamido)-3-(naphthalen-2-yl)propanamido)-1-(tert-butoxy)-1-oxohexan-2-yl)carbamoyl)glutamate (**7**)

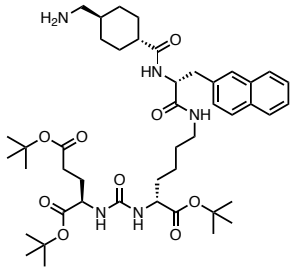

7

6 (0.081 g, 0.83 mmol) was dissolved in dry MeOH (10 mL) and Pd/C (10%) (0.003 g, 0.016 mmol) added. The reaction flask was evacuated before being flushed with two balloons of hydrogen gas and a third balloon left in the vessel for the duration of the experiment. TLC analysis of the reaction showed completion after stirring overnight. The Pd/C was removed via filtration through Celite and the solvent removed in vacuo, to yield 7 as a yellow oil. (0.062 g, 91%). ^{1}H NMR (400 MHz, Chloroform-d) δ 7.74 (dd, J = 16.2, 8.7 Hz, 3H), 7.65 (s, 1H), 7.42 – 7.31 (m, 3H), 5.75 (d, J = 18.6 Hz, 2H), 4.74 (s, 1H), 4.28 (d, J = 6.6 Hz, 1H), 4.08 (d, J = 6.4 Hz, 2H), 3.17 (d, J = 10.3 Hz, 2H), 3.06 (s, 2H), 2.72 (s, 3H), 2.31 (q, J = 7.0, 6.3 Hz, 3H), 2.16 – 1.98 (m, 4H), 1.92 – 1.81 (m, 2H), 1.69 (s, 4H), 1.43 (d, J = 1.7 Hz, 18H, 2 x ^{t}Butyl), 1.41 (s, 9H, 1 x ^{t}Butyl). HR-ESI-MS: calc for $[C_{45}H_{69}N_5O_9 + H]^+$ 824.5168 found 824.5174.

2,2',2'',2'''-(2-(4-(3-((4-((7,11-bis(tert-butoxycarbonyl)-2,2-dimethyl-19-(naphthalen-2-yl)-4,9,17-trioxo-3-oxa-8,10,16-triazanonadecan-18-yl)carbamoyl)cyclohexyl)methyl)thioureido)benzyl)-1,4,7,10-tetraazacyclododecane-1,4,7,10-tetrayl)tetraacetic acid (**8**)

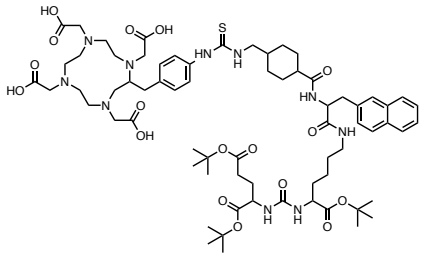

DOTA-NCS (Macrocyclics Ltd) (0.011 g, 18.2 µmol) was dissolved in $CHCl_3$ (1 mL) as was **7** (0.015 g, 18.32 µmol) separately dissolved in $CHCl_3$ (1 mL) to which triethylamine (2 x 5 µL, 35 µmol) was added to each solution. This was allowed to stir at RT overnight, after which the $CHCl_3$ was removed in vacuo. This was then purified using reverse phase semiprep HPLC (A: MeCN/0.1% TFA, B: H_2O/0.1% TFA, 5-80% A over 60 minutes, 4 mL/min). UV active fractions were analysed using LC-MS (HPLC method B), pure fractions were combined and freeze dried to yield the product as a white solid. (0.015 g, 60%) HR-ESI-MS: calc for $[C_{69}H_{103}N_{10}O_{17}S + H]^+$ 1375.7223 found 1375.7246.

((1-carboxy-5-(3-(naphthalen-2-yl)-2-(4-((3-(4-((1,4,7,10-tetrakis(carboxymethyl)-1,4,7,10-tetraazacyclododecan-2-yl)methyl)phenyl)thioureido)methyl)cyclohexane-1-carboxamido)propanamido)pentyl)carbamoyl)glutamic acid (**9**)

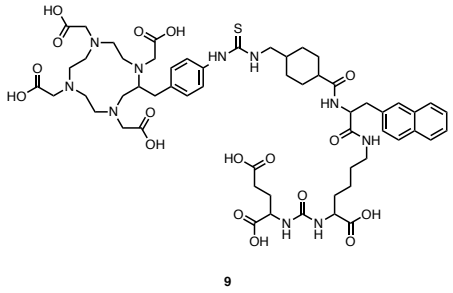

9

8 (0.005 g, 10.9 µmol) was dissolved in DCM/TFA (1:1) (4 mL) and allowed to stir at RT overnight. The reaction was then concentrated in vacuo, redissolved in deionised water and purified using reverse phase semiprep HPLC (A: MeCN/0.1% TFA, B: H_2O/0.1% TFA, 5-80% A over 60 minutes, 4 mL/min). UV active fractions were analysed using LC-MS (HPLC method B), pure fractions were combined and freeze dried to yield the product as a white solid. (0.004 g, 72%). HR-ESI-MS: calc for $[C_{57}H_{79}N_{10}O_{17}S + H]^+$ 1207.5345 found 1207.5377.

*2,2',2'',2'''-(2-(4-(3-(6-(tert-butoxy)-5-(3-(1,5-di-tert-butoxy-1,5-dioxopentan-2-yl)ureido)-6-oxohexyl)thioureido)benzyl)-1,4,7,10-tetraazacyclododecane-1,4,7,10-tetrayl)tetraacetic acid (***10***)*

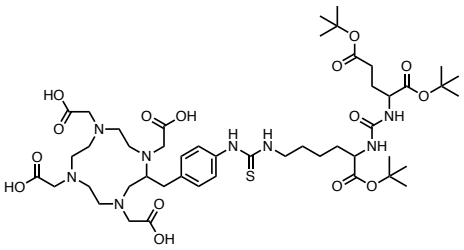

10

DOTA-NCS (Macrocyclics Ltd) (0.005 g, 10.2 µmol) was dissolved in $CHCl_3$ (1 mL) as was **3** (0.006 g, 10.2 µmol) separately dissolved in $CHCl_3$ (1 mL) to which triethylamine (2 x 20 µL, 41 µmol) was added to each solution. This was allowed to stir at RT overnight, after which the $CHCl_3$ was removed in vacuo. This was then purified using reverse phase semiprep HPLC (A: MeCN/0.1% TFA, B: H_2O/0.1% TFA, 5-80% A over 60 minutes, 4 mL/min). UV active fractions were analysed using LC-MS (HPLC method B), pure fractions were combined and freeze dried to yield the product as a white solid. (0.06 g, 62%) HR-ESI-MS: calc for $[C_{48}H_{78}N_8O_{15}S + H]^+$ 1039.53 found 1039.51.

*((1-carboxy-5-(3-(4-((1,4,7,10-tetrakis(carboxymethyl)-1,4,7,10-tetraazacyclododecan-2-yl)methyl)phenyl)thioureido)pentyl)carbamoyl)glutamic acid (***11***)*

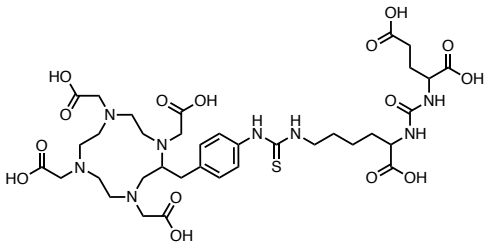

11

10 (0.005 g, 10.9 µmol) was dissolved in DCM/TFA (1:1) (4 mL) and allowed to stir at RT overnight. The reaction was then concentrated in vacuo, redissolved in deionised water and purified using reverse phase semiprep HPLC (A: MeCN/0.1% TFA, B: H_2O/0.1% TFA, 5-80% A over 60 minutes, 4 mL/min). UV active fractions were analysed using LC-MS (HPLC method B), pure fractions were combined and freeze dried to yield the product as a white solid. (0.004 g, 72%). HR-ESI-MS: calc for $[C_{36}H_{55}N_8O_{15}S + H]^+$ 871.35 found 871.35

6,6'-((((4-(4-(3-((4-((7,11-bis(tert-butoxycarbonyl)-2,2-dimethyl-19-(naphthalen-2-yl)-4,9,17-trioxo-3-oxa-8,10,16-triazanonadecan-18-yl)carbamoyl)cyclohexyl)methyl)thioureido)phenethoxy)pyridine-2,6-diyl)bis(methylene))bis((carboxymethyl)azanediyl))bis(methylene))dipicolinic acid (**12**)

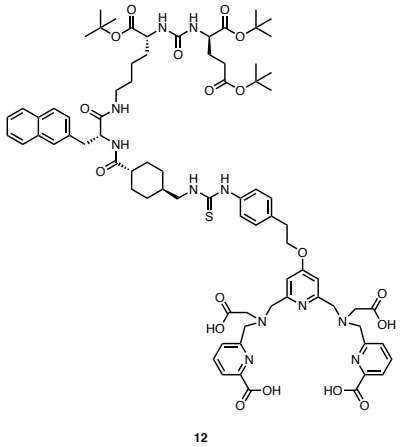

12

H_4pypa-NCS (0.01 g, 14.3 µmol) was dissolved in $CHCl_3$ (1 mL) as was **7** (0.012 g, 14.3 µmol) separately dissolved in $CHCl_3$ (1 mL) to which triethylamine (2 x 4 µL, 57 µmol) was added to each solution. This was allowed to stir at RT overnight, after which the $CHCl_3$ was removed in vacuo. This was then purified using reverse phase semiprep HPLC (A: MeCN/0.1% TFA, B: H_2O/0.1% TFA, 5-80% A over 60 minutes, 4 mL/min). UV active fractions were analysed using LC-MS (HPLC method B), pure fractions were combined and freeze dried to yield the product as a white solid. (0.012 g, 56%) ESI-MS: calc for $[C_{79}H_{101}N_{11}O_{18}S + H]^+$ 1525.80 found 1525.04.

((5-(2-(4-((3-(4-(2-((2,6-bis(((carboxymethyl)((6-carboxypyridin-2-yl)methyl)amino)methyl)pyridin-4-yl)oxy)ethyl)phenyl)thioureido)methyl)cyclohexane-1-carboxamido)-3-(naphthalen-2-yl)propanamido)-1-carboxypentyl)carbamoyl)glutamic acid (**13**)

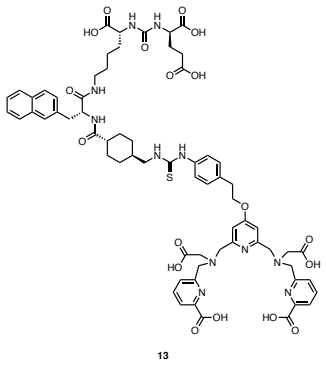

13

8 (0.01 g, 6.6 μmol) was dissolved in DCM/TFA (1:1) (4 mL) and allowed to stir at RT overnight. The reaction was then concentrated in vacuo, redissolved in deionised water and purified using reverse phase semiprep HPLC (A: MeCN/0.1% TFA, B: H_2O/0.1% TFA, 5-80% A over 60 minutes, 4 mL/min). UV active fractions were analysed using LC-MS (HPLC method B), pure fractions were combined and freeze dried to yield the product as a white solid. (0.006 g, 75%). HR-ESI-MS: calc for $[C_{67}H_{77}N_{11}O_{18}S + H]^+$ 1356.5247 found 1356.5298.

Oxidation of [^{201}Tl]Tl^{+} to [^{201}Tl]Tl^{3+}

This procedure is adapted from Rigby et al.[242] [^{201}Tl]TlCl (40 MBq, 100 µL) was added to one Pierce™ iodination bead in a 1.5 mL Eppendorf tube, followed by the addition of HCl (0.5 M, 10 µL). The tube was vortexed, and a small aliquot (2 µL) was removed for ITLC analysis. The supernatant was pipetted into a clean tube. For ITLC, acetone was used as the mobile phase and silica gel ITLC strips (ITLC-SG) as the stationary phase, giving good separation between [^{201}Tl]Tl^{+} (R_f = 0) and [^{201}Tl]Tl^{3+} (R_f = 1).

Radiolabelling of DOTA-PSMA with ^{201}Tl (9/17)

A 1 mg/mL solution of 9/17 was prepared in ammonium acetate solution (0.25M, pH 5). An aliquot of the 9/17 solution (20 µL, 0.1 µM) was added to [^{201}Tl]$TlCl_3$ (11 MBq, 20 µL), followed by ammonium acetate (0.25M, pH 5, 50 µL). This was vortexed and agitated in a Thermomixer (500 rpm) at RT for 60 minutes. Radiochemical yield and purity was evaluated using HPLC (method A, [^{201}Tl]$TlCl_3$ t_R = 2.03 min; , [^{201}Tl]Tl-11 t_R = 11.24 min).

Radiolabelling of DOTA-PSMA with ^{111}In (compound 9/11)

A 1 mg/mL solution of 9/17 was prepared in ammonium acetate solution (0.25M, pH 5). An aliquot of the 9/17 solution (20 µL, 0.1 µM) was added to [^{111}In]$InCl_3$ (12 MBq, 10 µL), followed by ammonium acetate (0.25M, pH 5, 50 µL). This was vortexed and heated to 95°C for 25 minutes. Radiochemical yield and purity was evaluated using HPLC (method A, [^{111}In]In-**11** t_R = 10.12 min).

Radiolabelling of H_4pypa-PSMA with ^{201}Tl

A 1 mg/mL solution of H_4pypa-PSMA was prepared in ammonium acetate solution (1M, pH 5). An aliquot of the H_4pypa-PSMA solution (20 µL, 0.1 µM) was added to [^{201}Tl]$TlCl_3$ (110 MBq, 200

µL), followed by ammonium acetate (1M, pH 5, 50 µL). This was vortexed and agitated in a Thermomixer (500 rpm) at RT for 10 minutes. Radiochemical yield and purity was evaluated using HPLC (method A, [^{201}Tl]$TlCl_3$ t_R = 2.03 min; , [^{201}Tl]Tl-pypa-PSMA t_R = 15.02 min).

HPLC methods

HPLC method A. Solvent A = water (+ 0.1% TFA), solvent B = acetonitrile (+ 0.1% TFA). Column = Agilent Eclipse XDB-C18 column (4.6 x 150 mm, 5 µM) analytical.

Time (minutes)	Flow rate (mL min^{-1})	% solvent A	% solvent B
0	1	100	0
2	1	100	0
25	1	5	95
25.1	1	100	0
30	1	100	0

HPLC method B. Solvent A = water (+ 0.1% TFA), solvent B = acetonitrile (+ 0.1% TFA). Column = Agilent Eclipse XDB-C18 column (4.6 x 150 mm, 5 µM) analytical.

Time (minutes)	Flow rate (mL min^{-1})	% solvent A	% solvent B
0	1	95	5
2	1	95	5
11	1	5	95
12	1	5	95
12.1	1	95	5
15	1	95	5

Tissue culture

DU145 (PSMA-negative) and DU145-PSMA (PSMA-positive) human prostate cancer cells were cultured in RPMI-1640 medium supplemented with 10% fetal bovine serum, 2 mM L-glutamine, and penicillin/streptomycin (Sigma-Aldrich, UK) and maintained at 37 ˚C in a humidified atmosphere with 5% CO_2.[248] Tissue culture was performed by George Firth and Dr Truc Pham.

Flow cytometry of PSMA expression

PSMA expression was evaluated using flow cytometry and the results can be found in Figure 5.2**.**The FACS analysis was performed by Dr Truc Pham, using REA-FITC control antibody and PSMA-FTIC anti-PSMA antibody.

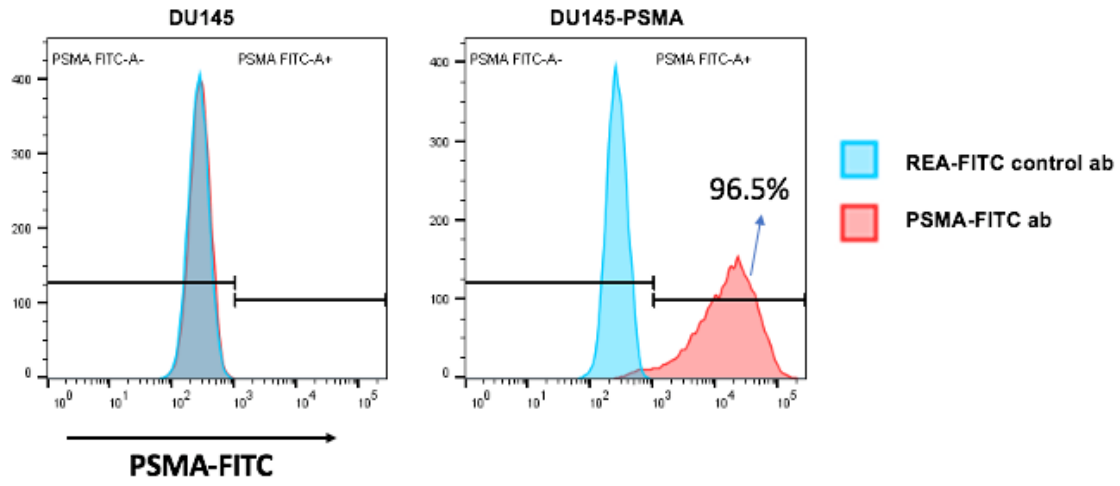

Figure 5.2 - FACS results showing the expression of the PSMA receptor of the DU145 PSMA positive and negative cells used in these experiments

Expression of GCP(II)/PSMA in the DU145-PSMA cell line and the absence of this receptor in the DU145 cell line was assessed using flow cytometry. 1×10^6 cells were suspended in 100 µL PBS containing 0.5% bovine serum albumin and then incubated with 2 µL of either Anti-PSMA anti-human VioBright-FITC antibody (Miltenyi Biotec, Clone REA408) or REA-control human IgG1 VioBright-FITC (Miltenyi Biotec, Clone REA293), for 15 minutes on ice. After this time the cells were washed twice with PBS and then analysed on a BD FACSMelody™. Gating and analysis were performed using FlowJo™ software (BD, v.10.8).

Cell uptake studies

DU145 PSMA positive and negative cells were seeded at 500,000 cells per well of a six well plate the day before the assay, and the cell culture media changed (1 mL) one hour prior to incubation with a radiotracer. Excess KCl (15 mmol/L) was used as a blocking agent for [^{201}Tl]TlCl, effectively saturating the Na^+/K^+ ATPase to evaluate if the metal is dissociating from the chelator and enter the cell.[137] 2-(phosphonomethyl)pentane-1,5-dioic acid (PMPA) which is a competitive inhibitor for the PSMA binding site, is also used as a blocking agent to appraise if the compound is bound to the correct receptor.[249] KCl or PMPA (75 µM) was added to the cells three minutes prior to the addition of the radioactive compound to allow the blocking to take effect. A radiotracer (200 kBq, 50-80 µL) was added to each well and incubated for either 15 or 60 minutes at 37°C in a cell incubator. After this time, the media was removed from each well, the cells were washed with PBS (2 x 1 mL) and then radioimmunoprecipitation (RIPA) assay buffer (0.5 mL) added. The cells were scraped from the plate and an aliquot (300 µL) removed. The media, PBS and RIPA buffer were collected for each well and gamma counted to calculate the cell uptake as a percentage of radioactivity bound.

SPECT scanning and biodistribution in healthy and DU145-PSMA tumour-bearing animals

Animal studies were carried out in accordance with the UK Home Office Animals (Scientific Procedures) Act 1986. Experiments complied with UK Research Councils' and Medical Research Charities' guidelines on responsibility in the use of animals in bioscience research, under UK Home Office project and personal licences. The reporting of this study complied with the Animal Research: Reporting in vivo experiments (ARRIVE) guidelines (https://www.nc3rs.org.uk/arrive-guidelines).

Healthy SCID/beige animals (male 5-7 weeks old, n = 3 per radiotracer) were injected via tail vein injection under isoflurane anaesthesia (1.5-2.5% in oxygen at 1 litre/min) with [^{201}Tl]TlCl (17 - 22.9 MBq), [^{201}Tl]$TlCl_3$ (11.2 - 23.8 MBq) or [^{201}Tl]Tl-pypa-PSMA (14.1 - 16.9 MBq). Mice were then kept under continuous anaesthesia on a heated pad for the duration of the experiment (1 hour) and one mouse per group was imaged by SPECT/CT until 1 hour post injection, when animals were euthanised by cervical dislocation.

To study tracer uptake in tumours, SCID/beige mice (male 5-7 weeks old, n = 3 per group) were injected subcutaneously with DU145-PSMA or DU145 cells (4 x 10^6 cells in 100 mL PBS) in the left shoulder. Once tumours had reached 5-10 mm in diameter (4 - 5 week after inoculation), [^{201}Tl]Tl-pypa-PSMA (10.7 - 24.5 MBq, 20 mmol) was administered via tail vein injection under isoflurane. Mice were maintained under continuous anaesthesia and imaged by SPECT/CT for up to 2-hour post injection when animals were euthanised by cervical dislocation. SPECT images were reconstructed at 0.3mm isotropic voxel size using HiSPECT (Scivis GmbH) reconstruction software package using standard reconstruction with 35% smoothing and 9 iterations. After euthanasia, organs were harvested from mice, weighed and gamma counted.

Blood and urine HPLC procedure

Urine was passed through a 0.22 µm filter and injected directly into the HPLC. Blood was taken via cardiac puncture, centrifuged to remove red blood cells and ice cold MeCN added to precipitate proteins. This was again centrifuged, and the supernatant removed, filtered through a 0.22 µm filter then diluted with water and injected into the HPLC (HPLC method A).

Image analysis

Images were analysed using VivoQuant 2.5 (InviCRO LLC. Boston, USA), enabling the delineation of regions of interest (ROIs) for quantification of radioactivity. The bed was removed from images. ROIs for the tumour and organs (heart, muscle etc) were drawn using CT images and volumes were determined. The total activity in the whole animal (excluding the majority of tail – out of field of view SPECT) at the time of [^{201}Tl] agents administration was defined as the injected activity (IA) and the percentage of injected activity per cm^3 (%IA/cm^3) and amount of radioactivity in tissues (MBq) was determined. A 5 mL syringe with 3 mL of 40 MBq [^{201}Tl]TlCl was used to calibrate the SPECT/CT and ensure correct co-registration between the SPECT and CT.

Statistical analysis

Data are average ± standard deviation. Statistical analysis was performed using Graphpad Prism Version 7.0c with unpaired t-tests used in uptake and a 2-way ANOVA with Sidak's multiple comparisons test used for *in vivo* studies; * $p \leq 0.05$, ** $p \leq 0.01$, *** $p \leq 0.001$, and **** $p \leq 0.0001$.

5.3 Results

5.3.1 Design, synthesis and characterisation of DOTA-PSMA (compound 9/11)

Although [^{201}Tl]Tl-DOTA is unstable, the timescale of decomposition may nevertheless be adequate on a PSMA timescale for possible delivery of ^{201}Tl to malignant tissue. Small peptides have short circulation times, hence a PSMA targeted bioconjugate was pursued.

To prepare the PSMA peptide for coupling to DOTA-NCS , a previously reported method was adapted.[247] In brief, L-glutamic acid di-*tert*-butyl ester was reacted with carbonyldiimidazole (CDI), forming the activated glutamic acid **1** (Scheme 1). This was then reacted with the cbz protected L-lysine *tert*-butyl ester to yield the urea **2**. The cbz group was then removed via catalytic hydrogenation, generating the urea derivative **3**. Cbz-3-(2-naphthyl)-D-alanine was added via HATU mediated amide coupling in DMF to furnish compound **4**, followed by a hydrogenation reaction to remove the cbz group (**5**). The coupling and cbz deprotection procedure was repeated with cbz-trans-4-(aminomethyl)cyclohexanecarboxylic acid, to generate **6** and **7**, respectively (Scheme 1).

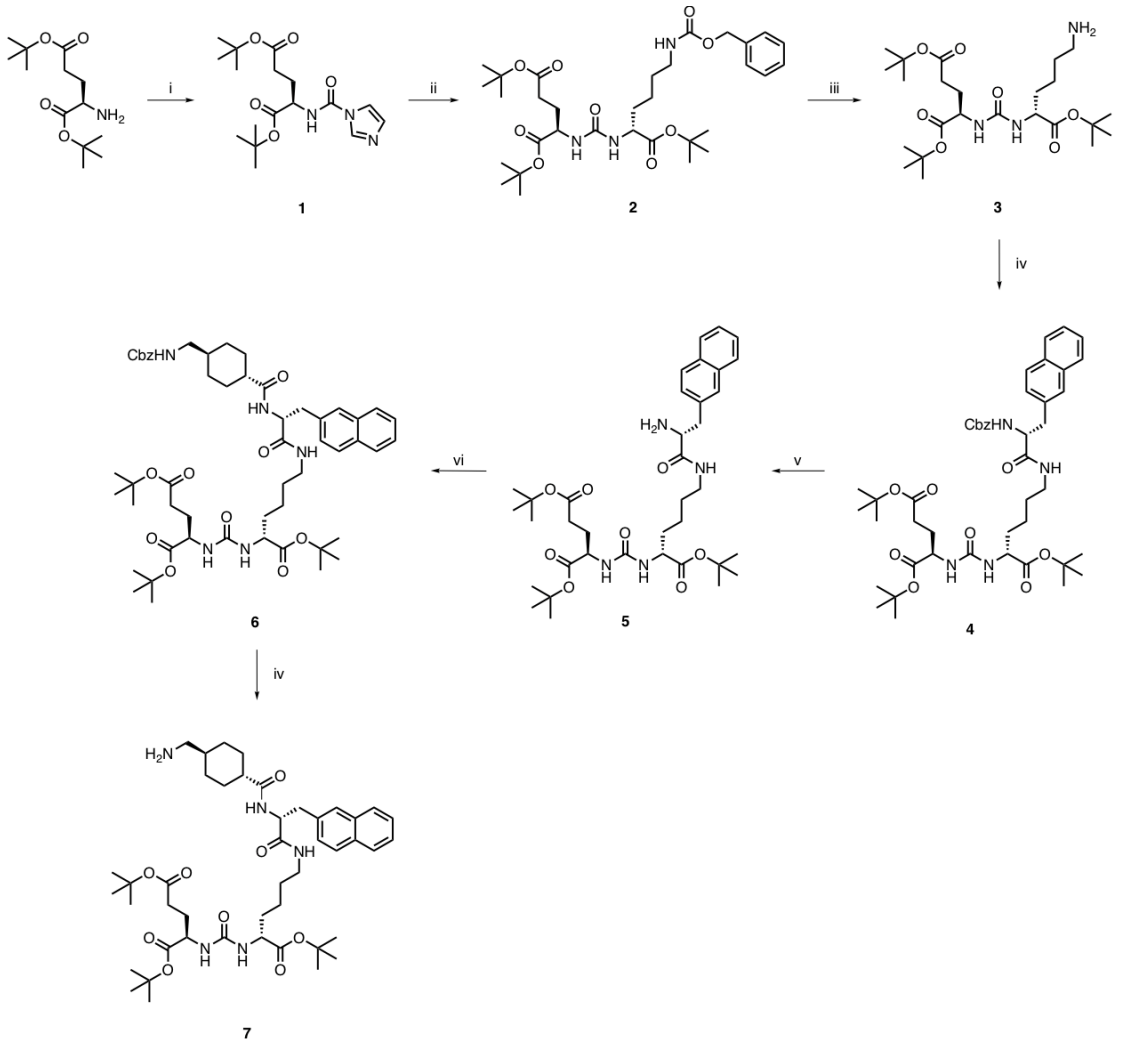

Scheme 1 - Reagents and conditions for the synthesis of compounds 1 - 7**. (i) CDI, MeCN/DMF (4:1), RT, 24 h, 51 %. (ii) H-Lys(cbz)-OtBu, DIPEA, DMF, RT, overnight, 83 %. (iii) Pd/C, MeOH, RT, overnight, 92 %. (iv) Cbz-3-(2-naphthyl)-D-alanine, HATU, DIPEA, DMF, RT, overnight, 55 %. (v) Pd/C, MeOH, RT, overnight, 89 %. (vi) cbz-trans-4-(aminomethyl)cyclohexanecarboxylic acid, HATU, DIPEA, DMF, RT, overnight, 63 %. (vii) Pd/C, MeOH, RT, overnight, 91 %.**

Reaction of DOTA-NCS (Macrocyclics Ltd, USA) with **7** in a basic solution of chloroform at ambient temperature led to formation of conjugate **8** (Scheme 2). The *tert*-butyl groups of **8** were cleaved using trifluoracetic acid in DCM (1:1) to generate **9**, which was purified using reverse phase HPLC. HR-MS confirmed the formation of the final product **9** (Scheme 2). LC-MS

of the final compound can be found in Figure 5.3, showing a single peak in the UV trace, corresponding to the correct mass of **9** ($[M+2H]^{2+}$).

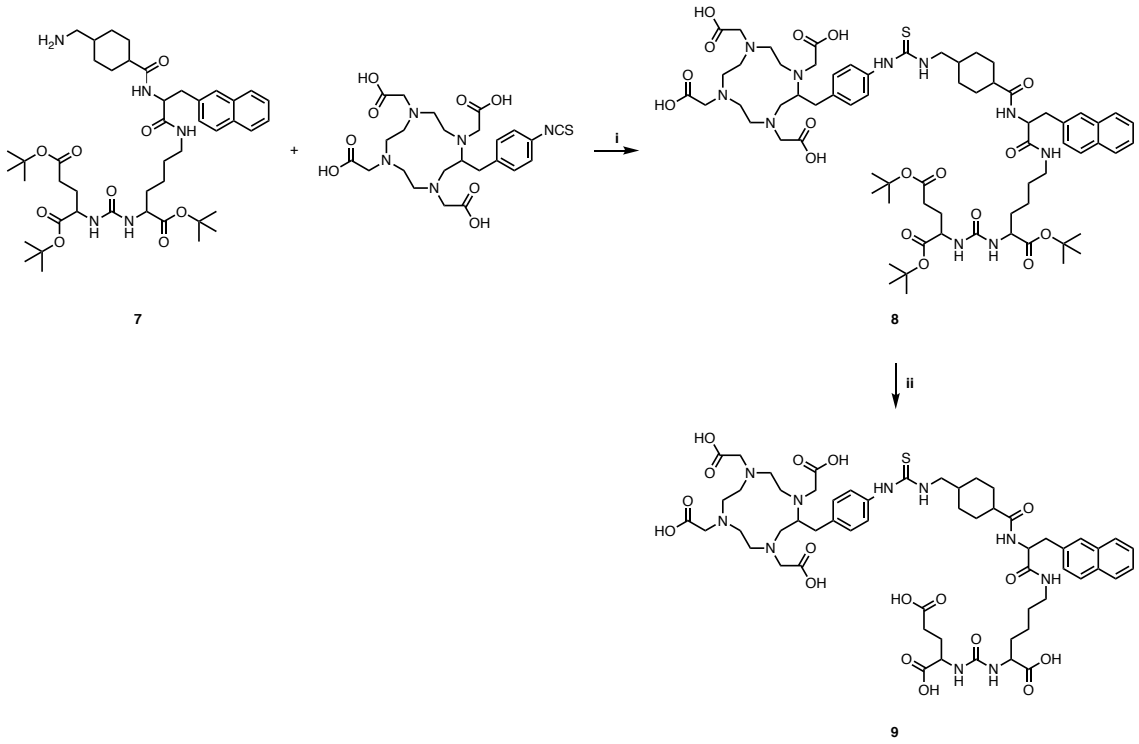

Scheme 2 - Reagents and conditions for the synthesis of compound 8 and 9. (i) $CHCl_3$, NEt_3, RT, overnight, 62 %. (ii) TFA/DCM, overnight, 80 %.

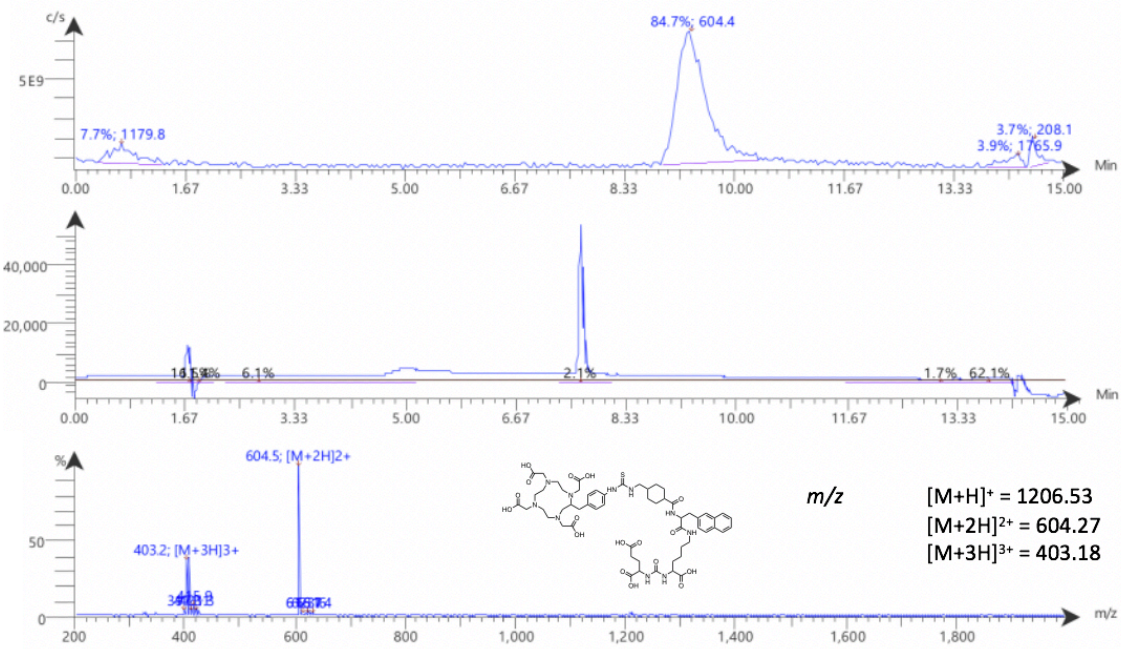

Figure 5.3 – LC-MS data of 9 showing a single peak in the UV corresponding the $[M+H]^+$ peak (1206.4). (HPLC method B)

To investigate what effect the linker has on the cell uptake, an alternative ligand without the lipophilic linker was prepared using **7** and DOTA-NCS (Macrocyclics Ltd, USA) using the same reaction conditions (Scheme 3). LC-MS of the final compound can be found in Figure 5.4, showing a single peak in the UV trace, corresponding to the correct mass of **11** ($[M+H]^+$).

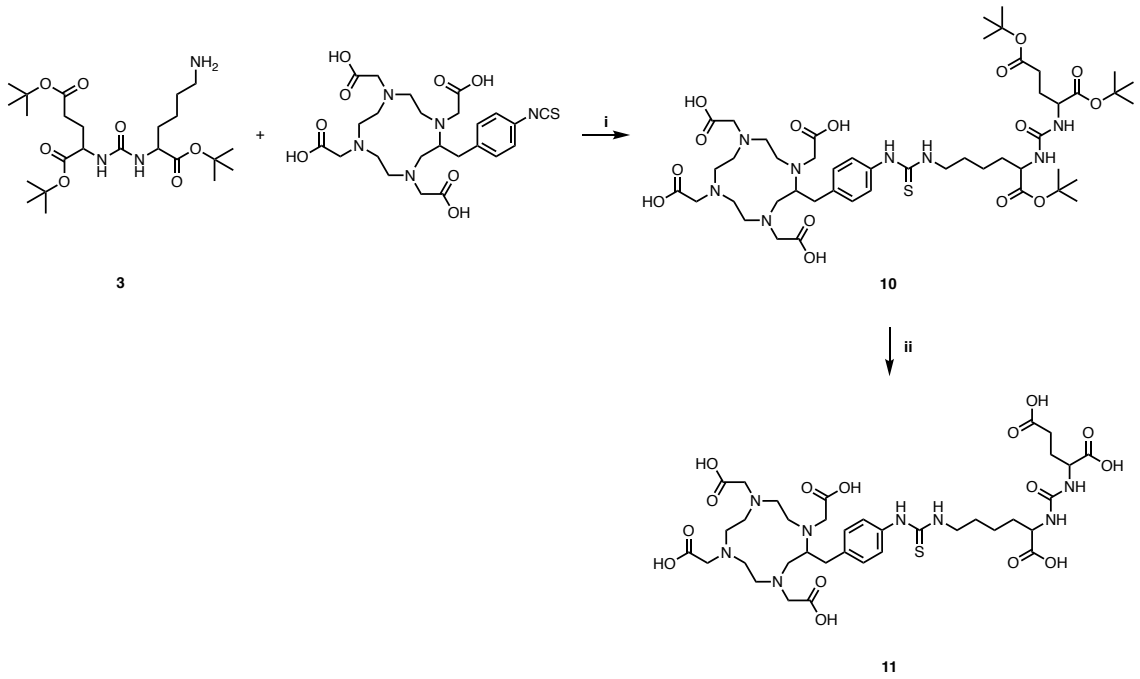

Scheme 3 - Reagents and conditions for the synthesis of compound 10 and 11. (i) $CHCl_3$, NEt_3, RT, overnight, 82 %. (ii) TFA/DCM, overnight, 85 %.

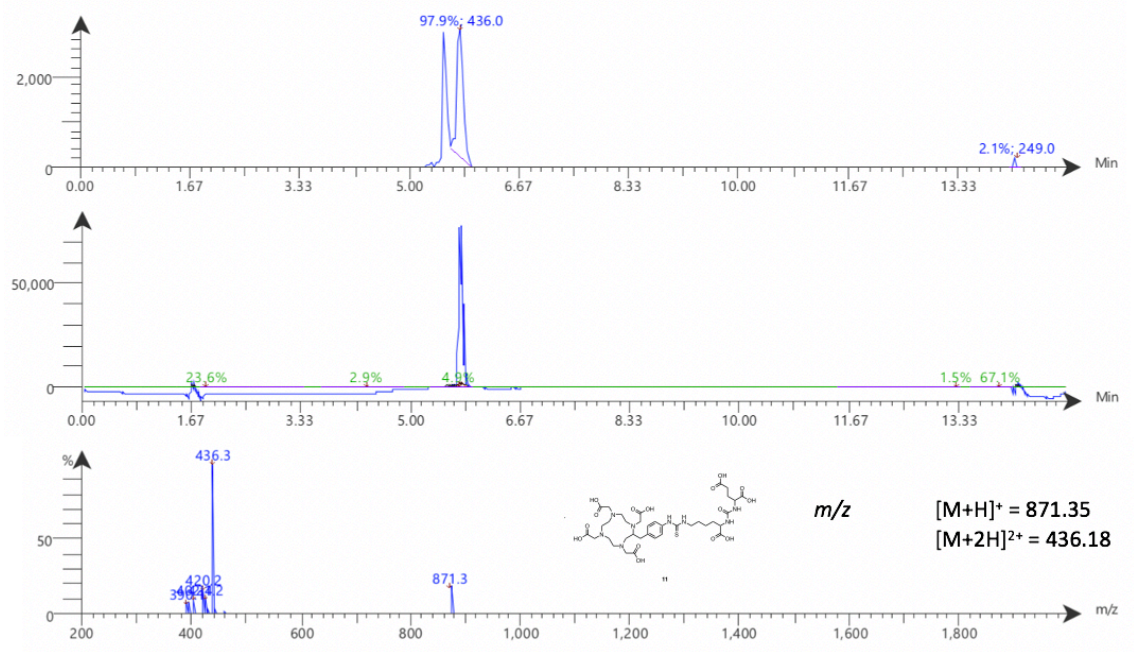

Figure 5.4 – LC-MS data of 11 showing a single peak in the UV corresponding the $[M+H]^+$ peak (871.3). (HPLC method B).

5.3.2 Radiolabelling with ^{111}In and ^{201}Tl

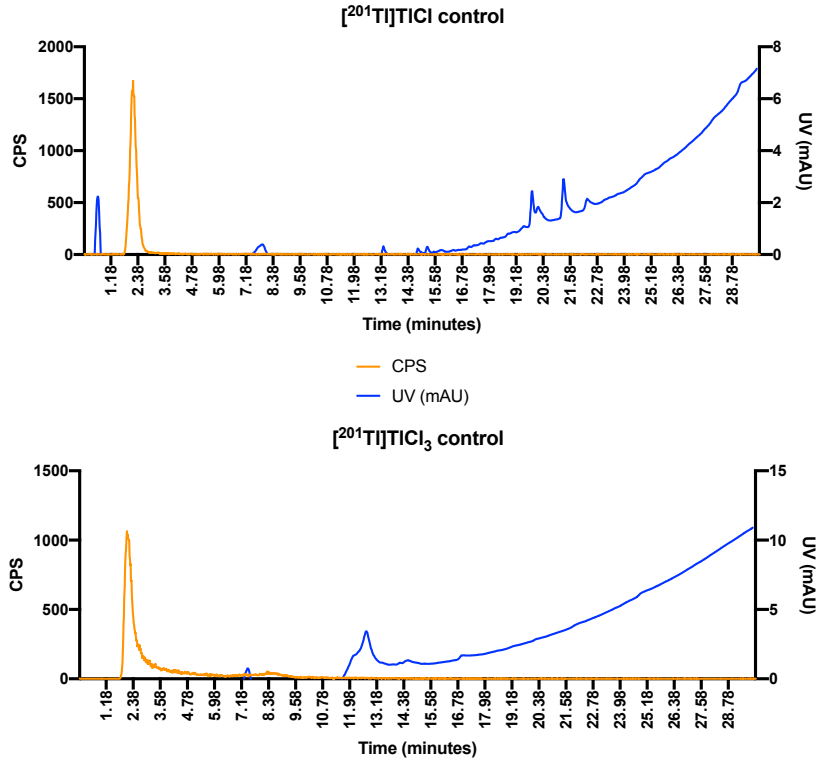

Figure 5.5 - Analytical HPLC trace of [^{201}Tl]TlCl (top) and [^{201}Tl]$TlCl_3$ (bottom) using HPLC method A (orange = counts per second, blue = UV) (HPLC method A).

9 and **11** were dissolved in ammonium acetate buffer (0.25 M, pH 5, 1 mg/mL) and an aliquot (30 µL) added to a solution of [^{201}Tl]$TlCl_3$ (80 µL, 15 MBq, prepared using chloramine-T) or [^{111}In]$InCl_3$ (10 µL, 12 MBq). The ^{201}Tl compounds were agitated for 60 minutes at RT (Figure 5.6A/B) and required purification using Oasis HLB reverse phase SPE (solid phase extraction) cartridges (Figure 5.6C/D). The retention times for the ^{201}Tl compound are very different to the unbound ^{201}Tl controls in Figure 5.5. The additional peaks in the UV trace are due to chloramine-T dissolved in the solution. The ^{111}In compounds were heated to 95°C for 20 minutes and did not need to be purified, as shown in Figure 5.6E/F. HPLC traces for the radiolabelling reactions of **11** can been seen in Figure 5.6, showing radiochemical yields of both compounds of greater than 95 %. Unfortunately, due to a computer breakdown, HPLC traces for **9** were corrupted and not

retrievable. Ideally this would have been repeated, but all the bioconjugate was used in experiments and not re-synthesised.

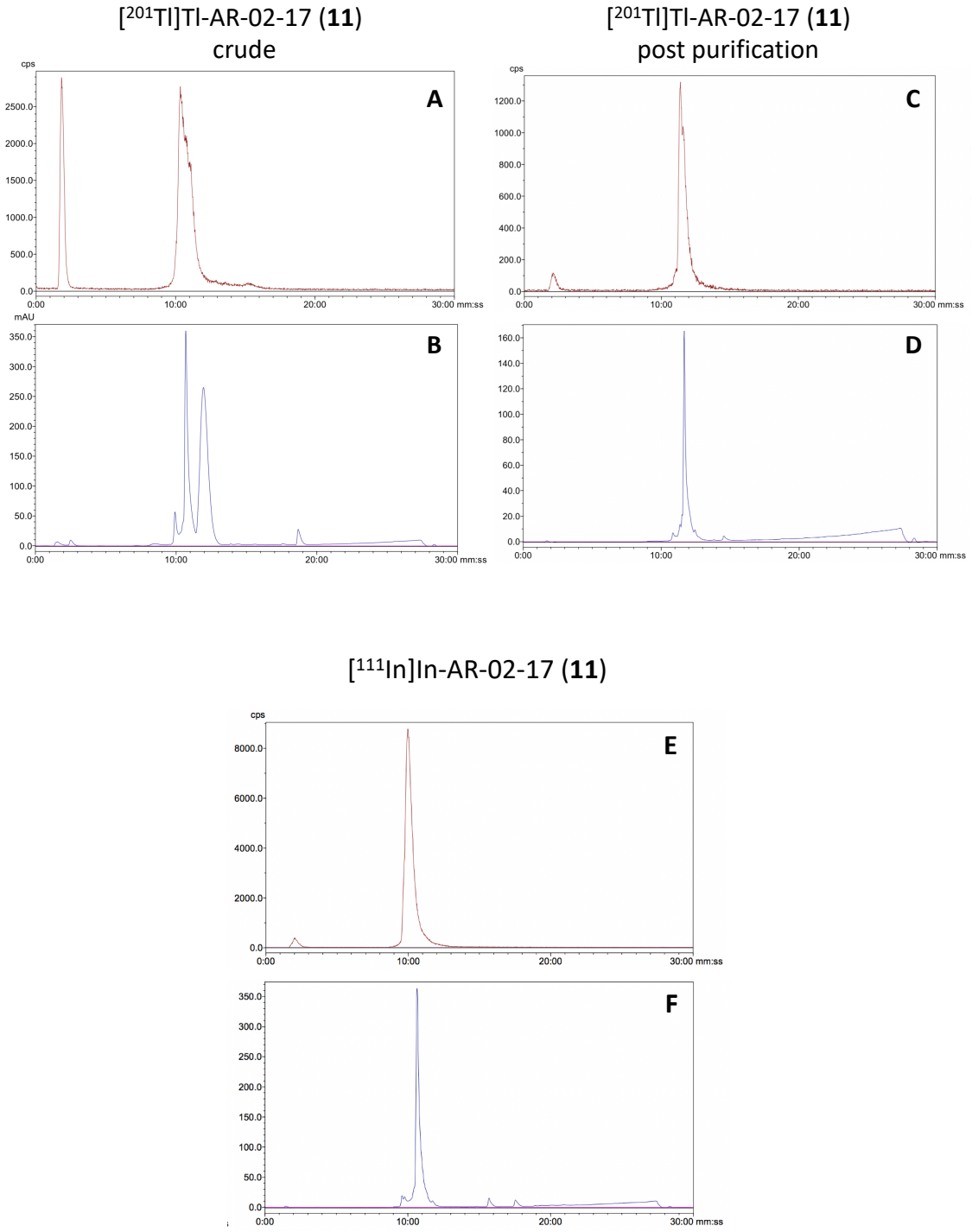

Figure 5.6 – Analytic HPLC traces of crude [^{201}Tl]Tl-11 (A = counts per second, B = UV trace), analytic HPLC traces of [^{201}Tl]Tl-11 post purification (C = counts per second, D = UV trace), and [^{111}In]In-11 (E = counts per second, F = UV trace) (HPLC method A).

5.4 *In vitro* evaluation of 9 and 11

5.4.1 Uptake studies in DU145 PSMA-positive and PSMA-negative cells

Cell uptake data can be seen in Figure 5.7. [^{201}Tl]Tl-**9** had an uptake of 6.48 ± 1.65 % in the DU145 PSMA positive cells and 8.06 ± 3.49 % in the PSMA negative cells. Following KCl blocking, the uptake dropped to 1.81 ± 0.1 % in the PSMA positive and 2.42 ± 0.2 % in the PSMA negative cells. The addition of PMPA did not influence cell uptake, which was comparable to tracer without blocking (6.52 ± 0.27 % in the PSMA positive and 7.86 ± 0.85 % in the PSMA negative cells). The [^{111}In]In-**9** control showed a more significant and characteristic PSMA-specific uptake of 2.58 ± 0.52 % in the PSMA positive and 0.25 ± 0.1 % in the negative, with KCl having no effect on the uptake (2.88 % in the PSMA positive and 0.77 in the PSMA negative). PMPA did decrease the uptake of the ^{111}In compound with uptake in the positive cell being 0.78 % and 0.65 % in the negative cells.

The effect of the linker on cell uptake was investigated by comparing ^{111}In-labelled **9** and **11**. [^{111}In]In-**11** had uptake of 0.62 ± 0.09 % in the positive and 0.17 ± 0.04 % in the negative, with again KCl having little effect on the cell uptake (0.64 ± 0.15 in the positive and 0.17 ± 0.03 % in the negative). PMPA did have a small effect on the uptake, decreasing it to 0.45 ± 0.28 % in the positive and 0.33 ± 0.23 % in the negative. In comparison, [^{201}Tl]Tl-**11** had comparable uptake to [^{201}Tl]Tl-**9** with 6.17 ± 1.38 % in the positive and 7.02 ± 2.35 % in the negative, with KCl reducing the uptake to 0.80 ± 0.29 % in the positive and 0.82 ± 0.44 % in the negative. As with [^{201}Tl]Tl-**11**, PMPA did not affect the uptake with 6.76 ± 1.28 % in the positive and 7.22 ± 1.99 % in the negative cells.

To determine *in vivo* specificity and stability, further *in vivo* studies were planned using [^{201}Tl]Tl-**9**. However, increased amount of activity is needed for *in vivo* studies, and when the activity in the reaction was increased, the radiochemical purity dropped significantly (n=3, < 5% RCY).

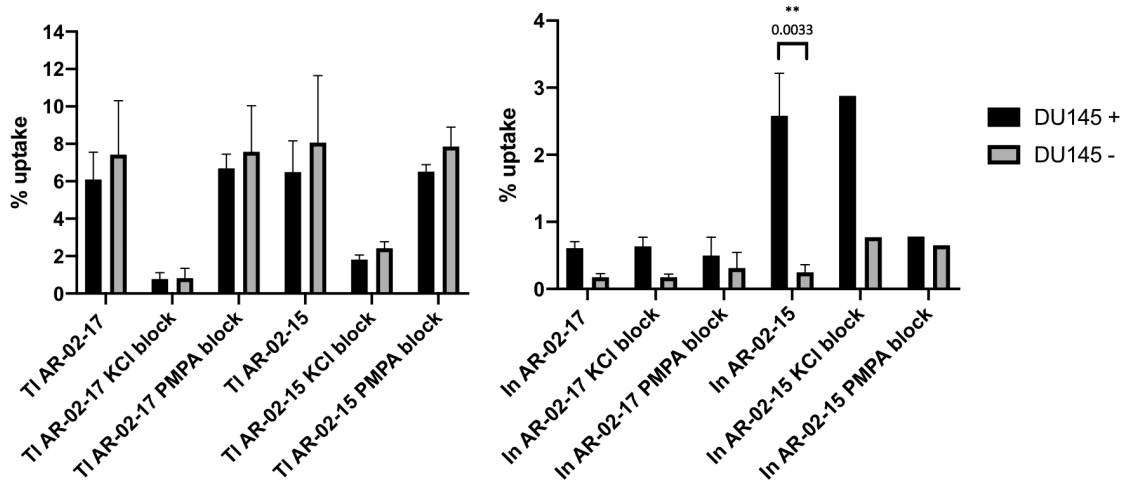

Figure 5.7 – Cell uptake experiments in DU145 PSMA positive and negative cell lines with either 9 or 11, radiolabelled with ^{201}Tl (left) or ^{111}In (right) after 60 minutes incubation at 37 °C. (n=1-3)

5.5 Design, synthesis and characterisation of H_4pypa-PSMA (AR-02-57)

H_4pypa-NCS was synthesised using the method previously described by Li *et al*.[214,215] To deliver ^{201}Tl to PSMA expressing cells, H_4pypa-NCS was coupled to a targeting vector via the same lipophilic linker (Scheme 4) used for the DOTA bioconjugates. Figure 5.8 shows an LC-MS trace of AR-02-57, corresponding to the $[M+H]^+$ and the analytical HPLC trace of AR-02-57 can be seen in Figure 5.8C. Unfortunately, AR-02-57 could not be synthesised in large enough quantities needed for NMR studies.

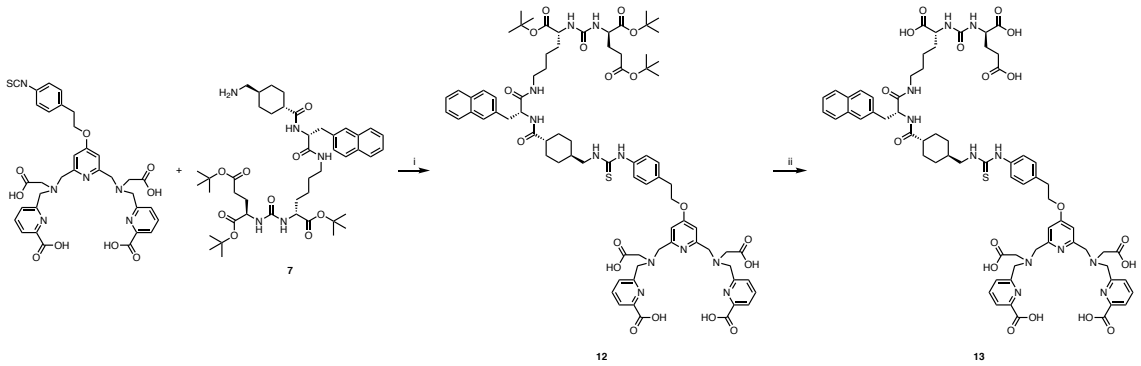

Scheme 4 – Reagents and conditions for the synthesis of compound 12 and 13. (i) $CHCl_3$, NEt_3, RT, overnight, 56 %. (ii) TFA/DCM, overnight, 75 %.

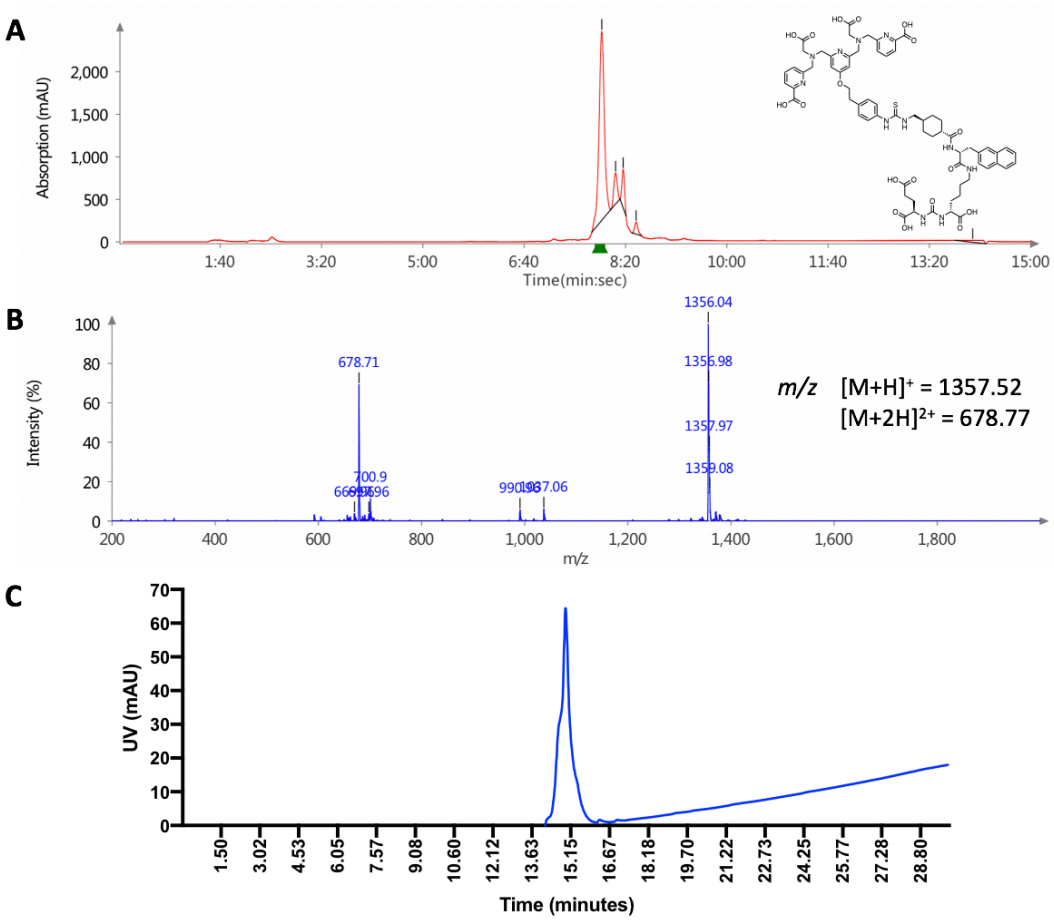

Figure 5.8 – UV signal from LC-MS of AR-02-57 (crude) (A), the mass signal from the same sample of AR-02-57 (HPLC method B) (B) and an analytic HPLC UV trace of AR-02-57 post semi prep purification (HPLC method A) (C).

5.5.1 Radiolabelling pypa-PSMA with Tl-201

The method previously described for the radiolabelling of H_4pypa (chapter 3) with ^{201}Tl was used to radiolabel **13**, in good radiochemical yields (95 ± 3%). The bioconjugate was dissolved in ammonium acetate buffer (1M, pH 5, 1 mg/mL), with an aliquot added to a solution of [^{201}Tl]$TlCl_3$ and agitated for 10 minutes at RT. HPLC analysis indicated that [^{201}Tl]Tl-pypa-PSMA eluted at 15.9 min (Figure 5.9).

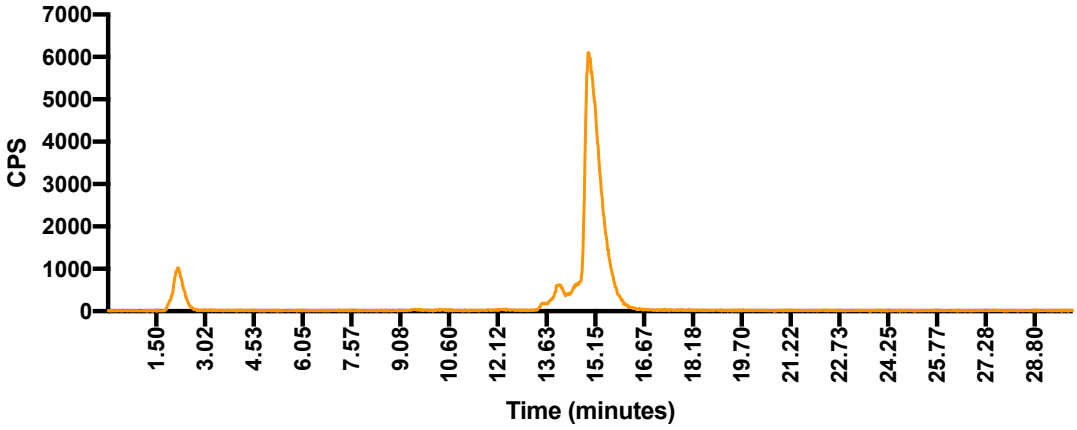

Figure 5.9 - Analytical HPLC trace of [^{201}Tl]Tl-pypa-PSMA using HPLC method A (orange = counts per second) (HPLC method A).

5.6 *In vitro* evaluation of [^{201}Tl]Tl-pypa-PSMA (AR-02-57)

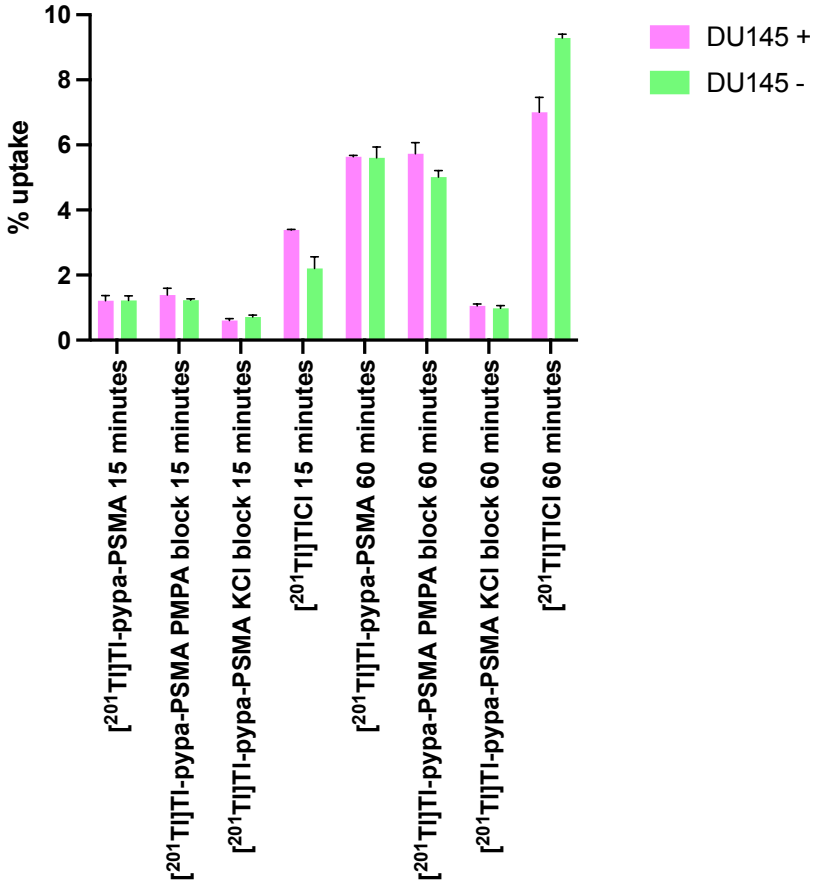

Figure 5.10 - Cell uptake experiments in DU145 PSMA positive and negative cell lines with [^{201}Tl]-pypa-PSMA or [^{201}Tl]TlCl after 15 or 60 minutes incubation at 37 °C. (n=1)

Figure 5.10 shows a cell uptake experiment where [^{201}Tl]Tl-pypa-PSMA or [^{201}Tl]TlCl was incubated with DU145 PSMA positive or PSMA negative cells. As with the DOTA bioconjugates, the compound appears to be unstable in the presence of cells. There is no difference between PSMA positive and PSMA negative cells, and uptake can be reduced using excess KCl, suggesting [^{201}Tl]Tl^{+} enters the cell and not the bioconjugate. This is supported by negligible effects of the PSMA inhibitor PMPA on the cell uptake.

5.7 *In vivo* evaluation of [^{201}Tl]Tl-pypa-PSMA (AR-02-57)

5.7.1 Biodistribution and *in vivo* stability in healthy animals

To compare the biodistribution of [^{201}Tl]Tl-pypa-PSMA, [^{201}Tl]TlCl and [^{201}Tl]$TlCl_3$, all three tracers were administered to healthy male SCID/beige mice. [^{201}Tl]TlCl and [^{201}Tl]$TlCl_3$ were used as controls to highlight the biodistribution of unbound [^{201}Tl]Tl^+ and [^{201}Tl]Tl^{3+}. Additionally, the biodistribution of [^{201}Tl]Tl^{3+} has not been published in the literature. Equally, it was unclear whether the stability issues found *in vitro* would be replicated *in vivo* where the conditions are more disparate and the ratio of cell microenvironment to tracer is far less.

Each tracer was administered intravenously (via tail vein) and SPECT/CT images acquired at 15-minute intervals up to 1 hour (Figure 5.11). SPECT/CT images show that Tl^+ and Tl^{3+} have high initial heart uptake followed by renal excretion, with a high degree of retention in the kidneys (Figure 5.12). After 1 hour, the mice were culled, and organs collected for *ex vivo* biodistribution (Figure 5.13). *Ex vivo* biodistribution data showed that blood clearance for [^{201}Tl]TlCl, [^{201}Tl]$TlCl_3$ and [^{201}Tl]Tl-pypa-PSMA was fast with 0.48 ± 0.03% injected activity per gram (IA/g), 0.59 ± 0.28% IA/g and 0.49 ± 0.08% IA/g at 1 h post injection (p.i.) (Figure 5.13) respectively. [^{201}Tl]TlCl and [^{201}Tl]$TlCl_3$ have a heart uptake of 10.32 ± 0.16% IA/g and 15.40 ± 2.62% IA/g 1 h p.i. respectively with [^{201}Tl]Tl-pypa-PSMA having lower uptake (7.96 ± 0.35% IA/g) (Figure 5.13). All three ^{201}Tl compounds are renally cleared, with [^{201}Tl]TlCl having 74.36 ± 6.29% IA/g, [^{201}Tl]$TlCl_3$ having 104.53 ± 6.88% IA/g and [^{201}Tl]Tl-pypa-PSMA having 61.01 ± 3.03% IA/g in the kidneys. Clearance through the liver was much lower again for all three groups with [^{201}Tl]TlCl having 12.32 ± 0.58% IA/g, [^{201}Tl]$TlCl_3$ having 17.45 ± 2.02% IA/g and [^{201}Tl]Tl-pypa-PSMA having 15.31 ± 4.21% IA/g. The *ex vivo* data supports the SPECT/CT quantification data, showing higher renal clearance and less heart uptake for [^{201}Tl]Tl-pypa-PSMA compared to [^{201}Tl]TlCl and [^{201}Tl]$TlCl_3$.

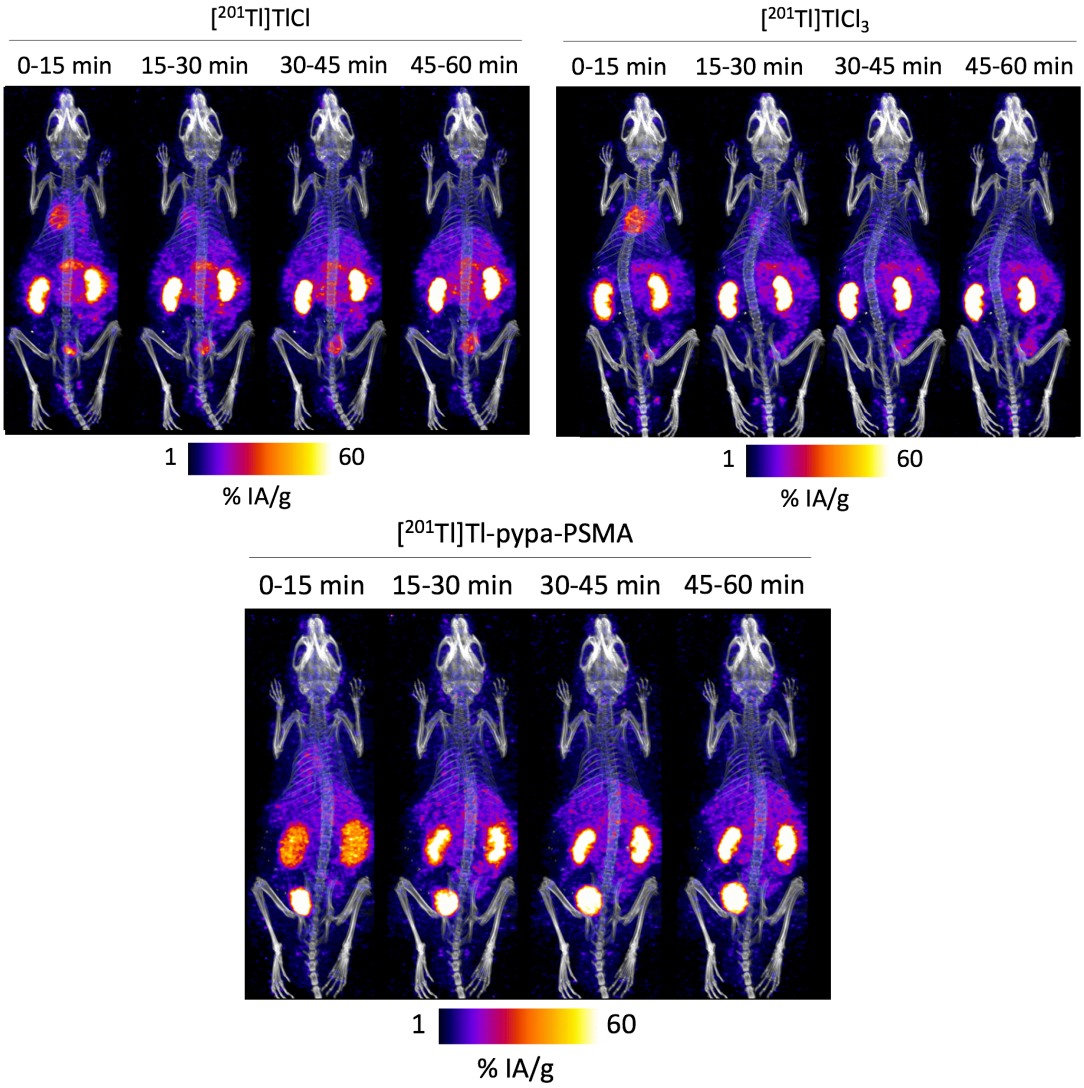

Figure 5.11 - In vivo images of mice injected with [^{201}Tl]TlCl, [^{201}Tl]$TlCl_3$ and [^{201}Tl]Tl-pypa-PSMA at 15, 30 , 45 and 60 minutes in healthy animals

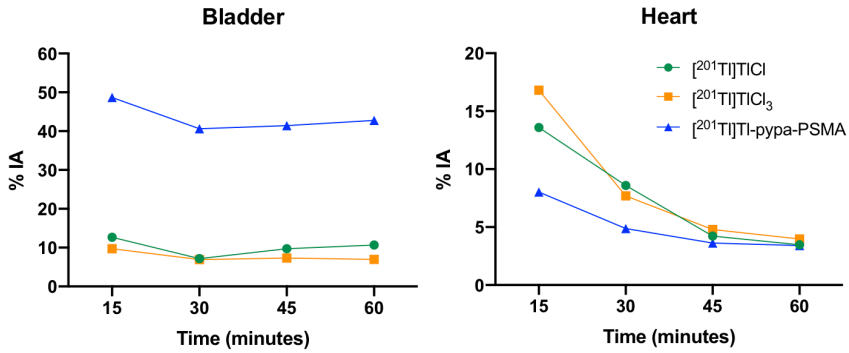

Figure 5.12 - % injected activity taken from regions of interest (ROIs) drawn from the SPECT images around organs of interest (bladder and heart) for [^{201}Tl]TlCl, [^{201}Tl]$TlCl_3$ and [^{201}Tl]Tl-pypa-PSMA at 15, 30 , 45 and 60 minutes.

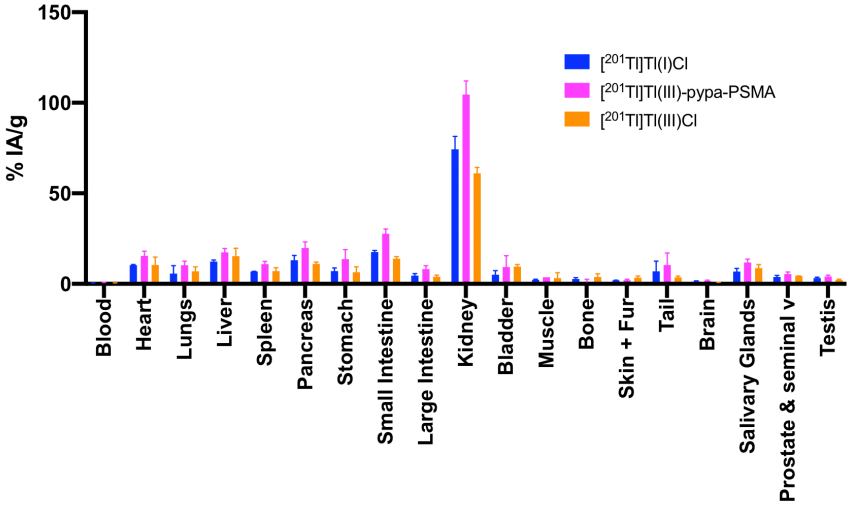

Figure 5.13 - The ex vivo biodistribution of of [^{201}Tl]TlCl, [^{201}Tl]$TlCl_3$ and [^{201}Tl]Tl-pypa-PSMA in healthy SCID beige mice, culled at one hour post injection (n = 3).

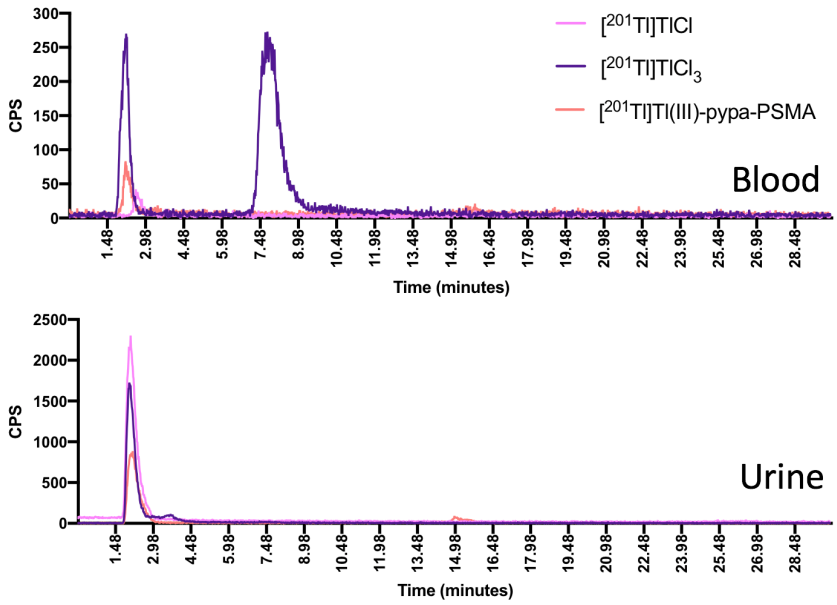

Figure 5.14 - HPLC traces for blood and urine samples obtained from mice injected with [^{201}Tl]TlCl (pink), [^{201}Tl]TlCl$_3$ (purple) and [^{201}Tl]Tl-pypa-PSMA (orange) culled 1 h p.i.

Blood metabolite and urine HPLC traces for [^{201}Tl]TlCl, [^{201}Tl]TlCl$_3$ and [^{201}Tl]Tl-pypa-PSMA all show a peak at t_R = 2.26, which corresponds to unchelated thallium (Figure 5.14). However, [^{201}Tl]TlCl$_3$ from the blood samples shows a second peak at t_R = 7.58 minutes, suggesting [^{201}Tl]Tl^{3+} may bind to serum proteins in the blood. Future studies will be needed to establish which protein, if any, [^{201}Tl]Tl^{3+} binds to in the blood. This peak was not observed in the blood sample for [^{201}Tl]Tl-pypa-PSMA, suggesting [^{201}Tl]Tl^{3+} is not released from the chelator (but not eliminating the possibility that [^{201}Tl]Tl^{+} is released), as this would have been observed if released. Again in the blood sample, the peak corresponding to [^{201}Tl]Tl-pypa-PSMA (Figure 5.14) at t_R = 15.02 was not detected. The lack of the 15.02 peak for [^{201}Tl]Tl-pypa-PSMA is likely due to the rapid blood clearance of the bioconjugate, as supported by the SPECT image and the low counts detected in the sample. In the urine (Figure 5.14), [^{201}Tl]Tl-pypa-PSMA has a large peak corresponding to unbound thallium, with a very small peak at 15.02 minutes for intact compound. This suggests [^{201}Tl]Tl-pypa-PSMA may be reduced during excretion rather than in

the blood, or it is being metabolised, leading to the metal being reduced and released from the chelator.

5.7.2 Biodistribution in animals bearing DU145 PSMA-positive and DU145 PSMA-negative tumours

The biodistribution of [^{201}Tl]Tl-pypa-PSMA was studied in SCID/beige mice bearing either (i) DU145 PSMA-expressing tumours (PSMA-positive) or (ii) DU145 tumours that did not express PSMA receptor (PSMA-negative), to determine if [^{201}Tl]Tl-pypa-PSMA accumulated in prostate cancer tissue via PSMA receptor binding. Each group of mice was administered [^{201}Tl]Tl-pypa-PSMA (10.7-24.5 MBq, 20 mmol) prior to SPECT/CT scanning for two hours. At the conclusion of the SPECT/CT scan, each mouse was culled, organs dissected, weighed and counted for radioactivity, to obtain quantitative data on radiotracer biodistribution.

SPECT imaging analysis indicated that radioactivity concentration in DU145 PSMA-positive tumours was consistently higher than that for DU145 PSMA-negative tumours, and at early time points, this difference was statistically significant. At 30 minutes, the ^{201}Tl radioactivity concentration in PSMA-positive DU145 tumours measured 3.45 ± 1.41% IA/g ($p = 0.0219$) and decreased to 2.85 ± 0.92% IA/g at 2 h p.i. (Figure 5.15C). For PSMA-negative DU145 tumours, ^{201}Tl radioactivity concentration at 30 minutes was 2.06 ± 0.15% IA/g and remained constant at approximately 2% IA/g until 2 h p.i. Biodistribution data 2 h p.i. corroborated SPECT imaging analysis: ^{201}Tl radioactivity concentration at 2 h p.i. in DU145 PSMA-positive tumours measured 3.68 ± 2.76% IA/g; in the PSMA negative tumours, this ^{201}Tl radioactivity concentration measured 2.85 ± 1.47% IA/g (Figure 5.15B). Imaging and *ex vivo* biodistribution data further evidenced that [^{201}Tl]Tl-pypa-PSMA is cleared from the blood via a renal pathway, with high levels of radioactivity observed in the kidneys and bladder/urine, in both imaging and *ex vivo* biodistribution data.

Ex vivo biodistribution data also indicated that tumour:blood ratio for PSMA-positive tumours (11.14 ± 1.42) was significantly higher than that for PSMA-negative tumours (3.88 ± 3.04) at 2 h

p.i. (p = 0.0385). The tumour:muscle ratio shows similar although not significant differences, with the PSMA-positive tumours having a 1.48 ± 0.41 ratio and PSMA-negative tumours having a 0.69 ± 0.2 ratio (Figure 5.15E). SPECT image analysis was also used to determine tumour:muscle ratios for [^{201}Tl]Tl-pypa-PSMA. The tumour:muscle ratio for animals bearing PSMA-negative tumours was approx. 1, from 30 min – 2 h p.i. However, the tumour:muscle ratio for animals bearing PSMA-positive tumours measured 2.11 ± 0.62 at 30 min, and decreased to 1.22 ± 0.36 at 2 h p.i.

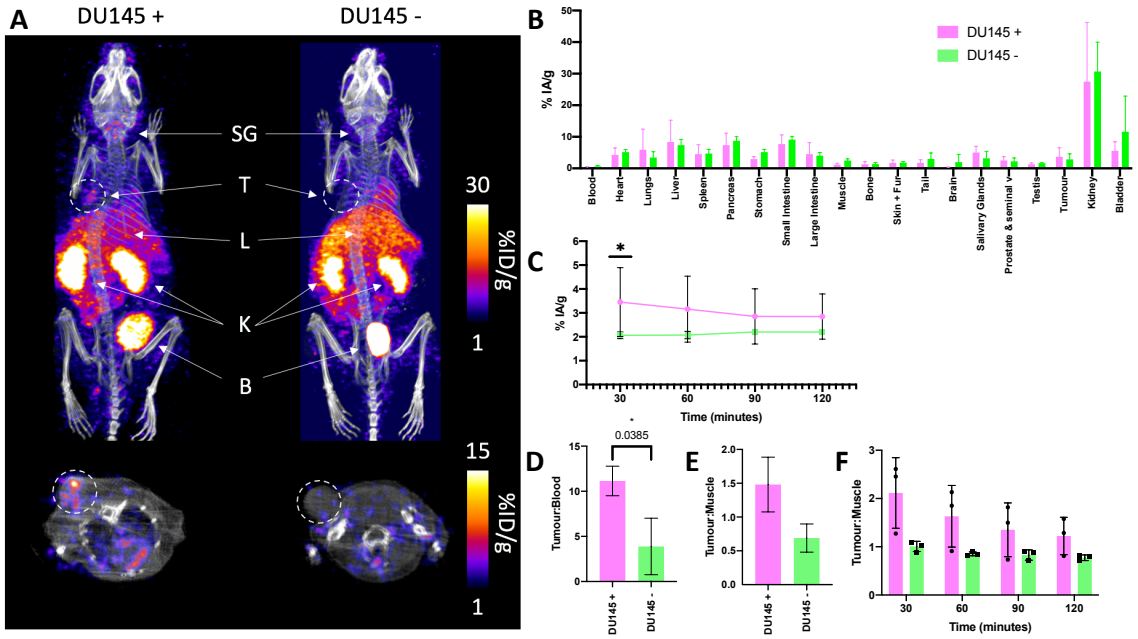

Figure 5.15 - A. In vivo SPECT image (0 – 30 minutes) of [^{201}Tl]Tl-pypa-PSMA in mice bearing DU145 PSMA positive and negative tumours at 0 – 30 minutes. SG = salivary glands, T = tumour, L = liver, K = kidneys, B = bladder. B. Ex vivo biodistribution of [^{201}Tl]Tl-pypa-PSMA in mice bearing DU145 positive and negative tumours 2 h p.i. (n=3 per group) (urine has been omitted for clarity). C. Uptake in DU145 PSMA positive and negative tumours drawn using regions of interest from the SPECT images at 30, 60, 90 and 120 minutes. Tumour to blood (D) and muscle (E) ratios using biodistribution data (2h p.i.). Tumour to blood ratios taken from ROIs drawn on the SPECT images at various time points (F).

5.8 Discussion

Cell uptake results using [^{201}Tl]Tl-DOTA-PSMA , suggest that under these *in vitro* conditions, ^{201}Tl appears to be reduced and then dissociates from the chelator. Further results in Chapter 4 show that [^{201}Tl]Tl-DOTA is stable in RPMI cell culture media, suggesting the DU145 PSMA positive and negative cells are making a reducing agent which is causing this reduction. The ^{111}In control demonstrates that the bioconjugate is binding to the desired PSMA target in the PSMA positive cells, which can be blocked by the competitive inhibitor PMPA, with minimal uptake in the PSMA negative cells. The lipophilic linker dramatically increases the uptake, highlighting the important role the linker can play in the uptake of radioactive compounds.

Moving from *in vitro* to *in vivo* was the next step in answering questions surrounding the stability of [^{201}Tl]Tl^{3+} complexes. Despite encouraging serum stability data for [^{201}Tl]Tl-pypa, cell uptake studies using [^{201}Tl]Tl-pypa and [^{201}Tl]Tl-pypa-PSMA suggested complex instability. Under the conditions of the cell uptake studies, the concentration of reducing agents in solution will be far higher than it would be *in vivo*, which could possibly lead to premature abandonment of potentially promising compound. Furthermore, there is no *ex vivo* biodistribution data or SPECT images of [$^{201}TlCl_3$ in the literature. This control group also revealed that unchelated [^{201}Tl]Tl^{3+} show biological behaviour which is indistinguishable from [^{201}Tl]Tl^{+}, which is an essential piece of information for the future development of [^{201}Tl]Tl^{3+} based radiopharmaceuticals.

These results suggest DOTA is entirely inadequate as a chelator for Tl^{3+}. Despite forming well characterised complexes with high affinity it remains vulnerable to release of Tl^{+} rapidly in the presence of cells. The PSMA conjugates (compounds **9** and **11**) showed biological properties consistent with PSMA specific targeting when labelled with $^{111}In^{3+}$, but when labelled with $^{201}Tl^{3+}$ the uptake did not differ biologically from [^{201}Tl]TlCl. The previous literature on the redox

instability of [^{201}Tl]Tl-DOTA has been ambiguous, but these results highlight the shortcomings of DOTA.

As shown in Chapter 4, H_4pypa formed well-defined complexes with improved *in vitro* stability compared to DOTA. *In vivo* experiments were used to evaluate the stability of the [^{201}Tl]Tl-pypa-PSMA bioconjugate. The serum stability experiments demonstrate the complex is adequately stable for use with small peptides, like PSMA. The bioconjugate also showed PSMA-specific uptake only in the earliest scans; later scans again did not show distribution expected of PSMA-targeting.

Despite encouraging serum stability results, which suggest that serum in the absence of cells does not contain the necessary reducing agents to render the [^{201}Tl]Tl-pypa unstable, but when in the presence of living cells, either *in vitro* or *in vivo*, it appears to. The hypothesis is that the [^{201}Tl]Tl-pypa-PSMA bioconjugate is internalised into tumour cells, whereupon Tl^{3+} is reduced to Tl^{+} in the more reducing intracellular environment. The Tl^{+} metal ion then dissociates from pypa and is effluxed from the cells.

This could account for the higher tumour uptake (Figure 5.15F) and higher tumour:muscle ratios at earlier time points that decrease over the course of the experiment. It may be the case that in the future, bioconjugates using [^{201}Tl]Tl^{+} may have an advantage over [^{201}Tl]Tl^{3+} based agents, as reduction would not be an issue while still delivering a cytotoxic dose of Auger electrons to cancer cells.

In Figure 5.15F, each data point has been plotted on the graph, one point is significantly lower in the DU145 PSMA positive tumours, compared to the other two points. This was due to one of the tumours being very necrotic, discovered during the *ex vivo* biodistribution. Due to the limitations of only using three mice, by increasing the number of mice in the future, it is likely to

show significance between the PSMA positive and PSMA negative tumours at the earlier time points. Figure 5.16 shows the tumour:muscle ratios with the necrotic tumour data removed. It shows significance at every time point, with the early time points having the most significance compared to the later time points.

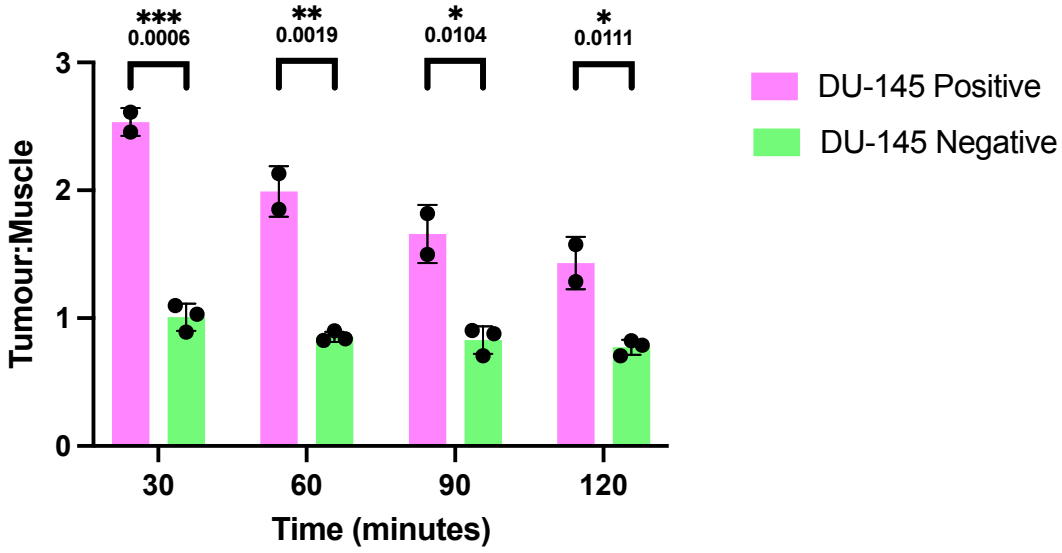

Figure 5.16 - Tumour to blood ratios taken from ROIs drawn on the SPECT images at 30, 60 90 and 120 minutes, with the necrotic tumour removed.

Compared to the previously published H_4pypa-PSMA bioconjugates radiolabelled with ^{111}In and ^{177}Lu by the Orvig group, the [^{201}Tl]Tl-pypa-PSMA compound has higher uptake background tissue such as the liver. SPECT/CT images of the [^{111}In]In-pypa-C7-PSMA617 and [^{177}Lu]Lu-pypa-C7-PSMA617, and PET/CT of [^{44}Sc]Sc-pypa-C7-PSMA617 show high uptake in PSMA specific organs like the kidneys, with minimal background uptake.

These observations are consistent with the need to avoid the bioreduction of Tl^{3+} to Tl^{+} leading to decomplexation. The ideal chelator needs to lower the redox potential enough to resist the reduction, this is likely the reason for the large difference in behaviour between ^{111}In and ^{201}Tl. *In vivo* studies following tumour growth inhibition were not yet deemed possible.

5.9 Conclusions

These results demonstrate that DOTA is wholly inadequate for the chelation of $[^{201}Tl]Tl^{3+}$ and the development of a radiopharmaceutical, hence alternative chelators needed to be investigated.

The $[^{201}Tl]$Tl-pypa-PSMA bioconjugate was evaluated in healthy and tumoured mice bearing DU145 PSMA positive and negative tumours. The healthy controls showed very different biodistributions to the thallium-201 bioconjugate. The tracer had higher uptake in non-PSMA expressing tissue, like the liver, compared to previously published pypa-PSMA tracers with other radiometals ^{44}Sc and ^{111}In, suggesting compound instability. It is possible to infer from these results that $[^{201}Tl]$Tl-pypa-PSMA is unstable, and the metal is reduced, leading to dissociation from the chelator. This provides a reason for the background uptake, but the lack of heart accumulation suggests this degradation occurs during excretion. Only $[^{201}Tl]Tl^{3+}$ released in the first few minutes would give a biodistribution matching $[^{201}Tl]$TlCl.

6 CONCLUSIONS AND FUTURE DIRECTIONS

As described in Chapter 2, the oxidation reaction of $[^{201}Tl]Tl^{+}$ to $[^{201}Tl]Tl^{3+}$ has been greatly improved from what has been previously reported in the literature. The iodobead method is a simple procedure using mild reaction conditions, that has the possibility for use with sensitive biomolecules. This would not be possible with the previous literature methods, as they use concentrated HCl, strong oxidising agents and high temperatures which will decompose biomolecules like peptides or antibodies. This allowed the DNA damaging potential of $[^{201}Tl]Tl^{3+}$ as well as $[^{201}Tl]Tl^{+}$ to be evaluated using a cell free isolated DNA method (Chapter 3). These experiments demonstrated that both oxidation states can cause SSBs and DSBs within 144 hours of incubation.

Once this optimised oxidation was established, a large number of chelators were screened with $[^{nat/201}Tl]Tl^{3+}$, as shown in Chapter 4. The information obtained from these studies has provided further details on which donor atoms Tl^{3+} has a preference for, as well as the total number of donors. The $[^{nat}Tl]Tl$-pypa complex was investigated the most thoroughly, and the $[^{201}Tl]Tl^{3+}$ complex was shown to have increased stability in human serum compared to the previously reported $[^{201}Tl]Tl^{3+}$ complexes with DTPA, EDTA and DOTA. A number of other $[^{201}Tl]Tl^{3+}$ complexes have shown good serum stability and will need further work to validate.

Combining work from the oxidation work in Chapter 2 and H_4pypa data within Chapter 4, a PSMA targeting bioconjugate was synthesised, incorporating H_4pypa via a lipophilic linker to the PSMA targeting vector. The H_4pypa-PSMA was radiolabelled with $[^{201}Tl]Tl^{3+}$, then evaluated in healthy male SCID/beige mice and the biodistribution compared to $[^{201}Tl]TlCl$ and $[^{201}Tl]TlCl_3$ showing very different biodistributions. Further *in vivo* studies were carried out again in male SCID/beige mice but bearing DU145 PSMA positive and PSMA negative tumours. In the PSMA positive

tumours, the tumour:background ratio was significantly higher than the PSMA negative tumours (if the very necrotic tumour is removed). The results also suggest compound instability, so further chelator development is needed.

Future directions could continue with the pursuit of suitable chelators for Tl^{3+}, as well as expand towards Tl^{+}, or non-bioconjugate methods of targeting radioactive thallium to tumours.

6.1 The pursuit for a Tl^{3+} chelator

From the data presented in Chapter 4 and 5, there are a number of other chelators that show encouraging data meaning they may be a superior chelator to H_4pypa for Tl^{3+}. For example, H_5decapa and H_4neunpa-NH_2 showed excellent stability in human serum after an hour incubation. Future steps for this project would be to synthesise the bioconjugate versions of the chelators (Scheme 5), using the same linker and targeting vector and performed the same DU145 PSMA positive and negative mouse models, to compare results with H_4pypa-PSMA. The bioconjugate version of H_5decapa would be very structurally similar to the bioconjugate in Scheme 5, so is worth investigating further. Additionally, H_4picoopa, H_2amidohox and H_4tetrapa-NH_2 all had favourable radiolabelling conditions, so their ^{201}Tl complex stabilities should be evaluated in serum.

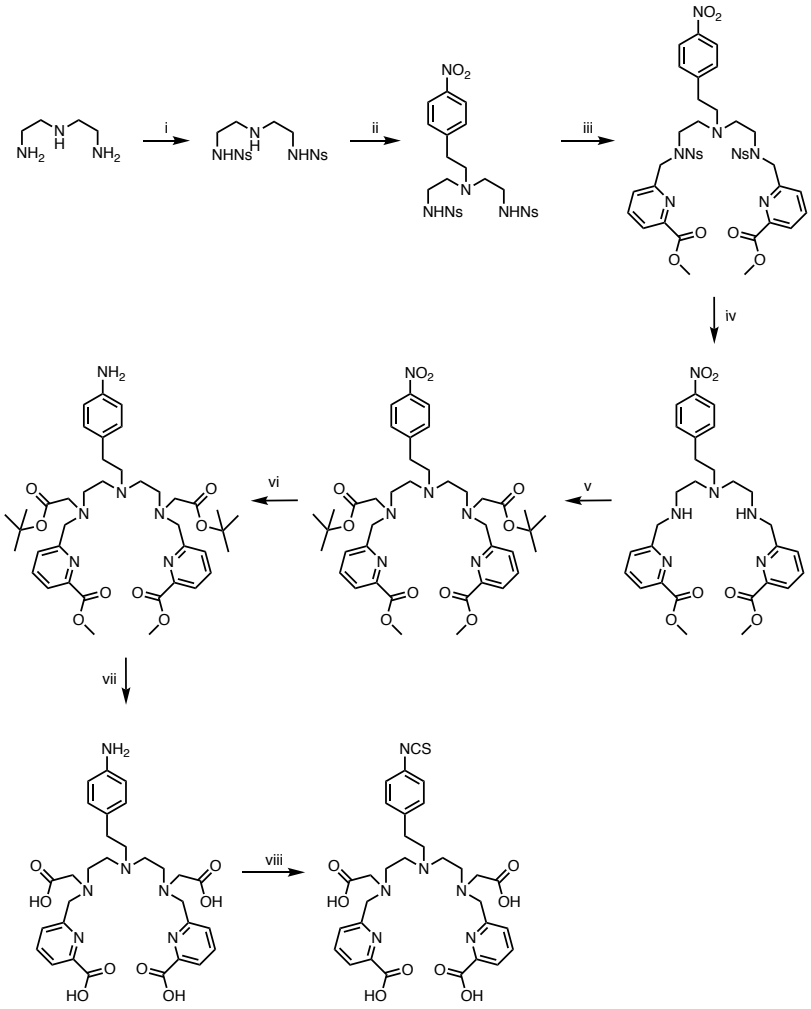

Scheme 5 – (i) NsCl, Na_2CO_3, THF (ii) 4-(2-bromoethyl)nitrobenzene, K_2CO_3, DMF (iii) methyl-6-bromomethylpicolinate, Na_2CO_3, DMF (iv) thiophenol, K_2CO_3, THF (v) *tertbutyl*-bromoacetate, Na_2CO_3, MeCN (vi) glacial acetic acid, Pd/C (10 %), (vii) LiOH, THF/H_2O (3:1) (viii) $SCCl_2$, DCM/H_2O.

The structure of H_2macropa and Py-Macrodipa can be seen in Figure 6.1. Justin Wilson's group have made a range of ligands based on these structures and tested them with a large number of metals, including $[^{223}Ra]Ra^{2+}$, $[^{225}Ac]Ac^{3+}$, $[^{nat}Gd]Gd^{3+}$ and $[^{nat}Lu]Lu^{3+}$.[250–258] These chelators have been shown to have rapid radiolabelling kinetics and form very inert complexes which are stable *in vitro* and *in vivo*. These metals have comparable ionic radii to Tl^{3+}, so are worth investigating with ^{201}Tl in the future. Additionally, bifunctional versions of a number of macropa

derivatives have previously been published, also taking advantage of an isothiocyanate coupling, so could use the same linker-PSMA used with H_4pypa as in Chapter 5.

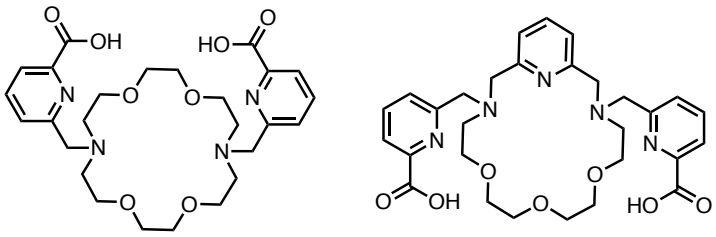

H_2macropa **Py-Macrodipa**

Figure 6.1 – The structure of H_2macropa and Py-Macrodipa

6.2 The pursuit of a Tl^+ chelator

As mentioned in the introduction (Chapter 1), [2,2,2]-crytands have been investigated for use with $[^{203}Pb]Pb^{2+}$. Due to the comparable ionic radii with $[^{201}Tl]Tl^+$, cryptands should be investigated for use with Tl^+. In collaboration with Dr Angelo Frei, the bioconjugate in Figure 6.2 has been synthesised for evaluation with $[^{201}Tl]Tl^+$. Dr Frei has performed NMR studies demonstrating that the chelator binds $[^{nat}Tl]Tl^+$ so further evaluation will be needed. As well as this, H_2macropa and Py-Macrodipa have also chelated metals with a similar ionic radius to $[^{nat}Tl]Tl^+$ as should also be investigated for use with the 1+ metal.

Unlike with $[^{201}Tl]Tl^{3+}$ agents, the possible bioreduction will not be an issue, which has been the largest stumbling block for the majority of the chelators screened.

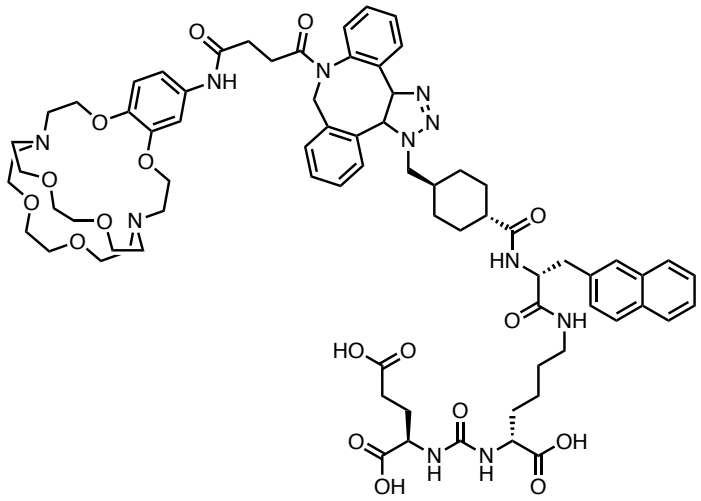

Figure 6.2 – The structure of the [2,2,2]-cryptand bioconjugate developed by Dr Angelo Frei

7 REFERENCE LIST

1 C. T. Winkelmann, S. M. Krause, P. J. McCracken, D. W. Brammer and J. G. Gelovani, *Nonhuman Primates in Biomedical Research, Volume 2 (2nd Edition)*, 2012.

2 F. Der Van Have, B. Vastenhouw, R. M. Ramakers, W. Branderhorst, J. O. Krah, C. Ji, S. G. Staelens and F. J. Beekman, U-SPECT-II: An ultra-high-resolution device for molecular small-animal imaging, *J. Nucl. Med.*, 2009, **50**, 599–605.

3 K. Charlton, The Supply of Medical Radioisotopes, *POSTNOTE*, 2017, 1–6.

4 A. Dash, F. F. Knapp and M. R. A. Pillai, Industrial radionuclide generators: A potential step towards accelerating radiotracer investigations in industry, *RSC Adv.*, 2013, **3**, 14890–14909.

5 M. D. Bartholomä, A. S. Louie, J. F. Valliant and J. Zubieta, Technetium and gallium derived radiopharmaceuticals: Comparing and contrasting the chemistry of two important radiometals for the molecular imaging era, *Chem. Rev.*, 2010, **110**, 2903–2920.

6 H. S. Stern, J. G. McAfee and G. Subramanian, Preparation, distribution and utilization of technetium-99m-sulfur colloid., *J. Nucl. Med.*, 1966, **7**, 665–675.

7 W. C. Eckelman, Unparalleled Contribution of Technetium-99m to Medicine Over 5 Decades, *JACC Cardiovasc. Imaging*, 2009, **2**, 364–368.

8 R. E. Boyd, Technetium-99m generators-The available options, *Int. J. Appl. Radiat. Isot.*, 1982, **33**, 801–809.

9 European Association of Nuclear Medicine (EANM), Radiopharmacy: an Update, *Technol.*

Guid.

10 A. E. Theobald and C. B. Sampson, *Sampson's textbook of radiopharmacy.*, 2010.

11 A. J. Chang, R. A. De Silva and S. E. Lapi, Development and Characterization of 89 Zr-Labeled Panitumumab for Immuno–Positron Emission Tomographic Imaging of the Epidermal Growth Factor Receptor, *Mol Imaging*, 2013, **12**, 17–27.

12 M. Ovacik and K. Lin, Tutorial on Monoclonal Antibody Pharmacokinetics and Its Considerations in Early Development, *Clin. Transl. Sci.*, 2018, **11**, 540–552.

13 M. Mumtaz, L. S. Lin, K. C. Hui and A. S. Mohd Khir, Radioiodine I-131 for the therapy of graves' disease., *Malays. J. Med. Sci.*, 2009, **16**, 25–33.

14 J. Strosberg, G. El-Haddad, E. Wolin, A. Hendifar, J. Yao, B. Chasen, E. Mittra, P. L. Kunz, M. H. Kulke, H. Jacene, D. Bushnell, T. M. O'Dorisio, R. P. Baum, H. R. Kulkarni, M. Caplin, R. Lebtahi, T. Hobday, E. Delpassand, E. Van Cutsem, A. Benson, R. Srirajaskanthan, M. Pavel, J. Mora, J. Berlin, E. Grande, N. Reed, E. Seregni, K. Öberg, M. Lopera Sierra, P. Santoro, T. Thevenet, J. L. Erion, P. Ruszniewski, D. Kwekkeboom and E. Krenning, Phase 3 Trial of ^{177} Lu-Dotatate for Midgut Neuroendocrine Tumors, *N. Engl. J. Med.*, 2017, **376**, 125–135.

15 A. Dash, M. R. A. Pillai and F. F. Knapp, Production of ^{177}Lu for Targeted Radionuclide Therapy: Available Options, *Nucl. Med. Mol. Imaging (2010).*, 2015, **49**, 85–107.

16 F. Buchegger, F. Perillo-Adamer, Y. M. Dupertuis and A. Bischof Delaloye, Auger radiation targeted into DNA: A therapy perspective, *Eur. J. Nucl. Med. Mol. Imaging*, 2006, **33**, 1352–1363.

17 M. Fjalling, P. Andersson, E. Forssell-Aronsson, J. Grétarsdóttir, V. Johansson, L. E. Tisell, B. Wängberg, O. Nilsson, G. Berg, A. Michanek, G. Lindstedt and H. Ahlman, Systemic Radionuclide Therapy Using Indium- 111- DTPA-D-Phe1-Octreotide in Midgut Carcinoid Syndrome, *J Nuci Med*, 1996, **37**, 1519–1521.

18 J. Grudzinski, I. Marsh, B. Titz, J. Jeffery, M. Longino, K. Kozak, K. Lange, J. Larrabee, A. Weichmann, A. Moser and B. Bednarz, CLR 125 Auger Electrons for the Targeted Radiotherapy of Triple-Negative Breast Cancer, *Cancer Biother. Radiopharm.*, 2018, **33**, 87–95.

19 M. F. bin Othman, E. Verger, I. Costa, M. Tanapirakgul, M. S. Cooper, C. Imberti, V. J. Lewington, P. J. Blower and S. Y. A. Terry, In vitro cytotoxicity of Auger electron-emitting [67Ga]Ga-trastuzumab, *Nucl. Med. Biol.*, 2020, **80**–**81**, 57–64.

20 M. F. bi. Othman, N. R. Mitry, V. J. Lewington, P. J. Blower and S. Y. A. Terry, Re-assessing gallium-67 as a therapeutic radionuclide, *Nucl. Med. Biol.*, 2017, **46**, 12–18.

21 V. Sopik and S. A. Narod, The relationship between tumour size, nodal status and distant metastases: on the origins of breast cancer, *Breast Cancer Res. Treat.*, 2018, **170**, 647–656.

22 J. P. Mach, S. Carrel, C. Merenda, B. Sordat and J. C. Cerottini, In vivo localisation of radiolabelled antibodies to carcinoembryonic antigen in human colon carcinoma grafted into nude mice, *Nature*, 1974, **248**, 704–706.

23 F. J. Primus, R. MacDonald and H. J. Hansen, Localization of GW-39 Human Tumors in Hamsters by Affinity-purified Antibody to Carcinoembryonic Antigen, *Cancer Res.*, 1977, **37**, 1544–1547.

24 D. M. Goldenberg, Advancing role of radiolabeled antibodies in the therapy of cancer, *Cancer Immunol. Immunother.*, 2003, **52**, 281–296.

25 J. ME, Radioimmunotherapy of B-Cell Non-Hodgkin's Lymphoma: From Clinical Trials to Clinical Practice Malik, *J. Nucl. Med.*, 2002, **43**, 1507–1529.

26 C. Hindorf, D. Emfietzoglou, O. Lindén, K. Kostarelos and S. E. Strand, Internal microdosimetry for single cells in radioimmunotherapy of B-cell lymphoma, *Cancer Biother. Radiopharm.*, 2005, **20**, 224–230.

27 J. Elgqvist, S. Frost, J. P. Pouget and P. Albertsson, The potential and hurdles of targeted alpha therapy - clinical trials and beyond, *Front. Oncol.*, 2014, **4 JAN**, 1–9.

28 J. L. Humm and L. M. Cobb, Nonuniformity of tumor dose in radioimmunotherapy, *J. Nucl. Med.*, 1990, **31**, 75–83.

29 T. K. Nikula, M. R. McDevitt, R. D. Finn, C. Wu, R. W. Kozak, K. Garmestani, M. W. Brechbiel, M. J. Curcio, C. G. Pippin, L. Tiffany-Jones, M. W. Geerlings, C. Apostolidis, R. Molinet, M. W. Geerlings, O. A. Gansow and D. A. Scheinberg, Alpha-emitting bismuth cyclohexylbenzyl DTPA constructs of recombinant humanized anti-CD33 antibodies: Pharmacokinetics, bioactivity, toxicity and chemistry, *J. Nucl. Med.*, 1999, **40**, 166–176.

30 S. Nilsson, R. H. Larsen, S. D. Fosså, L. Balteskard, K. W. Borch, J. E. Westlin, G. Salberg and Ø. S. Bruland, First clinical experience with α-emitting radium-223 in the treatment of skeletal metastases, *Clin. Cancer Res.*, 2005, **11**, 4451–4459.

31 D. Wild, M. Frischknecht, H. Zhang, A. Morgenstern, F. Bruchertseifer, J. Boisclair, A. Provencher-Bolliger, J. C. Reubi and H. R. Maecke, Alpha- versus beta-particle radiopeptide therapy in a human prostate cancer model (213Bi-DOTA-PESIN and 213Bi-

AMBA versus 177Lu-DOTA-PESIN), *Cancer Res.*, 2011, **71**, 1009–1018.

32 A. I. Kassis, Therapeutic Radionuclides: Biophysical and Radiobiologic Principles, *Semin. Nucl. Med.*, 2008, **38**, 358–366.

33 P. C. Chan, E. Lisco, H. Lisco and S. J. Adelstein, The Radiotoxicity of Iodine-125 in Mammalian Cells, *Radiat. Res.*, 1976, **67**, 332–343.

34 H. Burki, C. Koch and S. Wolff, Molecular suicide studies of 125I and 3H disintegration in the DNA of Chinese hamster cells., *Curr Top Radiat Res Q*, 1977, **12**, 408–425.

35 U. Hennrich and K. Kopka, Lutathera®: The first FDA-and EMA-approved radiopharmaceutical for peptide receptor radionuclide therapy, *Pharmaceuticals*, , DOI:10.3390/ph12030114.

36 J. Strosberg, G. El-Haddad, E. Wolin, A. Hendifar, J. Yao, B. Chasen, E. Mittra, P. L. Kunz, M. H. Kulke, H. Jacene, D. Bushnell, T. M. O'Dorisio, R. P. Baum, H. R. Kulkarni, M. Caplin, R. Lebtahi, T. Hobday, E. Delpassand, E. Van Cutsem, A. Benson, R. Srirajaskanthan, M. Pavel, J. Mora, J. Berlin, E. Grande, N. Reed, E. Seregni, K. Öberg, M. Lopera Sierra, P. Santoro, T. Thevenet, J. L. Erion, P. Ruszniewski, D. Kwekkeboom and E. Krenning, Phase 3 Trial of 177 Lu-Dotatate for Midgut Neuroendocrine Tumors , *N. Engl. J. Med.*, 2017, **376**, 125–135.

37 A. I. Kassis and S. J. Adelstein, Radiobiologic principles in radionuclide therapy, *J. Nucl. Med.*, 2005, **46**, 4–13.

38 J. P. Pouget, L. Santoro, L. Raymond, N. Chouin, M. Bardiès, C. Bascoul-Mollevi, H. Huguet, D. Azria, P. O. Kotzki, M. Pèlegrin, E. Vivès and A. Pèlegrin, Cell membrane is a more sensitive target than cytoplasm to dense ionization produced by auger electrons, *Radiat.*

Res., 2008, **170**, 192–200.

39 S. Paillas, R. Ladjohounlou, C. Lozza, A. Pichard, V. Boudousq, M. Jarlier, S. Sevestre, M. Le Blay, E. Deshayes, J. Sosabowski, T. Chardès, I. Navarro-Teulon, R. J. Mairs and J. P. Pouget, Localized Irradiation of Cell Membrane by Auger Electrons Is Cytotoxic Through Oxidative Stress-Mediated Nontargeted Effects, *Antioxidants Redox Signal.*, 2016, **25**, 467–484.

40 H. A. Macapinlac, N. Kemeny, F. Daghighian, R. Finn, J. Zhang, J. Humm, O. Squire and S. M. Larson, Pilot clinical trial of 5-[125I]iodo-2'-deoxyuridine in the treatment of colorectal cancer metastatic to the liver, *J Nucl Med*.

41 C. Rebischung, D. Hoffmann, L. Stéfani, M. D. Desruet, K. Wang, S. J. Adelstein, X. Artignan, F. Vincent, A. S. Gauchez, H. Zhang, D. Fagret, J. Vuillez, A. I. Kassis and J. Balosso, First human treatment of resistant neoplastic meningitis by intrathecal administration of MTX Plus 125IUdR, *Int. J. Radiat. Biol.*, 2008, **84**, 1123–1129.

42 A. Ku, V. J. Facca, Z. Cai and R. M. Reilly, Auger electrons for cancer therapy – a review, *EJNMMI Radiopharm. Chem.*, , DOI:10.1186/s41181-019-0075-2.

43 L. Li, T. S. Quang, E. J. Gracely, J. H. Kim, J. G. Emrich, T. E. Yaeger, J. M. Jenrette, S. C. Cohen, P. Black and L. W. Brady, A phase II study of anti-epidermal growth factor receptor radioimmunotherapy in the treatment of glioblastoma multiforme, *J. Neurosurg.*, 2010, **113**, 192–198.

44 L. J. Hofland and S. W. J. Lamberts, Somatostatin receptors and disease: Role of receptor subtypes, *Baillieres. Clin. Endocrinol. Metab.*, 1996, **10**, 163–176.

45 E. P. Krenning, M. De Jong, P. P. M. Kooij, W. A. P. Breeman, W. H. Bakker, W. W. De

Herder, C. H. J. Van Eijck, D. J. Kwekkeboom, F. Jamar, S. Pauwels and R. Valkema, Radiolabelled somatostatin analogue(s) for peptide receptor scintigraphy and radionuclide therapy, *Ann. Oncol.*, 1999, **10**, S23–S30.

46 R. Valkema, M. De Jong, W. H. Bakker, W. A. P. Breeman, P. P. M. Kooij, P. J. Lugtenburg, F. H. De Jong, A. Christiansen, B. L. R. Kam, W. W. De Herder, M. Stridsberg, J. Lindemans, G. Ensing and E. P. Krenning, Phase I study of peptide receptor radionuclide therapy with [111In-DTPA0]octreotide: The Rotterdam experience, *Semin. Nucl. Med.*, 2002, **32**, 110–122.

47 G. S. Limouris, A. Chatziioannou, D. Kontogeorgakos, D. Mourikis, M. Lyra, P. Dimitriou, A. Stavraka, A. Gouliamos and L. Vlahos, Selective hepatic arterial infusion of In-111-DTPA-Phe1- octreotide in neuroendocrine liver metastases, *Eur. J. Nucl. Med. Mol. Imaging*, 2008, **35**, 1827–1837.

48 S. Y. A. Terry and K. A. Vallis, Relationship between chromatin structure and sensitivity to molecularly targeted auger electron radiation therapy, *Int. J. Radiat. Oncol. Biol. Phys.*, 2012, **83**, 1298–1305.

49 S. Aghevlian, Y. Lu, M. A. Winnik, D. W. Hedley and R. M. Reilly, Panitumumab Modified with Metal-Chelating Polymers (MCP) Complexed to 111 In and 177 Lu - An EGFR-Targeted Theranostic for Pancreatic Cancer, *Mol. Pharm.*, 2018, **15**, 1150–1159.

50 D. L. Costantini, K. McLarty, H. Lee, S. J. Done, K. A. Vallis and R. M. Reilly, Antitumor effects and normal-tissue toxicity of111In-nuclear localization sequence-trastuzumab in Athymic mice bearing HER-positive human breast cancer xenografts, *J. Nucl. Med.*, 2010, **51**, 1084–1091.

51 M. E. Caplin, W. Mielcarek, J. R. Buscombe, A. L. Jones, P. L. Croasdale, M. S. Cooper, A. K. Burroughs and A. J. Hilson, Toxicity of high-activity 111in-octreotide therapy in patients with disseminated neuroendocrine tumours, *Nucl. Med. Commun.*, 2000, **21**, 97–102.

52 A. S. Kassis AI, Fayad F, Kinsey BM, Sastry KS, Taube RA, Radiotoxicity of 125I in mammalian cells, *Radiat Res.*, 1987, **111**, 305–318.

53 R. M. Reilly, R. Kiarash, R. G. Cameron, N. Porlier, J. Sandhu, R. P. Hill, K. Vallis, A. Hendler and J. Gariépy, 111In-labeled EGF is selectively radiotoxic to human breast cancer cells overexpressing EGFR, *J. Nucl. Med.*, 2000, **41**, 429–438.

54 L. Song, N. Falzone and K. A. Vallis, EGF-coated gold nanoparticles provide an efficient nano-scale delivery system for the molecular radiotherapy of EGFR-positive cancer, *Int. J. Radiat. Biol.*, 2016, **92**, 716–723.

55 R. M. Reilly, P. Chen, J. Wang, D. Scollard, R. Cameron and K. A. Vallis, Preclinical pharmacokinetic, biodistribution, toxicology, and dosimetry studies of 111In-DTPA-human epidermal growth factor: An auger electron-emitting radiotherapeutic agent for epidermal growth factor receptor-positive breast cancer, *J. Nucl. Med.*, 2006, **47**, 1023–1031.

56 T. A. Slastnikova, E. Koumarianou, A. A. Rosenkranz, G. Vaidyanathan, T. N. Lupanova, A. S. Sobolev and M. R. Zalutsky, Modular nanotransporters: A versatile approach for enhancing nuclear delivery and cytotoxicity of Auger electron-emitting 125I, *EJNMMI Res.*, 2012, **2**, 1–10.

57 J. A. Violet, G. Farrugia, C. Skene, J. White, P. Lobachevsky and R. Martin, Triple targeting of Auger emitters using octreotate conjugated to a DNA-binding ligand and a nuclear

localizing signal, *Int. J. Radiat. Biol.*, 2016, **92**, 707–715.

58 B. Lippert, *Cisplatin: Chemistry and Biochemistry of a Leading Anticancer Drug*, 2006.

59 B. Rosenberg, Fundamental studies with cisplatin., *Cancer*, 1985, **55**, 2303-l6.

60 A. M. Osman, E. M. El-Sayed, E. El-Demerdash, A. Al-Hyder, M. El-Didi, A. S. Attia and F. M. A. Hamada, Prevention of cisplatin-induced nephrotoxicity by methimazole, *Pharmacol. Res.*, 2000, **41**, 113–119.

61 R. C. Lange, R. P. Spencer and H. C. Harder, The antitumor agent cis-Pt(NH3)2Cl2: Distribution and dose calculations for 193mPt and 195mPt, *J. Nucl. Med.*, 1972, **14**, 191–195.

62 M. Sathekge, J. Wagener, S. V. Smith, N. Soni, B. Marjanovic-Painter, C. Zinn, C. Van de Wiele, Y. D'Asseler, G. Perkins and J. R. Zeevaart, Biodistribution und dosimetrie von 195mPt-cisplatin bei gesunden probanden bildgebendes radionuklid für die einzelphotonen-emissionscomputertomographie, *NuklearMedizin*, 2013, **52**, 222–227.

63 B. Pang, X. Qiao, L. Janssen, A. Velds, T. Groothuis, R. Kerkhoven, M. Nieuwland, H. Ovaa, S. Rottenberg, O. Van Tellingen, J. Janssen, P. Huijgens, W. Zwart and J. Neefjes, Drug-induced histone eviction from open chromatin contributes to the chemotherapeutic effects of doxorubicin, *Nat. Commun.*, 2013, **4**, 1908–1913.

64 S. Imstepf, V. Pierroz, P. Raposinho, M. Bauwens, M. Felber, T. Fox, A. B. Shapiro, R. Freudenberg, C. Fernandes, S. Gama, G. Gasser, F. Motthagy, I. R. Santos and R. Alberto, Nuclear Targeting with an Auger Electron Emitter Potentiates the Action of a Widely Used Antineoplastic Drug, *Bioconjug. Chem.*, 2015, **26**, 2397–2407.

65 L. M. Ickenstein, K. Edwards, S. Sjöberg, J. Carlsson and L. Gedda, A novel 125I-labeled daunorubicin derivative for radionuclide-based cancer therapy, *Nucl. Med. Biol.*, 2006, **33**, 773–783.

66 S. A. Jannetti, G. Carlucci, B. Carney, S. Kossatz, L. Shenker, L. M. Carter, B. Salinas, C. Brand, A. Sadique, P. L. Donabedian, K. M. Cunanan, M. Gönen, V. Ponomarev, B. M. Zeglis, M. M. Souweidane, J. S. Lewis, W. A. Weber, J. L. Humm and T. Reiner, PARP-1-targeted radiotherapy in mouse models of glioblastoma, *J. Nucl. Med.*, 2018, **59**, 1225–1233.

67 A. Ray Chaudhuri and A. Nussenzweig, The multifaceted roles of PARP1 in DNA repair and chromatin remodelling, *Nat. Rev. Mol. Cell Biol.*, 2017, **18**, 610–621.

68 H. L. Ko and E. C. Ren, Functional aspects of PARP1 in DNA repair and transcription, *Biomolecules*, 2012, **2**, 524–548.

69 T. C. Wilson, S. A. Jannetti, N. Guru, N. Pillarsetty, T. Reiner and G. Pirovano, Improved radiosynthesis of 123I-MAPi, an auger theranostic agent, *Int. J. Radiat. Biol.*, 2020, **0**, 000.

70 G. Pirovano, S. A. Jannetti, L. M. Carter, A. Sadique, S. Kossatz, N. Guru, P. D. de Souza França, M. Maeda, B. M. Zeglis, J. S. Lewis, J. L. Humm and T. Reiner, Targeted brain tumor radiotherapy using an auger emitter, *Clin. Cancer Res.*, 2020, **26**, 2871–2881.

71 C. J. Shen, I. Minn, R. F. Hobbs, Y. Chen, A. Josefsson, M. Brummet, S. R. Banerjee, C. F. Brayton, R. C. Mease, M. G. Pomper and A. P. Kiess, Auger radiopharmaceutical therapy targeting prostate-specific membrane antigen in a micrometastatic model of prostate cancer, *Theranostics*, 2020, **10**, 2888–2896.

72 A. P. Kiess, I. Minn, Y. Chen, R. Hobbs, G. Sgouros, R. C. Mease, M. Pullambhatla, C. J.

Shen, C. A. Foss and M. G. Pomper, Auger radiopharmaceutical therapy targeting prostate-specific membrane antigen, *J. Nucl. Med.*, 2015, **56**, 1401–1407.

73 Y. Chen, C. A. Foss, Y. Byun, S. Nimmagadda, M. Pullambhatla, J. J. Fox, M. Castanares, S. E. Lupold, J. W. Babich, R. C. Mease and M. G. Pomper, Radiohalogenated prostate-specific membrane antigen (PSMA)-based ureas as imaging agents for prostate cancer, *J. Med. Chem.*, 2008, **51**, 7933–7943.

74 A. Fasih, H. Fonge, Z. Cai, J. V. Leyton, I. Tikhomirov, S. J. Done and R. M. Reilly, 111In-Bn-DTPA-nimotuzumab with/without modification with nuclear translocation sequence (NLS) peptides: An Auger electron-emitting radioimmunotherapeutic agent for EGFR-positive and trastuzumab (Herceptin)-resistant breast cancer, *Breast Cancer Res. Treat.*, 2012, **135**, 189–200.

75 D. L. Costantini, C. Chan, Z. Cai, K. A. Vallis and R. M. Reilly, 111In-labeled trastuzumab (Herceptin) modified with nuclear localization sequences (NLS): An auger electron-emitting radiotherapeutic agent for HER2/neu-amplified breast cancer, *J. Nucl. Med.*, 2007, **48**, 1357–1368.

76 R. Ladjohounlou, C. Lozza, A. Pichard, J. Constanzo, J. Karam, P. Le Fur, E. Deshayes, V. Boudousq, S. Paillas, M. Busson, M. Le Blay, M. Jarlier, S. Marcatili, M. Bardies, F. Bruchertseifer, A. Morgenstern, J. Torgue, I. Navarro-Teulon and J. P. Pouget, Drugs that modify cholesterol metabolism alter the p38/JNK-mediated targetedand nontargeted response to alpha and auger radioimmunotherapy, *Clin. Cancer Res.*, 2019, **25**, 4775–4790.

77 G. Ngo Ndjock Mbong, Y. Lu, C. Chan, Z. Cai, P. Liu, A. J. Boyle, M. A. Winnik and R. M. Reilly, Trastuzumab labeled to high specific activity with 111in by site-specific

conjugation to a metal-chelating polymer exhibits amplified auger electron-mediated cytotoxicity on HER2-positive breast cancer cells, *Mol. Pharm.*, 2015, **12**, 1951–1960.

78 T. Das, S. Chakraborty, S. Banerjee and M. Venkatesh, On the preparation of a therapeutic dose of 177Lu-labeled DOTA-TATE using indigenously produced 177Lu in medium flux reactor, *Appl. Radiat. Isot.*, 2007, **65**, 301–308.

79 R. L. Siegel, K. D. Miller and A. Jemal, Cancer statistics, 2018, *CA. Cancer J. Clin.*, 2018, **68**, 7–30.

80 M. Nguyen-Nielsen and M. Borre, Diagnostic and Therapeutic Strategies for Prostate Cancer, *Semin. Nucl. Med.*, 2016, **46**, 484–490.

81 U. Elasser-Beile, P. Buhler and P. Wolf, Targeted therapies for prostate cancer against the prostate specific antigen, *Curr. Drug Targets*, 2009, **10**, 118–125.

82 S. F. Slovin, Targeting castration-resistant prostate cancer with monoclonal antibodies and constructs, *Immunotherapy*, 2013, **5**, 1347–1355.

83 A. Barve, W. Jin and K. Cheng, Prostate Cancer Relevant Antigens and Enzymes for Targeted Drug Delivery, *J Control Release*, 2014, **20**, 1-7118–132.

84 W. Diao, H. Cai, L. Chen, X. Jin, X. Liao and Z. Jia, Recent advances in Prostate-Specific Membrane Antigen-Based Radiopharmaceuticals, *Curr. Top. Med. Chem.*, 2019, **19**, 33–56.

85 M. Zaviacic, M. Ruzicková, J. Jakubovský, L. Danihel, P. Babál and J. Blazeková, The significance of prostate markers in the orthology of the female prostate, *Bratisl. Lek. List.*, 1994, **95**, 491–497.

86 R. Sokoloff, K. C. Norton, C. L. Gasior, K. M. Marker and L. S. Grauer, A dual-monoclonal sandwich assay for prostate-specific membrane antigen: Levels in tissues, seminal fluid and urine, *Prostate*, 2000, **43**, 150–157.

87 P. M. Smith-Jones, S. Vallabahajosula, S. J. Goldsmith, V. Navarro, C. J. Hunter, D. Bastidas and N. H. Bander, In vitro characterization of radiolabeled monoclonal antibodies specific for the extracellular domain of prostate-specific membrane antigen, *Cancer Res.*, 2000, **60**, 5237–5243.

88 P. M. Smith-Jones, S. Vallabhajosula, S. St. Omer, V. Navarro, S. J. Goldsmith and N. H. Bander, 177Lu-DOTA-HuJ591: A new radiolabeled monoclonal antibody (MAb) for targeted therapy of prostate cancer, *J. Label. Compd. Radiopharm.*, 2001, **44**, S90–S92.

89 S. Vallabhajosula, P. M. Smith-Jones, V. Navarro, S. J. Goldsmith and N. H. Bander, Radioimmunotherapy of Prostate Cancer in Human Xenografts Using Monoclonal Antibodies Specific to Prostate Specific Membrane Antigen (PSMA): Studies in Nude Mice, *Prostate*, 2004, **58**, 145–155.

90 D. J. George, M. R. McDevitt, E. Barendswaard, D. Ma, L. Lai, M. J. Curcio, G. Sgouros, A. M. Ballangrud, W. H. Yang, R. D. Finn, V. Pellegrini, J. Geerlings, M. Lee, M. W. Brechbiel, N. H. Bander, C. Cordon-Cardo and D. A. Scheinberg, An α-particle emitting antibody ([213Bi]J591) for radioimmmunotherapy of prostate cancer, *Prostate J.*, 2001, **3**, 1.

91 S. Hammer, U. B. Hagemann, S. Zitzmann-Kolbe, A. Larsen, C. Ellingsen, S. Geraudie, D. Grant, B. Indrevoll, R. Smeets, O. Von Ahsen, A. Kristian, P. Lejeune, H. Hennekes, J. Karlsson, R. M. Bjerke, O. B. Ryan, A. S. Cuthbertson and D. Mumberg, Preclinical efficacy of a PSMA-targeted thorium-227 conjugate (PSMA-TTC), a targeted alpha therapy for prostate cancer, *Clin. Cancer Res.*, 2020, **26**, 1985–1996.

92 S. M. Hillier, K. P. Maresca, F. J. Femia, J. C. Marquis, C. A. Foss, N. Nguyen, C. N. Zimmerman, J. A. Barrett, W. C. Eckelman, M. G. Pomper, J. L. Joyal and J. W. Babich, Preclinical evaluation of novel glutamate-urea-lysine analogues that target prostate-specific membrane antigen as molecular imaging pharmaceuticals for prostate cancer, *Cancer Res.*, 2009, **69**, 6932–6940.

93 K. P. Maresca, S. M. Hillier, F. J. Femia, D. Keith, C. Barone, J. L. Joyal, C. N. Zimmerman, A. P. Kozikowski, J. A. Barrett, W. C. Eckelman and J. W. Babich, A series of halogenated heterodimeric inhibitors of prostate specific membrane antigen (PSMA) as radiolabeled probes for targeting prostate cancer, *J. Med. Chem.*, 2009, **52**, 347–357.

94 K. Kopka, M. Benešová, C. Bařinka, U. Haberkorn and J. Babich, Glu-ureido-based inhibitors of prostate-specific membrane antigen: Lessons learned during the development of a novel class of low-molecular-weight theranostic radiotracers, *J. Nucl. Med.*, 2017, **58**, 17S-26S.

95 M. Czerwińska, A. Bilewicz, M. Kruszewski, A. Wegierek-Ciuk and A. Lankoff, Targeted radionuclide therapy of prostate cancer-from basic research to clinical perspectives, *Molecules*, 2020, **25**, 1–32.

96 M. Benesová, M. Schäfer, U. Bauder-Wüst, A. Afshar-Oromieh, C. Kratochwil, W. Mier, U. Haberkorn, K. Kopka and M. Eder, Preclinical evaluation of a tailor-made DOTA-conjugated PSMA inhibitor with optimized linker moiety for imaging and endoradiotherapy of prostate cancer, *J. Nucl. Med.*, 2015, **56**, 914–920.

97 C. Kratochwil, F. L. Giesel, M. Eder, A. Afshar-Oromieh, M. Benešová, W. Mier, K. Kopka and U. Haberkorn, [177Lu]Lutetium-labelled PSMA ligand-induced remission in a patient with metastatic prostate cancer, *Eur. J. Nucl. Med. Mol. Imaging*, 2015, **42**, 987–988.

98 H. Ahmadzadehfar, E. Eppard, S. Kürpig, R. Fimmers, A. Yordanova, C. D. Schlenkhoff, F. Gärtner, S. Rogenhofer and M. Essler, Therapeutic response and side effects of repeated radioligand therapy with 177Lu-PSMA-DKFZ-617 of castrate-resistant metastatic prostate cancer, *Oncotarget*, 2016, **7**, 12477–12488.

99 M. S. Hofman, J. Violet, R. J. Hicks, J. Ferdinandus, S. Ping Thang, T. Akhurst, A. Iravani, G. Kong, A. Ravi Kumar, D. G. Murphy, P. Eu, P. Jackson, M. Scalzo, S. G. Williams and S. Sandhu, [177 Lu]-PSMA-617 radionuclide treatment in patients with metastatic castration-resistant prostate cancer (LuPSMA trial): a single-centre, single-arm, phase 2 study, *Lancet Oncol.*, 2018, **19**, 825–833.

100 F. E. Von Eyben, A. Singh, J. Zhang, K. Nipsch, D. Meyrick, N. Lenzo, K. Kairemo, T. Joensuu, I. Virgolini, C. Soydal, H. R. Kulkarni and R. P. Baum, 177Lu-PSMA radioligand therapy of predominant lymph node metastatic prostate cancer, *Oncotarget*, 2019, **10**, 2451–2461.

101 M. D. Oliver Sartor, P. D. Johann de Bono, M.B., Ch.B., M. D. Kim N. Chi, P. D. Karim Fizazi, M.D., M. D. Ken Herrmann, M. D. Kambiz Rahbar, M. D. Scott T. Tagawa, M. D. Luke T. Nordquist, M. D. Nitin Vaishampayan, M. D. Ghassan El-Haddad, M. D. Chandler H. Park, M. D. Tomasz M. Beer, M. D. Alison Armour, M.B., Ch.B., P. D. Wendy J. Pérez-Contreras, M.P.A., Michelle DeSilvio, P. D. Euloge Kpamegan, P. D. Germo Gericke, M.D., M. D. Richard A. Messmann, M.D., M.H.S., Michael J. Morris and M. D. Bernd J. Krause, Lutetium-177–PSMA-617 for Metastatic Castration-Resistant Prostate Cancer, *N. Engl. J. Med.*, 2021, **385**, 1091–1103.

102 Novartis, FDA grants Priority Review for investigational targeted radioligand therapy 177Lu-PSMA-617 for patients with metastatic castration-resistant prostate cancer (mCRPC).

103 O. Sartor, J. de Bono, K. N. Chi, K. Fizazi, K. Herrmann, K. Rahbar, S. T. Tagawa, L. T. Nordquist, N. Vaishampayan, G. El-Haddad, C. H. Park, T. M. Beer, A. Armour, W. J. Pérez-Contreras, M. DeSilvio, E. Kpamegan, G. Gericke, R. A. Messmann, M. J. Morris and B. J. Krause, Lutetium-177–PSMA-617 for Metastatic Castration-Resistant Prostate Cancer, *N. Engl. J. Med.*, 2021, **385**, 1091–1103.

104 C. Kratochwil, F. Bruchertseifer, F. L. Giesel, M. Weis, F. A. Verburg, F. Mottaghy, K. Kopka, C. Apostolidis, U. Haberkorn and A. Morgenstern, 225Ac-PSMA-617 for PSMA-targeted a-radiation therapy of metastatic castration-resistant prostate cancer, *J. Nucl. Med.*, 2016, **57**, 1941–1944.

105 C. Kratochwil, F. Bruchertseifer, H. Rathke, M. Hohenfellner, F. L. Giesel, U. Haberkorn and A. Morgenstern, Targeted a-therapy of metastatic castration-resistant prostate cancer with 225 Ac-PSMA-617: Swimmer-Plot Analysis Suggests efficacy regarding duration of tumor control, *J. Nucl. Med.*, 2018, **59**, 795–802.

106 M. Sathekge, F. Bruchertseifer, O. Knoesen, F. Reyneke, I. Lawal, T. Lengana, C. Davis, J. Mahapane, C. Corbett, M. Vorster and A. Morgenstern, 225Ac-PSMA-617 in chemotherapy-naive patients with advanced prostate cancer: a pilot study, *Eur. J. Nucl. Med. Mol. Imaging*, 2019, **46**, 129–138.

107 M. Sathekge, F. Bruchertseifer, M. Vorster, I. O. Lawal, O. Knoesen, J. Mahapane, C. Davis, F. Reyneke, A. Maes, C. Kratochwil, T. Lengana, F. L. Giesel, C. van de Wiele and A. Morgenstern, Predictors of overall and disease-free survival in metastatic castration-resistant prostate cancer patients receiving 225Ac-PSMA-617 radioligand therapy, *J. Nucl. Med.*, 2020, **61**, 62–69.

108 M. Sathekge, O. Knoesen, M. Meckel, M. Modiselle, M. Vorster and S. Marx, 213Bi-PSMA-

617 targeted alpha-radionuclide therapy in metastatic castration-resistant prostate cancer, *Eur. J. Nucl. Med. Mol. Imaging*, 2017, **44**, 1099–1100.

109 C. Müller, C. A. Umbricht, N. Gracheva, V. J. Tschan, G. Pellegrini, P. Bernhardt, J. R. Zeevaart, U. Köster, R. Schibli and N. P. van der Meulen, Terbium-161 for PSMA-targeted radionuclide therapy of prostate cancer, *Eur. J. Nucl. Med. Mol. Imaging*, 2019, **46**, 1919–1930.

110 A. Mckillop and E. C. Tayler, Recent Advances in Organothallium Chemistry, *Advacne Organomet. Chem.*, 1973, **11**, 147–206.

111 J. B. Cavanagh, N. H. Fuller, H. R. . Johnson and P. Rudge, The Effects of Thallium Salts, with Particular Reference to the Nervous System Changes: A REPORT OF THREE CASES, *QJM An Int. J. Med.*, 1974, **43**, 293–319.

112 J. C. Munch, Human thallotoxicosis, *J. Am. Med. As- sociation*, 1934, **102**, 1929–1934.

113 D. Reed, J. Crawley, S. J. Pieper and L. T. Kurland, Thallotoxicosis: Acute Manifestations and Sequelae, *JAMA J. Am. Med. Assoc.*, 1963, **183**, 516–522.

114 E. Browning, *Toxicity of Industrial Metals*, 1961.

115 H. . Schelbert, H. Henning, P. Rigo, D. Chauncey, R. O'Rourre and W. L. Ashburn, Considerations of 201Tl as a Myocardial Radionuclide Imaging Agent in Man, *Invest. Radiol.*, 1976, **11**, 163–171.

116 P. R. Bradley-Moore, E. Lebowitz, M. W. Greene, H. L. Atkins and A. N. Ansari, Thallium-201 for medical use. II:Biologic Behavior, *J. Nucl. Med.*

117 L. J. MULLINS and R. D. MOORE, The movement of thallium ions in muscle., *J. Gen.*

Physiol., 1960, **43**, 759–773.

118 P. J. Gehring and P. B. Hammond, THE INTERRELATIONSHIP BETWEEN THALLIUM AND POTASSIUM IN ANIMALS, *J. Pharmacol. Exp. Ther.*, 1967, **155**, 187–201.

119 P. J. Gehring and P. B. Hammond, THE UPTAKE OF THALLIUM BY RABBIT ERYTHROCYTES, *J. Pharmacol. Exp. Ther.*, 1964, **145**, 215–221.

120 M. Sessler, P. Geck, F. Maul, G. Hor and D. Munz, New aspects of cellular thallium uptake: Tl+-Na+-2Cl(–)-cotransport is the central mechanism of ion uptake, *Nukl.*, 1986, **25**, 24–27.

121 D. J. Pennell, S. R. Underwood, D. Campos Costa and P. J. Ell, *Thallium myocardial perfusion tomography in clinical cardiology*, Springer Science & Business Media, 2012, 1992.

122 P. J. Cannon, M. B. Weiss and W. J. Casarella, Studies of regional myocardial blood flow: Results in patients with left anterior descending coronary artery disease, *Semin. Nucl. Med.*, 1976, **6**, 279–303.

123 H. F. Weich, H. W. Strauss and B. Pitt, The extraction of thallium 201 by the myocardium, *Circulation*, 1977, **56**, 188–191.

124 H. L. Atkins, T. F. Budinger, E. Lebowitz, A. N. Ansari, M. W. Greene, R. G. Fairchild and K. J. Ellis, Thallium-201 for medical use. Part 3: Human distribution and physical imaging properties., *J. Nucl. Med.*, 1977, **18**, 133–140.

125 N. D. CHARKES, D. M. SKLAROFF, J. GERSHON-COHEN and R. E. CANTOR, Tumor Scanning With Radioactive 131-Cesium., *J. Nucl. Med.*, 1965, **6**, 300–306.

126 E. Lebowitz, A. N. Ansari, P. Richards and E. Belgrave, Thallium-201 For Medical Use I, *J. Nucl. Med.*, 1974, **16**, 151–155.

127 P. H. Cox, A. J. Belfer and W. B. Van Der Pompe, Thallium 201 chloride uptake in tumours, a possible complication in heart scintigraphy, *Br. J. Radiol.*, 1976, **49**, 767–768.

128 C. I. Caluser, H. M. Abdel-Dayem, H. A. Macapinlac, A. Scott, J. H. Healey, A. Huvos, H. Kalaigian, S. D. J. Yeh and S. M. Larson, The value of thallium and three-phase bone scans in the evaluation of bone and soft tissue sarcomas, *Eur. J. Nucl. Med.*, 1994, **21**, 1198–1205.

129 W. D. Kaplan, T. Takvorian and J. H. Morris, Thallium-201 brain tumor imaging: A comparative study with pathologic correlation, *J. Nucl. Med.*, 1987, **28**, 47–52.

130 L. Ramanna, A. Waxman, G. Binney, S. Waxman, J. Mirra and G. Rosen, Thallium-201 Scintigraphy in Bone Sarcoma : Comparison with Gallium-67 and Technetium-MDP in the Evaluation of Chemotherapeutic response, *J. Nucl. Med.*, 1990, **31**, 567–572.

131 A. I. Kassis, S. J. Adelstein, C. Haydock and K. S. R. Sastry, Thallium-201: An experimental and a theoretical radiobiological approach to dosimetry, *J. Nucl. Med.*, 1983, **24**, 1164–1175.

132 R. W. Howell, Radiation spectra for Auger-Electron emitting radionuclides: Report No. 2 of AAPM Nuclear Medicine Task Group No. 6, *Med. Phys.*, 1992, **19**, 1371–1383.

133 R. Salim and P. Taherparvar, Monte Carlo single-cell dosimetry using Geant4-DNA: the effects of cell nucleus displacement and rotation on cellular S values, *Radiat. Environ. Biophys.*, 2019, **58**, 353–371.

134 N. Falzone, B. Q. Lee, J. M. Fernandez-Varea, C. Kartsonaki, A. E. Stuchbery, T. Kibedi and K. A. Vallis, Absorbed dose evaluation of Auger electron-emitting radionuclides: impact of input decay spectra on dose point kernels and S-values, *Phys. Med. Biol.*, 2017, **62**, 2239–2253.

135 N. Falzone, J. M. Fernández-Varea, G. Flux and K. A. Vallis, Monte Carlo evaluation of Auger electron-emitting theranostic radionuclides, *J. Nucl. Med.*, 2015, **56**, 1441–1446.

136 S. M. Mahdi and S. B. Babak, Dosimetry study on Auger electron-emitting nuclear medicine radioisotopes in micrometer and nanometer scales using Geant4-DNA simulation, *Int. J. Radiat. Biol.*, 2020, **96**, 1452–1465.

137 K. M. Osytek, P. J. Blower, I. M. Costa, G. E. Smith, V. Abbate and S. Y. A. Terry, In vitro proof of concept studies of radiotoxicity from Auger electron-emitter thallium-201., *EJNMMI Res.*, 2021, **11**, 63.

138 M. F. bi. Othman, N. R. Mitry, V. J. Lewington, P. J. Blower and S. Y. A. Terry, Re-assessing gallium-67 as a therapeutic radionuclide, *Nucl. Med. Biol.*, 2017, **46**, 12–18.

139 G. M. Segall and M. J. Davis, Prone versus supine thallium myocardial SPECT: a method to decrease artifactual inferior wall defects., *J. Nucl. Med.*, 1989, **30**, 548–55.

140 A. V. Mudring and F. Rieger, Lone pair effect in thallium(I) macrocyclic compounds, *Inorg. Chem.*, 2005, **44**, 6240–6243.

141 F. A. Cotton, G. Wilkinson, C. A. Murillo and M. Bochmann, *Advanced Inorganic Chemistry*, 1999.

142 Y. Nagame, H. Nakahara and Y. Murakami, Production of thallium-199 by alpha

bombardment of gold, *Int. J. Appl. Radiat. Isot.*, 1976, **30**, 669–672.

143 V. I. Chernov, S. V Triss, V. S. Skuridin and Y. B. Lishmanov, Thallium-199: a new radiopharmaceutical for myocardial perfusion imaging, *Int. J. Card. Imaging*, 1996, **12**, 119–126.

144 T. I. Kostelnik and C. Orvig, Radioactive Main Group and Rare Earth Metals for Imaging and Therapy, *Chem. Rev.*, , DOI:10.1021/acs.chemrev.8b00294.

145 E. W. Price and C. Orvig, Matching chelators to radiometals for radiopharmaceuticals, *Chem. Soc. Rev.*, 2014, **43**, 260–290.

146 A. J. Blake, D. Fenske, W. Li, V. Lippolis and M. Schröder, Cadmium(II), bismuth(III), lead(II) and thallium(I) crown thioether chemistry: synthesis and crystal structures of [(CdI2)2([24]aneS8)], [(BiCl3)2([24]aneS8)], [Pb2 ([28]aneS8)][ClO4]4 and [Tl([24]aneS8)]-PF6 ([24]aneS8 = 1,4,7,10,13,16,19,22-octathiacy, *J. Chem. Soc., Dalt. Trans.,* 1998, 3961–3968.

147 F. Wiesbrock and H. Schmidbaur, Complexity of coordinative bonding in thallium(I) anthranilates and salicylates, *J. Am. Chem. Soc.*, 2003, **125**, 3622–3630.

148 N. N. Greenwood and A. Earnshaw, *Chemistry of the Elements*, 1997.

149 A. G. Lee, The coordination chemistry of thallium(I), *Coord. Chem. Rev.*, 1972, **8**, 289–349.

150 M. Ouchi and T. Hakushi, *Coord. Chem. Rev.*, 1996, 148, 171–181.

151 H. Tamura, K. Kimura and T. Shono, THALLIUM(I)-SELECTIVE PVC MEMBRANE ELECTRODES BASED ON BIS(CROWN ETHER)S, *J. Electroanal. Chem.*, 1980, **115**, 115–121.

152 A. J. Blake, J. A. Greig and M. Schroder, Thallium thioether chemistry. Synthesis and

crystal structure of [Tl[9]aneS, *J. Chem. Soc. Dalt. Trans.*, 1991, 529–532.

153 A. J. Blake, G. Reid and M. Schroder, Thallium Macrocyclic Chemistry: Synthesis and Crystal Structures of [Tl([18]aneN2S4)]PF6 and [Tl([18]aneS6)]PF6 ([18]aneN2S4 = 1,4,10,13-tetrathia-7,16-diazacyclooctadecane, [18]aneS6 = 1,4,7,10,13,16-hexathiacyclooctadecane), *J. Chem. Soc., Dalt. Trans.,* 1992, 2987–2992.

154 R. D. Shannon, Revised effective ionic radii and systematic studies of interatomic distances in halides and chalcogenides, *Acta Crystallogr. Sect. A*, 1976, **32**, 751–767.

155 A. Vyth, P. J. Fennema and J. B. van der Schoot, 201Tl-diethyldithiocarbamate: a possible radiopharmaceutical for brain imaging, *Pharm. Weekbl. Sci. Ed.*, 1983, **5**, 213–216.

156 P. J. Gawne, F. Clarke, K. Turjeman, A. P. Cope, N. J. Long, Y. Barenholz, S. Y. A. Terry and R. T. M. de Rosales, PET imaging of liposomal glucocorticoids using 89Zr-oxine: Theranostic applications in inflammatory arthritis, *Theranostics*, 2020, **10**, 3867–3879.

157 F. Man, P. J. Gawne and R. T.M. de Rosales, Nuclear imaging of liposomal drug delivery systems: A critical review of radiolabelling methods and applications in nanomedicine, *Adv. Drug Deliv. Rev.*, 2019, **143**, 134–160.

158 J. Pellico, P. J. Gawne and R. T. M. De Rosales, Radiolabelling of nanomaterials for medical imaging and therapy, *Chem. Soc. Rev.*, 2021, **50**, 3355–3423.

159 J. F. de Bruine, E. A. van Royen, A. Vyth, J. M. B. V de Jong and J. B. Van Der Schoot, Thallium-201 Diethyldithiocarbamate : An Alternative to Iodine-123 N-isopropyl-p-iodoamphetamine, *J. Nucl. Med.*, 1985, **26**, 925–931.

160 E. A. van Royen, J. F. de Bruïne, T. C. Hill, A. Vyth, M. Limburg, B. L. Byse, D. H. O'Leary, J.

M. de Jong, A. Hijdra and J. B. van der Schoot, Cerebral blood flow imaging with thallium-201 diethyldithiocarbamate SPECT, *J. Nucl. Med.*, 1987, **28**, 178–183.

161 N. M. Hijnen, A. de Vries, R. Blange, D. Burdinski and H. Grull, Synthesis and in vivo evaluation of 201Tl(III)-DOTA complexes for applications in SPECT imaging, *Nucl. Med. Biol.*, 2011, **38**, 585–592.

162 T. Fodor, I. Bányai, A. Bényei, C. Platas-Iglesias, M. Purgel, G. L. Horváth, L. Zékány, G. Tircsó and I. Tóth, [TIIII(dota)]: An extraordinarily robust macrocyclic complex, *Inorg. Chem.*, 2015, **54**, 5426–5437.

163 J. Blixt, J. Glaser, P. Solymosi and I. Toth, Equilibria and Dynamics of Tl(edta)X2-Complexes (X = Halide, Pseudohalide) Studied By Multinuclear NMR, *Inorg. Chem.*, 1992, **31**, 5299–5297.

164 S. Musso, G. Anderegg, H. Riiegger, C. W. Schläpfer and V. Gramlich, Mixed-Ligand Chelate Complexes of Thallium(III), Characterized by Equilibrium Measurements, NMR and Raman Spectroscopy, and X-ray Crystallography, *Inorg. Chem.*, 1995, **34**, 3329–3338.

165 A. R. Jalilian, A. Khorrami, M. B. Tavakoli, M. Kamali-Dehghan and Y. Y. Kamrani, Development of [201Tl](III)-DTPA-human polyclonal antibody complex for inflammation detection, *Radiochim. Acta*, 2007, **95**, 669–675.

166 G. S. Sivagurunathan, K. Ramalingam and C. Rizzoli, Nanothallium(III) sulfide from dithiocarbamate precursors: Synthesis, single crystal X-ray structures and characterization, *Polyhedron*, 2013, **65**, 316–321.

167 N. Alexander, K. Ramalingam and C. Rizzoli, Supramolecularly linked linear polymers of thallium(I) dithiocarbamates: Steric influence on the supramolecular interactions of

methyl and ethylcyclohexyl dithiocarbamates of thallium(I), *Inorganica Chim. Acta*, 2011, **365**, 480–483.

168 T. Brotin, D. Cavagnat, P. Berthault, R. Montserret and T. Buffeteau, Water-soluble molecular capsule for the complexation of cesium and thallium cations, *J. Phys. Chem. B*, 2012, **116**, 10905–10914.

169 T. Brotin, S. Goncalves, P. Berthault, D. Cavagnat and T. Buffeteau, Influence of the cavity size of water-soluble cryptophanes on their binding properties for cesium and thallium cations, *J. Phys. Chem. B*, 2013, **117**, 12593–12601.

170 L. L. Chapellet, J. P. Dognon, M. Jean, N. Vanthuyne, P. Berthault, T. Buffeteau and T. Brotin, Experimental and Theoretical Study of the Complexation of Cesium and Thallium Cations by a Water-Soluble Cryptophane, *ChemistrySelect*, 2017, **2**, 5292–5300.

171 T. Brotin, P. Berthault, D. Pitrat and J. C. Mulatier, Selective Capture of Thallium and Cesium by a Cryptophane Soluble at Neutral pH, *J. Org. Chem.*, 2020, **85**, 9622–9630.

172 A. W. McDonagh, B. L. McNeil, B. O. Patrick and C. F. Ramogida, Synthesis and Evaluation of Bifunctional [2.2.2]-Cryptands for Nuclear Medicine Applications, *Inorg. Chem.*, 2021, **60**, 10030–10037.

173 A. R. Jalilian, Y. Yari-Kamrani, M. Kamali-Dehghan and S. Rajabifar, Preparation and evaluation of [201Tl](III)-DTPA complex for cell labeling, *J. Radioanal. Nucl. Chem.*, 2008, **275**, 109–114.

174 A. R. Jalilian, M. Akhlaghi, B. Shirazi, R. Aboudzadeh, G. Raisali, M. Salouti and M. Babaii, [201Tl](III)-bleomyein for tumor imaging, *Radiochim. Acta*, 2006, **94**, 453–459.

175 A. R. Jalilian, M. A. Hosseini, A. Karimian, F. Saddadi and M. Sadeghi, Preparation and biodistribution of [^{201}Tl](III)vancomycin complex in normal rats, *Nukleonika*, 2006, **51**, 203–208.

176 A. R. Jalilian, Y. Yari-Kamrani, M. Kamali-Dehghan and S. Rajabifar, Preparation and evaluation of [201Tl](III)-DTPA complex for cell labeling, *J. Radioanal. Nucl. Chem.*, 2008, **275**, 109–114.

177 Y. Fazaeli, A. R. Jalilian, S. Feizi and N. Shadanpour, Development of a radiothallium (III) labeld porphyrin complex as a potential imaging agent, *Radiochim. Acta*, 2013, **101**, 795–800.

178 A. J. Alexander and D. E. Hughes, Monitoring of IgG Antibody Thermal Stability by Micellar Electrokinetic Capillary Chromatography and Matrix-Assisted Laser Desorption/Ionization Mass Spectrometry, *Anal. Chem.*, 1995, **67**, 3626–3632.

179 C. Nowak, J. K. Cheung, S. M. Dellatore, A. Katiyar, R. Bhat, J. Sun, G. Ponniah, A. Neill, B. Mason, A. Beck and H. Liu, Forced degradation of recombinant monoclonal antibodies: A practical guide, *MAbs*, 2017, **9**, 1217–1230.

180 G. Gaza-Bulseco and H. Liu, Fragmentation of a recombinant monoclonal antibody at various pH, *Pharm. Res.*, 2008, **25**, 1881–1890.

181 V. Kumar, Evaluation of stannous oxidation in the preparation of ultrahigh-purity 99m Tc(V)-DMSA., *Nucl. Med. Commun.*, 2001, **22**, 1261–1266.

182 J. D. Young, V. Abbate, C. Imberti, L. K. Meszaros, M. T. Ma, S. Y. A. Terry, R. C. Hider, G. E. Mullen and P. J. Blower, ^{68} Ga-THP-PSMA: A PET Imaging Agent for Prostate Cancer Offering Rapid, Room-Temperature, 1-Step Kit-Based Radiolabeling, *J. Nucl. Med.*, 2017,

58, 1270–1277.

183 Y. Fazaeli, A. R. Jalilian, M. M. Amini, K. Ardaneh, A. Rahiminejad, F. Bolourinovin, S. Moradkhani and A. Majdabadi, Development of a 68Ga-Fluorinated Porphyrin Complex as a Possible PET Imaging Agent, *Nucl. Med. Mol. Imaging (2010).*, 2012, **46**, 20–26.

184 V. Bocci, Efficient Labelling of Tissue-soluble Proteins with Iodine-Ill using Chloramine T, *Nature*, 1964, **203**, 985–986.

185 A. Jalilian, I. Atomic, E. Agency, M. Sciences and M. Sciences, Preparation and evaluation of [201Tl](III) - DTPA-HIgG for inflammation detection Preparation and evaluation of [Tl](III) -DTPA-HIgG for inflammation detection, *Iran J. Radiat. Res.*, 2006, **4**, 105–114.

186 W. H. Koppenol, The reduction potential of the couple O3/O3-, *FEBS Lett.*, 1982, **140**, 169–172.

187 F. C. Greenwood, W. M. Hunter and J. S. Glover, The Preparation of I-131-Labelled Human Growth Hormone of High Specific, *Biochem. J.*, 1963, **89**, 114–123.

188 P. J. Blower, M. R. B. Puncher, A. G. Kettle, S. George, S. Dorsch, A. Leak, L. H. Naylor and M. J. O'Doherty, Iodine-123 salmon calcitonin, an imaging agent for calcitonin receptors: Synthesis, biodistribution, metabolism and dosimetry in humans, *Eur. J. Nucl. Med.*, 1998, **25**, 101–108.

189 A. R. Vasudeva Murphy and B. Sanjiva Rao F.A.Sc, Oxidaiton By Chloramine-T, *Proc. Indian Acad. Sci. - Sect. A*, 1951, **35**, 459–464.

190 U. Tilstam and H. Weinmann, Trichloroisocyanuric acid: A safe and efficient oxidant, *Org. Process Res. Dev.*, 2002, **6**, 384–393.

191 M. R. Gill and K. A. Vallis, Transition metal compounds as cancer radiosensitizers, *Chem. Soc. Rev.*, 2019, **48**, 540–557.

192 P. Balagurumoorthy, K. Chen, S. J. Adelstein and A. I. Kassis, Auger electron-induced double-strand breaks depend on DNA topology., *Radiat. Res.*, 2008, **170**, 70–82.

193 S. K. Sahu, A. I. Kassis, G. M. Makrigiorgos, J. Baranowska-Kortylewicz and S. J. Adelstein, The effects of indium-111 decay on pBR322 DNA, *Radiat Res*, 1995, **141**, 193–198.

194 J. Kotzerke, R. Punzet, R. Runge, S. Ferl, L. Oehme, G. Wunderlich and R. Freudenberg, 99mTc-labeled HYNIC-DAPI causes plasmid DNA damage with high efficiency, *PLoS One*, , DOI:10.1371/journal.pone.0104653.

195 P. Balagurumoorthy, S. James Adelstein and A. I. Kassis, Novel Method For Quantifying Radiation-Induced Single-Strand- Break Yields In Plasmid DNA Highlights Tenfold Discrepancy, *Anal. Biochem.*, 2011, **412**, 242–246.

196 E. Verger, J. Cheng, V. de Santis, M. Iafrate, J. A. Jackson, C. Imberti, G. O. Fruhwirth, P. J. Blower, M. T. Ma, D. R. Burnham and S. Y. A. Terry, Validation of the plasmid study to relate DNA damaging effects of radionuclides to those from external beam radiotherapy, *Nucl. Med. Biol.*, 2021, **100**–**101**, 36–43.

197 A. I. Kassis, R. S. Harapanhalli and S. J. Adelstein, Strand Breaks in Plasmid DNA after Positional Changes of Auger Electron-Emitting Iodine- 125: Direct Compared to Indirect Effects, *Radiat. Res.*, 1999, **152**, 530–538.

198 M. Terrissol, S. Edel and E. Pomplun, Computer evaluation of direct and indirect damage induced by free and DNA-bound Iodine-125 in the chromatin fibre, *Int. J. Radiat. Biol.*, 2004, **80**, 905–908.

199 P. N. Lobachevsky and R. F. Martin, Plasmid DNA breakage by decay of DNA-associated Auger emitters: Experiments with 123I/125I-iodoHoechst 33258, *Int. J. Radiat. Biol.*, 2004, **80**, 915–920.

200 C. A. Schneider, W. S. Rasband and K. W. Eliceiri, NIH Image to ImageJ: 25 years of image analysis, *Nat. Methods*, 2012, **9**, 671–675.

201 P. Balagurumoorthy, K. Chen, R. C. Bash, S. J. Adelstein and A. I. Kassis, Mechanisms underlying production of double-strand breaks in plasmid DNA after decay of 125I-Hoechst, *Radiat. Res.*, 2006, **166**, 333–344.

202 S. K. Sahu, Z. P. Kortylewicz, J. Baranowska-Kortylewicz, R. A. Taube, S. J. Adelstein and A. I. Kassis, Strand breaks after the decay of iodine-125 in proximity to plasmid pBR322 DNA, *Radiat. Res.*, 1997, **147**, 401–408.

203 A. I. Kassis and S. J. Adelstein, 5-[125I]iodo-2'-deoxyuridine in the radiotherapy of solid CNS tumors in rats, *Acta Oncol. (Madr).*, 1996, **35**, 935–939.

204 A. I. Kassis, A. M. Kirichian, K. Wang, E. S. Semnani and S. J. Adelstein, Therapeutic potential of 5-[125I]iodo-2'-deoxyuridine and methotrexate in the treatment of advanced neoplastic meningitis, *Int. J. Radiat. Biol.*, 2004, **80**, 941–946.

205 P. Balagurumoorthy, K. Wang, S. J. Adelstein and A. I. Kassis, DNA double-strand breaks induced by decay of 123I-labeled Hoechst 33342: Role of DNA topology, *Int. J. Radiat. Biol.*, 2008, **84**, 976–983.

206 F. Reissig, G. Wunderlich, R. Runge, R. Freudenberg, A. Lühr and J. Kotzerke, The effect of hypoxia on the induction of strand breaks in plasmid DNA by alpha-, beta- and Auger electron-emitters 223Ra, 188Re, 99mTc and DNA-binding 99mTc-labeled pyrene, *Nucl.*

Med. Biol., 2020, **80**–**81**, 65–70.

207 S. J. Adelstein and A. I. Kassis, Strand breaks in plasmid DNA following positional changes of Auger-electron-emitting radionuclides, *Acta Oncol. (Madr).*, 1996, **35**, 797–801.

208 A. I. Kassis, R. S. Harapanhalli and S. J. Adelstein, Comparison of strand breaks in plasmid DNA after positional changes of Auger electron-emitting iodine-125, *Radiat. Res.*, 1999, **151**, 167–176.

209 Y. Cheng, N. Korolev and L. Nordenskiöld, Similarities and differences in interaction of K+ and Na+ with condensed ordered DNA. A molecular dynamics computer simulation study, *Nucleic Acids Res.*, 2006, **34**, 686–696.

210 E. W. Price, J. F. Cawthray, G. A. Bailey, C. L. Ferreira, E. Boros, M. J. Adam and C. Orvig, H4octapa: An acyclic chelator for 111 In radiopharmaceuticals, *J. Am. Chem. Soc.*, 2012, **134**, 8670–8683.

211 E. W. Price, B. M. Zeglis, J. F. Cawthray, C. F. Ramogida, N. Ramos, J. S. Lewis, M. J. Adam and C. Orvig, H4octapa-trastuzumab: Versatile acyclic chelate system for In-111 and Lu-177 imaging and therapy, *J. Am. Chem. Soc.*, 2013, **135**, 12707–12721.

212 E. W. Price, B. M. Zeglis, J. S. Lewis, M. J. Adam and C. Orvig, H6phospa-trastuzumab: Bifunctional methylenephosphonate-based chelator with 89Zr, 111In and 177Lu, *J. Chem. Soc. Dalt. Trans.*, 2014, **43**, 119–131.

213 G. A. Bailey, E. W. Price, B. M. Zeglis, C. L. Ferreira, E. Boros, M. J. Lacasse, B. O. Patrick, J. S. Lewis, M. J. Adam and C. Orvig, H2azapa: A versatile acyclic multifunctional chelator for 67Ga, 64Cu, 111In, and 177Lu, *Inorg. Chem.*, 2012, **51**, 12575–12589.

214 L. Li, M. D. G. Jaraquemada-Peláez, H. T. Kuo, H. Merkens, N. Choudhary, K. Gitschtaler, U. Jermilova, N. Colpo, C. Uribe-Munoz, V. Radchenko, P. Schaffer, K. S. Lin, F. Bénard and C. Orvig, Functionally Versatile and Highly Stable Chelator for 111In and 177Lu: Proof-of-Principle Prostate-Specific Membrane Antigen Targeting, *Bioconjug. Chem.*, 2019, **30**, 1539–1553.

215 L. Li, M. D. G. Jaraquemada-Peláez, E. Aluicio-Sarduy, X. Wang, D. Jiang, M. Sakheie, H. T. Kuo, T. E. Barnhart, W. Cai, V. Radchenko, P. Schaffer, K. S. Lin, J. W. Engle, F. Bénard and C. Orvig, -: Thermodynamic Stability, Radiolabeling, and Biodistribution of a Prostate-Specific-Membrane-Antigen-Targeting Conjugate, *Inorg. Chem.*, 2020, **59**, 1985–1995.

216 D. S. Mendelson, M. S. Gordon, L. S. Rosen, H. Hurwitz, M. K. Wong, B. J. A. Alvarez, B. K. Seon, C. P. Theuer and B. R. Leigh, Phase I study of TRC105 (anti-CD105 [endoglin] antibody) therapy in patients with advanced refractory cancer., *J. Clin. Oncol.*, 2010, **28**, 3013.

217 F. H. Karzai, A. B. Apolo, L. Cao, R. A. Madan, D. E. Adelberg, H. Parnes, D. G. McLeod, N. Harold, C. Peer, Y. Yu, Y. Tomita, M. J. Lee, S. Lee, J. B. Trepel, J. L. Gulley, W. D. Figg and W. L. Dahut, A phase i study of TRC105 anti-endoglin (CD105) antibody in metastatic castration-resistant prostate cancer, *BJU Int.*, 2015, **116**, 546–555.

218 L. Li, M. de Guadalupe Jaraquemada-Peláez, E. Aluicio-Sarduy, X. Wang, T. E. Barnhart, W. Cai, V. Radchenko, P. Schaffer, J. W. Engle and C. Orvig, Coordination chemistry of [Y(pypa)]-and comparison immuno-PET imaging of [44Sc]Sc- And [86Y]Y-pypa-phenyl-TRC105, *Dalt. Trans.*, 2020, **49**, 5547–5562.

219 J. L. J. Dearling, S. D. Voss, P. Dunning, E. Snay, F. Fahey, S. V. Smith, J. S. Huston, C. F. Meares, S. T. Treves and A. B. Packard, Imaging cancer using PET - the effect of the

bifunctional chelator on the biodistribution of a 64Cu-labeled antibody, *Nucl. Med. Biol.*, 2011, **38**, 29–38.

220 S. A. Graves, R. Hernandez, J. Fonslet, C. G. England, H. F. Valdovinos, P. A. Ellison, T. E. Barnhart, D. R. Elema, C. P. Theuer, W. Cai, R. J. Nickles and G. W. Severin, Novel Preparation Methods of 52Mn for ImmunoPET Imaging, *Bioconjug. Chem.*, 2015, **26**, 2118–2124.

221 E. B. Ehlerding, C. A. Ferreira, E. Aluicio-Sarduy, D. Jiang, H. J. Lee, C. P. Theuer, J. W. Engle and W. Cai, 86/90 Y-Based Theranostics Targeting Angiogenesis in a Murine Breast Cancer Model, *Mol. Pharm.*, 2018, **15**, 2606–2613.

222 M. W. Brechbiel, Bifunctional chelates for metal nuclides, *Q. J. Nucl. Med. Mol. Imaging*, 2008, **52**, 166–173.

223 E. K. Sarbisheh and E. Price, *Radiopharmaceutical Chemistry, Springer International Publishing*, 2019.

224 M. G. Ferrier, Y. Li, M. K. Chyan, R. Wong, L. Li, S. Spreckelmeyer, D. K. Hamlin, T. Mastren, M. E. Fassbender, C. Orvig and D. S. Wilbur, Thorium chelators for targeted alpha therapy: Rapid chelation of thorium-226, *J. Label. Compd. Radiopharm.*, 2020, **63**, 502–516.

225 L. Southcott, X. Wang, L. Wharton, H. Yang, V. Radchenko, M. Kubeil, H. Stephan, M. de Guadalupe Jaraquemada-Peláez and C. Orvig, High denticity oxinate-linear-backbone chelating ligand for diagnostic radiometal ions [111In]In3+and [89Zr]Zr4+, *Dalt. Trans.*, 2021, **50**, 3874–3886.

226 E. K. Sarbisheh, A. K. Salih, S. J. Raheem, J. S. Lewis and E. W. Price, A High-Denticity Chelator Based on Desferrioxamine for Enhanced Coordination of Zirconium-89, *Inorg.*

Chem., 2020, **59**, 11715–11727.

227 D. Burdinski, J. Lub, J. A. Pikkemaat, D. Moreno Jalón, S. Martial and C. Del Pozo Ochoa, Triethylenetetramine penta- and hexa-acetamide ligands and their ytterbium complexes as paraCEST contrast agents for MRI, *Dalt. Trans.*, 2008, 4138–4151.

228 A. Ingham, T. I. Kostelnik, B. L. McNeil, B. O. Patrick, N. Choudhary, M. D. G. Jaraquemada-Peláez and C. Orvig, Getting a lead on Pb2+-amide chelators for 203/212Pb radiopharmaceuticals, *Dalt. Trans.*, 2021, **50**, 11579–11595.

229 U. Pandey, N. Gamre, S. P. Lohar and A. Dash, A systematic study on the utility of CHX-A''-DTPA-NCS and NOTA-NCS as bifunctional chelators for 177Lu radiopharmaceuticals, *Appl. Radiat. Isot.*, 2017, **127**, 1–6.

230 N. Oshima, H. Akizawa, H. Kitaura, H. Kawashima, S. Zhao, Y. Zhao, K. ichi Nishijima, Y. Kitamura, Y. Arano, Y. Kuge and K. Ohkura, 111In-DTPA-D-Phe− 1-Asp0-D-Phe1-octreotide exhibits higher tumor accumulation and lower renal radioactivity than 111In-DTPA-D-Phe1-octreotide, *Nucl. Med. Biol.*, 2017, **54**, 18–26.

231 L. Southcott, X. Wang, N. Choudhary, L. Wharton, B. O. Patrick, H. Yang, K. Zarschler, M. Kubeil, H. Stephan, M. D. G. Jaraquemada-Peláez and C. Orvig, H2pyhox - Octadentate Bis(pyridyloxine), *Inorg. Chem.*, 2021, **60**, 12186–12196.

232 N. Choudhary, H. Scheiber, J. Zhang, B. O. Patrick, M. De Guadalupe Jaraquemada-Peláez and C. Orvig, H4HBEDpa: Octadentate Chelate after A. E. Martell, *Inorg. Chem.*, 2021, **60**, 12855–12869.

233 N. Choudhary, K. E. Barrett, M. Kubeil, V. Radchenko, J. W. Engle, H. Stephan, M. De Guadalupe Jaraquemada-Peláez and C. Orvig, Metal ion size profoundly affects H3glyox

chelate chemistry, *RSC Adv.*, 2021, **11**, 15663–15674.

234 A. Hu, I. Keresztes, S. N. MacMillan, Y. Yang, E. Ding, W. R. Zipfel, R. A. Distasio, J. W. Babich and J. J. Wilson, Oxyaapa: A Picolinate-Based Ligand with Five Oxygen Donors that Strongly Chelates Lanthanides, *Inorg. Chem.*, 2020, **59**, 5116–5132.

235 L. Wharton, E. Kurakina, V. Radchenko, P. Schaffer and C. Orvig, Chemical Promiscuity of Non-Macrocyclic Multidentate Chelating Ligands for Radiometal Ions: H4neunpa-NH2vs H4noneunpa, *Inorg. Chem.*, 2021, **60**, 4076–4092.

236 E. W. Price, J. F. Cawthray, G. A. Bailey, C. L. Ferreira, E. Boros, M. J. Adam and C. Orvig, H4octapa: An acyclic chelator for 111In radiopharmaceuticals, *J. Am. Chem. Soc.*, 2012, **134**, 8670–8683.

237 L. S. Natrajan, N. M. Khoabane, B. L. Dadds, C. A. Muryn, R. G. Pritchard, S. L. Heath, A. M. Kenwright, I. Kuprov and S. Faulkner, Probing the structure, conformation, and stereochemical exchange in a family of lanthanide complexes derived from tetrapyridyl-appended cyclen, *Inorg. Chem.*, 2010, **49**, 7700–7709.

238 L. Allott, C. Da Pieve, J. Meyers, T. Spinks, D. M. Ciobota, G. Kramer-Marek and G. Smith, Evaluation of DFO-HOPO as an octadentate chelator for zirconium-89, *Chem. Commun.*, 2017, **53**, 8529–8532.

239 A. R. Jalilian, A. Hakimi, J. Garousi, F. Bolourinovin, M. Kamali-Dehghan and G. Aslani, Development of [201Tl](III) oxinate complex for in vitro cell labeling, *Iran. J. Radiat. Res.*, 2008, **6**, 145–150.

240 A. R. Jalilian, M. A. Hosseini, A. Majdabadi and F. Saddadi, Evaluation of [201 Tl](III) Vancomycin in normal rats, *Nucl. Med. Rev.*, 2008, **11**, 1–4.

241 M. Toma, A. Sánchez, J. Casas, J. Sordo, M. García-Tasende, E. Castellano, J. Ellena and I. Berdan, New thallium(III) chloride complexes with pyridine carboxylic acids: from molecular compounds to supramolecular associations, *Cent. Eur. J. Chem.*, 2003, **1**, 441–464.

242 A. Rigby, J. E. Blower, P. J. Blower, S. Y. A. Terry and V. Abbate, Targeted auger electron-emitter therapy: Radiochemical approaches for thallium-201 radiopharmaceuticals, *Nucl. Med. Biol.*, 2021, **98**–**99**, 1–7.

243 M. Benešová, U. Bauder-Wüst, M. Schäfer, K. D. Klika, W. Mier, U. Haberkorn, K. Kopka and M. Eder, Linker Modification Strategies to Control the Prostate-Specific Membrane Antigen (PSMA)-Targeting and Pharmacokinetic Properties of DOTA-Conjugated PSMA Inhibitors, *J. Med. Chem.*, 2016, **59**, 1761–1775.

244 H. T. Kuo, H. Merkens, Z. Zhang, C. F. Uribe, J. Lau, C. Zhang, N. Colpo, K. S. Lin and F. Bénard, Enhancing Treatment Efficacy of 177Lu-PSMA-617 with the Conjugation of an Albumin-Binding Motif: Preclinical Dosimetry and Endoradiotherapy Studies, *Mol. Pharm.*, 2018, **15**, 5183–5191.

245 G. M. Sheldrick, SHELXTL Version 5.1, *Bruker AXS Inc., Madison, Wisconsin, USA*.

246 G. M. Sheldrick, Crystal structure refinement with SHELXL, *Acta Crystallogr. Sect. C Struct. Chem.*, 2015, **71**, 3–8.

247 P. A. Duspara, M. S. Islam, A. J. Lough and R. A. Batey, Synthesis and reactivity of N -alkyl carbamoylimidazoles: Development of N -methyl carbamoylimidazole as a methyl isocyanate equivalent, *J. Org. Chem.*, 2012, **77**, 10362–10368.

248 F. Kampmeier, J. D. Williams, J. Maher, G. E. Mullen and P. J. Blower, Design and

preclinical evaluation of a 99mTc-labelled diabody of mAb j591 for SPECT imaging of prostate-specific membrane antigen (PSMA), *EJNMMI Res.*, 2014, **4**, 1–10.

249 P. F. Jackson, D. C. Cole, B. S. Slusher, S. L. Stetz, L. E. Ross, B. A. Donzanti and D. A. Trainor, Design, synthesis, and biological activity of a potent inhibitor of the neuropeptidase N-acetylated α-linked acidic dipeptidase, *J. Med. Chem.*, 1996, **39**, 619–622.

250 A. Hu, E. Aluicio-Sarduy, V. Brown, S. N. Macmillan, K. V. Becker, T. E. Barnhart, V. Radchenko, C. F. Ramogida, J. W. Engle and J. J. Wilson, Py-Macrodipa: A Janus Chelator Capable of Binding Medicinally Relevant Rare-Earth Radiometals of Disparate Sizes, *J. Am. Chem. Soc.*, 2021, **143**, 10429–10440.

251 D. J. Fiszbein, V. Brown, N. A. Thiele, J. J. Woods, L. Wharton, S. N. Macmillan, V. Radchenko, C. F. Ramogida and J. J. Wilson, Tuning the Kinetic Inertness of Bi3+Complexes: The Impact of Donor Atoms on Diaza-18-Crown-6 Ligands as Chelators for 213Bi Targeted Alpha Therapy, *Inorg. Chem.*, 2021, **60**, 9199–9211.

252 D. S. Abou, N. A. Thiele, N. T. Gutsche, A. Villmer, H. Zhang, J. J. Woods, K. E. Baidoo, F. E. Escorcia, J. J. Wilson and D. L. J. Thorek, Towards the stable chelation of radium for biomedical applications with an 18-membered macrocyclic ligand, *Chem. Sci.*, 2021, **12**, 3733–3742.

253 N. A. Thiele, D. J. Fiszbein, J. J. Woods and J. J. Wilson, Tuning the Separation of Light Lanthanides Using a Reverse-Size Selective Aqueous Complexant, *Inorg. Chem.*, 2020, **59**, 16522–16530.

254 A. Hu, S. N. MacMillan and J. J. Wilson, Macrocyclic Ligands with an Unprecedented Size-Selectivity Pattern for the Lanthanide Ions, *J. Am. Chem. Soc.*, 2020, **142**, 13500–13506.

255 E. Aluicio-Sarduy, N. A. Thiele, K. E. Martin, B. A. Vaughn, J. Devaraj, A. P. Olson, T. E. Barnhart, J. J. Wilson, E. Boros and J. W. Engle, Establishing Radiolanthanum Chemistry for Targeted Nuclear Medicine Applications, *Chem. - A Eur. J.*, 2020, **26**, 1238–1242.

256 N. A. Thiele, J. J. Woods and J. J. Wilson, Implementing f-block metal ions in medicine: tuning the size selectivity of expanded macrocycles, *Inorg. Chem.*, 2019, **58**, 10483–10500.

257 J. J. Wilson, M. Ferrier, V. Radchenko, J. R. Maassen, J. W. Engle, E. R. Batista, R. L. Martin, F. M. Nortier, M. E. Fassbender, K. D. John and E. R. Birnbaum, Evaluation of nitrogen-rich macrocyclic ligands for the chelation of therapeutic bismuth radioisotopes, *Nucl. Med. Biol.*, 2015, **42**, 428–438.

258 N. A. Thiele, V. Brown, J. M. Kelly, A. Amor-Coarasa, U. Jermilova, S. N. MacMillan, A. Nikolopoulou, S. Ponnala, C. F. Ramogida, A. K. H. Robertson, C. Rodríguez-Rodríguez, P. Schaffer, C. Williams, J. W. Babich, V. Radchenko and J. J. Wilson, An Eighteen-Membered Macrocyclic Ligand for Actinium-225 Targeted Alpha Therapy, *Angew. Chemie - Int. Ed.*, 2017, **56**, 14712–14717.